THÈSE DE DOCTORAT
DE L'UNIVERSITÉ PIERRE ET MARIE CURIE

Spécialité : Physique

École doctorale : « Physique en Île-de-France »

réalisée

dans le groupe Quantronique
SPEC - CEA Saclay
France

présentée par

Vivien SCHMITT

pour obtenir le grade de :

DOCTEUR DE L'UNIVERSITÉ PIERRE ET MARIE CURIE

Sujet de la thèse :

Design, fabrication and test of a four superconducting quantum-bit processor

soutenue le 3 septembre 2015

devant le jury composé de :

Pr.	Frank K. Wilhelm	Président du jury
Dr.	Olivier Buisson	Rapporteur
Pr.	Alexey Ustinov	Rapporteur
Dr.	Benjamin Huard	Examinateur
Dr.	Denis Vion	Membre invité
Dr.	Daniel Esteve	Directeur de thèse

A Céline

Remerciements

Ces quelques dernières années passées dans la chaleur du groupe Quantronique ont été une expérience hors du commun, et l'endroit rêvé pour faire une thèse, entouré de toutes ces personnalités tellement complètes et passionnées.

Je veux remercier chaleureusement l'ensemble du groupe Quantronique, que Daniel dirige d'une manière à y faire régner une ambiance si amicale et propice aux échanges.

Merci à tous les permanents ou assimilés du groupe, Cristian, Daniel, Denis, Fabien, Hélène, Hugues, Marcelo, Pascal, Patrice B., Patrice R., Philippe et Pief qui font l'âme de cette équipe.

Merci à Denis, pour le temps inestimable que tu as passé à essayer de me transmettre ta connaissance profonde de tout ou presque tout, je suis certain que ce sens du détail me sera encore très utile à l'avenir. Et un énorme merci pour avoir passé tant de temps à essayer de me rendre plus clair lors de mes exposés, je sais que cela a été un travail fastidieux.

Merci à Alexandre Blais et Baptiste Royer pour avoir éclairci quelques zones d'ombre dans les simulations de JBA.

Je veux aussi remercier toutes les personnes qui ont rendu cette thèse possible, l'administration et le secrétariat du SPEC ; tous les membres de l'atelier, Dominique, Jean-Claude et Vincent ; Pascal qui a su transcrire mes idées farfelues en pièces de mécanique ; Pief et Thomas dont j'ai largement abusé de la patience avec mes soucis de salle blanche.

Et enfin un grand merci à tous les jeunes membres du groupe que j'ai côtoyés, dans le désordre, Jean-Damien, Landry, Andreas, Cécile, Olivier, Kiddy, Camille, Chloé, Audrey, Pierre et Leandro, les moins jeunes aussi, Yui, Simon, Xin, Max, Romain, Michael, Carlès, Caglar, Sebastian et Marc ; vous avez énormément contribué à la bonne ambiance qui a toujours régnée dans le groupe.

Et enfin, pour avoir accepté mes aller-retours les dimanches matin, pour m'avoir supporté quand les choses fonctionnaient moins bien qu'espéré, et pour tout le reste, un grand merci à ma moitié, Céline.

La famille Quantronique fin 2013
De gauche à droite :
Kiddi, Caglar, Pascal, Michael, Pief, Daniel, Patrice, Camille, Yvan, Philippe, Patrice, Yui,
Hugues, Marcelo, Vivien, Olivier,
Fabien, Simon, Denis, Audrey, Cristian, Xin et Cécile

Contents

Chapter 1

Introduction: the making of superconducting quantum processors

The research reported in this thesis deals with the design, the fabrication and the test of superconducting processors with the aim of running, on simple cases, quantum codes overcoming classical ones.

1.1 The origins of quantum computing

1.1.1 From entanglement to quantum computing

The strong interest for quantum information dates back to the experimental demonstration of the violation of Bell inequalities in the early 1980s (see [1] and references therein to earlier work). These experiments shed light on the concept of entangled state first considered by Einstein, Podolski and Rosen when establishing their paradox [2]. An entangled state of two systems cannot be factorized in a product state of the two systems. It was established that EPR entangled pairs can be used to implement cryptography codes that could be perfectly safe [3, 4].

On the side of computing, a series of works thought about making a quantum Turing machine based on reversible dynamics. In a different direction, Feynman pointed out that given the difficulty to simulate the evolution of a quantum system with a classical computer, it would be very useful to build a universal quantum system able to simulate other ones [5]. The first blueprint for a universal digital quantum computer as we understand it now was proposed by Deutsch [6] in 1985. Such a machine performs the evolution of a register of two-level systems called quantum bits (qubits) using quantum logic gates operating on them. The interest for quantum computing raised significantly when quantum codes outperforming classical ones were proposed during the 1990s. In particular, Shor proposed a quantum algorithm able to factorize numbers

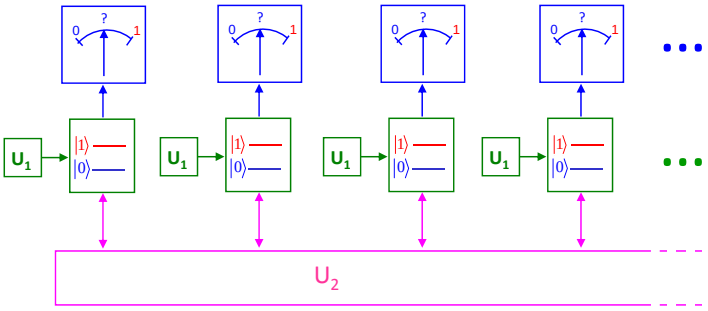

Figure 1.1: Sketch of a universal quantum processor. Any unitary evolution can be implemented on the qubit register using single (U_1) and two-qubit gates (U_2). Each qubit can be read out independently.

with an exponential speed-up compared to known classical algorithms [7, 8].

1.1.2 Blueprint(s) for a quantum processor

The blueprint of a quantum processor, sketched in Fig. 1.1, based on the unitary evolution of a N qubit register and on qubit readout operations, is not so different from that of a classical processor.

The main difference is that the qubit register is not restricted to be one of the 2^N computational basis states of the register, but can be any coherent superposition of them. In this scheme, the qubits should be logical qubits protected against decoherence processes detrimental for quantum coherence, and thus for the computation performed. The five criteria to meet for making a quantum processor have been summarized by DiVincenzo [9]: a quantum processor consists of a register of quantum bits (1) with good quantum coherence (2), on which one can apply any unitary evolution using a universal set of quantum gates (3), that can be read-out individually with high fidelity (4), and that can be reset (5).

Let us mention here that the unitary evolution of a qubit register is not the unique implementation possible of quantum computing. There is the one-way quantum computing [10] consists in preparing a highly-entangled state, which is the resource, and in performing subsequent single qubit projective readout operations afterwards. Another implementation that has already led to an industrial development is adiabatic quantum computing [11]. In this scheme, one follows the ground state of a system whose Hamiltonian slowly evolves from a simple form with a well-known ground-state to a more subtle one whose ground state encodes the solution of the searched problem. This strategy, well suited for addressing optimization problems, has been implemented by the DWave company [12, 13]. Although quantum speed-up has not been yet demonstrated for the DWave machine, this machine was used for solving non-trivial problems.

1.1.3 Physical implementations of quantum bits

Numerous implementations have been considered for making quantum processors: NMR, trapped ions and atoms, optical circuits, and of course electrical circuits; see [14] for different implementations. Electrical circuits that can be fabricated with the standard methods of microelectronics and are thus potentially more easily scalable than other implementations are very appealing, even though macroscopic electrical circuits are intrinsically less quantum coherent than microscopic objects such as ions, atoms or spins. At the time of writing, the most advanced platform for quantum information processing is based on trapped ions ([15] and refs. therein), but no quantum processor based on the unitary evolution of a qubit register and able to solve a non trivial problem has yet been operated.

1.2 State of the art of superconducting quantum processors

Among quantum bit electrical circuits, superconducting quantum bit circuits based on Josephson junctions are the most advanced, and elementary processors have already been implemented.

1.2.1 Superconducting qubits

Following the first demonstration in 1999 of quantum coherence in a superconducting Cooper pair box circuit [16], different superconducting qubits have been proposed and investigated [17], and very significant progress has been achieved in term of quantum coherence, gate fidelity, and qubit readout [17]. Nowadays, the sole superconducting qubit architecture still used for making circuits is the circuit quantum electrodynamics (circuit-QED) architecture [18, 19]. Circuit-QED is similar to cavity-QED in which an atomic hyperfine transition is strongly coupled to a microwave cavity [20], but with the atom replaced by a Cooper pair box. In circuit-QED, Cooper pair box qubits are nowadays of the transmon type [21], and are embedded in a microwave resonator that can be planar or three-dimensional.

1.2.2 The transmon qubit

The Hamiltonian of the Cooper pair box writes $H = E_c\hat{n}^2 - E_j \cos\hat{\delta}$ where n is the number of Cooper pairs transferred across the junction and δ the phase difference across the junction, $E_c = (2e)^2/2C$ the charging energy and E_j the Josephson energy of the junction. Here $\hat{\delta}$ and $\hat{n}$ are conjugated variables and satisfy the commutation relation $\left[\hat{\delta}, \hat{n}\right] = i$. The transmon is a Cooper pair box in the slightly anharmonic regime $E_j \gg E_c$, and can be strongly electrically coupled to a microwave resonator, as sketched in Fig. 1.2. The two lowest energy states $|g\rangle$ and $|e\rangle$ form a quasi two-level system used as a qubit. The

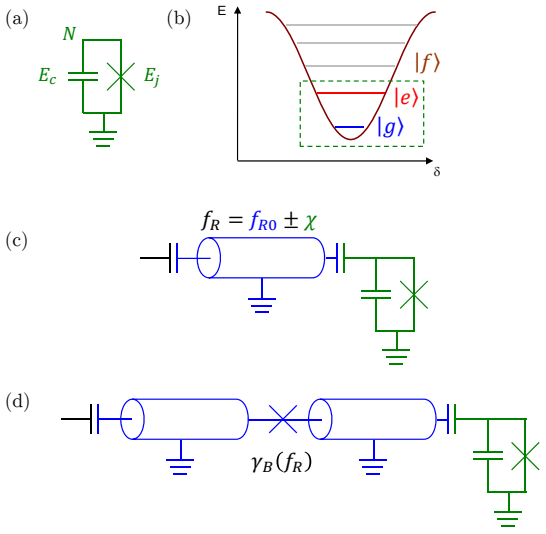

Figure 1.2: (a) Cooper pair box circuit: a Josephson junction of Josephson energy E_j in parallel with a capacitance with charging energy $E_c = (2e)^2/2C$. (b) Josephson potential energy of the Cooper pair box as a function of the phase difference δ across the junction. Energy levels of the Cooper pair box in the transmon regime. The two first level of this anharmonic spectrum define a qubit. (c) Circuit QED qubit architecture: a Cooper pair box is capacitively coupled to a microwave resonator. The resonator frequency change ($\pm\chi$) with the qubit state is used for qubit readout. (d) Josephson bifurcation (JBA) readout scheme used in this thesis. The Josephson junction embedded in the readout resonator makes it non linear; the switching between two dynamical states of the resonator occurs at a rate γ_B depending on the qubit state; this switching can provide high fidelity qubit readout.

transmon is capacitively coupled to a microwave resonator whose frequency is shifted by the qubit state. This frequency shift is exploited for reading the qubit state using the so-called dispersive readout method. When sending a microwave pulse to the resonator, the phase of the reflected (or transmitted) signal conveys information on the qubit state. This method is simple, but requests to use a quantum limited amplifier for reaching high fidelity single-shot readout. Such amplifiers were not available at the beginning of this work. In order to achieve high fidelity single-shot readout of the transmon, the Quantronics group had implemented a readout variant [22] in which the readout resonator is also made slightly non-linear by including a Josephson junction in its inductor. This non-linearity induces a bifurcation transition between two different dynamical states with different amplitude and phase, when excited close to resonance, as first demonstrated in [23]. Under proper conditions, one can map the qubit state to the dynamical state of this so-called Josephson Bifurcation Amplifier (JBA).

1.2.3 Superconducting quantum processors

Before the beginning of this thesis work, a prototype of superconducting quantum processor had been operated at Yale in 2009 [24]. It was a two-qubit transmon processor fitted with a universal set of gates but not with individual qubit readout. Although such a limited processor could only provide a partial answer at each run, it was sufficient for demonstrating the proper operation of a series of gates implementing the Grover quantum search algorithm on four items. Another implementation of a two-qubit processor had also been made for the phase qubit at UCSB, and used for running the Deutsch-Jozsa algorithm [25]. The Quantronics group decided to implement an elementary superconducting quantum processor fitted with individual JBA readout of the transmon [26]. This project to which I contributed during one and a half year formed the core of the Ph.D. thesis of Andreas Dewes [27].

1.3 Operating the Grover search algorithm in a two-qubit processor

The aim of this first project was to implement and test a 2-qubit processor fitted with high fidelity single shot readout. This work is summarized in Chapter 2 that also provides most of the theoretical material needed in this thesis.

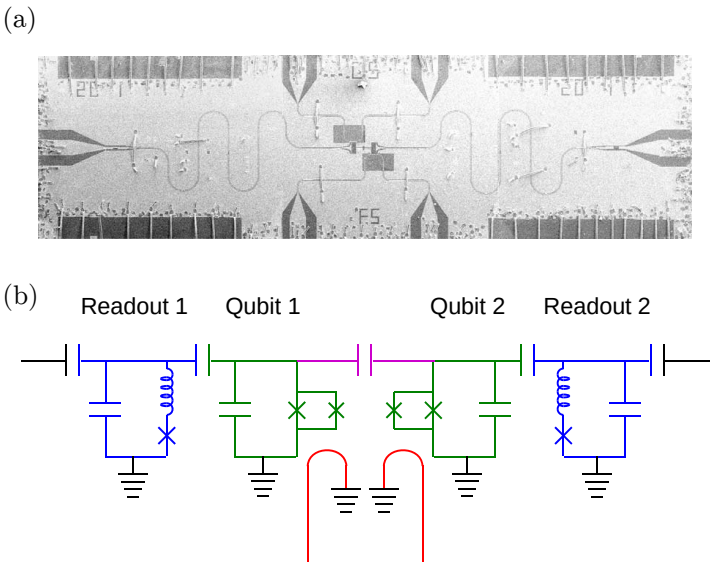

Figure 1.3: Two-qubit processor. (a) Optical micrograph of the two-transmon qubit circuit. (b) Electrical equivalent scheme. The qubits are capacitively coupled, and each of them is fitted with its non-linear readout resonator.

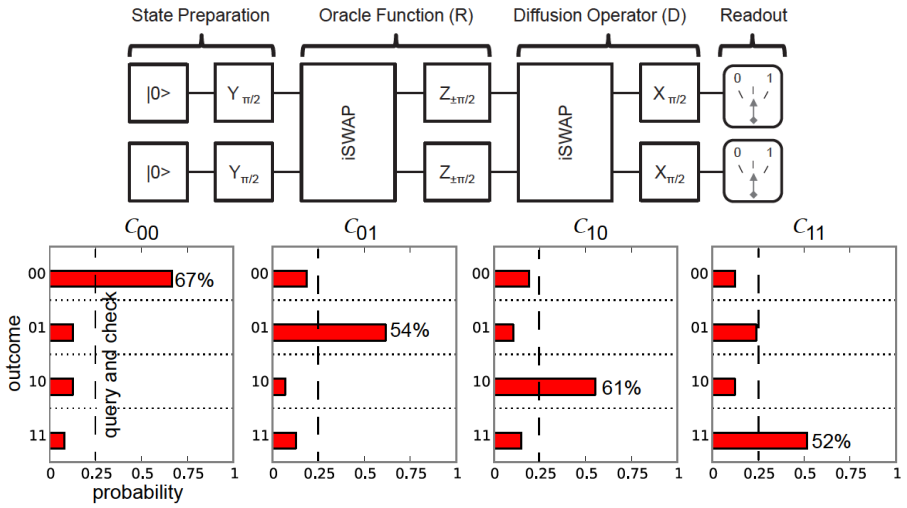

Figure 1.4: Grover search algorithm on four items. (top) Gate sequence used. The algorithm proceeds as follows: the preparation creates a superposition of all the computational basis states; one of the four possible oracle functions (operators) is applied. The oracle is defined by a combination of the $Z_{\pm\pi/2}$ operators; a decoding sequence is applied on the qubit register, and readout is performed. (bottom) Raw success probability of the Grover search algorithm, for the four possible cases. The dashed lines indicate the success probability of the classical query and check algorithm. The larger success probability achieved demonstrates quantum speedup.

Our processor shown on Fig. 1.3 is composed of 2 frequency tunable transmons fitted with JBA readout, and that are capacitively coupled. Although this coupling is not tunable, the effective interaction it induces between the qubits can be be switched *on (off)* by placing the qubits *on (off)* resonance using local current lines that control the qubit frequencies with the flux induced in the transmon SQUID loops. When the qubits are on resonance, the effective interaction yields a swapping evolution of the qubit states. This evolution can be used for obtaining an entangling gate which forms, with single qubit gates, a universal set of gates. The process tomography of this $\sqrt{iSWAP}$ two-qubit gate [28] shows an overall gate fidelity of 90 %. With this processor, we implemented the Grover quantum search algorithm on 4 items [26], as shown on Fig. 1.4. This case of the Grover search algorithm is interesting because it ideally succeeds at each run after a single call of the discriminating function (here an operator) provided to the user, whereas the classical "query and check" strategy obviously achieves a success probability of 1/4. The raw data yield an average success probability of $\sim 60\,\%$, always above the classical limit of 25 %, which demonstrated the quantum speedup of the implementation of the Grover search algorithm in our processor despite its imperfections.

1.4 Towards a scalable superconducting quantum processor

1.4.1 A more scalable design

The design of our 2-qubit processor being clearly not scalable, the main part of this thesis consists in developing a more scalable strategy suitable for making larger processors. There are different scalability issues, and our aim is not to address all of them. An obvious road-block is the readout: achieving high fidelity individual qubit readout of a register is a difficult problem whatever the implementation considered. The other main scalability issue is the necessity to implement quantum error correction as soon as the complexity of the processor and of the algorithm gets large. We simply aim at making a general purpose quantum processor approaching the DiVincenzo criteria, and able to run quantum algorithms on a still very small qubit-register. This processor should furthermore require as moderate as possible resources in term of signal generation and digitization. We have designed, fabricated and tested a 4-qubit processor, schematized on Fig. 1.5, in which tunable-transmon qubits are driven and read by frequency multiplexed signals carried by a single microwave transmission line. This circuit implements multiplexed JBA readout of the transmons, and the two-qubit gates are performed by bringing the two qubits close to resonance with a high quality factor microwave resonator, the coupling-bus, to which all the transmons are capacitively coupled.

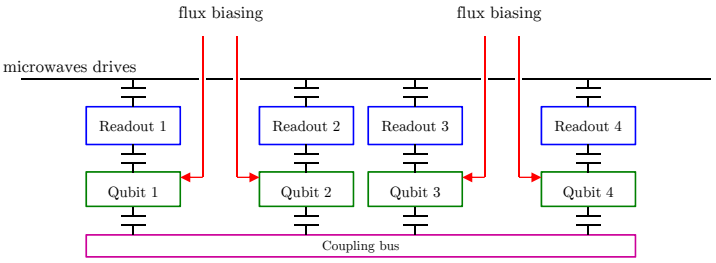

Figure 1.5: Schematics of the four-qubit processor operated. Each tunable qubit is coupled to its JBA readout resonator; and to a common bus resonator, for mediating qubit-qubit interactions. The readout resonators are staggered in frequency and coupled to a single transmission line, carrying all the qubit drive and readout signals.

1.4.2 Fabrication issues

As shown on the processor scheme, each qubit is fitted with its own flux line for frequency tuning. The simplicity of this design yields however delicate fabrication issues:

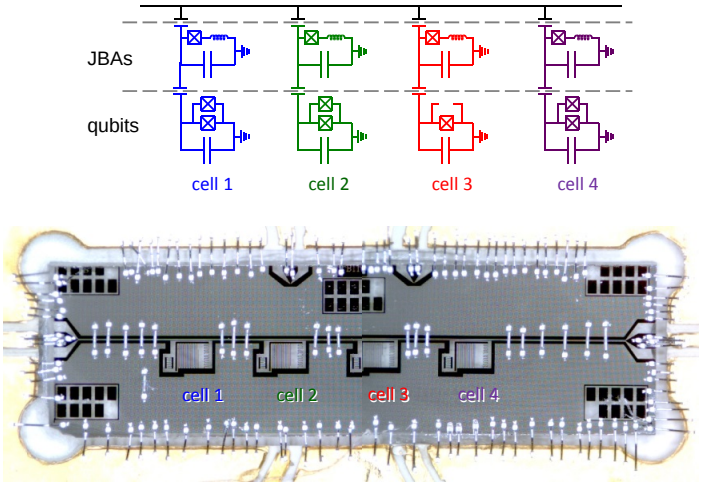

Figure 1.6: Four-qubit sample used for multiplexed readout. (top) Equivalent electrical scheme of the circuit. Four qubit-JBA resonator cells are coupled to a single transmission line carrying qubit driving and readout signals. The transmon qubits are tunable with a global magnetic field. (bottom) Optical micrograph of the sample showing the four cells. Bonding wires connect the signal lines from the chip to the printed circuit board, and reconnect all the ground electrodes.

- One has to fabricate Josephson junctions for the qubits and for the JBAs at distant places on the chip. This requires junctions with a well defined geometry in order to obtain the suitable non-linear Josephson inductances needed in the circuit.

- The presence of the common drive and readout line, of individual flux-lines coming close to the transmon qubits, and of the coupling-bus coupled to all transmons induces crossing problems between microwave transmission lines. For making these crossings without perturbing the transmission of the lines, we have fabricated aluminum airbridges connecting the conductors of a transmission line over another line.

1.4.3 Demonstrating multiplexed qubit readout

Prior to the fabrication and operation of a complete quantum processor, we describe the operation of a 4-transmon qubit circuit shown in Fig. 1.6, in which we perform multiplexed qubit readout and individual qubit driving through a single transmission line. In this circuit, the transmon qubits are only tunable by applying a global magnetic field.

The four JBA readout resonators are staggered in frequency, with a 60 MHz separation. Our first aim is to probe if single shot qubit readout is possible. For

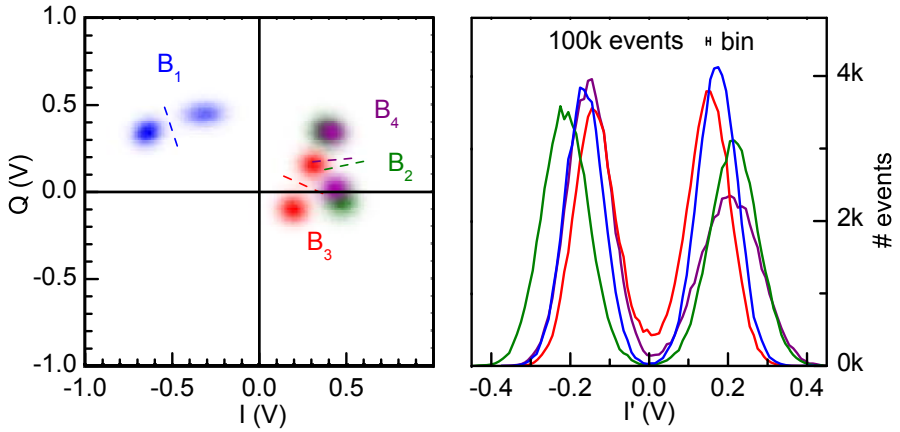

Figure 1.7: (left) Density plot of 10^5 single-shot readouts of the 4-qubit register after applying $\pi/2$ pulses on all qubits. The four (I_i, Q_i) (colors (blue, green, red, purple) stand for $i = (1-4)$). The dots for the four JBA signals form separated clouds corresponding to the non-bifurcated and bifurcated states of the JBA resonators. (right) Histogram of the projection perpendicularly to the best separatrix lines showing a good discrimination of the bifurcation states of the JBA resonators.

readout, one has to send a microwave pulse close to the resonance frequency of each non-linear readout resonator, and to analyze its complex amplitude transmitted after the interaction with the JBA resonator. For synthesizing the drive signals, we mix a single carrier frequency with a sum of ac signals produced by an AWG in order to obtain a set of pulses at the different JBA frequencies. After passing through the circuit, the readout signal is first analogically demodulated with the carrier, which yields the sum of the four readout signals at the different detuning frequencies between the carrier and the JBA resonators. This signal is digitized and numerically demodulated at the four sideband frequencies, yielding 4 pairs of (I_i, Q_i) quadratures that contain the information on qubit readout. The density plot of the quadratures in the four complex planes is shown on the left panel of Fig. 1.7 after applying $\pi/2$ pulses on all qubits that prepare equal weight superpositions of all qubit states. One observes that all points pertaining to a given pair of quadratures form two clouds that can be well discriminated by choosing suitable separatrices. The probability p_i of getting the outcome High (H_i) corresponding to the bifurcated state of JBA i is measured by repeating a measurement sequence and counting the number of H shots. We have checked that each cloud corresponds to a given state of the qubit, which demonstrates single shot readout. One observes that the simultaneous operation of the four JBAs does not prevent us from demodulating the signals as properly as achieved in single JBA measurements.

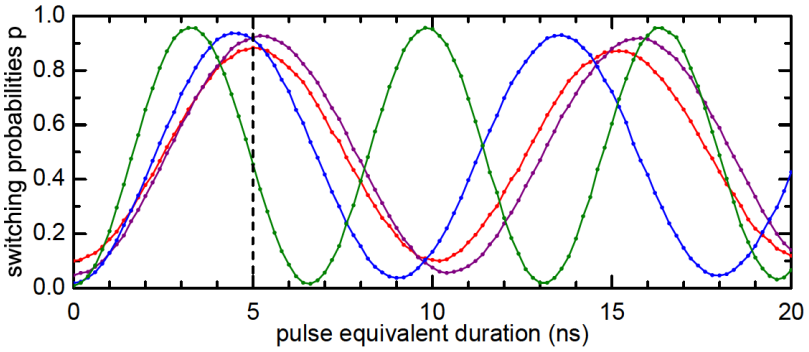

Figure 1.8: Rabi oscillations experiment simultaneously performed on the 4 qubits. (dots) Raw switching probability of the 4 JBA resonators (same color code as previous figures). The duration takes into account the Gaussian shape of the pulses.

With the improved design of the JBA non-linear readout resonators, we achieve a readout contrast reaching up to 96.5 % for individual qubit readout. Given the errors are mainly due to residual thermal excitation of the qubits and to relaxation, we estimate that the intrinsic readout fidelity of the JBA readout method could reach 99.8 %. We have probed the presence of a possible crosstalk when performing readout on different qubits simultaneously and found it negligible. Given the lack of individual frequency control of the qubits, one has to operate the global circuit at a compromise point, where the qubits are simultaneously not too detuned from their readout resonators. As a first test of the simultaneous operation of the drive and readout circuits for the 4 qubits, we have performed an experiment demonstrating simultaneous Rabi oscillations of the four qubits as shown on Fig. 1.8. Note the qubits are not driven strictly simultaneously because each Rabi drive signal would induce a Stark frequency shift on the other qubits, but the readout operations are completely overlapping in time.

1.4.4 Testing a 4-qubit processor

Finally, we describe in Chapter 5 the test of the full 4-qubit processor shown on Fig. 1.9. This circuit consists of four qubit-readout cells coupled to the same drive-readout line. The coupling of each qubit to a high quality factor coupling bus resonator mediates the qubit-qubit interactions.

In this circuit, individual flux control lines and a coupling bus have been added compared to the previously described experiment. For the crossings between the lines, we have added an extra fabrication step of aluminum airbridges at the end of the process. These airbridges can be seen on on Fig. 1.9.b.

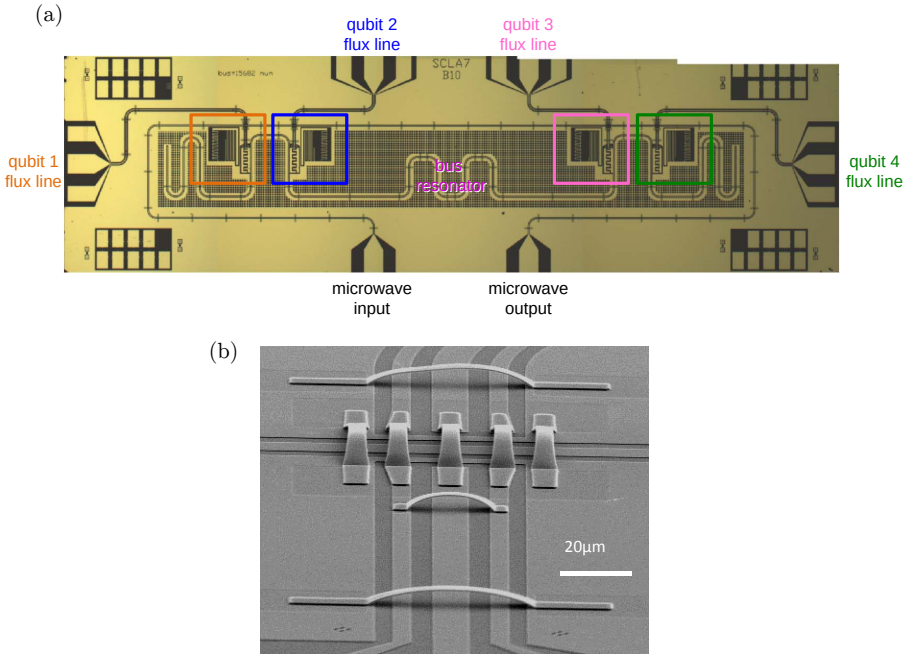

Figure 1.9: (a) Optical micrograph of the four-qubit processor. The frames indicate the four cells. Each cell consists of a transmon qubit, coupled to a common bus resonator, and to a JBA resonator, itself coupled to a single transmission line carrying all the qubit drive and readout signals. The frequency of each qubit is tuned by passing current in its dedicated flux line. (b) SEM image of the airbridges used for line crossings.

We found that this processor suffers from losses in the JBA resonators and of short coherence times of the qubits. The origin of these imperfections is not known, but it could arise from the extra fabrication steps needed for making the airbridges. Because of these imperfections, this circuit cannot be used it as a general purpose quantum processor as it was expected to be. We show nevertheless the operation of its new functionalities. First, our new design of the frequency control flux lines forcing the return current to flow in separate conductors without inducing flux in other transmons, as is often the case in multiple flux line circuits, yields a really small crosstalk between flux controls. Second, the airbridges fabricated for making the line crossings work properly without inducing extra losses. Third, we probe the two-qubit interaction mediated by the coupling bus. This qubit-qubit interaction is obtained by placing two qubits on resonance at a frequency slightly above the coupling bus frequency, which mediates the swapping interaction. The coherent swap between two qubits is shown on Fig. 1.10. The duration needed for obtaining a maximally entangling $\sqrt{iSWAP}$ universal two-qubit gate is $\sim 15\,\mathrm{ns}$.

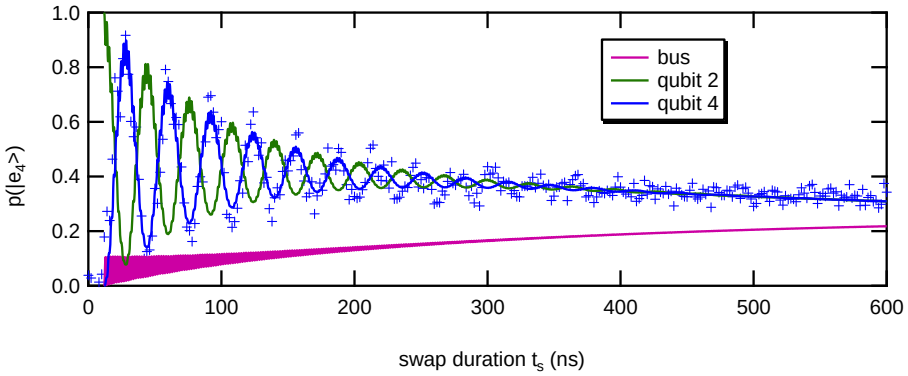

Figure 1.10: Coherent swapping oscillations between qubit 2 and qubit 4 mediated by coupling them through the bus resonator. The symbols are the measured excitation probability of qubit 4 corrected from readout errors. The solid lines are the simulated excitation probabilities of qubit 2 (green), qubit 4 (blue) and of the bus resonator (magenta).

Chapter 2

Operating a transmon based two-qubit processor

In the aim to develop a quantum processor based on superconducting qubits able to run quantum algorithms, the Quantronics group decided to first make and operate the simplest possible processor, namely a two-qubit processor having a universal set of quantum gates and individual single-shot readout. Designing, fabricating and operating such a processor was the Ph.D. research project of Andreas Dewes [27] to which I contributed during the first year of my own Ph.D. research. The processor we developed and its schematic equivalent circuit are shown in Fig. 2.1. With this elementary but functional processor, we generated and probed entanglement between qubits, performed the process tomography of a two-qubit entangling gate, and ran a quantum algorithm. We implemented the Grover search algorithm on four objects, and demonstrated its quantum speedup.

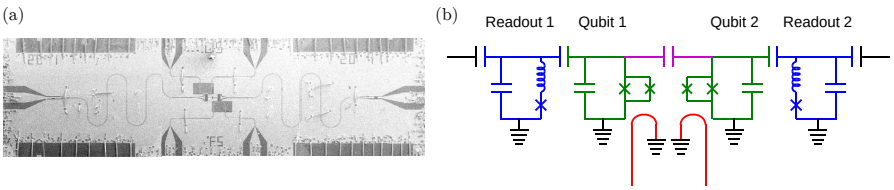

Figure 2.1: Prototype implementation of the processor. (a) SEM image. (b) Electrical equivalent circuit.

The goal of this chapter is to present the work done on this two-qubit processor. All the building blocks needed to understand this work are presented, given that they will be also useful for the next chapters: the different elements composing the circuits, the transmon qubit, its operation, and its readout are first presented. Then, the operating mode of the processor, the operation and characterization of single and two qubit gates are explained. Finally, the im-

plementation and operation of the Grover search algorithm in this processor is summarized.

2.1 Superconducting qubits based on Josephson junctions

The superconducting qubit we use is the transmon version of the Cooper pair box qubit developed at Yale [21]. It is made of a simple capacitor and two Josephson junctions arranged in a SQUID configuration.

2.1.1 The Josephson junction

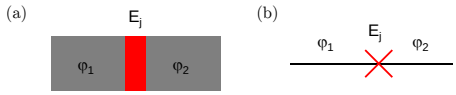

Figure 2.2: Josephson junction. (a) The two superconducting electrodes are in gray while the insulating barrier is show in red. (b) electrically equivalent circuit

As shown on Fig. 2.2, a Josephson junction [29] consists of two superconducting electrodes connected with a weak link, typically a thin insulating layer, through which Cooper pair can tunnel. The electron tunnel Hamiltonian between the electrodes yields the Josephson coupling between the electrodes. A Josephson junction provides a non-dissipative single degree of freedom, the phase difference $\varphi = \varphi_2 - \varphi_1$ between its electrodes, conjugated of the number n of Cooper pairs transferred across the junction. The Josephson Hamiltonian is

$$\hat{H} = -E_j \cos\hat{\varphi} \tag{2.1}$$

with E_j the Josephson energy of the junction. The supercurrent between the electrodes, proportional to the time-derivative of n, takes the form

$$I_{12} = I_c \sin\varphi \tag{2.2}$$

with $I_c = E_J/\varphi_0$ the maximum supercurrent through the junction, and $\varphi_0 = \hbar/2e \approx 2.05/2\pi \times 10^{-15}$ Wb the reduced flux quantum.

Considering first the phase as a classical variable gives the second Josephson relation

$$V = \varphi_0 \frac{\partial\varphi}{\partial t}. \tag{2.3}$$

For small currents $I_{12} \ll I_c$, the Josephson junction behaves as a phase dependent inductance

$$L_j(\varphi) = \frac{\varphi_0}{I_c \cos\varphi} \approx L_{j0}\left[1 + \frac{\varphi^2}{2} + \mathcal{O}\left(\varphi^4\right)\right], \tag{2.4}$$

where $L_{j0} = \varphi_0/I_c$ is the bare Josephson inductance. The Josephson inductance

$$L_j(\varphi) \approx \frac{\varphi_0}{I_c\sqrt{1-(I_{12}/I_c)^2}} \approx L_{j0}\left[1+\frac{(I_{12}/I_c)^2}{2}+\mathcal{O}\left((I_{12}/I_c)^4\right)\right] \tag{2.5}$$

thus depends non linearly on the supercurrent across the junction, increases with current, and even diverges at the critical current.

2.1.2 The SQUID: a flux tunable Josephson junction

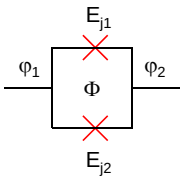

Figure 2.3: The SQUID: a flux controlled Josephson junction.

Two Josephson junctions in parallel constitute a SQUID[1] as depicted on Fig. 2.3. When the loop inductance is negligible, a SQUID behaves as a tunable Josephson junction controlled by the flux Φ threading the loop. The Josephson Hamiltonian takes the form

$$\hat{H} = -E_j^*(d,\Phi)\cos\hat{\varphi}, \tag{2.6}$$

with $E_j^*(d,\Phi) = E_j\sqrt{\frac{1+d^2+(1-d^2)\cos\Phi}{2}}$ being the adjustable Josephson energy and $E_{j1(2)} = E_j(1\pm d)/2$ the Josephson energies of the two individual junctions, expressed as a function of the SQUID asymmetry d.

[1]Superconducting quantum interference device

2.1.3 The Cooper Pair Box

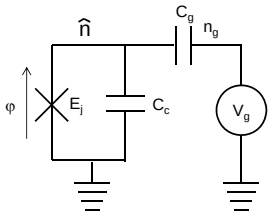

Figure 2.4: The Cooper pair box: schematic electrical circuit.

The Cooper Pair Box (CPB) circuit introduced by the Quantronics group is shown in Fig. 2.4. It consists of a Josephson junction in parallel with a capacitor C_c, subject to an external electric field, which can be applied by a voltage source through a gate capacitor. Its Hamiltonian [30] is

$$\hat{H} = E_c \left(\hat{n} - n_g\right)^2 - E_j \cos\hat{\varphi} \tag{2.7}$$

with $E_c = 2e^2/(C_c + C_g)$ the total charging energy of a single Cooper pair on the top superconducting island[2], and $n_g = C_g V_g/2e$ the reduced gate charge. The circuit variable $\hat{n}$ (number of Cooper pairs on the island) and $\hat{\varphi}$ (superconducting phase difference across the junction) satisfy the commutation relation $[\hat{\varphi}, \hat{n}] = i$. In the phase representation, this Hamiltonian writes

$$\hat{H} = E_c \left(-i\frac{\partial}{\partial\varphi} - n_g\right)^2 - E_J \cos\hat{\varphi}. \tag{2.8}$$

This form is convenient because it yields a analytical equation for the eigenstate wave-functions in terms of Mathieu functions [31, 21]. The eigenstate energies are given by

$$E_k = \frac{E_c}{4}\mathcal{M}_A\left[k + 1 - (k-1)\,(\mathrm{mod}2) + 2n_g\,(-1)^k, -\frac{2E_J}{E_c}\right], \tag{2.9}$$

where k is integer, and where $\mathcal{M}_A\,[r, q]$ stands for the Mathieu characteristic value a_r for even Mathieu functions with characteristic exponent r and parameter q. The spectrum being anharmonic, the ground and the first excited states $|g\rangle$ and $|e\rangle$ are used to define a qubit (Fig. 2.5), although the effect or other upper levels still needs to be taken into account. When using a SQUID for the Josephson junction, one can tune the qubit transition energy $E_{ge} = E_1 - E_0$.

[2] in other situations, the charging energy can be defined as the charging energy of a single electron on the island by $E_c = \frac{1}{2}e^2/\left(C_c + C_g\right)$

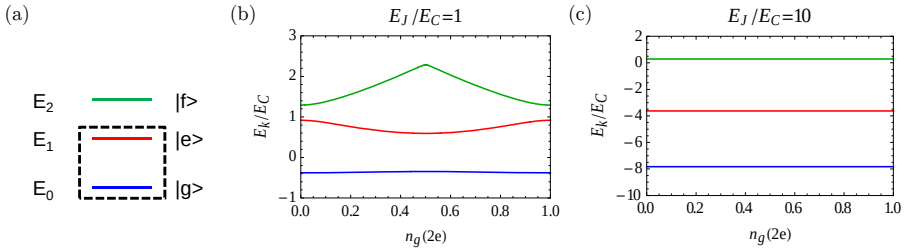

Figure 2.5: Energy levels of the Cooper pair box. (a) The anharmonicity of the spectrum allows to define a qubit as the two lowest energy states. (b-c) First three energies levels of the CPB as a function of the reduced gate charge n_g for $E_J/E_c = 1$ and 10.

2.1.4 Different Cooper pair box flavors

Nakamura, Pashkin and Tsai [16] first demonstrated at NEC in 1999 the coherent manipulation of a Cooper Pair Box qubit. This CPB was operated in the charge regime, meaning that its eigenstates consisted of a superposition of at most two subsequent number states of the box island. Although the achieved coherence time was rather short $\simeq 5\,\mathrm{ns}$, this first demonstration of coherent Rabi oscillations with an electrical circuit triggered a huge interest in superconducting quantum circuits.

The Quantronics group operated in 2001 a variant of the CPB in the intermediate regime $E_J/E_C \sim 1$: the Quantronium [32]. This circuit was fitted with single-shot readout, though with limited fidelity, and with a strategy for reducing decoherence due to the gate charge noise that plagues single electron circuits. This strategy consists in operating the Cooper Pair Box at an optimal working point, the so-called sweet spot, where the transition energy $E_{ge} = E_e - E_g$ is stationary with respect to gate charge variations. It provided a huge gain for the coherence time measured in a two-pulse Ramsey experiment up to $0.5\,\mu\mathrm{s}$.

A next important step was achieved at Yale in 2004 [19] when Schoelkopf, Wallraff, Girvin and collaborators inspired by cavity QED physics [33, 20] embedded a Cooper pair box in a planar microwave resonator, creating the field of circuit quantum electrodynamics (cQED). The interest of cQED is to isolate the Cooper Pair Box from the outside electromagnetic noise inducing decoherence, and to provide a sensitive readout method through the dependence of the resonator frequency on the quantum state of the CPB, called cavity pull. Another architecture variant that we will not discuss in this thesis consists in embedding a Cooper pair box in a 3D cavity [34], in even closer analogy with cQED.

2.2 The transmon

The transmon, developed at Yale in 2007 [21], is now the most widely used superconducting qubit. It is a Cooper pair box for which the strategy used to make the it less sensitive to charge noise was pushed at its maximum: a large shunting capacitance C_c places the Cooper pair box in the regime $E_j \gg E_c$, in which the CPB is an oscillator made anharmonic by the phase dependence of the Josephson inductance. The great advantage of this regime is to make the CPB first transition frequency almost completely insensitive to charge and thus to charge noise, leading to increased coherence. Within this approximation, the qubit transition energy $E_{ge} = E_1 - E_0$ is given by

$$E_{ge} \approx \sqrt{2E_J E_c} - \frac{E_c}{4}. \tag{2.10}$$

When one replaces the Josephson junction by a flux tunable SQUID, one finds

$$E_{ge} \approx E_{ge}^{max} \left(\frac{1 + d^2 + (1 - d^2)\cos\Phi}{2} \right)^{\frac{1}{4}} \tag{2.11}$$

with E_{ge}^{max} is the maximum transition energy of the qubit.

In the transmon regime ($E_j \gg E_c$), the matrix elements $|\langle i+1|\hat{n}|i\rangle|$ are well approximated with the one of the harmonic oscillator

$$|\langle i+1|\hat{n}|i\rangle| \approx \sqrt{i+1} \left(\frac{E_J}{8E_c} \right)^{\frac{1}{4}}. \tag{2.12}$$

So the immunity to charge noise comes at the price of the anharmonicity $\alpha = E_{ef} - E_{ge}$, with $E_{ef} = E_2 - E_1$, that is reduced in comparison to the initially developped Cooper pair box. This anharmonicity shown on Fig. 2.6 tends to $E_c/4$ when $E_J \gg E_c$, which limits the speed of a resonant drive at the qubit transition frequency as discussed below.

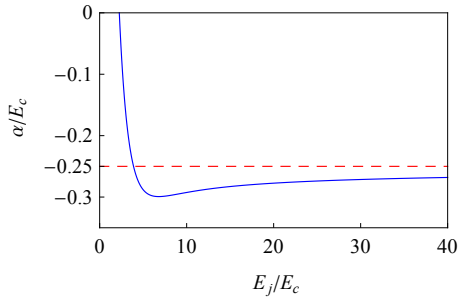

Figure 2.6: Reduced anharmonicity α/E_c as a function of E_J/E_c

We describe in the next subsections the different operations on a single qubit including state manipulation and state readout.

2.2.1 Single qubit gates

Two knobs are available to control the transmon qubit state: the applied electric field or gate voltage V_g, and the flux Φ applied to the loop. We will discuss the effect of both drives on the Bloch sphere that corresponds to the Hilbert space spanned by the $\{|g\rangle, |e\rangle\}$ states, in the frame rotating at the qubit frequency $f_{ge} = E_{ge}/h$.

2.2.1.1 Single qubit gates with resonant gate-charge microwave pulses

The transmon is driven quasi-resonantly at a frequency f_d close to its transition frequency f_{ge} by applying a coherent microwave electric field to its capacitor, or equivalently a microwave gate voltage $V_d(t) = V_d^S(t)\cos(\omega_d t + \varphi_d(t))$. Such a drive corresponds to the Hamiltonian

$$\hat{H}_d = -2e\beta V_d(t)\,\hat{n} \tag{2.13}$$

with $\beta = C_g/(C_c + C_g)$.

Under the Hamiltonian 2.13 and for a low amplitude $V_d^S(t)$, the qubit state rotates in the Bloch sphere around an axis defined by

$$\vec{H}_d/\hbar = -\frac{\Omega_{R0}(t)}{2}\left(\cos\varphi_d(t)\,\vec{x} + \sin\varphi_d(t)\,\vec{y}\right) - \frac{\delta}{2}\vec{z} \tag{2.14}$$

at a Rabi frequency $\Omega_R = \sqrt{|\Omega_{R0}|^2 + \delta^2}$ with $\delta = \omega_{ge} - \omega_d$ and $\Omega_{R0}(t) = 4e\beta V_d^S(t)\,|\langle 0|\hat{n}|1\rangle|\,e^{i\varphi_d(t)}$. We show on figure 2.7 the measured excited state population after a weak Rabi pulse with variable duration and frequency, the so-called Rabi chevrons.

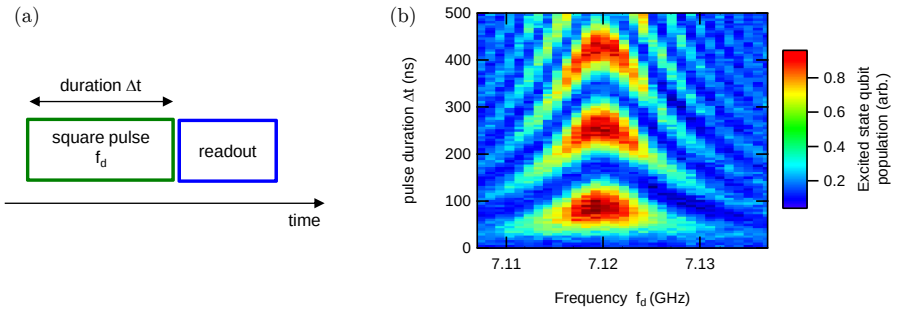

Figure 2.7: Rabi oscillations under quasi-resonant weak drive. (a) Pulse sequence used. (b) Qubit excited state probability displaying characteristic chevrons

The reduced anharmonicity α of the transmon sets an upper limit to the driving speed for ensuring negligible leakage to the upper levels of the transmon.

Indeed, in the Hilbert space spanned by the states $\{|g\rangle, |e\rangle, |f\rangle\}$ and in the frame rotating at ω_d, Hamiltonian 2.13 writes

$$H_d/\hbar = \begin{pmatrix} 0 & \Omega^*_{R0}/2 & 0 \\ \Omega_{R0}/2 & \delta & \Omega^*_{R0}/\sqrt{2} \\ 0 & \Omega_{R0}/\sqrt{2} & 2\delta+\alpha \end{pmatrix}_{\{|g\rangle,|e\rangle,|f\rangle\}} . \tag{2.15}$$

For strong enough drives such that the Rabi frequency $|\Omega_{R0}|$ becomes non negligible compared to the anharmonicity $|\alpha|$, the $|f\rangle$ state is populated from the $|e\rangle$ state by the non-diagonal element $\Omega_{R0}/\sqrt{2}$.

Gaussian pulses To get rid of this unwanted population, one has to keep the drive low enough by using for instance a slowly varying Gaussian shaped pulse [35]. For a NOT gate (π pulse) in a time of $\sim 10\,\text{ns}$ and typical anharmonicity of $\alpha \approx 400 - 500\,\text{MHz}$, we observe almost no population of the $|f\rangle$ state, but a remaining population of the $|g\rangle$ state of about 1%. In this thesis work, we only use Gaussian-shaped pulses, since the single qubit gate fidelity is mainly limited by other factors.

If more accuracy is needed [36], this imperfect drive can be improved in applying a pulse having its amplitude and its phase varying in time ($V_d^S(t) \in \mathbb{C}$). This method called "Derivative removal by adiabatic gate" (DRAG) [37], mainly consists in driving the qubit at its ac-Stark shifted resonance frequency.

2.2.1.2 Z rotations using phase driven gates

In the rotating frame at the qubit frequency f_{ge}, any change of the qubit frequency f_{ge} to $f_{ge} + \delta f_{ge}$ induces a rotation around the Z axis of the Bloch sphere at the frequency δf_{ge} . The application of a frequency shift pulse $\delta f_{ge}(t)$ with total duration τ thus induces a Z rotation by an angle $\varphi = 2\pi \int_\tau \delta f_{ge}(t)dt$, provided that the evolution is adiabatic and does not induce a population exchange between qubit levels. In practice, one applies trapezoidal flux pulses on the qubit SQUID with rise and fall times of order 1-2 ns, which does not induce any significant population change; the area under the trapeze determines the phase accumulation (Eq. 2.11).

2.2.2 Decoherence: relaxation and dephasing

The ability to control the parameters $\{\lambda\} = \{n_g, \Phi_{ext}\}$ of the qubit Hamiltonian goes together with opening noise channels on these parameters, which induces decoherence of the qubit [31, 21].

The coupling Hamiltonian to the fluctuations of a parameter λ is

$$\delta H/\hbar = -1/2(\vec{D_\lambda}.\vec{\sigma})\delta\lambda$$

with $\vec{D_\lambda}.\vec{\sigma} = D_{\lambda,x}\sigma_x + D_{\lambda,y}\sigma_y + D_{\lambda,z}\sigma_z$ and $D_{\lambda,u}$ being the sensitivity of H to a small variation of λ along u in the qubit subspace.

From the previous sections, we see that the transverse terms $D_{\lambda,x}$ and $D_{\lambda,y}$ induce relaxation and excitation, whereas the longitudinal $D_{\lambda,z}$ induces dephasing. We gather under $D_{\lambda,\perp}$ the terms in the equatorial plane of the Bloch sphere ($D_{\lambda,x}$ and $D_{\lambda,y}$).

The different $D_{\lambda,u}$ terms are linked to qubit matrix elements by

$$\begin{cases} D_{n_g,z} & = 2\frac{E_c}{\hbar}\left(\langle g|\hat{n}|g\rangle - \langle e|\hat{n}|e\rangle\right) \\ D_{\Phi_{ext},z} & = 2\frac{E_j}{\hbar}\left|\left(\langle g|\cos\hat{\varphi}|g\rangle - \langle e|\cos\hat{\varphi}|e\rangle\right)\sin\frac{\Phi_{ext}}{2}\right| \\ D_{n_g,\perp} & = 4\frac{E_c}{\hbar}\left|\langle g|\hat{n}|e\rangle\right| \\ D_{\Phi_{ext},\perp} & = \frac{1}{2}\frac{E_j}{\hbar}d\left|\langle g|\sin\hat{\varphi}|e\rangle\cos\frac{\Phi_{ext}}{2}\right| \end{cases}. \tag{2.16}$$

The relaxation rate is linked to $D_{\lambda,\perp}$ by

$$\Gamma_\lambda^{rel} = \frac{\pi}{2}D_{\lambda,\perp}^2 S_\lambda(\omega_{ge}), \tag{2.17}$$

where $S_\lambda(\omega_{ge})$ is the noise spectral density on the parameter λ, taken at the qubit frequency.

Similarly, the pure dephasing rate is

$$\Gamma_\lambda^\phi = \pi D_{\lambda,z}^2 S_\lambda(\omega = 0), \tag{2.18}$$

where the noise spectral density of λ is taken at $\omega = 0$ or at a cutoff frequency that depends on the precise experimental protocol. In the case of $1/f$ noise spectrum, the decay of Ramsey oscillations is no longer exponential but Gaussian $\sim \exp -\left(\Gamma_\lambda^\phi t\right)^2$ with an 'effective rate' (defined as the inverse of a $1/e$ decay time)

$$\Gamma_\lambda^\phi = 3.7A\left|\frac{\partial\omega_{ge}}{\partial\lambda}\right|, \tag{2.19}$$

where A is the amplitude of the $1/f$ noise at 1 Hz.

The above expressions allow to calculate the relaxation and dephasing rates due to noise on the gate charge n_g and on the SQUID flux Φ_{ext}.

2.2.2.1 Relaxation

Gate charge noise The gate charge noise arises from the impedance Z_g in series with the gate capacitance. Assuming this impedance at thermal equilibrium, the noise spectral density on the gate voltage is

$$S_{V_g}(\omega) = \frac{\hbar\omega}{2\pi}\left[\coth\left(\frac{\hbar\omega}{2k_BT}\right) + 1\right] Re\left[Z_g(\omega)\right]. \tag{2.20}$$

In the limit of low temperature $k_BT \ll \hbar\omega$, the relaxation rate is

$$\Gamma_{V_g}^{rel} = 16\pi\beta^2\omega_{ge}\frac{Re\left[Z_g(\omega)\right]}{R_K}\left|\langle g|\hat{n}|e\rangle\right|^2 \tag{2.21}$$

with $R_K = h/e^2$.

Flux noise Relaxation can also occur through the flux line used to control the qubit frequency; the mutual inductance M between the SQUID and the flux line inductance with total impedance Z_f yields:

$$S_{\Phi_{ext}}(\omega) = \left(\frac{M}{\Phi_0}\right)^2 \frac{\hbar\omega}{2\pi}\left[\coth\left(\frac{\hbar\omega}{2k_BT}\right)+1\right] Re\left[\frac{1}{Z_f(\omega)}\right], \tag{2.22}$$

which yields a relaxation rate

$$\Gamma^{rel}_{\Phi_{ext}} = \frac{\hbar\omega_{ge}}{4}\left(\frac{E_j dM}{\Phi_0}\right)^2 Re\left[\frac{1}{Z_f(\omega_{ge})}\right]\left|\langle g|\sin\hat{\varphi}|e\rangle\cos\frac{\Phi_{ext}}{2}\right|^2 \tag{2.23}$$

that is in our system much smaller than the measured relaxation rates, and consequently negligible.

Other decoherence sources The external decoherence sources considered here are often not the dominant ones. Other less controlled decoherence sources include [38]:

- Spurious two level systems (TLS) that induce relaxation [39, 40].
- Dielectric losses in the substrate. Several designs have been operated in order to reduce this impact [41, 42].
- Out of equilibrium quasiparticles that tunnel across the Josephson junctions also lead to relaxation [43].

T1 measurement We show on Fig. 2.8 the pulse sequence used to measure the relaxation rate Γ_1 as well as a typical relaxation curve. This measure consists in applying a π pulse on the qubit, waiting a given time Δt before measuring the averaged qubit state population. The relaxation time $T_1 = 1/\Gamma_1$ is the decay time of the exponential.

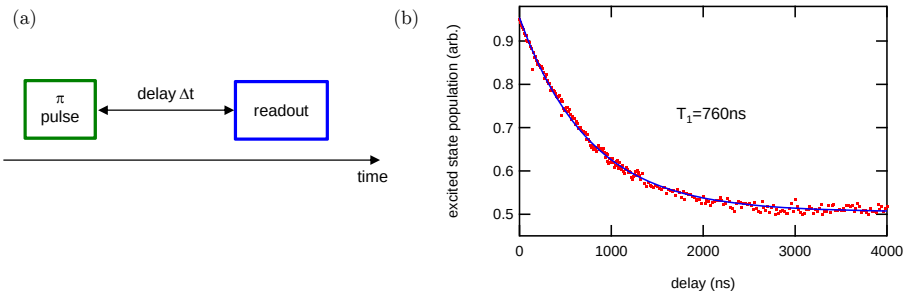

Figure 2.8: T_1 measurement. (a) Pulse sequence. (b) Population of the excited state as a function of the delay time Δt.

2.2.2.2 Pure dephasing

Gate noise At low frequency, thermal noise is negligible, and the gate charge noise is dominated by $1/f$ noise arising from microscopic fluctuations with typical amplitude $A \approx 10^{-5}$. In the transmon limit $E_j \gg E_c$, an upper bound of the Gaussian dephasing rate is [44]

$$\Gamma^{\phi}_{n_g} \leq 3.7 \times 2^7 \frac{A\pi}{\hbar} E_c \sqrt{\frac{2}{\pi}} \left(\frac{2E_j}{E_c}\right)^{5/4} \exp -\sqrt{\frac{32E_j}{Ec}}. \tag{2.24}$$

This mechanism yields negligible dephasing rates compared to what is observed in our experiments.

Flux noise For the same reason, the thermal flux noise is negligible at low frequency. Similarly to charge noise, microscopic uncontrolled fluctuators with a $1/f$ noise with a typical amplitude $A = 10^{-6} - 10^{-5}$ yields an effective dephasing rate

$$\Gamma^{\phi}_{\Phi_{ext}} \approx \frac{1}{2} A \omega^{max}_{ge} \left| \sin\left(\Phi_{ext}\right) \left(1 - d^2\right) \left(\frac{1 + d^2 + (1 - d^2)\cos\left(\Phi_{ext}\right)}{2}\right)^{-3/4} \right|. \tag{2.25}$$

This contribution is often the major part of the measured dephasing rate.

Measurement of the Ramsey coherence time T_2^* The coherence time is measured using a Ramsey two-pulse sequence as shown in Fig. 2.9.

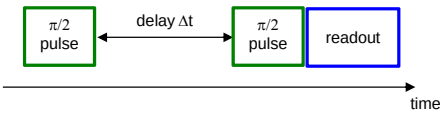

Figure 2.9: Ramsey pulse sequence used for T_2 measurements.

The decay time of the excitation probability is the coherence time $T_2^* = 1/\Gamma_2$ that contain both relaxation rate Γ^{rel} and pure dephasing Γ^{ϕ} as $\Gamma_2 = \Gamma^{\phi} + \Gamma^{rel}/2$

2.2.3 Qubit state readout

The readout of transmon qubits is now always performed in the circuit-quantum electrodynamics (Circuit-QED) framework introduced by [19, 18], with some variants.

2.2.3.1 Cavity quantum electrodynamics

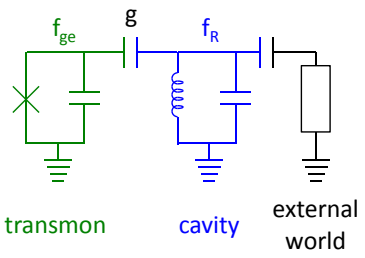

Figure 2.10: Cavity quantum electrodynamics schematics, showing a transmon capacitively coupled to a cavity, connected to the outside world.

As depicted in Fig. 2.10, a resonator is capacitively coupled to the transmon leading to the Jaynes-Cummings Hamiltonian

$$H/\hbar = \omega_R a^\dagger a + \frac{1}{2}\omega_{ge}\sigma_Z + g\left(a\sigma_+ + a^\dagger\sigma_-\right) \tag{2.26}$$

with g the coupling constant between the qubit and the resonator.

Cavity shift In the dispersive regime, for which the the qubit and the resonator are far detuned ($|\Delta| = |\omega_R - \omega_{ge}| \gg g$) and exchange no energy, one can approximate[3] the Hamiltonian 2.26 as

$$H/\hbar = \omega'_R a^\dagger a + \frac{1}{2}\omega_{ge}\sigma_Z + \chi\sigma_Z a^\dagger a, \tag{2.27}$$

where the multi-level structure of the transmon has been taken into account in $\chi = \chi_{ge} - \frac{\chi_{ef}}{2}$ [21], the dispersive shift calculated with the first $\chi_{ge} = \frac{g_{ge}^2}{\omega_{ge}-\omega_R}$ and second $\chi_{ef} = \frac{g_{ef}^2}{\omega_{ef}-\omega_R}$ excited state cavity shift, and $\omega'_R = \omega_R - \chi_{ef}/2$. The 'coupling constants' g_{ij} scale as the matrix element $|\langle i|\hat{n}|i+1\rangle|$ so that $g_{ef} \approx \sqrt{2}g_{ge}$ in the transmon regime. The dispersive Hamiltonian may be rewritten in the form

$$H/\hbar = \left(\omega'_R + \chi\sigma_Z\right) a^\dagger a + \frac{1}{2}\omega_{ge}\sigma_Z, \tag{2.28}$$

where the oscillator state remains harmonic but with a frequency that depends on the qubit state, as sketched in Fig. 2.11. Typical qubit readout is performed in measuring the transmission (or reflexion) coefficients of the resonator in which the CPB is embedded.

[3]This approximation is only valid while the number photon in the resonator $n = \left\langle a^\dagger a \right\rangle$ remains small compare to $n_{crit} = \Delta^2/4g^2$

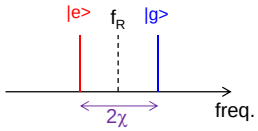

Figure 2.11: Qubit state dependent cavity shift

2.2.3.2 Linear dispersive readout

The simplest way to implement qubit readout is to send a microwave pulse at the bare resonator frequency f_R and to measure the phase of the reflected pulse. The reflected pulse acquires a phase $\delta\varphi = \pm 2 \arctan(2\chi/\kappa)$ that depends on the qubit state, with $\kappa = \omega_R/Q$ the resonator linewidth, as depicted in Fig. 2.12.

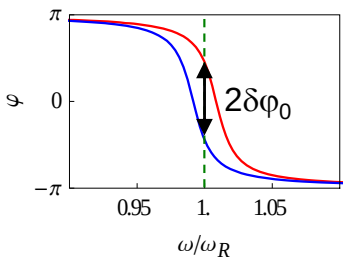

Figure 2.12: Phase of a reflected microwave pulse as a function of the frequency for qubit in state $|g\rangle$ (blue) and $|e\rangle$ (red).

This method, known as "linear dispersive readout", can be used to accurately detect the qubit state if one is able to discriminate the two outgoing signals out of the noise in a time shorter than the qubit lifetime.

Linear dispersive readout using homodyne detection Technically, to get both quadratures of the reflected signal, we use an IQ mixer as a demodulator, as shown in Fig. 2.13. Fed with the outgoing signal $A\cos(\omega_R t + \varphi_R)$ and a microwave carrier $L\cos(\omega_R t)$ at the same frequency, the IQ mixing gives two output

$$\begin{cases} I_D &= AL\cos(\omega_R t + \varphi_R)\cos(\omega_R t) = \frac{AL}{2}\left[\cos\varphi_R + \cos(2\omega_R t + \varphi_R)\right] \\ Q_D &= AL\sin(\omega_R t + \varphi_R)\cos(\omega_R t) = \frac{AL}{2}\left[\sin\varphi_R + \cos(2\omega_R t + \varphi_R)\right] \end{cases} . \tag{2.29}$$

These two outputs are then low-pass filtered, giving access to the two quadratures

$$\begin{cases} I_D = \frac{AL}{2}\cos\varphi_R \\ Q_D = \frac{AL}{2}\sin\varphi_R \end{cases} . \tag{2.30}$$

This method makes possible to determine the projected qubit state from the outgoing signal with a good accuracy if the noise added in amplifying the signal remains under a certain level. At the beginning of this project, linear dispersive readout of transmons had not been demonstrated with high single-shot fidelity because of the noise added by the cryogenic amplifiers used for amplifying the signal. High fidelity single-shot had been achieved in the Quantronics group in 2009 [22] using a non-linear readout resonator called Josephson Bifurcation Amplifier (JBA) [45]. Under proper drive conditions, this non linear resonator has two possible dynamical states and can latch either state depending on the projected qubit state. This mapping of the qubit state onto the latched resonator state makes the JBA a suitable high fidelity readout for a transmon. It is now described in more details.

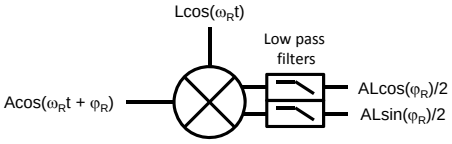

Figure 2.13: Homodyne detection using IQ down-conversion.

2.2.3.3 The Josephson bifurcation amplifier

The JBA is a LC resonator made slightly non-linear by inserting a Josephson junction in series with the geometric inductance. It is operated at a driving frequency and amplitude for which it bifurcates between two different internal dynamical states.

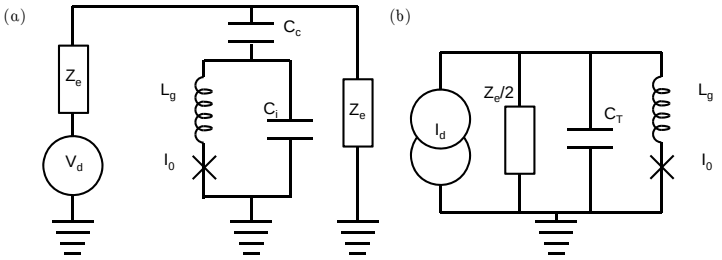

Figure 2.14: (a) Electrical scheme of a JBA. (b) Simplified equivalent circuit close to resonance, with $I_d = V_d/Z_e$ and $C_T = C_j + C_c$.

Figure 2.14. represent its actual lumped element circuit (a) and its equivalent circuit around the resonance frequency (b).

Theory The dynamics of this system at zero temperature (and zero quantum fluctuations) can be fully described by the charge on the capacitor q (treated

as classical variable) under a drive $V_e \cos(\omega_m t)$. The equation of motion is

$$\ddot{q} + \frac{\omega_r}{Q}\dot{q} + \omega_r^2 q + \frac{p\dot{q}^2\ddot{q}}{2I_0^2} = \frac{V_e}{L_T}\cos(\omega_m t), \tag{2.31}$$

with $\omega_r = 1/\sqrt{C_T(L_g + L_J)}$ the resonance frequency of the resonator at low power, $Q = Z_i/Z_e$ the quality factor of this resonance ($Z_i = \sqrt{(L_J + L_g)/C_T}$), and $p = L_J/(L_J + L_g)$.

Using the reduced parameters

$$\begin{cases} \Delta_m = \omega_m - \omega_r \\ \Omega = 2Q\Delta_m/\omega_r \\ u(t) = \sqrt{\frac{pQ}{2\Omega}}\frac{\omega_m}{I_0} q(t) \\ \beta = \left(\frac{V_e}{\varphi_0 \omega_m}\right)^2 \left(\frac{pQ}{2\Omega}\right)^3 \end{cases}, \tag{2.32}$$

the slowly varying envelope of $u(t)$ of the oscillations at ω_m is given by

$$\frac{du}{d\tau} = -\frac{u}{\Omega} - iu\left(|u|^2 - 1\right) - i\sqrt{\beta}. \tag{2.33}$$

We display on Fig. 2.15 the stationary solutions of Eq. 2.33 for different values of the reduced drive power β. One observes that for same driving parameters, the system can have two stable dynamical states, labeled L and H.

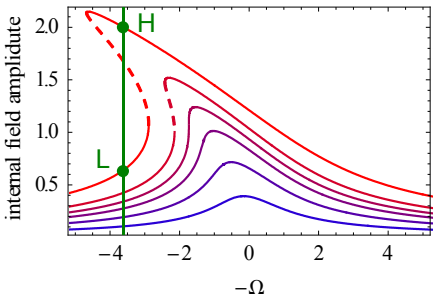

Figure 2.15: Internal field stationary amplitude for different reduced drive amplitudes $\beta_c/10$, $\beta_c/3$, $2\beta_c/3$, β_c, $3\beta_c/2$, and $3\beta_c$ (from blue to red). Dashed lines represent unstable solutions.

The points where the system bifurcates from a low amplitude state L to a high amplitude state H (and inversely) are given by the equation

$$\beta_\pm = \frac{2}{27}\left[1 + \left(\frac{3}{\Omega}\right)^2 \pm \left(1 - \frac{3}{\Omega^2}\right)^{3/2}\right]. \tag{2.34}$$

Figure 2.16 represents the two switching branches $\beta_\pm$ expressed as a function of the relative drive power.

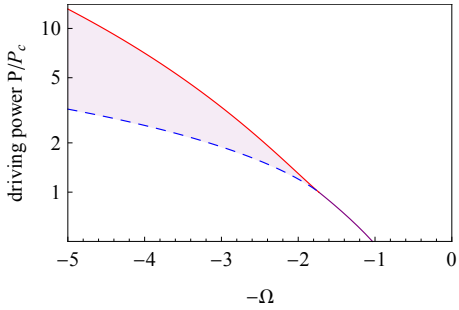

Figure 2.16: Bifurcation branches $\beta_\pm$ as a fonction of the reduced detuning.

Dynamics with thermal or quantum fluctuations The switching between the L and H states is a stochastic process governed by quantum and thermal fluctuations. It is well described by the Dykman theory as explained in [45, 46, 44, 47, 48]: slightly below the bifurcation line β_+, the switching from L and H is characterized by a switching rate $\Gamma_s(P_e, f_m)$ that increases with temperature and decreases with the distance to the line (in power or frequency). A particularly simple result is that at low temperature, the quantum dynamics is the same as the thermal dynamics but with an effective 'quantum temperature' $T = \hbar\omega_r/2k_B$. If the JBA drive signal is applied during a time τ, the rate $\Gamma_s(P_e, f_m)$ translates into a switching probability $P_{s,\tau}(P_e, f_m)$ that increases from 0 to 1 with increasing drive power P_e or decreasing drive frequency f_m. The switching curves $P_{s,\tau,f_{m0}}(P_e)$ and $P_{s,\tau,P_{e0}}(f_m)$ (called S curves in the following) have characteristic widths δP_e and δf_m simply related by the slope $\partial\beta_+/\partial f_m$ of the β_+ bifurcation line.

Hamiltonian of the non-linear resonator One can also describe the undriven non-linear resonator by adding a quartic Kerr term to the Hamiltonian of the harmonic oscillator:

$$H/\hbar = \omega_r a^\dagger a + \frac{K}{2}\left(a^\dagger a\right)^2, \tag{2.35}$$

with $K = -\pi p^3 \omega_R \frac{Z_e}{R_k}$ the Kerr non-linearity.

JBA as qubit readout In the same way as for the linear resonator, the JBA bare frequency is shifted depending on the qubit state, and the JBA-qubit system is described by

$$H/\hbar = \left(\omega_R + \chi\sigma_Z + \frac{K}{2}a^\dagger a\right) a^\dagger a + \frac{1}{2}\omega_{ge}\sigma_Z. \tag{2.36}$$

The whole stability diagram described in Fig. 2.16 is now shifted by the two qubit states, leading to the two bistability regions of Fig. 2.17. Accordingly,

one has now two S curves, the width δP_e (resp. $\delta\omega_m$) of which needs to be compared to their separation ΔP converted in frequency with

$$\Delta f = 2\chi = \Delta P \partial f_m / \partial \beta_+. \tag{2.37}$$

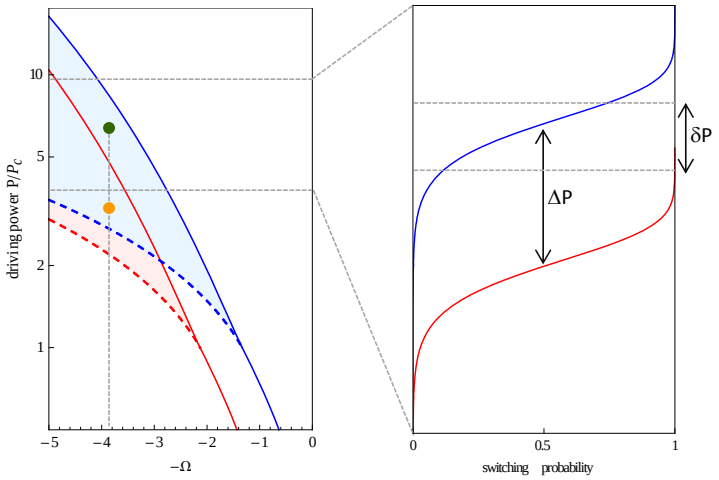

Figure 2.17: (a) Stability diagram for the two possible qubit states $|g\rangle$ (blue) and $|e\rangle$ (red) for a typical operating point (green). (b) Switching probability as a function of power for the selected frequency.

To operate the JBA as a qubit readout one chooses a drive frequency in the bistability regions and a drive power between the bifurcation lines $\beta_{+,\langle g\rangle}$ and $\beta_{+,\langle e\rangle}$ corresponding to the two qubit states (green dot on Fig. 2.17.a). The qubit projected in its excited state will make the JBA bifurcate to its H state whereas the projection in the ground state will leave the JBA in its L state. After an amount of time just long enough to let the JBA reach its H state if it switches, one reduces the drive power (orange dot) to place the driving point in the bistable regions for both qubit states, thus latching JBA dynamics. At this point, nor relaxation or excitation of the qubit can further impact the JBA dynamical state.

The internal state of the resonator leaks out to build the measured signal, which is measured using the technique described in Sec. 2.2.3.2, without any time limitation because of the latched character of the signal.

In theory, this detector could perfectly map the qubit state to the outgoing signal, yielding perfect readout. However, different effects can reduce the readout fidelity:

- An imperfect separation of the switching curves can lead to incorrect mapping of the qubit states to the JBA ones, as shown in Fig. 2.17.b.

- The bifurcation dynamics lasting for a finite time, relaxation can occur before the JBA reaches H, leading to an incorrect result.
- During the long signal acquisition step (orange dot), the JBA can switch back from H to L if the drive frequency is chosen too high (retrapping process), producing a wrong result.

Performance of transmon readout with the JBA Experimentally, we apply the JBA driving pulse depicted in Fig. 2.18.a with a reduction of amplitude on the latching plateau of $10 - 20\%$. The output signal is measured and averaged during a time t_m on the latching plateau, after a small dead time corresponding to the transient. One obtains in this way a single point in the IQ plane. Fig. 2.18.b, shows 20000 subsequent measurement points when the switching probability is 84%. The points are distributed in two well separated regions that correspond to both H and L JBA states. These switching-non switching events can be displayed as a voltage histogram (see Fig. 2.18.c) along the red curve of Fig. 2.18.b. A threshold can be defined to calculate the switching probability.

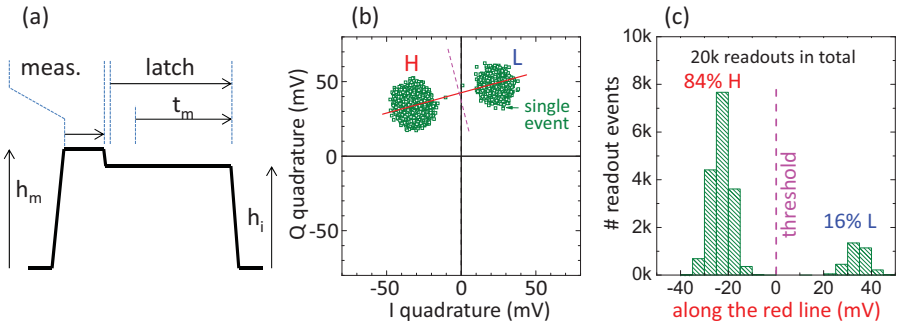

Figure 2.18: Experimental measurement of the JBA switching probability. (a) driving pulse applied at frequency f_r. (b) outgoing signal demodulated at frequency f_r, averaged during the time t_m. Each green point represents a single measurement sequence. (c) Histogram of the measured quadratures along the red axis defined on (b).

Keeping the same threshold, a switching curve is measured by varying the amplitude of the whole pulse. Figure 2.19 shows the S curves for the qubit prepared in its ground, first and second excited states. The maximum difference between the switching curves (dashed lines) indicates the optimal point for mapping the qubit states to the JBA ones. At this maximum difference, the minimum readout errors are $p(H|g) \approx 8\%$ when the qubit is in its ground state and $p(L|e) \approx 16\%$ when the qubit is in its excited state. The maximum contrast is 76%, which characterizes the fidelity of a single measurement.

When measuring qubit state populations based on precisely measured switching probabilities, these readout errors can be corrected for if needed, as detailed in [27].

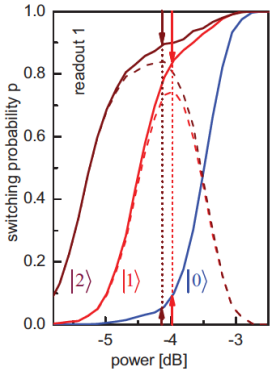

Figure 2.19: Switching curves of a JBA for a qubit in state $|g\rangle$(blue), $|e\rangle$(red) and $|f\rangle$(green) as a function of the drive power.

Shelving to level $|f\rangle$ The use of only the first two transmon levels $|g\rangle$ and $|e\rangle$ gives a readout contrast limited by the overlap of the switching curves. A trick to increase S separation is to transfer the $|e\rangle$ state to the $|f\rangle$ state prior to measurement, which increases artificially the qubit dependent cavity shift. This escape from the computational basis allowed us to get an improved fidelity of 81% as shown with the brown curve on Fig. 2.19. This improved sensitivity is also due to the impossible direct relaxation from $|f\rangle$ to $|g\rangle$ during the measurement time.

2.2.3.4 Cavity induced relaxation and dephasing

In a circuit-QED architecture, the qubit is connected to the outside dissipative word only through its readout resonator and directly feels the resonator field, as shown in Fig. 2.20. This leads to two important effects.

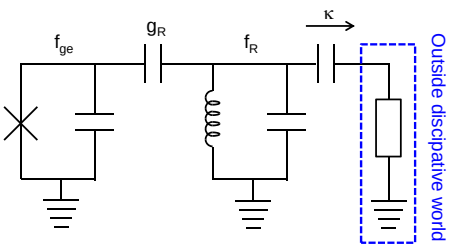

Figure 2.20: Electrical scheme of a transmon in a cQED geometry.

Purcell effect First, the impedance in series with the coupling capacitance is now made of the resonator capacitively coupled to the $50\,\Omega$ environment; it is frequency dependent, and Eq. 2.21 takes the simple form

$$\Gamma_p = \kappa \frac{g_R^2}{\Delta^2 + \kappa^2}, \tag{2.38}$$

with κ the resonance linewidth, $\Delta = \omega_R - \omega_{ge}$ the qubit resonator detuning, and g_R the coupling constant between the qubit and its readout resonator. This enhanced relaxation rate around the resonator frequency is known as the Purcell effect [49].

Dephasing due to photon noise in the resonator The coupling to a resonator also yields dephasing because the photon population in the resonator shifts the qubit frequency and is subject to shot noise [50, 51, 52]. The dephasing rate Eq. 2.27

$$H/\hbar = \omega_R a^\dagger a + \frac{1}{2}\left(\omega_{ge} + \chi a^\dagger a\right)\sigma_Z\,,$$

rewrites

$$\Gamma_{th}^{\phi} = \frac{8\chi^2}{\kappa}\bar{n}_{th} \tag{2.39}$$

with $\bar{n}_{th}$ the average population.

2.3 Processor operation

The processor we have fabricated and operated consists of two tunable transmon qubits I and II that are directly capacitively coupled, and fitted with individual JBA readouts. The schematics of the circuit is depicted on Fig. 2.21: the two non-linear readout resonators are displayed in blue, whereas the two qubits are in green; the qubits are coupled to each other through a coupling capacitance C_{qq} described in Sec. 2.3.1. The current lines shown in red allow to tune the flux in the SQUIDs and thus to control the qubit frequencies within a few nanoseconds[4], which provides the requested frequency agility for gate operation.

[4]The response function of the line is actually measured in-situ, and taken into account for generating the desired pulse shape at the SQUID level.

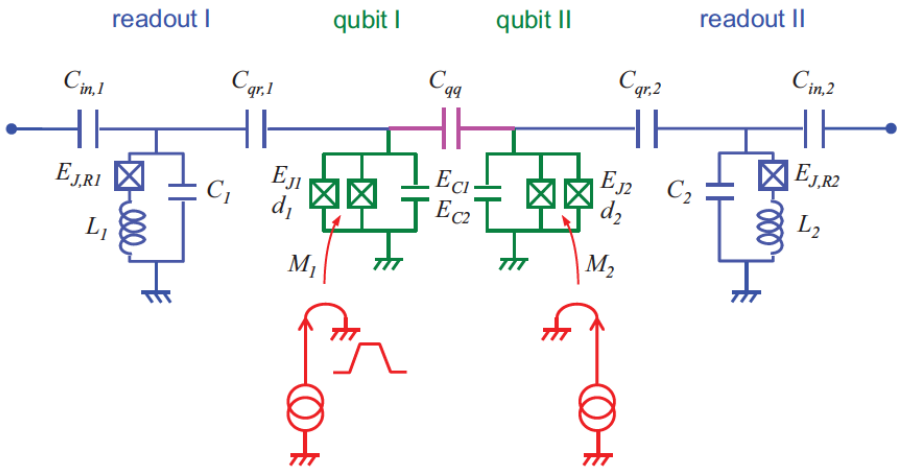

Figure 2.21: Schematic circuit of the two-qubit processor operated. The two qubits are capacitively coupled to each other and to their own readout resonators.

The qubit frequencies at the different operation points are shown in Fig. 2.22. The two readout resonators are the highest frequencies in the system: $f_r^{I(II)} = 6.84$ (6.70) GHz. For readout, the transmons are moved close to their readout resonators with detunings $\Delta_{rr}^{I(II)} = f_r^{I(II)} - f_{ge}^{rI(II)} = 0.640$ (0.700) GHz, before the readout tones are applied. Since the qubits are directly coupled, as it will be described in Sec. 2.3.1, one places them at the same frequency only for performing two-qubit operations. Drives for single qubit gates are applied through the readout resonators. Despite the filtering that it induces, the relative low quality factor $Q \sim 730$ of the readout modes as well as the relative small detunings $\Delta_{rm}^{I(II)} \sim 1.6\,\text{GHz}$ allow us to implement fast single qubit gates ($t_g < 50\,\text{ns}$ for a π pulse).

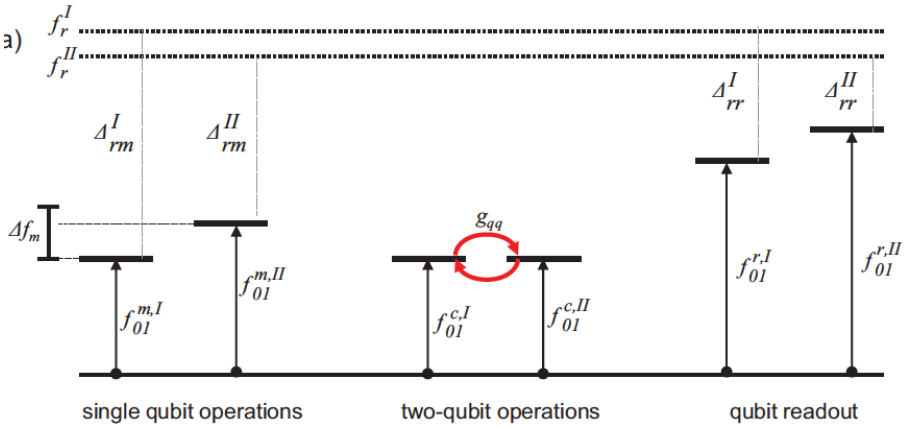

Figure 2.22: Qubit and JBA frequencies for single qubit operations, two-qubit operations, and readout.

Simultaneous readout At the end of a pulse sequence or algorithm, the readout is performed on both qubits simultaneously. The readout process is characterized by a 4×4 readout matrix that gives the probability of the different possible outcomes $\{LL, LH, HL, HH\}$ after having initialized the two qubit register in states $\{|gg\rangle, |ge\rangle, |eg\rangle, |ee\rangle\}$. This readout matrix, which takes into account all readout errors including crosstalk between the two channels, is non purely diagonal. By applying its inverse to the JBA state probability vector deduced from repeated identical measurement sequences, one obtains the average populations of the different qubit states and their correlations.

2.3.1 Two-qubit interaction yielding a universal gate

In order to obtain a universal set of gates able to implement any unitary evolution of the qubit register, one needs an entangling interaction [25].

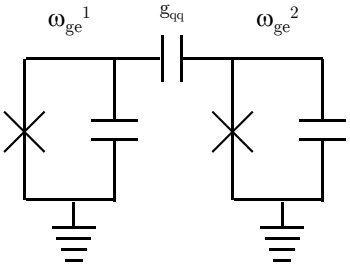

Figure 2.23: Electrical scheme of the capacitively coupled transmons.

The capacitive coupling through C_{qq} between the two qubits, see Fig. 2.23, yields the coupling Hamiltonian

$$\hat{H}_{qq} = \frac{1}{2} C_{qq} \hat{V}_{qq}^2 \approx \frac{4e^2 C_{qq}}{C_{\Sigma 1} C_{\Sigma 2}} \hat{n}_1 \hat{n}_2 + ... \tag{2.40}$$

Writing this Hamiltonian in the uncoupled qubit state basis yields

$$\hat{H}_{qq}/\hbar = g_{qq} \left(\hat{\sigma}_I^+ \hat{\sigma}_{II}^- + \hat{\sigma}_I^- \hat{\sigma}_{II}^+ \right), \tag{2.41}$$

with $\hbar g_{qq} = 4e^2 C_{qq}/C_{\Sigma 1} C_{\Sigma 2}$ the coupling constant between the two qubits. The evolution operator induced by the swapping Hamiltonian 2.41 is

$$U_{iSWAP}(t, \Delta_{qq}) = \begin{pmatrix} 1 & 0 & 0 & 0 \\ 0 & \cos t g_e - i \frac{\Delta_{qq}}{g_e} \sin t g_e & i \frac{g_{qq}}{g_e} \sin t g_e & 0 \\ 0 & i \frac{g_{qq}}{g_e} \sin t g_e & \cos t g_e + i \frac{\Delta_{qq}}{g_e} \sin t g_e & 0 \\ 0 & 0 & 0 & 1 \end{pmatrix} \tag{2.42}$$

with Δ_{qq} the detuning between the qubits, and $g_e = \sqrt{4g_{qq}^2 + \Delta_{qq}^2}$ the effective swapping frequency. This evolution operator efficiently entangles the qubits when they are on resonance, yielding there the maximally entangling $\sqrt{iSWAP}$ gate for $t_g = \pi/4g_{qq}$ and the $iSWAP$ gate for $t_g = \pi/2g_{qq}$. By non-adiabatically changing the detuning Δ_{qq}, one efficiently turns the effective interaction on and off.

As shown in Fig. 2.24, starting from a far off-resonant condition $\Delta_{qq} \gg g_{qq}$ and placing the qubit at resonance $\Delta_{qq} = 0$ for a time t_g prior to detuning them again does induce the expected swapping.

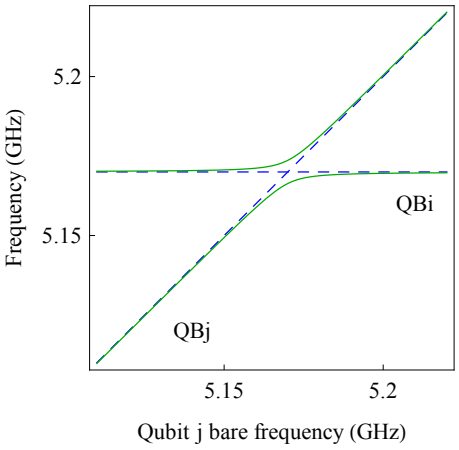

Figure 2.24: Avoided level crossing between the two qubits, when varying qubit j bare frequency, with qubit i bare frequency fixed.

Swapping evolution The swapping evolution is readily characterized by initializing the qubit register in state $|ge\rangle$. To do so, a π pulse is applied to one qubit, the two qubits are placed in resonance during a varying time, and they are re-decoupled and measured, as shown in Figure 2.25. The data shown are corrected to get rid of readout errors as explained in 2.3, and the average qubit joined populations are shown. A swap between states $|eg\rangle$ and $|ge\rangle$ is observed, as well as relaxation to $|gg\rangle$ and dephasing. The dashed line represents the master equation simulated data with the parameters independently measured. Only the qubit dephasing rates are left as fit parameters[5]. The simulated data well agrees with the experiment and gives a swapping frequency $2g_{qq}/2\pi = 8.3\,\mathrm{MHz}$. The $\sqrt{iSWAP}$ ($iSWAP$) is obtained in a time $t_{\sqrt{iSWAP}} = 31\,\mathrm{ns}$ ($t_{iSWAP} = 62\,\mathrm{ns}$), indicated with gray lines on Fig. 2.25.

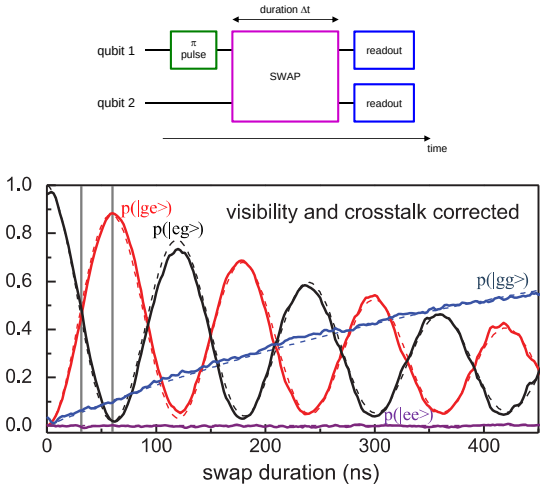

Figure 2.25: Swapping experiment (top) Pulse sequence used. (bottom) Measured two-qubit state probability (full lines) and master equation simulation (dashed lines).

As in the case of σ_Z gates detailed in Sec. 2.2.1.2, the displacement of qubit I to place it on resonance with qubit II introduces a large spurious extra phase $\varphi = 2\pi t_{gate}\delta f \sim 30 - 100 \times 2\pi$. We compensate this phase up to a 2π multiple. The phase compensation calibration is determined via quantum state tomography.

[5]The first order pure dephasing rate vanishes because of the qubit insensitivity to flux noise at resonance.

2.3.2 Quantum state tomography

The state of the two-qubit register is described by its density matrix ρ. The diagonal elements of this density matrix, i.e. the state populations, are directly obtained from repeated measurements of the qubit register as already explained. Standard quantum state tomography [53] is needed for fully determining the density matrix, in particular its non-diagonal elements, whereas quantum process tomography is needed for fully characterizing the fidelity of the $\sqrt{iSWAP}$ gate.

Two-qubit state tomography

The density matrix of a two-qubit register can be decomposed on the generalized Pauli basis of tensorial products of two single qubit Pauli matrices $\{\hat{\sigma}_v\} = \{I, X, Y, Z\}$:

$$\rho = \sum_{v_1,\ldots,v_n} \frac{c_{v_1,\ldots,v_n} \hat{\sigma}_{v_1} \otimes \ldots \otimes \hat{\sigma}_{v_n}}{2^{2n}}. \tag{2.43}$$

The coefficients $c_{v_1,\ldots,v_n}$ with $v_i \in \{I, X, Y, Z\}$ can be obtained by a trace operation: $c_{v_1,\ldots,v_n} = Tr\left[\hat{\sigma}_{v_1} \otimes \ldots \otimes \hat{\sigma}_{v_n} \rho\right]$ and are determined experimentally by measuring the qubits along the 16 directions $\{\hat{\sigma}_{v_1} \otimes \hat{\sigma}_{v_2}\} = \{I, X, Y, Z\}_1 \otimes \{I, X, Y, Z\}_2$ of the Hilbert space. This is readily performed by applying suitable $\pi/2$ rotations bringing subsequently each direction along the σ_Z direction prior to readout in the computational basis.

Because of measurement errors, the Eq. 2.43 can yield to an unphysical ρ matrix [6]. We use the so called *Maximum likelihood method* widely described in [27] to determine the best density matrix compatible with the measurement outcomes.

Density matrix evolution during swapping

Examples of state tomography measured in this way are shown in Figure 2.26: they correspond to the $\sqrt{iSWAP}$ (a) and $iSWAP$ (b) gates including their σ_Z phase compensation pulse. The displayed density matrices are those obtained after the final maximum likelihood step.

[6] Realistic density matrix has to be positive ($\langle\psi|\rho|\psi\rangle \geq 0$ for all possible states $|\psi\rangle$) and has to have a unit trace $Tr(\rho) = 1$.

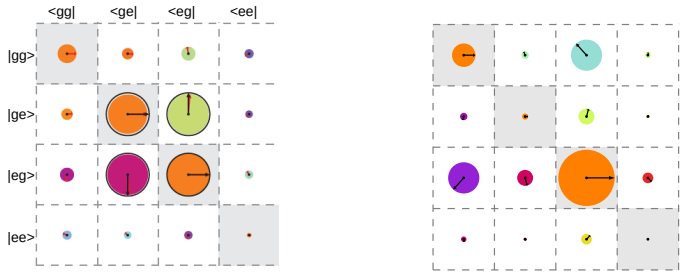

Figure 2.26: Two-qubits tomography after a $\sqrt{iSWAP}$ gate (a) and an $iSWAP$ gate (b) starting from state $|ge\rangle$. The circle sizes represent absolute values $|\rho_{ij}|$ whereas the arrows and the colors both represent the corresponding phases $\arg(\rho_{ij})$.

2.4 Gate tomography

For determining the fidelity of the $\sqrt{iSWAP}$ gate operation implemented in our processor and for characterizing its errors, we have performed the full quantum process tomography [54] of the gate.

2.4.1 Quantum process tomography of the $\sqrt{iSWAP}$ gate

We use the method known as Standard Quantum Process Tomography (SQPT, to be compared with other methods [55, 56, 57]), which consists in determining how the implemented gate transforms a complete basis B of operators acting on the two-qubit Hilbert space. For this basis, we take again all tensorial products of Pauli operators. The transform of B yield the so-called χ matrix that contains the whole information on the quantum process. In practice, we transform the 16 basis states $|\psi_i\rangle \in \{|g\rangle, |e\rangle, (|g\rangle + |e\rangle)/\sqrt{2}, (|g\rangle + i\,|e\rangle)/\sqrt{2}\}^{\otimes 2}$ where $\otimes 2$ denotes the 2-dimensional Kronecker product of all possible permutations. As explained in [27], the quantum state tomography for all these register states yields the symmetric χ matrix represented in Fig. 2.27. The error process matrix $\tilde{\chi} = \chi\chi_{ideal}^{-1}$ obtained by removing the targeted transformation from the measured one is also represented. It shows an overall fidelity $F_g = 0.90$, and shows the different types of error. Relaxation during gate operation is the main error source, followed by imprecise swap duration and imperfect corrected σ_Z compensation.

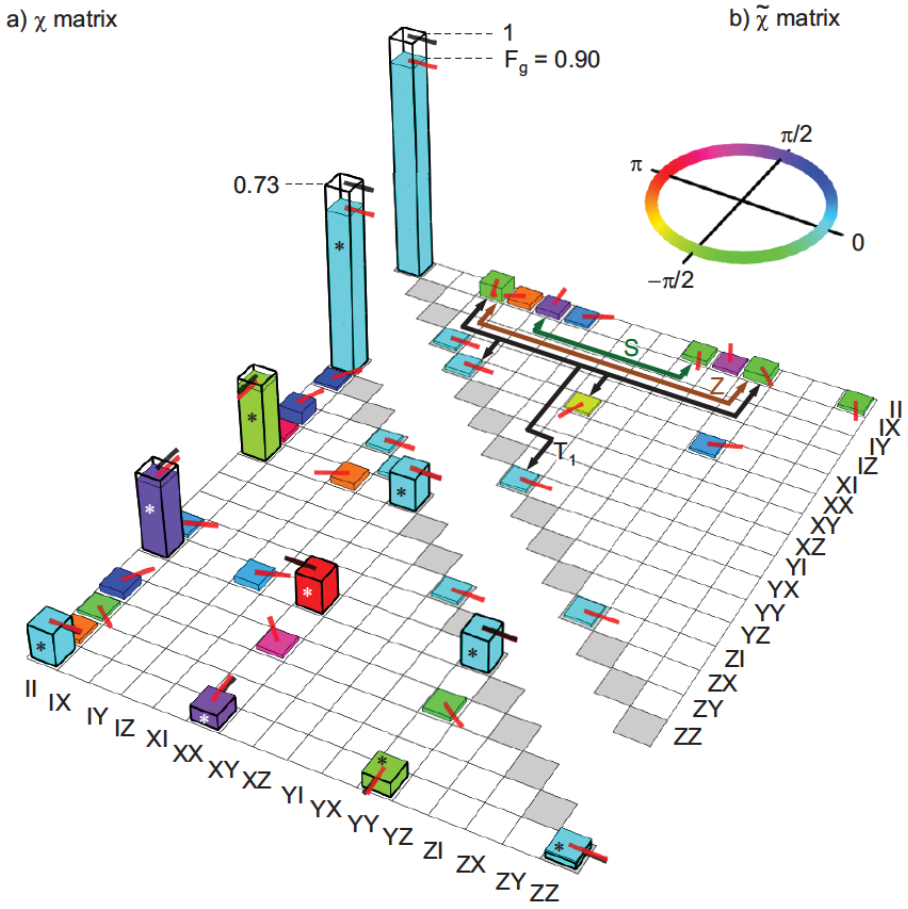

Figure 2.27: Reconstructed half χ matrix (a) and error process matrix $\tilde{\chi}$ (b). Each non-zero matrix coefficient is shown as a bar, the height of which encodes the amplitude ; the phase is represented both by the bar color and a red pointer. Solid empty boxes and black pointers corresponds to the ideal gate, for a sake of comparison. Elements marked by T_1, S and Z are errors due to relaxation, imprecise swap duration, and imperfect σ_Z compensation, respectively.

2.5 Running the Grover search quantum algorithm

With the two-qubit gate just described and a set of single qubit gates, one disposes of a universal set of quantum gates allowing to implement any unitary evolution of the qubit register[7]. We decided to implement the Grover search algorithm [58] on four objects because it provides an interesting benchmark for quantum speedup.

[7]In the sense that no feedback is needed

2.5.1 The Grover search algorithm

For finding a single state among $N = 2^n$ ones in a classical bit register, one needs a function able to discriminate the solution, and one has to call it an average number of time $\mathcal{O}(N)$ for succeeding in the search. In the case of a search in a quantum register, the discriminating function is replaced by a discriminating quantum operator, called the Oracle, which changes the sign of the state corresponding to the search solution, and leaves the other states unchanged. The Grover search algorithm then finds the solution by calling the Oracle only $\mathcal{O}\left(\sqrt{N}\right)$ times. Whereas for a classical search, the algorithm consists only in repeating the experiment with the N different possible states, the quantum algorithm operates very differently:

- Start with a fully superposed quantum state $\left\{\frac{|g\rangle+|e\rangle}{\sqrt{2}}\right\}^{\otimes n}$
- Repeat $\mathcal{O}\left(\sqrt{N}\right)$ times the following sequence to increase the weight of the solution in the register state:
  - apply the given and unknown Oracle operator
  - apply a fixed operator called diffusion (or symmetry) operator.
- Measure the register state in the computational basis $\{|g\rangle, |e\rangle\}^{\otimes n}$

The Grover search algorithm on 4 objects In the particular case $N = 4$, the Grover search algorithm requests only a single call of the Oracle for finding the solution with certainty. This is already quite amazing, and provides a rather clear case of quantum speedup. Note that a classical query & check classical algorithm would succeed with a probability 1/4 after a single call.

The algorithm is fully described in figure 2.28. The four possible oracle functions consist in a $iSWAP$ gate followed by one of the 4 possible gates $Z^I_{\pm\pi/2}.Z^{II}_{\pm\pi/2}$. These oracle functions π-shift a single state among 4. In the two-qubits case, the diffusion operator is again a $iSWAP$ gate followed by $X^I_{\pi/2}.X^{II}_{\pi/2}$. The state readout at the end is supposed to fully represent the oracle function applied.

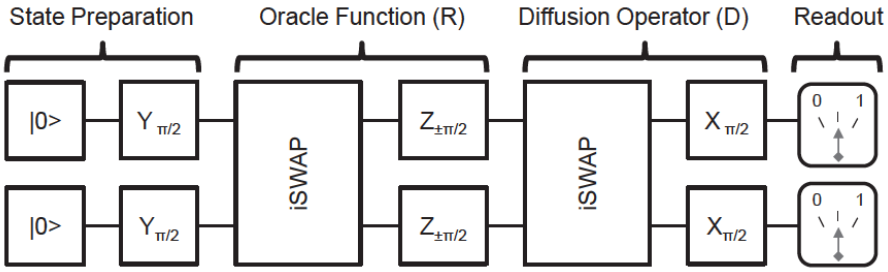

Figure 2.28: Grover algorithm sequence (see text)

2.5.2 Running the Grover search algorithm

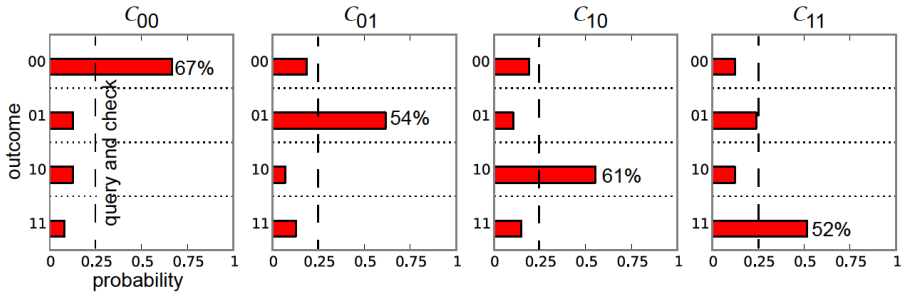

Figure 2.29: Single-run success probabilities of the implemented Grover search algorithm, for the 4 possible oracle operators. The success probability is always larger than the success probability of the query-and-check classical algorithm.

We have implemented the Grover search algorithm for the four possible Oracles. As shown in Fig. 2.29, the raw data shows a success probability for a single run that ranges between 52% and 67%, well above the 25% success probability of a classical algorithm. This result [26] provided the second demonstration of quantum speedup with an electrical quantum processor after the demonstration performed at UCSB for the Shor algorithm [59].

Chapter 3

Design of a 4 qubit processor

Towards a more scalable architecture

We have demonstrated in the previous chapter a two-qubit processor fitted with individual qubit control and individual qubit readout. The frequency agility of the flux controlled transmons was used to switch on and off the interaction induced by a fixed capacitive coupling, which implements a $iSWAP$ interaction. Using this controlled interaction, we obtained a universal set of gates able to implement any unitary operation. With this processor, we could run algorithms and record an outcome after each run, and this outcome was faithful enough for demonstrating the quantum speedup of the Grover search algorithm. This architecture is however not suited for scaling up the processor size, and a more scalable architecture for drive, coupling and readout is clearly needed. Section 3.1 describes the architecture we propose, the following sections discussing single-qubit gates, two-qubit gates and multi-qubit readout.

3.1 A $N + 1$ line architecture

Our goal is to make a simple quantum processor prototype sufficiently versatile to run any algorithm with any choice of qubits, and get the result in a single shot at the end of the run, by reading out simultaneously all the qubits. We aim also at limiting the complexity and the hardware expense.

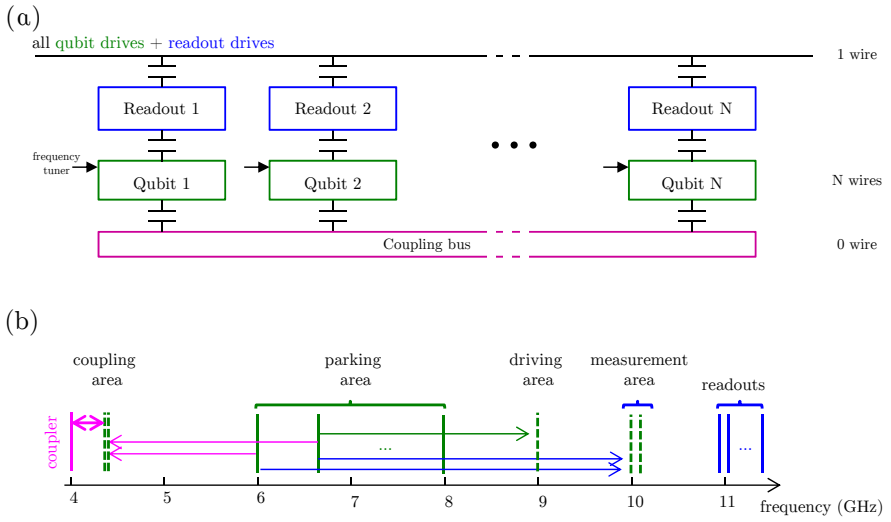

Figure 3.1: (a) '$N+1$ architecture' of a simple N-qubit processor with a single wire used for drives and readouts, and N wires to control the qubit frequencies. (b) Frequency domain overview of the processor: qubit frequencies are shown (green) at various positions corresponding to different operation (parking, driving, coupling and readout), whereas coupling bus (magenta) and readout resonators (blue) are fixed.

The architecture that we propose is shown in Fig. 3.1. It is a '$N+1$ architecture', meaning that it requires $N+1$ lines connected to the processor to perform all the operations and readouts on N qubits. This architecture reuses many of the characteristics of the simple 2-qubit processor described in chapter 1 with few important changes to make it more scalable:

- We propose first to apply single qubit gate drives via a common transmission line coupled to all the qubits, through their readouts.
- Second, we target a versatile processor in which any pair of qubits can be selected for applying an $iSWAP^{\alpha}$ gate similar to the one described in chapter 1. To do so, rather than directly coupling the qubits to each other, we couple them capacitively to a common high quality factor resonator, playing the role of a coupling bus [60]. To perform the gate, we intend to place the two selected qubits on resonance, at a frequency close but different from that of the bus.
- Third, for simultaneous single-shot high fidelity readout, we keep the idea of having a Josephson bifurcation amplifier (JBA) per qubit. For a sake of scalability, we intend to frequency multiplex all the readout signals on the same line (also used for single qubit drives), adapting the multiplexed linear dispersive readout demonstrated for flux qubits in [61].

- Consequently, as for the two-qubit processor of the first chapter, a key feature of our architecture is the frequency agility of the qubits. They have to be moved from their parking frequencies, to a frequency suited for single qubit gates, then to resonance with another qubit for implementing swap gates, and finally to a frequency close of their readout resonator for projecting their states. Consequently, each transmon needs its own frequency control line called flux line (hence N wires), which has to be much faster than any gate duration, but at the same time slow enough to be adiabatic (i.e. not changing the population of the qubit eigenstates).

Figure 3.1.b shows on a frequency axis the positions corresponding to the different operations applied to the qubits in our architecture.

We define the computational basis of our processor as the eigenbasis of the system when each qubit is at its parking position with the other modes (readouts and coupling bus) being empty.

Considering that all the qubits will suffer from decoherence and relaxation, all the operations have to be done as quickly as possible. In the rest of this chapter, we detail how the operations are performed rapidly and the various spurious effects.

In Section 3.2, we discuss the theoretical accuracy of fast single-qubit gates as well as their undesired effects on non-targeted qubits (all drives being applied through a single line potentially affecting all the qubits). We then discuss in Section 3.3 two-qubit gates, in terms of coupling constant and expected maximum fidelity. We also detail the effect of the undesired residual couplings between qubits at their parking frequencies.

In Section 3.4, we discuss the parameter chosen for readout, the resulting readout accuracy, and the possible readout crosstalk of simultaneous readout by the intrinsic non-linearity of the JBAs.

Last, we discuss in Section 3.5 the problem of frequency crowding potentially limiting scalability, and check that the parameters chosen yield to coherence and life times long enough to perform simple algorithm.

3.2 Single qubit gates

We discuss single qubit gates in the frames rotating at the qubit transition frequencies. Rotations around the Z axis of the Bloch sphere are performed using adiabatic frequency changes, whereas rotation around X and Y axis are obtained by applying Rabi pulse with suitable amplitude, duration and phase.

3.2.1 Z axis rotations

A σ_Z gate on qubit i is performed with a current pulse in its flux line i, starting at its parking position.

For this, we use a 1 GHz bandwidth flux line, a pulse generator with a 1 ns time resolution and 14 bits depth to encode frequency changes up 8 GHz.

A phase $\varphi = \int \delta f\,(t)\,dt \in [-\pi, \pi]$ is easily obtained in 10 ns (10 samples) by a qubit displacement δf of order 100 MHz. The 14 bits depth makes the phase tunable with an accuracy of $1\,\text{bit} \times 1\,\text{ns} = 10^{-3}\pi$.

Spurious drives The spurious flux φ_k induced in the loop of qubit k when driving the qubit $i \neq k$ induces correspond to a unitary operation given by

$$U_k = \begin{pmatrix} 1 & 0 \\ 0 & c_{ik}\varphi_i \end{pmatrix}, \tag{3.1}$$

where φ_i is the phase applied to qubit i and c_{ik} is the relative crosstalk between flux line i and qubit k. This c_{ik} crosstalk have to be minimized at the design step of the processor geometry with the help of microwave simulations (See Sec. 3.6.1). Any residual crosstalk is finally corrected by applying a calibrated correction matrix to the vector of flux pulse amplitudes.

3.2.2 X and Y axis rotations

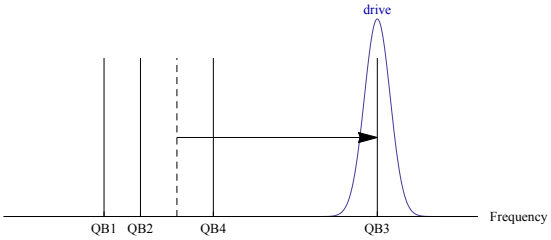

Figure 3.2: Selective drive method

As in chapter 1, X and Y rotations are applied resonantly to a selected qubit i, in the shortest possible time t_g compatible with the 3-level nature of the transmon qubit. More precisely, to avoid spurious excitation of the third level or incomplete rotation of a π pulse, we indent to either use Gaussian π pulses of 20 ns ($\pm 3\sigma$) or 10 ns long DRAG pulses [62, 63] yielding errors below 1%.

However, contrary to Chapter 2, since all the qubits are driven through a single line in our architecture, two important differences have to be considered:

- As a first consequence, the Rabi pulse on selected qubit i is also felt by all other qubits $k \neq i$. In order to minimize the corresponding spurious drive, qubit i is moved away from the parking region to the drive position. The residual drive of qubit k and its compensation are evaluated in next section.

- Since qubit i is moved back and forth away from its parking position, it accumulates extra phase that needs to be compensated by a Z gate.

3.2.2.1 Displacement induced phase

As in Sec. 3.2.1, the accumulated phase due to the displacement is $\varphi = \int \left(\omega_{ge}(t) - \omega_{ge}^{parking}(t)\right) dt$. To avoid any extra Z rotation during X or Y pulse, one needs to make this accumulated phase to be zero (or 2π multiple). For fast flux pulse and a detuning $\Delta^{drive-parking} = \omega_{ge}^{drive} - \omega_{ge}^{parking} \sim 2 - 4\,\text{GHz}$, this acquired phase is of the order of $\varphi \sim t_g \Delta^{drive-parking} \sim (20 - 40)\ 2\pi$ but only a small amount $\varphi\,[2\pi] \in [-\pi, \pi]$ of it has to be compensated using a σ_Z gate as in Sec. 3.2.1.

3.2.2.2 Spurious drive on the other qubits

The evolution induced on qubit k is given by 3.2 (in the rotating frame at ω_{ge}^k)

$$U^k = \begin{pmatrix} \frac{e^{\frac{it\delta}{2}}\left(\Omega_R \cos\left(\frac{\Omega_R t}{2}\right) - i\delta \sin\left(\frac{\Omega_R t}{2}\right)\right)}{\Omega_R} & \frac{ie^{\frac{it\delta}{2}} \epsilon \sin\left(\frac{\Omega_R t}{2}\right)}{\Omega} \\ \frac{ie^{-\frac{1}{2}it\delta} \epsilon \sin\left(\frac{\Omega_R t}{2}\right)}{\Omega_R} & \frac{e^{-\frac{1}{2}it\delta}\left(\Omega_R \cos\left(\frac{\Omega_R t}{2}\right) + i\delta \sin\left(\frac{\Omega_R t}{2}\right)\right)}{\Omega_R} \end{pmatrix}_{\{|g^k\rangle, |e^k\rangle\}} \tag{3.2}$$

with $\delta = \omega_{ge}^k - \omega_d$ the detuning between the two qubits, Ω_{R0} is the Rabi drive strength at resonance and $\Omega_R^2 = \Omega_{R0}^2 + \delta^2$ the actual Rabi frequency of the detuned qubit.

It is shown in Fig. 3.3 for a particular bad choice of the parameter exacerbating the error.

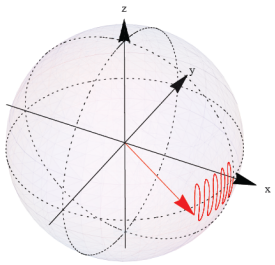

Figure 3.3: Spurious Rabi oscilation in the Bloch sphere

We see on the off-diagonal terms of Eq. 3.2, that the variation of the complex amplitudes oscillate periodically, cancel every $t_L = L\pi/\Omega_R \sim L\pi/\delta$ (L integer) and have a maximum value $a_R = \frac{\Omega_{R0}}{\Omega_R} = \frac{1}{\sqrt{1+\epsilon^{-2}}} \sim \epsilon$ with $\epsilon = \Omega_{R0}/\delta$.

The diagonal terms show a complicated phase evolution: taken at all t_L times, this variation is $\varphi_L = \frac{2L\pi\delta}{\Omega_R} \approx \pi L \epsilon^2$

At large detuning $\epsilon \to 0$, this spurious drive becomes negligible; however the detuning δ is in practice limited to $2 - 4\,\text{GHz}$ and we choose this value ($\epsilon = 1/40 - 1/80$ given gate duration t_g). This yields to an amplitude variation that can reach 2.5%.

If full cancellation of this error is needed, we can choose precisely the parking frequencies and the drive frequency and strength to verify $\Omega_R^k = 2L\Omega_{R0}^i$, with an easily reachable MHz precision.

In that case, the phase error can be cancelled using a compensating σ_Z gate (typically $\varphi \approx \frac{\pi\epsilon}{2} \sim 2.5°$).

3.2.2.3 Alternatives

The spurious drive discussed above and its necessary compensation due to limited detunings is inherent to our $N+1$ architecture. An alternative solution is to have one drive per qubit, either by adding N driving wires (leading to a $2N+1$ architecture) or by using the flux lines as a charge driving line of the transmon [64]. This latter alternative comes at the expense of more hardware on each flux line (bias tees and filters).

3.3 Two-qubits gates

For obtaining a universal set of gates, it is sufficient to combine single qubit gates and an entangling two-qubit gate. Direct constant capacitive coupling between qubits, as done is Chapter 2, being not scalable, we use a bus resonator as already mentioned [19, 65].

3.3.1 Coupling with bus resonator

We consider the system formed by a resonator coupled to a register of qubits. The overall Hamiltonian takes the Tavis-Cummings form:

$$H/\hbar = \omega_R a^\dagger a + \sum_i \omega_{ge}^i \sigma_Z^i + \sum_i g_i(\sigma_+^i a + \sigma_-^i a^\dagger) \tag{3.3}$$

where g_i is the coupling constant between the resonator mode and qubit i.

In the limit where $\omega_{ge}^i - \omega_R \gg g_i$, one can trace out resonator mode degrees of freedom (see Sec. 3.3.3 for validity) and end up with an effective Hamiltonian

$$H/\hbar = \sum_i \omega_{ge}^i \sigma_Z^i + \sum_{i \neq j} J_{ij} \sigma_X^i \sigma_X^j \tag{3.4}$$

with

$$J_{ij} = g_i g_j \left(\frac{1}{\Delta_i} + \frac{1}{\Delta_j} \right), \tag{3.5}$$

where $\Delta_i = \omega_r - \omega_{qe}^i$.

The important difference with the direct coupling used in chapter 2 is the frequency dependence of the coupling constant J_{ij}, giving a supplementary knob to switch on or off the interaction.

3.3.2 iSWAP gate

When two particular qubits are placed on resonance close to the bus frequency, the interaction terms in Eq. 3.4 yield an effective $iSWAP$ interaction with frequency $J_{ij}/2\pi$, via virtual photon exchange.

We choose to perform a $\sqrt{iSWAP}$ gate in 20 ns, compatible with the 1 ns resolution of our pulse control system. This corresponds to $J_{ij}/2\pi = 12.5$ MHz

Given the chosen bus-qubit coupling $g_i/2\pi = 50$ MHz, one finds the bus-qubits detuning is

$$\Delta_{bus-coupling} = 2g_i^2/J_{ij} \simeq 2\pi\ 400\ \text{MHz}. \tag{3.6}$$

3.3.3 Validity of the empty bus approximation

In order to check that the bus remains empty during the interaction, we calculate the unitary evolution operator of the complete system composed of two qubit symmetrically coupled to the bus. Instead of looking at the bus population, we consider the matrix element $\langle ge0|U|eg0\rangle$, as shown on Fig. 3.4, reaching -1 for a complete swap with no energy left in the resonator. We see that even with the fast oscillations with the bus, one can find a place where the swap is almost perfect $|\langle ge0|U|eg0\rangle| > 0.9999$.

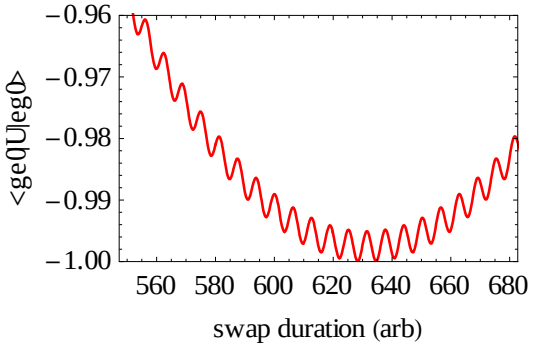

Figure 3.4: $\langle ge0|U|eg0\rangle$ matrix element as a function of the swap duration

In reality, the two coupling constants between the qubit and the bus can slightly differ due to geometrical constrains. We show on Fig. 3.5 the minimum value of the same matrix element as a function of the asymmetry. We see that an asymmetry of 5% leads to a swap element of -0.995, corresponding to a gate fidelity greater than 99.5%.

3.3.4 Residual coupling

Since the coupling between the two qubits cannot be completely switched off, a residual partial $SWAP$ evolution occurs at their parking positions. Solving

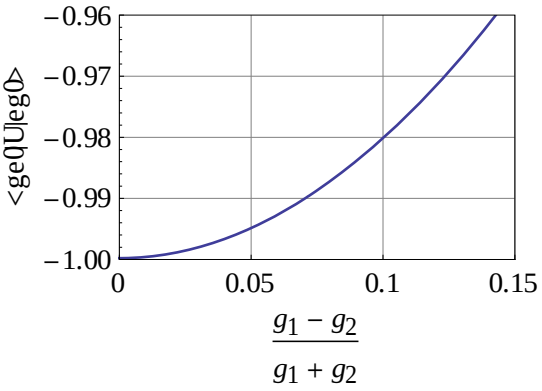

Figure 3.5: $\langle ge0|U|eg0\rangle$ matrix element as a function of the qubit-bus coupling asymmetry.

Eq. (3.4 -3.6) for two qubits i and j out of resonance yields a $SWAP$ frequency f_{qq} and amplitude a_{qq}

$$\begin{aligned} f_{qq} &= \sqrt{4J_{ij}^2 + \Delta_{ij}^2} \sim \Delta_{ij} \\ a_{qq} &= \frac{2J_{ij}}{\sqrt{4J_{ij}^2+\Delta_{ij}^2}} \sim \frac{2J_{ij}}{\Delta_{ij}} \ll 1 \end{aligned} \quad , \tag{3.7}$$

at large detuning, with $\Delta_{ij} = \omega_i - \omega_j$.

Accepting a qubit-qubit detuning $\Delta_{qubit-qubit}/2\pi = 400$ MHz at the parking frequencies, and requesting a swap amplitude $a_{qq} \leq 1\%$ yields an upper bound for the effective coupling $J_{ij}/2\pi \leq 2$ MHz. Given this constraint, we find a lower bound for the qubit-bus detuning at parking

$$\Delta_{bus-park}/2\pi \geq 2\,\text{GHz}. \tag{3.8}$$

3.4 Simultaneous readout of transmons

At the end of any algorithm (or at intermediate error correcting steps), the qubit register (or at least, part of it) has to be read out:

- each measured qubit should be read with a high fidelity that does not depend on the simultaneous readout of other qubits. In other words, readout crosstalk should be kept at a negligible level [9].
- Ideally, this measurement should also be quantum non-demolishing (QND) in order to be able to continue the computation with the projected qubit, which can be useful in certain algorithms. However, it is always possible to replace a QND readout by transferring the state to be measured to another fresh qubit using a C-not gate just before measurement.

3.4.1 Frequency multiplexing of readouts

As already explained in chapter 1, qubit readout is usually obtained in cQED from the state dependent frequency shift of a readout resonator. Measuring the reflection or transmission coefficients of a microwave pulse reflected from (or transmitted through) this resonator allows to discriminate the two qubit states.

This readout method can be frequency multiplexed using frequency-staggered readout resonators (sketched in Fig. 3.6), provided that all the signals are sufficiently amplified to extract their in- and out-of-phase quadratures and so the projected qubit state.

Multiplexed readout of qubits was first performed in circuit QED for flux qubits using a wide-band HEMT cryogenic amplifier [61, 66]. However the single-shot sensitivity was not reached with a high fidelity.

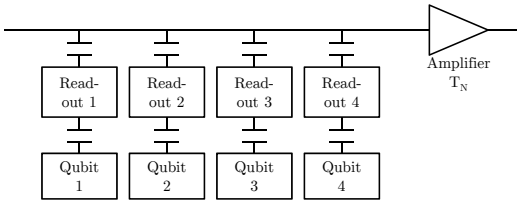

Figure 3.6: Multiplexed readout method

In order to reach this sensitivity, an additional amplification stage with better signal to noise ratio is needed and two options are possible: either use one quantum limited amplifier inserted before the HEMT to amplify all the readout signals, or as in chapter 1, use one JBA per qubit

3.4.2 Amplification schemes for multiplexing

3.4.2.1 Linear readout with a quantum limited amplifier

Single-shot readout and continuous measurements have been performed with different kind of quantum limited amplifiers (Josephson parametric amplifier and Josephson parametric converter) mainly for single-qubit. To readout a set of qubits, with readout cavities in a Δf range, the quantum limited amplifier needs to have a larger bandwidth and not to saturate even when simultaneously fed by all the readout signals.

At the beginning of this thesis work, quantum limited parametric amplifiers had bandwidth of the order of a few tens of MHz and maximum output power of the order of -100 dBm that made them not suited for a scalable multiplexed readout.

Recent implementations of Josephson parametric amplifiers [67, 68] demonstrate larger bandwidths (up to few GHz) and higher saturation power (up

to−80 dBm) that allowed this kind of amplifier to readout simultaneously up to 4 qubits with a high fidelity [64].

3.4.2.2 Multiplexing several Josephson bifurcation amplifiers

On our side, we decided at the beginning of this thesis to frequency multiplex Josephson parametric amplifiers (JBA) used in our previous experiment (Chapter 2). Each qubit is fitted with its own complete non-linear readout device that provides a (nearly) quantum limited discriminator, only requesting commercial low noise cryogenic HEMT amplifier .

However, the JBAs are non-linear resonators, so that the dynamics of one might affect the switching probability the others via their outgoing signals. This imposes to separate their frequencies *more* than for linear multiplexed readout, leading to a larger frequency span for measuring the same number of qubits. Technically, this requires only to control readout signals over a larger bandwidth.

3.4.3 JBA characteristics

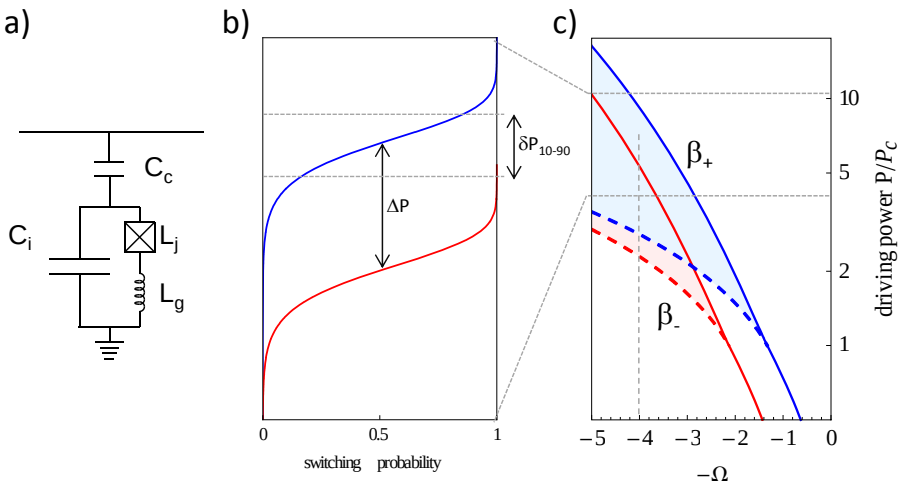

Figure 3.7: (a) Equivalent electrical circuit of the JBA. (b) JBA switching curve for the qubit in its ground (blue) and excited (red) state. (c) JBA stability diagram for both qubit states

As explained in Sec. 2.2.3.3, a JBA is operated in its bistable regime. At a given driving frequency, the resonator switches from its low to its high amplitude state at a driving power that depends on the qubit state. This switching is a stochastic process governed by quantum noise at low temperature, and its rate increases with power. For a given shape of readout pulse, this stochastic

switching translates into a power dependent switching probability. This so-called S switching curve is characterized by its $10-90\%$ width δP_{10-90}. As shown in Fig. 2.2.3.3.b, a good JBA readout has its switching width δP_{10-90} much smaller than the power separation $\Delta P = 2\chi \frac{\partial P_d}{\partial f_d}|_{\beta_+}$ between the two switching curves for the two qubit states (β_+denote the L to H switching line show in Fig. 2.2.3.3.c).

A few parameters control the dynamics of the JBA:

- The resonator characteristic impedance $Z_c = \sqrt{\frac{L_g+L_J}{C_i+C_c}}$. In practice, this impedance can be designed in the $30-80\,\Omega$ range. We choose a relatively low $Z_c \simeq 35\,\Omega$ to get rather high current at low photon number.
- The resonator frequency is fixed by other constraints explained in Sec. 3.1. In our design, this frequency is at about 11 GHz.
- The resonator non-linearity is a key parameter that is best expressed in terms of participation factor $p = L_J/L_{tot}$ with L_g, L_J, and $L_{tot} = L_J + L_g$ the geometrical, Josephson and total inductances, respectively.
- The resonator external quality factor Q_e defining the coupling to the readout line and controlling the speed of the switching dynamics. Internal losses in the resonator are assumed negligible, i.e. $Q_i \gg Q_e$.

These last two parameters are now discussed.

3.4.3.1 Choice of JBA parameters

3.4.3.1.1 External quality factor, sensitivity and measuring speed As shown in formula 2.38, at large qubit-resonator detuning, the relaxation rate of the qubit through the cavity is inversely proportional to the cavity quality factor Q_e. We thus choose the largest possible value of $Q_e \simeq 3000$ compatible with a fast energy loading of the resonator in a time $\tau_R = \frac{Q}{\omega_R} \simeq 50\,\text{ns}$. This time τ_R is the rise/decay time of the resonator at low power (linear regime) and can be quite different from the characteristic time scales of the dynamics at large driving power. Numerical simulations of the experiment of chapter 1 show that $Q_e \approx 600$ leads to a switching time $\tau_p \sim 30\,\text{ns}$. τ_p is the time needed to separate the trajectories that switches from those that do not, and is larger than the qubit projection time.

The new chosen value corresponds to a switching time $\tau_p \sim 100\,\text{ns}$, which can be made shorter than the Purcell relaxation times at readout as discussed in Sec. 3.5.2. Moreover, this slower JBA has a narrower power width $\delta P_{10-90} \approx 1\,\text{dB}$ and consequently a smaller frequency width $\delta f_{10-90} = \delta P_{10-90} \left(\frac{\partial P_d}{\partial f_d}|_{\beta_+}\right)^{-1} \approx 0.8\,MHz$, which makes it easier discriminating the two qubit states.

3.4.3.1.2 Non linearity As shown by Eqs. 2.32, the reduced non linearity p impacts directly the resonator energy just before and after switching (L and H states at switching), but simulation shows that it has a small impact on the JBA switching speed. The internal number of photon at switching determines our ability to discriminate the L and H states in a given time; we target a readout signal at switching of $-100\,\mathrm{dBm}$, which should allow us to measure the quadratures of the outgoing signal within a few microseconds with sufficient accuracy to perfectly discriminate the two resonator states. Using *2.2.3.3*, this leads to a non linearity $p \simeq 0.15$ for a typically used reduced detuning of $\Omega = 2Q\frac{\Delta f}{f} \sim 4 - 10$.

3.4.3.2 Qubit-readout coupling

We decide to be in the regime where the two switching curves are completely separated, accepting an error of 10^{-5} due to this overlap. This imposes us to choose a value of $2\chi \geq 4\,\mathrm{MHz}$.

The qubit state dependent cavity shift χ and Purcell relaxation rate $\Gamma_{purcell}$ are strongly dependent on the coupling constant g and of the qubit-resonator detuning $\Delta_{readout-JBA}$. We show in Fig. 3.8 the relaxation time as a function

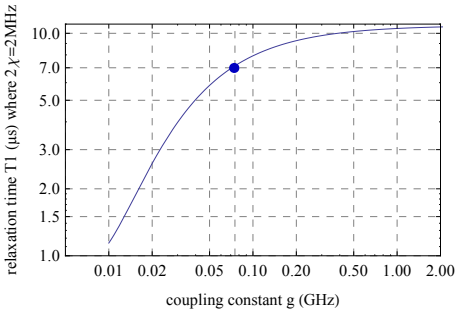

Figure 3.8: Purcell relaxation time as a function of the coupling constant g where $2\chi = 4$ MHz

of the coupling constant g, take at the selected point where $2\chi = 4\,\mathrm{MHz}$.

Since the qubit projection time is fixed by the JBA parameters to $\tau_p \sim 100\,\mathrm{ns}$, we also accept a relaxation during measurement of $1 - 2\%$ leading us to a Purcell relaxation time at readout of $5 - 10\,\mu\mathrm{s}$ while keeping a low coupling to avoid spurious effects. We choose a reasonable value of $g/2\pi = 75\,\mathrm{MHz}$ leading a relaxation of the excited state of $\sim 1.5\%$ at the optimal detuning $\Delta_{readout-JBA}/2\pi \simeq 1\,\mathrm{GHz}$.

3.5 Processor Parameters

The relative detunings chosen in the 3 previous sections already provide a picture of the the overall frequency staging.

3.5.1 Final choice

In order to ensure negligible thermal excitation of the bus resonator (which has the lowest frequency in the system), we choose its frequency to be $f_{bus} = 4\,\text{GHz}$. This yields a thermal population of $\sim 10^{-3}$ at 30 mK.

We also choose the readout resonators to be the highest frequencies in the system to keep the transmon frequencies below their readout resonator frequencies at readout and avoid the straddling regime in which the resonator dispersive shifts cancel [69]. This leads us to the frequency staging shown on Fig. 3.9.

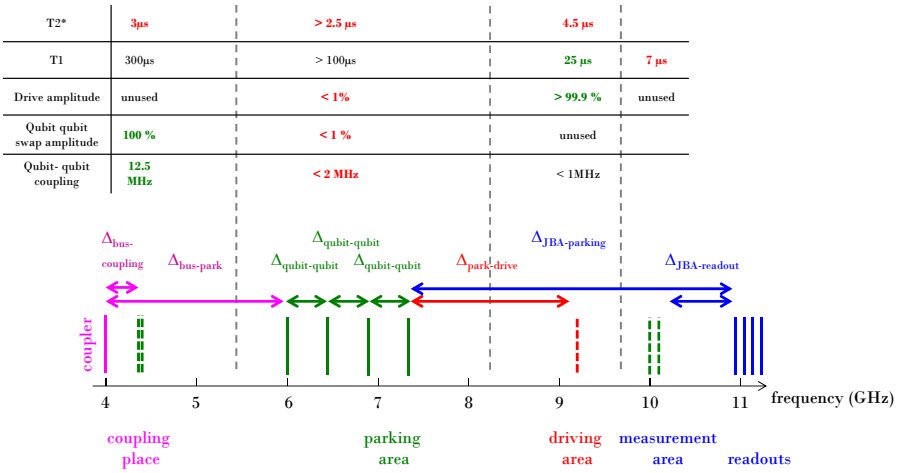

Figure 3.9: Overall frequency staging

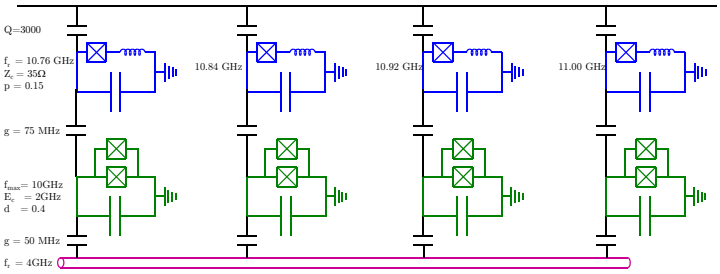

Figure 3.10: Complete schematics, with relevant physical parameters

3.5.2 Overall decay and coherence rates

Assuming a standard amplitude ($A = 10^{-5}$) for the $1/f$ flux noise in transmon SQUID loops, Eq. 2.25 predicts that a transmon with a symmetric SQUID (i.e.

whose frequency can go well below the bus frequency) would have a coherence time $T_2 \simeq 1\mu s$ at the bus frequency as show in Fig. 3.12.

Since there is no need for the transmon frequency to reach the bus frequency, an asymmetric design of transmon would be appropriate (see Fig. 3.11), thus reducing the decoherence rate Γ_2 due to flux noise, as shown on Fig. 3.12.

We get a minimum coherence time around the parking place ($6 - 7$ GHz) of $T_2 = 2$ µs.

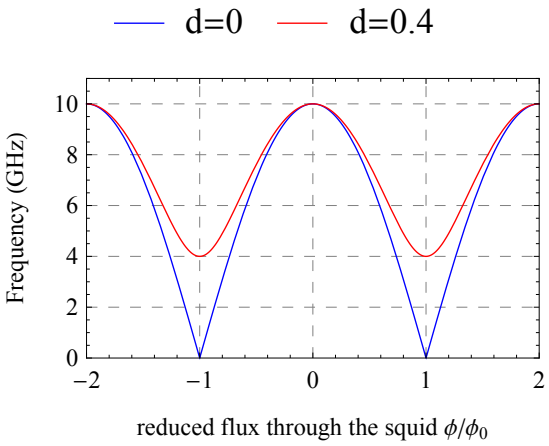

Figure 3.11: Transmon frequency as a function of the reduced flux through the loop for $d = 0$ (blue) and $d = 0.4$ (red).

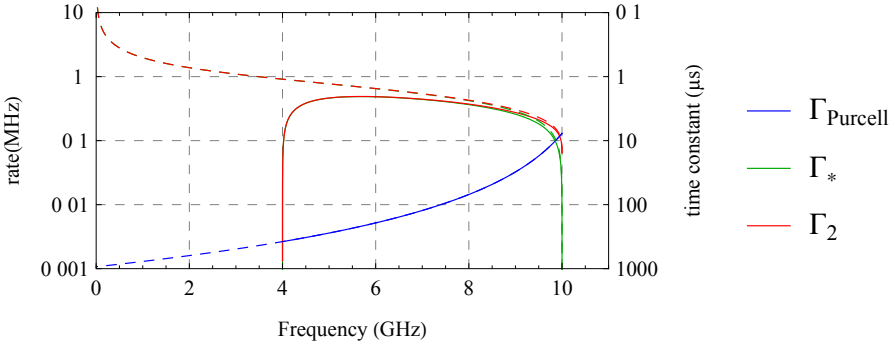

Figure 3.12: Decay and coherence rates as a function of the frequency for two different junction asymmetry $d = 0$ (dashed lines) and $d = 0.4$ (solid lines)

3.6 Sample design

We need now to translate the physical parameters from the previous sections into an actual geometrical design that we can fabricate. This section explains general rules used for sample design (Sec. 3.6.1) as well as how we perform microwave simulations (Sec. 3.6.2) to extract the relevant parameters (Sec. 3.6.4). The geometry of the design highly depends on the substrate material, sapphire in our case, which is chosen because of its low microwave losses.

3.6.1 Overall design

We first need to place the different components and their connecting lines. As shown in Fig. 3.13, topological constraints impose crossings at least between some of the lines, given that connections are located on the sample edges[70]. Because such crossings can introduce impedance mismatching and crosstalks of the crossing lines, we decide to cross the flux biasing lines carrying signals at relatively low frequency ($f \leq 1$ GHz) with the drive-readout line on which a small signal loss (≤ 1 dB) cannot be not too detrimental.

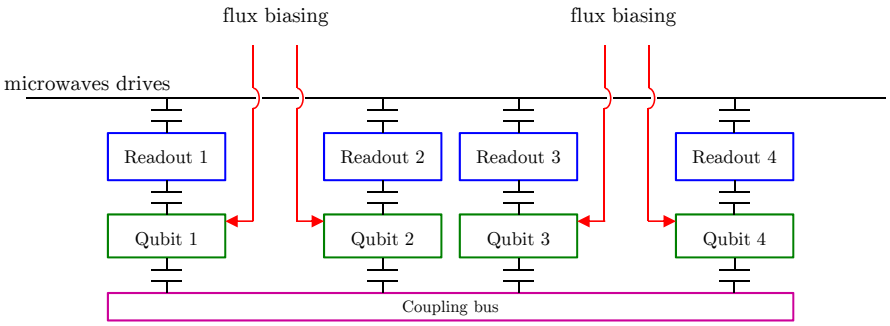

Figure 3.13: Geometric placement of the different components. The flux biasing lines cross the microwave drive and readout line.

Flux lines

In our design, the frequency control of the qubit is performed by applying current pulses to the flux lines. In order minimize the crosstalk of flux line i to other qubits j, one has to prevent the current returning to ground to flow away from flux line i, from low frequency to microwave frequencies ($DC - 1$ GHz). For that purpose, we use a separate ground (red lateral lines in Fig. 3.14), which is reconnected to the common ground only at the chip edges.

At DC frequencies, the only path to ground is obviously though this separate ground; at microwave frequencies (1 GHz), simulations confirm that only less than 1% of return current flows in other ground, and a negligible part of it can approach other qubits.

The only remaining source of crosstalk is thus the field induced by flux line i on qubit j. This contribution is negligible, given the quadrupolar nature of the CPW mode and of the symmetric double loop design.

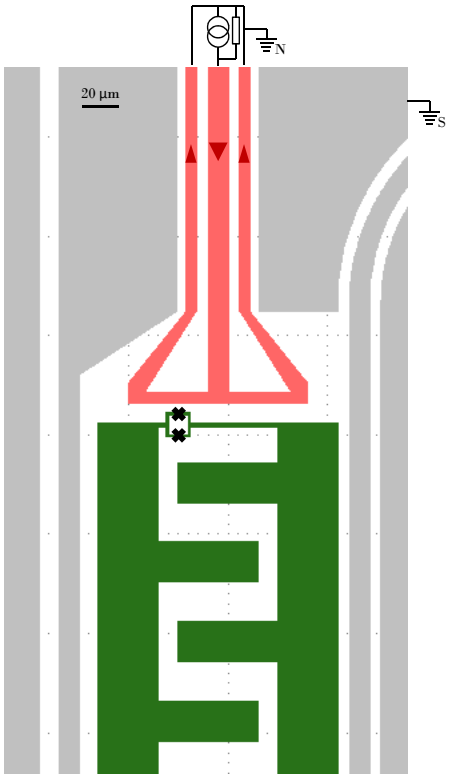

Figure 3.14: Design of our flux lines. The qubit is shown in green while the flux line is in red. The ground symbol "S" ("N") represents connection to the main ground via superconducting (normal) material.

3.6.2 Microwave simulations

Microwave design is not always intuitive because none of the designed element are purely capacitive or inductive. Although approximate formulas and experience are good guides, numerical simulations are however necessary to check the correct behavior of different elements at high frequencies and to obtain precise values of the relevant electrical parameters.

Although the experiment will involve non-linear resonator in the quantum regime, they can be considered as simple linear elements working in the classical regime at the design step. Each Josephson junction (or SQUID) is thus replaced in the simulations by its equivalent linear inductance $L_j = \Phi_0^2/E_j$.

Given our circuit is essentially planar, we perform our simulations with a so called 2.5D simulator, well adapted to this task and requiring less memory than a full 3D simulator. We choose a professional software called SONNET. Since our circuit is only made of thin film superconductors, we model it with ideal metal sheets with zero resistivity.

This simulator can give us:

- the resonance frequencies of the transmons and of their readout resonators,
- the coupling between a transmon, its readout resonator, and the drive-readout line,
- the spurious cross-talk between lines,
- the decay rates (or quality factor) of the resonators relaxation rates due to dielectric losses or coupling to the $50\,\Omega$ matched external lines.

Since simulation times increase extremely fast with the size of the simulated circuit, we make many different simulations of only parts of it, like a particular crossing, or at most, a single cell of the processor, including the transmission line, a readout resonator, a qubit and a part of the coupling bus.

Signals are connected to the simulated lines via ports, which are characterized by their internal impedance Z_{pi} (Fig. 3.15).

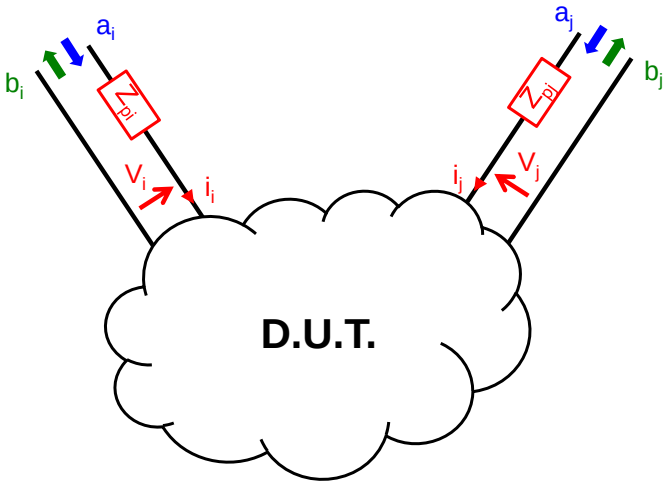

Figure 3.15: Schematic of a microwave simulation. Two ports i and j are connected to the device (D.U.T.). Note that port impedance Z_{pi} are complex numbers.

The simulator calculates for each targeted frequency the microwave currents and charges in all conducting materials; it outputs the S matrix (reflexion/transmission), or equivalently the Y admittance and Z impedance matrices

(Eqs. 3.9). As other commercial softwares, SONNET offers an ABS[1] functionality able to get a fine frequency meshing from a small number of simulated frequencies, which decreases simulation times.

3.6.3 Transmission, admittance and impedance matrices

The transmission, admittance and impedance matrices are defined by:

$$\begin{array}{l} Y_{ij} = \frac{I_i}{V_j}|_{V_{k\neq j}=0} \\ Z_{ij} = \frac{V_i}{I_j}|_{I_{k\neq j}=0} \\ S_{ij} = \frac{b_i}{a_j}|_{a_{k\neq j}=0} \end{array} \tag{3.9}$$

We see from Eqs. 3.9 and Fig. 3.15 that the Z_{ij} and Y_{ij} coefficients depend only of the device under test while the S_{ij} coefficients include also the port impedances Z_{pi}.

To deduce relevant parameters from the simulations, as done in the next part (3.6.4), we exploit the relations between these different matrices. The scattering matrix is obtained from the admittance and impedance ones using

$$\begin{array}{c} S = \left(1_N - \sqrt{Z_p} Y \sqrt{Z_p}\right)\left(1_N + \sqrt{Z_p} Y \sqrt{Z_p}\right)^{-1} \\ Z = Y^{-1} \end{array} \tag{3.10}$$

with 1_N the identity matrix and $Z_p = \begin{pmatrix} Z_{p1} & & 0 \\ & \ddots & \\ 0 & & Z_{pN} \end{pmatrix}$ the diagonal complex port impedance matrix.

3.6.4 Extraction of the relevant parameters

The first parameters that we want to obtain from simulation are the readout resonator frequency and quality factor. Figure 3.16 shows the simulated design and the S parameters. The resonance at $f = 11.96\,\text{GHz}$ is fit to extract the quality factor $Q = 3500$.

This direct method works well for not too large quality factors. At quality factors $Q > 10000$, obtaining accurate results from such a simulation of the S matrix becomes very long. A better solution consists in introducing an internal port k in the circuit directly connected to the resonator and in simulating the admittance Y_k as seen from this port (See Fig. 3.17). Indeed, a resonance occurs when the imaginary part of Y_k crosses zero. In the same way as the quality factor of a parallel RLC circuit is given by $Q = R/Z_c$ with Z_c the characteristic impedences of the resonator (See also [71]), the quality factor of the simulated circuit is given by

$$\begin{cases} Im\left[Y_i\left(\omega_0\right)\right] = 0 \\ Q = \frac{\omega_0}{2} \frac{Im\left[Y_i'(\omega_0)\right]}{Re[Y_i(\omega_0)]} \end{cases} \tag{3.11}$$

[1] Adaptive Band Synthesis

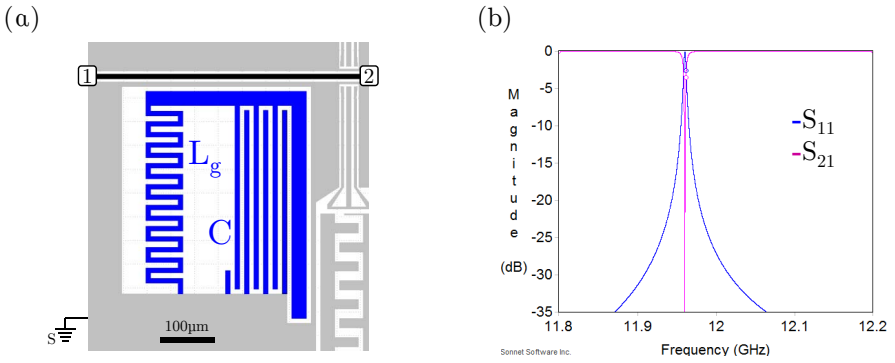

Figure 3.16: Readout resonator coupled to the transmission line. (a) drawing placed in the simulator. (b) simulated reflexion (S_{11}) and transmission (S_{21}) parameter as a function of the frequency.

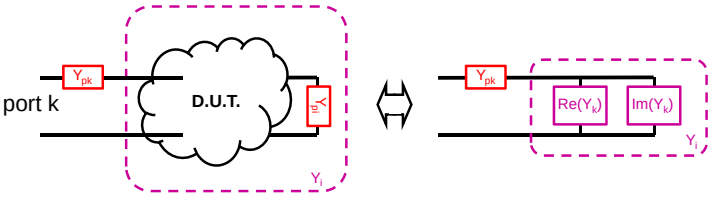

Figure 3.17: Impedance Z_k as seen from the port

Two points have to be made here:

- Introducing such a port at any place where it does not exist in the actual circuit does not change at all the physics (resonances, quality factor, etc), provided this port has an infinite impedance. However, simulating with a finite port impedance is also possible since the simulated Y and Z matrices do not depend of port impedances.

- In equation 3.11, the admittance Y_k as seen from the port differs from the matrix element Y_{kk} given by the simulator (except when port k is the only port), because Y_k include the impedances of ports $i \neq k$ while Y_{kk} do not. $Y_k = 1/Z_k$ is actually obtained from the S matrix coefficient

$$S_{kk} = \frac{Z_k - Z_{pk}}{Z_k + Z_{pk}}, \tag{3.12}$$

which includes the effect of all port impedances but Z_{pk}.

We apply below this method to extract the qubit resonance frequency and its quality factor, leading to the relaxation time T_1 up to a factor close to unity.

3.6.4.1 Qubit resonance width

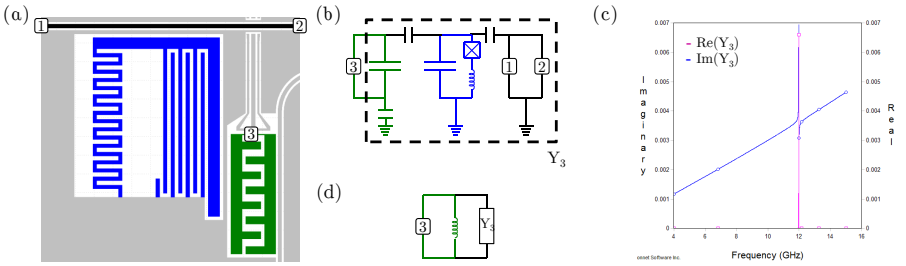

Figure 3.18: Simulation performed to check qubit quality factor. (a) drawing placed in the simulator. (b) equivalent circuit of the drawing. (c) complex admittance seen from port 3 (port 1 and 2 having 50Ω impedence). (d) equivalent model in adding a paralell inductance

Figure 3.18.a shows the simulated geometry, with real port 1 and 2 and the internal port 3 introduced at the level of the transmon SQUID. In this simulation, the SQUID inductance is actually removed and Y_3 will include only the capacitive part of the qubit and the rest of the circuit (Fig. 3.18.b). The inductance can be added later in parallel with Y_3 (Fig. 3.18.d) to place the qubit resonance at any targeted frequency. Figure 3.18.c shows the real and imaginary parts of Y_3, the peak at $\approx 12GHz$ corresponding to the readout resonance. Adding to Y_3 a variable Josephson admittance $1/jL_J\omega$ and using Eq. 3.11 we obtain a relaxation time $T_1 \approx Q/\omega_{ge}$ that increases with the qubit-readout detuning. We see on Fig. 3.19 that the relaxation time extracted in this way follows the Purcell approximation (Eq. 2.38) up to a detuning of order 2 GHz and then gets shorter because of a spurious coupling of the qubit to the outside world.

3.6.4.2 Qubit readout coupling constant

The method above also leads to the coupling constant between the qubit and its readout, indeed, $Im(Y_3^{tot})$ crosses zeros at both qubit and readout resonances (see Fig. 3.20). The separation between the zeros varies with L_j and reproduces the anticrossing. The minimum separation correspond to $2g$ up to a reduced matrix element $|\langle g|\hat{n}|e\rangle|$ of order unity. One can easily reach the targeted coupling in a few iterations with slightly different geometries changing the effective capacitance between the readout and transmon capacitors.

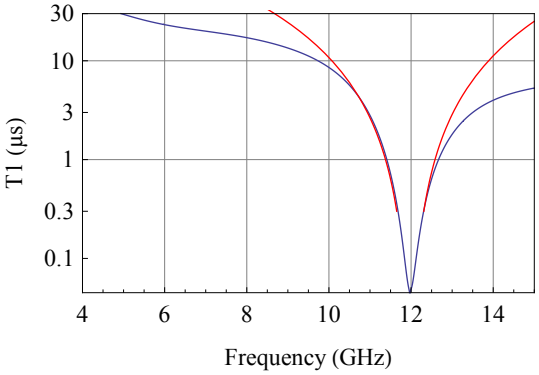

Figure 3.19: Extracted relaxation time T_1 from microwave simulations (blue) and theoretical Purcell decay time (red)

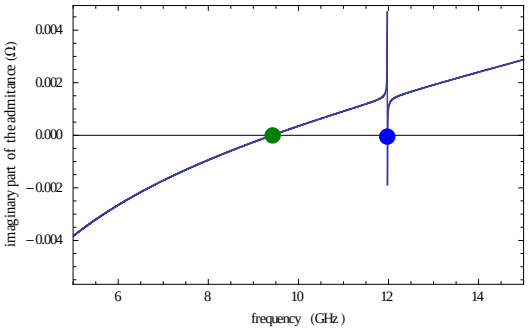

Figure 3.20: Imaginary part of the admittance, with a parallel inductance of $L_j = 6$ nH. The resonances are shown with green and blue dots.

The same method is applied to the qubit-bus coupling.

3.7 Complete design

The full result of the design is shown in Fig. 3.21, including the pads to wire-bond the circuit to input and output lines.

In the next chapter, we explain how this design was fabricated, as well as another simpler design used for testing the multiplexed readout.

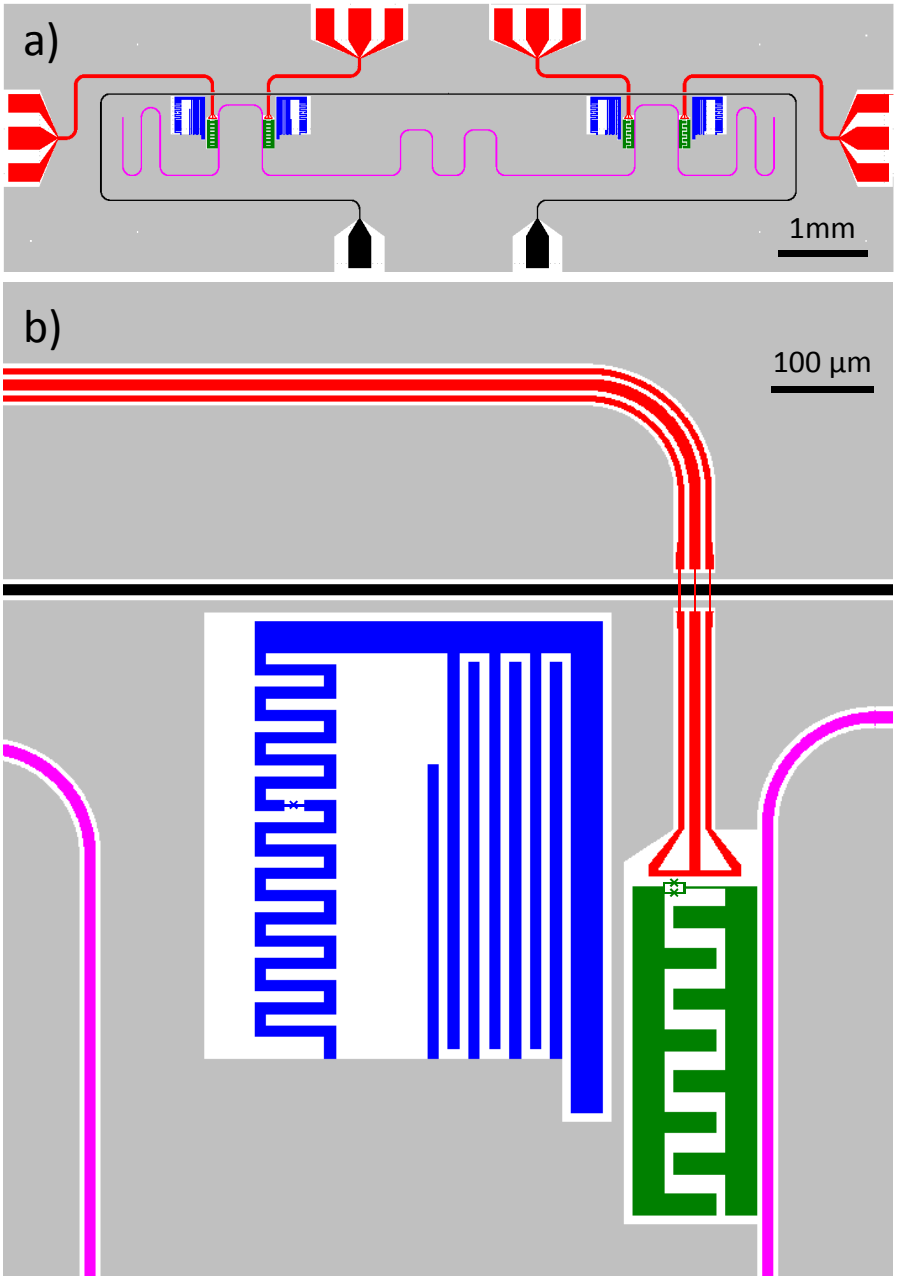

Figure 3.21: Complete design of the sample (a) Full view. (b) Zoomed view on the first cell

Chapter 4

Sample fabrication

In this chapter, we discuss the fabrication of the samples made during this thesis work.

As already mentioned, the substrate of mono-crystalline sapphire is chosen for its particularly low loss tangent. Moreover, this material has a relatively high dielectric constant ($\varepsilon_r \sim 10$) well suited for microwave circuits, because capacitors can be made compact, which means small parasitic inductance and consequently higher frequencies of the spurious resonances. The surface of the substrate is the crystallographic C-plane (1,1,1,0), chosen for its in-plane isotropic dielectric constant. Given the equipment in our fabrication facility, we work on 2 inch wafers. With the standard 10 mm x 3 mm size of the sample chips chosen before my thesis, such a wafer can contain up to 44 chips.

The chip design explained in Chapter 3 is shown in Fig. 4.1. Because it comprises relatively large structures of $\sim$ mm - µm size (shown in gray) as well as small patterns down to $\sim$ 100 nm (JBAs Josephson junction in red and qubit SQUID in blue), fabrication involves both optical and electron-beam lithography. The process flow usually starts on the whole wafer for a certain number of steps; at some point, the wafer is cut into chips that are processed one by one for the remaining steps. Two different process flows have been used in this work:

- Process flow 1
  - Deposition and patterning of large structures by optical lithography (full wafer);
  - Fabrication of JBA Josephson junctions by electron-beam lithography and deposition-oxidization (full wafer);
  - Fabrication of the qubits by electron beam lithography and deposition-oxidization (full wafer);
  - Fabrication of microwave bridges (introduced in Chapter 3) for implementing crossings and ground re-coupling (full wafer);
  - Dicing with diamond saw or scribing of the wafer.

- Process flow 2
  - Optical lithography of the main pattern (full wafer);
  - Deposition of the resist for e-beam lithography (full wafer);
  - Dicing or scribing of chips;
  - Fabrication of both qubits and JBA junctions at the same time by e-beam lithography and deposition-oxidization (chip per chip).

Both methods present advantages and drawbacks: Process flow 1 is easy to control because of the large size of the wafers, and makes possible a systematic variation of the qubit junction size on the different chips, which is useful to obtain a chip with the targeted resistance of the Josephson junctions; the price to pay is two long e-beam lithography steps and the loss of the full wafer if something goes wrong. Process flow 2 offers more flexibility because fabrication parameters like Josephson junctions areas, oxidation pressure and duration, can be adjusted on a chip according to results obtained on previously fabricated chips, and because only one chip is lost if something goes wrong. But this flow is slower and forbids fabrication of microwave airbridges, not feasible on small samples.

In the following, we detail, the fabrication of the large patterns (Section 4.1), of the JBA Josephson junctions and qubits (Section 4.2), of the microwave airbridges (Section 4.3), and in Section 4.4 the mounting of sample chips.

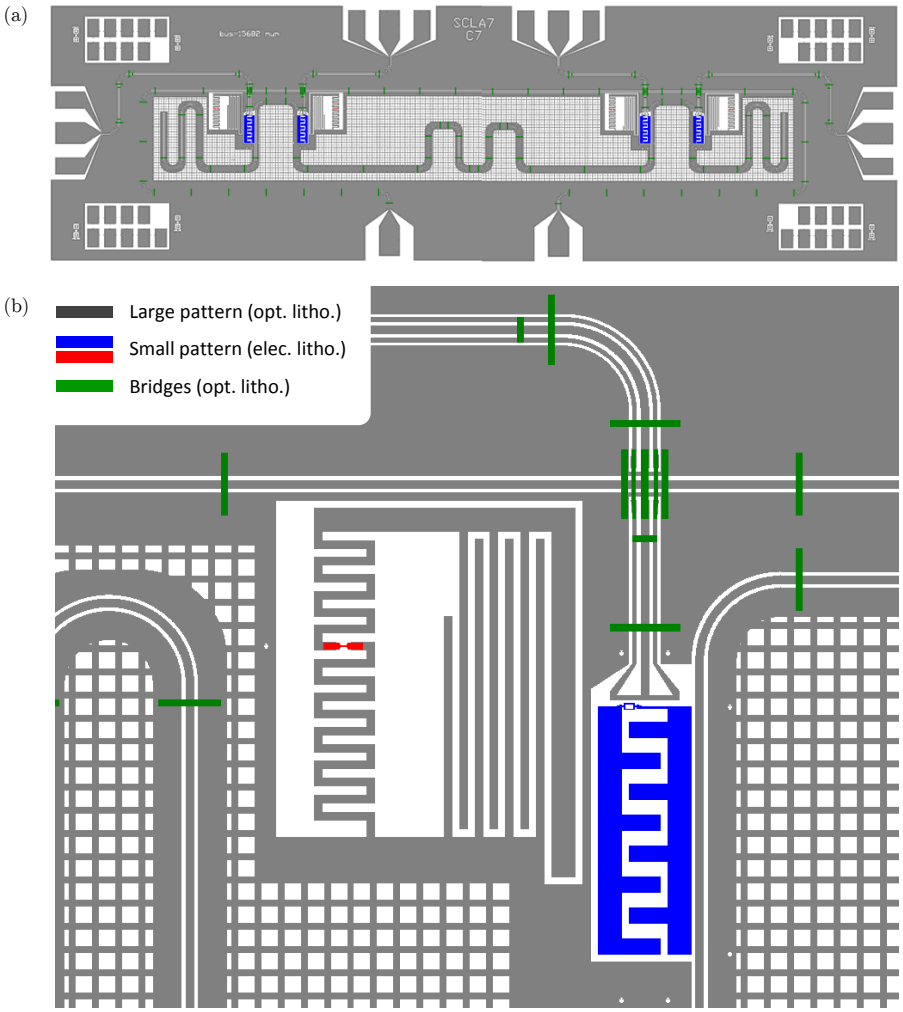

Figure 4.1: Chip design of the 4-qubit processor fabricated in this thesis. The gray, red, blue, and green colors correspond to four subsequent fabrication steps. (a) Single chip in a 2" wafer. (b) Zoom on the first (left) qubit-readout cell of a chip.

4.1 Fabrication of large structures using optical lithography

The superconducting metal chosen for large structures is niobium, for several reasons: it is a conventional BCS superconductor easy to deposit in thin films; it has a $T_C = 9.2\,\mathrm{K}$ critical temperature sufficiently high to make possible measurement of test structures at 4.2 K and 1 K, easily reachable temperatures

with liquid helium. Many experiments have proven its ability to be used for good enough quality factors ($Q > 10^6$) of resonators at a few GHz. Moreover, contrary to aluminum, its critical magnetic field is high enough to be compatible with the flux lines we have designed, which will carry a few milliamperes on 150 nm thick and 10 µm wide wires. Finally, despite its type II superconductivity, niobium can be made free of magnetic vortices at the low magnetic fields required to vary the qubit frequencies by patterning the film as grids (see gray ground planes in Fig. 4.1).

The best niobium thin films being obtained by RF magnetron sputtering, we use this technique to deposit an homogeneous film over the whole wafer, and then pattern it by removing the metal between the electrodes by reactive ion etching [72]. More precisely, the recipe to make the global pattern represented on Fig. 4.2 is the following (see also Fig. 4.3):

- Cleaning of the sapphire wafer in an oxygen plasma at $\sim 8\,\mathrm{W/cm^2}$ during 3 minutes to suppress any organic trace.
- Niobium sputtering (a): deposition of 150 nm at a rate of $\sim 2\,\mathrm{nm/s}$ by RF magnetron sputtering.
- Photo-resist (b): spin 500 nm of Shipley S1813 resist + bake on a hot plate at 110 °C for 2 minutes.
- Photo-lithography (c): UV exposure (monochromatic, line I) through the mask shown in Fig. 4.2, in hard contact, with a dose of $200\,\mathrm{mJ/cm^2}$ on a manual mask aligner[1].
- Development (d): dissolution of exposed resist in pure MF319 developer (TMAH[2]).
- Etching (e): Reactive ion etching of uncovered niobium using a gas mixture of CF_4 (20 c.c./min) and Ar (10 c.c./min) at a pressure of 50 µbar. The etching is monitored by an optical interferometer and lasts approximately 5 minutes at $\sim 0.6\,\mathrm{W}/cm^2$.
- Lift-off (f): Removal of remaining (and partially cross-linked) resist in a bath of warm (70 °C) 1165 remover (NMP[3]).

[1] MJB4 - SÜSS MicroTec
[2] Tetramethylammonium hydroxide
[3] N-methyl-2-pyrrolidine

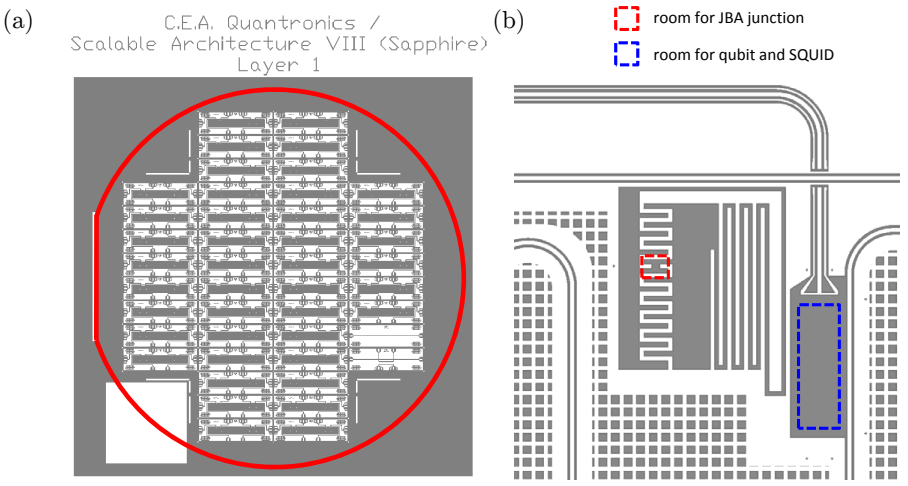

Figure 4.2: (a) Mask used for optical lithography of the main pattern. The 2" wafer perimeter is shown in red. (b) Zoom on the first cell of a chip (shown in Fig. 4.1) showing the room left for fabricating the JBA junction (red rectangle) and a qubit (blue rectangle) in subsequent steps.

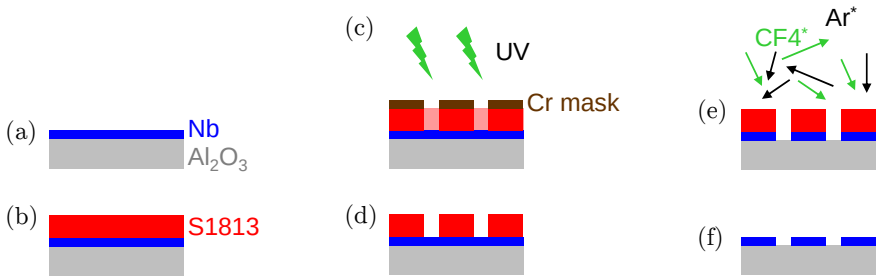

Figure 4.3: Fabrication of the main pattern by (a) magnetron sputtering of Nb, (b-d) optical lithography, and (e) reactive ion etching of unprotected Nb.

4.2 Fabrication of Josephson junctions and qubits

The Josephson junctions of the Josephson bifurcation amplifiers as well as the transmon qubits (see Fig. 4.5) are fabricated by overlapping two aluminum layers, the first of which being oxidized to form the tunnel barrier. This stack is obtained by the Fulton and Dolan bridge technique [73], i.e by e-beam lithography and double-angle evaporation through a suspended shadow mask (see Fig. 4.6). The shadow mask is a resist bilayer made of a spacer layer and of

the mask layer itself. The spacer is made of LOR[4], that we dissolve to create the desired undercut below the mask, without e-beam exposure. Because of the insulating property of sapphire, an aluminum layer is deposited on top of the bilayer, to avoid charging effects during e-beam exposure.

The exact recipe is the following:

- Bilayer resist stack
  - Spacer resist (a): 1 µm thick LOR5B resist, bake out at 190 °C for 5 minutes.
  - Mask resist (b): $\sim$ 300 nm thick PMMA 950 kg/mol, bake out at 180 °C for 1 min 30 sec.
  - Discharge layer (c): a 7 nm layer of aluminum is evaporated on top of the bilayer.
- e-beam exposure (d): 25 keV beam, dose of $300 - 400\,\mu C/cm^2$ with an e-beam lithongraphy machine[5]. The e-beam pattern (Fig. 4.5) is aligned on marks of the main pattern realized by optical lithography; the focus is periodically corrected using a laser interferometer measuring the distance between the sample and the electronic microscope objective. This exposure step lasts for $3 - 4$ hours when exposing the JBA junctions (i) on the whole wafer and for $\sim$ 12 hours when exposing all the qubits (ii-iii).
- Resist developing
  - Al discharge layer removal (e) using a 1.2 % water solution of TMAH (1 : 1 MF-CD-26 to H_2O).
  - Development (f): exposed resist is dissolved in 1 : 3 MIBK[6] to isopropanol in approximately 1 min 30 sec.
  - Undercut (g) is obtained by dissolving the spacer resist with the same TMAH solution. This method makes possible to tune the undercut by observing it with an optical microscope and by immersing the sample several times until the targeted undercut is obtained. A 1.5 µm wide undercut is usually achieved in $2 - 3$ minutes.
  - Under-mask cleaning: sample is cleaned in an oxygen plasma asher for $\sim$ 30 s ($\sim$ 15 nm of resist ashed) to remove possible resist residues from the substrate. Note that this highly oxidizing step has to be skipped when a recontact to previously deposited material is required and when some residues on the surface are not detrimental (e.g. for JBA junctions recontact to JBA resonators).
- Junction fabrication in a single vacuum cycle:

[4] polydimethylglutarimide
[5] eLine - Raith
[6] Methyl-isobutyl-ketone

  - Pumping down to 10^{-7} mbar.
  - Ion milling to outgas the substrate and deoxidize the metal electrodes to be recontacted: Neutralized 500eV Ar ion beam at 0.8 mA/cm^2 during 10 seconds (i.e. 50 Ar atom per electrode (substrate) atom).
  - First aluminum layer (h): 30 nm of aluminum is deposited with e-gun evaporation at a rate of 1 nm/s through the mask with an angle of $-30°$.
  - Oxidation (i): the whole chamber is placed in a static O_2/Ar (15/85 %) atmosphere to oxide the aluminum layer surface. This oxidation controls the tunnel resistance and so the Josephson energy of the future junction. The oxidation parameters are 1 mbar during 50 sec for the JBA junctions, and 25 mbar during 10 min for the qubit ones.
  - Second aluminum layer (j): 60 nm deposited with an angle of $+30°$. Note that the total Al/AlOx/Al thickness (90 nm) is sufficient for the new junction arms to soar from the substrate to the top of previously fabricated electrodes.

- Lift-off (k): The resist stack covered with aluminum is finally removed with a warm (70 °C) bath of PG remover (NMP).

In the case of a process flow 1, the previous recipe is followed twice: once for JBA junctions and once for qubit and SQUID fabrication. For qubit SQUID fabrication, the size of the junctions vary along the different samples between -50 % and $+50$ % compared to the targeted value.

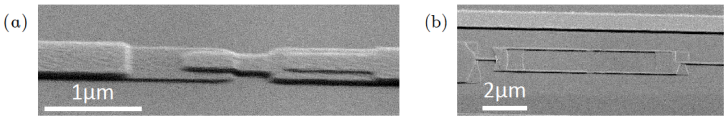

Figure 4.4: SEM pictures of the Josephson junctions under angle: (a) JBA junction, where we see the overlap between the two aluminum layers. (b) qubit SQUID, the junctions are hardly visible.

We show in Fig. 4.4 the obtained junctions, for the qubit and the JBA. We also fabricate in the corner of each sample some test structures with junctions identical to those of the processor. These test junctions can be measured without damaging those of the processors. The room temperature resistance R_N of a junction gives the Josephson critical current and energy

$$I_c = \frac{\pi\Delta}{2eR_N},\ E_J = \varphi_0 I_c, \tag{4.1}$$

with $\Delta \approx 180 - 190\,\mu$eV the energy gap of our evaporated aluminum. A correction factor of $\approx +15$ % needs to be applied on the critical current to take

into account the reduction of tunnel resistance when temperature drops from room temperature to cryogenic temperatures.

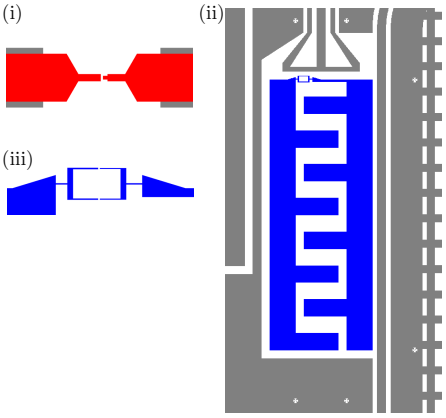

Figure 4.5: Patterns of (i) the JBA junction and of (ii) the transmon, including (iii) its SQUID, are defined by e-beam lithography.

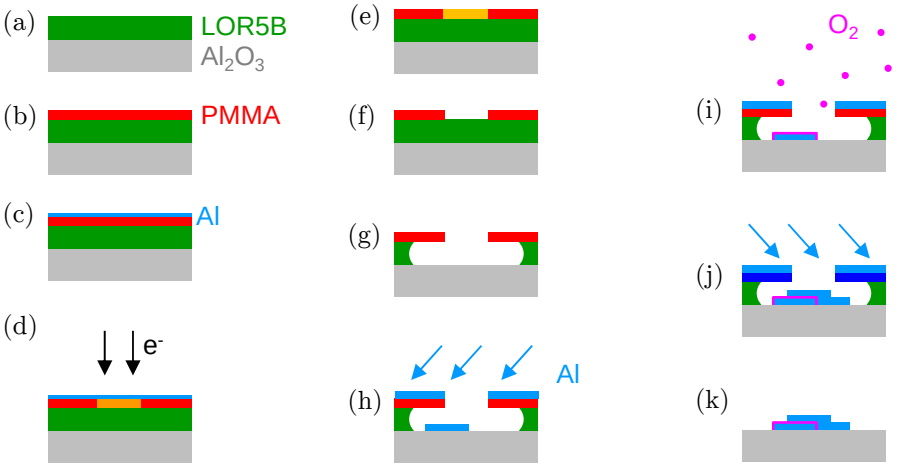

Figure 4.6: Fabrication process of the JBA junctions and transmon qubits by (a-g) e-beam lithography and (h-k) double angle evaporation of aluminum with intermediate oxidation.

4.3 Airbridge fabrication

To implement the line crossings and mass re-connections of our processor design (see Section 6 of Chapter 3 and Fig. 4.8), we have developed an airbridge

fabrication process, adapted from similar processes previously developed in other laboratories [70, 74]. A key feature of this technique is to use the rounding effect of a patterned and re-flowed thick resist layer, leading to smoothed resist profiles.

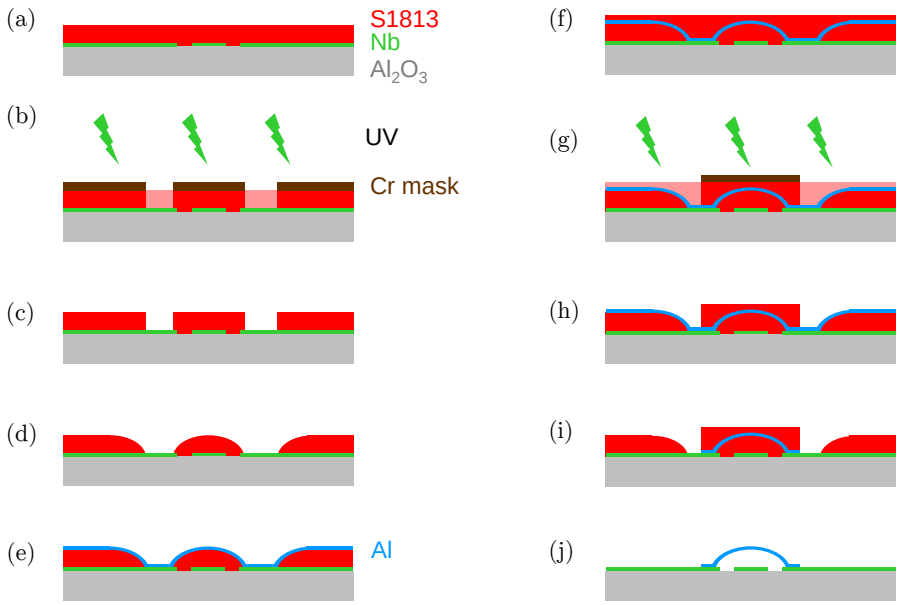

Figure 4.7: Bridge fabrication by (a-c) optical lithography, (d) reflow, (e) aluminum evaporation, (f-h) second optical lithography and (i,j) aluminum etching.

This fabrication process is described on Figure 4.7 and can be divided in four major steps detailed below:

- Bridge "pillars" patterning by positive UV lithography (where the bridges are to be contacted to the existing niobium layer)
  - Photo-resist (a): Spin on the cleaned wafer of a $\sim 4\,\mu m$ thick S1828 resist layer, bake at 110 °C for 5 minutes (1 min/µm minimum). This thickness will define the bridge height.
  - Exposure (b): large dose of $900\,mJ/cm^2$ of UV light (line I), due to large resist thickness. The mask (Fig. 4.8, orange) is aligned with an accuracy of $< 1\,\mu m$ on top of the main pattern.
  - Development (c): exposed resist removed in MF319 developer. Special care is needed to completely get rid of resist residues at the "base" of the pillars.

- Resist reflow (d): patterned photoresist is baked at 140 °C for 4 minutes. The resist is rounded by surface tension effect, which defines the lateral profile of the future bridge. This rounding is visible with optical microscope.

- Aluminum bridge deposition in a single vacuum cycle:

  - Ion milling: to allow good galvanic contact the niobium surface is ion milled with neutralized 500 eV Ar ion beam at 0.8 mA/cm^2 during 100 seconds (i.e. $\sim$ 500 Ar atom per electrode atom). Note that this steps also burns the top surface of the resist mask.
  - Deposition (e): 500 nm of aluminum is evaporated at right angle all over the wafer. This thickness is that of the future bridges and thus define their strength.

- Bridge pattering by positive UV lithography and etching:

  - Photo-resist (f): spin $\sim$ 2 µm thick S1828 resist layer, bake it at about 110 °C for 7 minutes. This thickness is sufficient to completely planarize the new resist (i.e. fill the holes defined in the previous lithography step).
  - Exposure (g): The whole wafer is exposed except bridge arches (Fig. 4.8, green) with a dose of 1000 mJ/cm^2. This dose has to be controlled properly to pierce the 7 µm thick resist without overdosing and enlarging too much the pattern.
  - Development (h): develop in a solution of H_2O 1 : 1 AZ developer, which has a low etching rate of aluminum used for the bridges compared to many other resist developers. The exposed resist is dissolved in 2 min 30 sec. Special care is needed to get rid of resist residues around the pillars.
  - Etching (i): the unprotected aluminum is then etched by immersion during 15 minutes in a commercial aluminum etchant[7] and agitation to prevent hydrogen bubbles from sticking to the surface and stopping the etching.
  - Removal of burnt resist: resist cross-linked during the ion milling step, is eliminated by a 5 minute long exposure to an oxygen plasma in a asher ($\sim$ 2 W/cm^2).

[7] MicroChemical aluminum etchant: H_3PO_4 : 73 %, HNO_3 : 3.1 %, CH_3COOH : 3.3 %, H_2O : 20.6 %

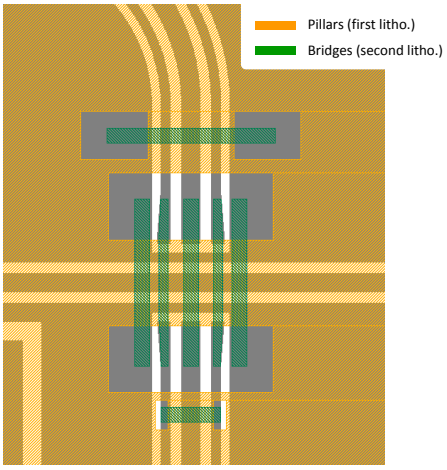

Figure 4.8: Series of two masks used for optical lithography of aluminum airbridges. First mask (orange) defines the bridge pillars and recontacts (positive lithography before deposition), while second mask (green) defines the bridge itself (positive lithography before etching).

The result of this process is shown on Fig. 4.9 where we clearly see the bridge profile resulting from the resist reflow.

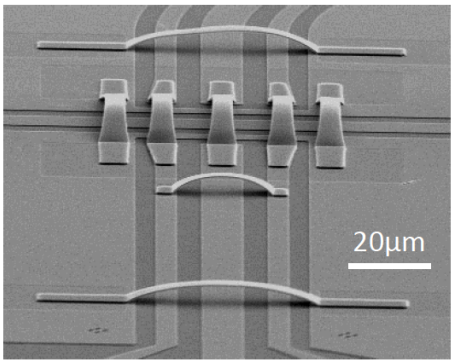

Figure 4.9: SEM picture of airbridges taken with angle. We see two transmission lines crossing with airbridges.

4.4 Cutting and mounting

As already mentioned, at a given step that depends on the process flow, the 2 inch wafer is cut. The 44 rectangular chips with size $3 \times 10\,\text{mm}$ are cut apart either with a diamond dicing saw or a manual diamond scriber. Prior to cutting, the full wafer is protected with an additional photoresist layer:

either a thick Shipley S1828 layer for process flow 1 with bridges, or a 1 µm thick UV3 layer for process flow 2 with electronic resist bilayer. After cutting, the samples are placed correspondingly either in a hot bath of 1165 remover to dissolve both the protecting layer and the resist used to fabricate the airbridges, or in isopropanol to dissolve the UV3.

Once cut and cleaned, the samples of process flow 1 are electrically characterized by measuring their test structure junctions. Note that due to the 20 µm width of the transmon capacitance "fingers", it is also possible to measure directly the actual qubit SQUID resistances. The samples of process flow 2 are processed one by one and characterized in the same way.

Sample holder and wire-bonding

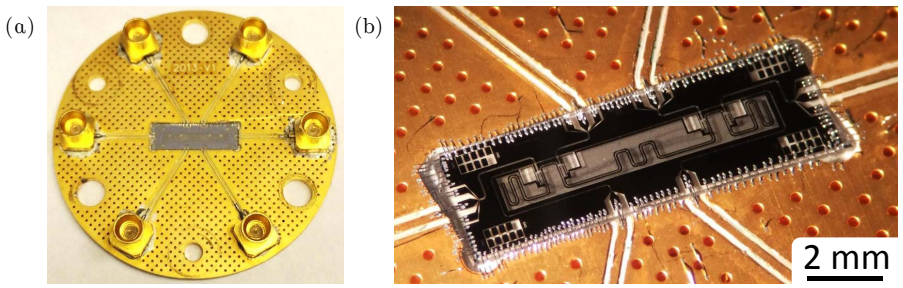

Figure 4.10: (a) Printed chip board with sample installed in its groove. (b) Zoomed view on the sample and its wire-bonds.

A sample selected for low temperature characterization is then stuck with wax or vacuum grease in a groove of a Rogers[8] TMM10i circular printed circuit board (PCB). The sample pads and ground planes of the chip are wire-bonded to the PCB lines and grounds using a 33 µm diameter aluminum[9] wire, superconducting at the temperature of a dilution refrigerator. The 50 Ω coplanar waveguide transmission lines of the PCB are terminated by 50 Ω right-angle mini-SMP connectors with a typical reflexion coefficient of -26 dB @ 12GHz. The PCB is metalized on both sides with gold-coated copper, and ground planes of both sides are connected to each other with standard metalized vias.

The PCB is placed on a sample holder with a cover (see Fig. 4.11) matching precisely its size and having a small enough cavity above the chip to avoid spurious resonances in the relevant frequency window (DC-15GHz). The closed sample holder is finally anchored at the mixing chamber of a conventional wet dilution refrigerator.

[8] Rogers corporation
[9] Al : 99%, Si : 1%

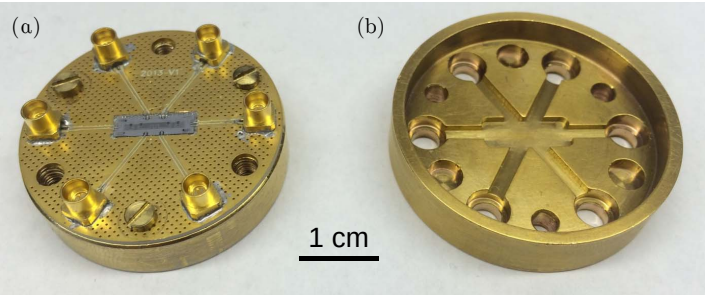

Figure 4.11: (a) PCB on its sample holder. (b) cover, with grooves facing the transmission lines on the PCB and the chip and holes for connectors.

Chapter 5

Multiplexed readout of transmon qubits

As explained in Chapter 3, our proposition for making a scalable quantum processor is to multiplex the readout of many transmon qubits using a single line that carries all the readout signals. In this chapter, we show how we have implemented and tested this readout strategy on a four-qubit register. We first describe the sample used for this test in section 5.1, then describe in section 5.4 the readout of a single qubit and its performance for an optimal coupling, and finally demonstrate in section 5.5 the simultaneous readout of the four qubits, and discuss the performance reached and the perspectives.

5.1 Sample and experimental setup

5.1.1 Sample

The sample used in this experiment is shown in Fig. 5.1.b. It consists in four almost identical cells 1-4 depicted in Fig. 5.1.a. Each of these cells is composed of a flux tunable transmon qubit capacitively coupled to a JBA readout resonator made of lumped elements, itself capacitively coupled to the transmission line. As for the two-qubit processor described in chapter 2, the non-linearity is obtained by introducing in the resonator inductance a Josephson junction (the inductance of which depends on the current). The readout resonators of the different cells have staggered frequencies obtained by varying the resonator capacitance. As shown in Fig. 5.1.c, the resonator interdigitated capacitances are decreased from cell to cell by removing about half a finger when moving to the next one. The sample is fabricated on sapphire using the chip by chip process flow number 2 described in Chapter 4. The common readout line and the readout resonators are patterned in a niobium film by optical lithography and reactive ion etching. The JBA junctions and the qubit (capacitor and SQUID), see Fig. 5.1.d-e, are fabricated using electron-beam lithography and double-angle evaporation of aluminum through a suspended PMMA shadow

mask. As already explained, airbridges cannot be fabricated with this process flow, and the top and bottom ground electrodes separated by the transmission line are reconnected by bonding of 25µm Al-Si(1%) wires. In this experiment, only two ports of the chip are used, out of the 6 available ones.

5.1.2 Low temperature setup

As shown on Fig. 5.2.b, the microwave line that carries the qubit readout and drive signals from room temperature to the sample thermally anchored at temperature $T \sim 30\,\mathrm{mK}$ is attenuated at several intermediate temperatures in order to ensure a low electronic temperature at the sample stage. A bandpass filter is also inserted in the line to prevent spurious high frequency noise from reaching the sample. On the output line, the readout signals are routed to a cryogenic amplifier thermally anchored at 4.2 K through two $4-8\,\mathrm{GHz}$ circulators and a $4-8\,\mathrm{GHz}$ bandpass filter that prevents noise outside the bandwidth, at the amplifier input port, from reaching the sample. The sample is placed in a superconducting coil, the ensemble being placed inside a Cryoperm cylindrical box[1] that shields the static magnetic field induced by the circulator magnets. Another Cryoperm shield is added all around the 30 mK stage of the dilution fridge in order to protect the experiment from fluctuating magnetic field coming from the environment.

5.1.3 Microwave setup

The microwave setup used in this experiment is shown in Fig. 5.2.a. The hardware for the qubit drive is shown in brown whereas hardware for readout drive and acquisition is shown in purple. Both qubit and readout signals are generated using a single sideband mixing technique discussed in Sec. 5.2.1. Then, the simultaneous readout outcomes for all qubits are obtained from the output signal using further amplification and a two-stage demodulation technique discussed in Sec. 5.2.2.

5.2 Experimental techniques

5.2.1 Single sideband mixing

In order to obtain the microwave pulses at the different relevant frequencies, we use a single sideband mixing technique based on IQ mixers whose functional diagram is described in Fig. 5.3. In this method a continuous carrier is applied to the LO port, and ac modulated signals are applied on both on the I and Q ports to translate the frequency to the targeted value and define the pulse envelope; the resulting microwave pulse is picked on the RF port.

[1] MµShield ®

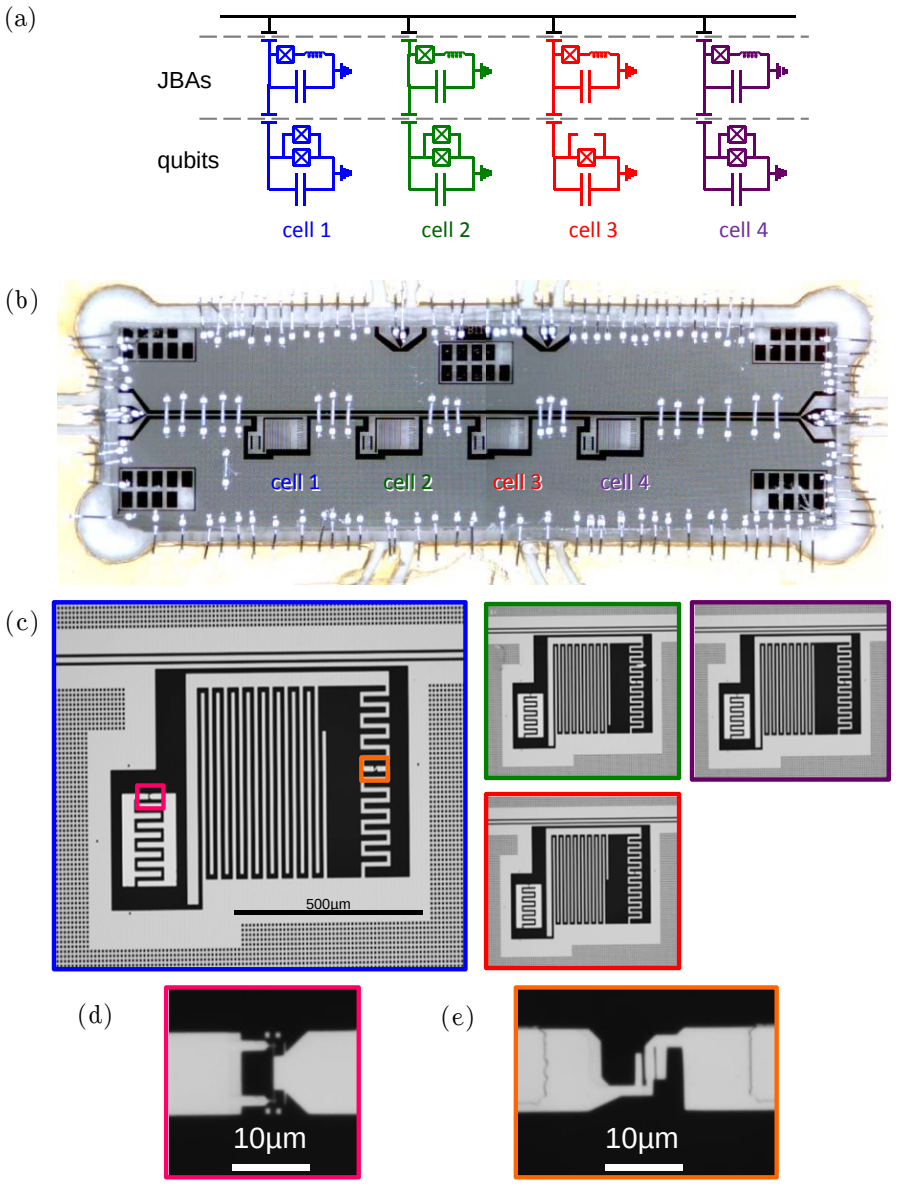

Figure 5.1: 4-qubit sample used for testing the multiplexed JBA readout. (a) Equivalent electrical circuit showing the four cells composed of a flux tunable transmon coupled to a JBA resonator, itself coupled to the readout line. Note that one junction of qubit 3 is broken and thus acts as an open circuit. (b) Optical micrograph of the chip connected to a printed circuit board. (c) Optical micrographs of the qubit cells 1-4 (blue, green, red, purple). The JBA capacitance decreases from cell to cell in order to obtain staggered frequencies with 70 MHz steps. (d-e) Optical micrographs of the Josephson junctions of the qubit SQUID (d) and of the JBA readout resonator (e).

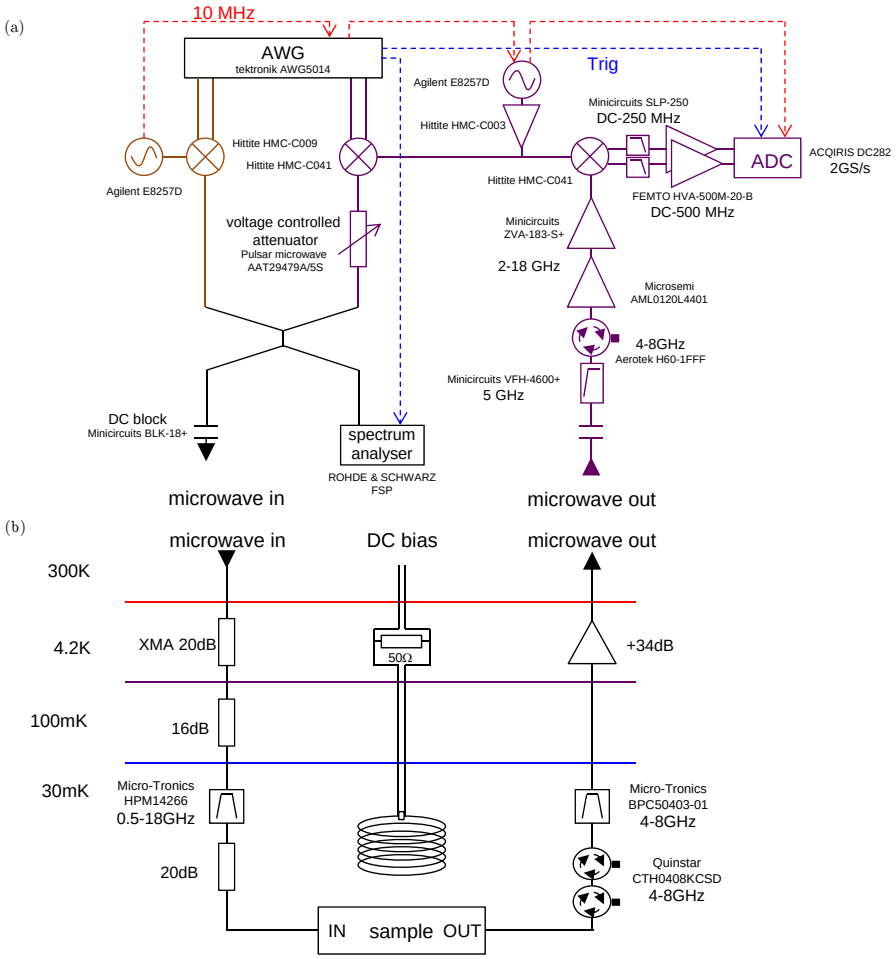

Figure 5.2: (a) Room temperature microwave experimental setup. Qubit drives are shown in brown and readout lines in purple. An arbitrary waveform generator (AWG) delivers the driving and readout pulses, which are mixed with continuous microwaves. The red dashed lines carry a 10 MHz reference signal for synchronizing the microwave generators, the AWG, as well as the measuring apparatus, which are triggered by the AWG. (b) Electrical setup in the dilution refrigerator, showing the attenuated and filtered input line, the isolated and amplified output line, as well as the global magnetic field generation.

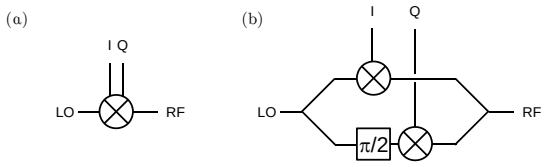

Figure 5.3: IQ mixer. (a) symbolic representation; (b) functional diagram.

Ideally, in order to generate a pulse with a suitable envelope $A(t)$, a microwave frequency $\omega_{RF} = \omega_{LO} + \delta\omega$ away from the LO signal $LO(t) = A_{LO}\cos(\omega_{LO}t)$, and a given phase φ, one applies I and Q signals with the same envelope $A(t)$, the same frequency $\delta\omega$, but a $\pi/2$ phase difference:

$$\begin{bmatrix} I(t) \\ Q(t) \end{bmatrix} = A(t) \begin{bmatrix} \cos(\delta\omega\, t + \varphi) \\ \sin(\delta\omega\, t + \varphi) \end{bmatrix}. \tag{5.1}$$

The resulting output RF signal takes the requested form:

$$\begin{aligned} RF(t) &= LO(t)\, I(t) + LO\left(t - \frac{\pi}{2}\right) Q(t) \\ &= A_{LO} A(t) \left[\cos(\omega_{LO}\, t)\cos(\delta\omega\, t + \varphi) - \sin(\omega_{LO}\, t)\sin(\delta\omega\, t + \varphi)\right] \\ &= A_{LO} A(t) \cos\left[(\omega_{LO} + \delta\omega)\, t + \varphi\right] \\ &\propto A(t)\cos(\omega_{RF}\, t + \varphi)\,. \end{aligned} \tag{5.2}$$

The IQ mixers suffer however from important imperfections. Their use requires a careful calibration procedure, and a careful check of the outgoing signal in order to obtain a signal at a single sideband frequency, and with the desired amplitude and phase. These imperfections are:

- saturation-bandwidth: the I and Q ports have limited bandwidth and saturate easily. Although the few GHz bandwidth is not a limiting factor for our application, the saturation at a few dBm RF power had to be calibrated.

- amplitude imbalance: contrary to the ideal case of Eq. 5.2, the IQ mixing rather takes the form $RF(t) = LO(t)\, I(t) + \alpha LO(t - \pi/2)\, Q(t)$, where α is a coefficient that deviates from 1 by about $1 - 2\,\mathrm{dB}$.

- phase imbalance: the imperfect phase shifting leads to a modified mixing $RF(t) = LO(t)\, I(t) + LO\left(t - \beta\frac{\pi}{2}\right) Q(t)$ with $\beta \sim 1$. The phase imbalance is typically $5 - 10°$ for a well chosen LO power.

These three main imperfections decreasing with increasing LO power, the signal of the microwave generators is first amplified as shown on Fig. 5.2.a in order to operate the mixers at the maximum possible LO power. Even under this condition, the imbalance effects cannot be neglected, and corrections are needed. We compensate these imperfections by applying I and Q signals with slightly

different amplitudes and phases deduced from a calibration. The calibration coefficients are periodically checked and tuned by minimizing the signal at the unwanted sideband frequency $(\omega_{LO} - \delta\omega)/2\pi$, using the spectrum analyzer.

The calculation done above for a single microwave frequency ω_{RF} is also valid for obtaining a sum of RF signals from a sum of I and Q signals with amplitudes $\{A_i\}$, frequencies $\{\delta\omega_i\}$, and phases $\{\varphi_i\}$, with the very same LO frequency. Consequently, one can frequency multiplex a series of j simultaneous pulses using only one IQ mixer and only two channels of an AWG.

5.2.2 Demodulation and horizontal synchronization

On the acquisition side, a similar mixer is also used to demodulate the output signal, since a mixer is a reciprocal device. The signal $s(t) = A_S(t)\cos(\omega_{RF}\, t + \varphi_S)$ is down-converted with a local oscillator $LO(t) = A_{LO}\cos(\omega_{LO} t)$. The output quadratures on the I and Q ports - also known as IF (intermediate frequency) ports - are

$$\begin{bmatrix} I(t) \\ Q(t) \end{bmatrix} = \begin{bmatrix} s(t) \times LO(t) \\ s(t) \times LO(t + \pi/2) \end{bmatrix} \tag{5.3}$$

$$= A_s(t) A_{LO} \cos(\omega_{RF} t + \varphi_S) \begin{bmatrix} \cos(\omega_{LO} t) \\ \sin(\omega_{LO} t) \end{bmatrix} \tag{5.4}$$

Writing ω_{RF} as $\omega_{LO} + \delta\omega$, and neglecting low-pass filtered terms at $\omega_{RF} + \omega_{LO}$, the I and Q quadratures takes the form

$$\begin{bmatrix} I(t) \\ Q(t) \end{bmatrix} = \frac{1}{2} A_S(t) A_{LO} \begin{bmatrix} \cos(\delta\omega\, t + \varphi_S) \\ -\sin(\delta\omega\, t + \varphi_S) \end{bmatrix}. \tag{5.5}$$

This signal is then digitized in a time window during which its amplitude A_S is constant, with a sampling period dt and a spurious trigger jitter $0 < \epsilon \leq dt$ that is independently measured precisely by the digitizers. Sample k reads thus

$$\begin{bmatrix} I(k) \\ Q(k) \end{bmatrix} = \frac{1}{2} A_S A_{LO} \begin{bmatrix} \cos(\delta\omega \{k\, dt + \epsilon\} + \varphi_S) \\ -\sin(\delta\omega \{k\, dt + \epsilon\} + \varphi_S) \end{bmatrix}. \tag{5.6}$$

This digital signal is then numerically demodulated using tabulated values of the cosine functions at the known signal frequency $\delta\omega$. To do so, a compiled C DLL computes

$$\begin{bmatrix} I_{\delta\omega}(k) \\ Q_{\delta\omega}(k) \end{bmatrix} \equiv \frac{1}{N} \sum_{i=0}^{N} \begin{bmatrix} I(k) \\ Q(k) \end{bmatrix} \cos(k\, \delta\omega\, dt), \tag{5.7}$$

which can be written

$$\begin{bmatrix} I_{\delta\omega}(k) \\ Q_{\delta\omega}(k) \end{bmatrix} = \frac{1}{4} A_S A_{LO} \begin{bmatrix} \cos(\delta\omega\, \epsilon + \varphi_S) \\ -\sin(\delta\omega\, \epsilon + \varphi_S) \end{bmatrix}, \tag{5.8}$$

assuming a large sample size $N \gg 1$. The jitter delay ϵ being known, I and Q are corrected using the rotation matrix

$$\begin{aligned} M &\equiv \begin{pmatrix} \cos\delta\omega\,\epsilon & \sin\delta\omega\,\epsilon \\ -\sin\delta\omega\,\epsilon & \cos\delta\omega\,\epsilon \end{pmatrix} \\ \begin{bmatrix} I^{corr}_{\delta\omega}(k) \\ Q^{corr}_{\delta\omega}(k) \end{bmatrix} &\equiv M \begin{bmatrix} I_{\delta\omega}(k) \\ Q_{\delta\omega}(k) \end{bmatrix} \\ &= \frac{1}{4} A_S A_{LO} \begin{bmatrix} \cos\varphi_S \\ \sin\varphi_S \end{bmatrix} \end{aligned} \tag{5.9}$$

which gives access to the amplitude A_S and phase φ_S of the signal initially oscillating at ω_{RF}.

As for the case of up-conversion (Sec. 5.2.1), this down-conversion process suffers from the same imperfections since it uses the same IQ mixer:

- saturation: the incoming signal (RF port) being usually much smaller than the LO power, the device is used in its "linear" regime and this effect is negligible.
- amplitude/phase imbalance: the pump power being in the specified range, the amplitude and phase imbalance have the same value than in the single sideband mixing case. But these effects, can be mainly ignored in our application since the absolute amplitude and phase do not matter, but only their changes.
- trigger jitter: the numerical demodulation being performed at frequencies up to $\delta f = 200\,\mathrm{MHz}$ at $2\,\mathrm{GSamples/s}$, the jitter delay $0 < \epsilon \leq 0.5\,\mathrm{ns}$ corresponds to a phase jitter $d\varphi = 2\pi\,\delta f\,\epsilon$ that can reach 36°, larger than the typical phase shifts to be measured. This is why ϵ has to be measured by the digitizer for each acquired trace.

Once again, this calculation done for a single RF signal is valid for a sum $s(t) = \sum_{i=1}^{j} A_{S,i}(t)\cos(\omega_{RF,i}\,t + \varphi_{S,i})$ of j signals undergoing an analog demodulation with the same mixer and LO frequency, followed by j digital demodulations at all known intermediate frequencies $\{\delta\omega_i\}$, because digital demodulation of signal i at the frequency of component $m \neq i$ averages to zero. Consequently, one obtain from such a multiplexed demodulation a series $\{(\mathrm{I}_i,\mathrm{Q}_i)\}$ couples per acquisition.

5.3 Sample characterization

5.3.1 JBA readout resonator characterization

We first probe the readout resonators by measuring the sample S_{21} transmission coefficient (amplitude and phase) of the sample as a function of frequency with a vector network analyzer (VNA). The transmission curves shown in Fig. 5.4 show four resonances, the shape of which varies with the measurement powers.

At sufficiently low power (dark blue curves), the JBA resonators simply behave as linear resonators. The frequency separation is 70 MHz between subsequent resonators. At higher power (other curves), an abrupt change (more clearly visible on the phase) is the signature of the bifurcation phenomenon: the JBA switches from its low amplitude dynamical state L to the high amplitude one H, as explained in section 2.2.3.3. The switching back and forth between the two states can even be observed for some driving parameters, as shown for instance on the data taken at -95 dBm power around 7.64 GHz, where the phase undergoes multiples jumps (see orange curve - this unstable behavior is due here to the way the VNA ramps its probe frequency).

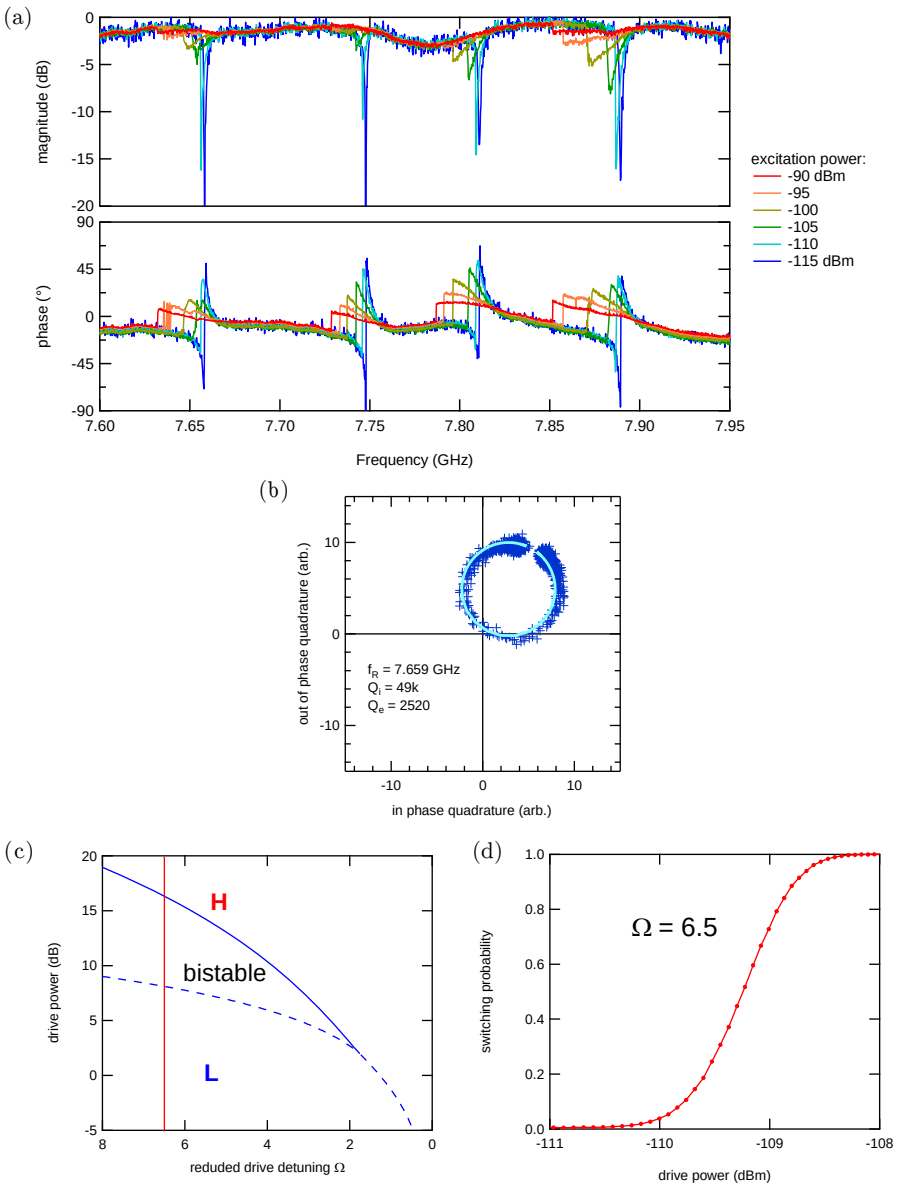

Figure 5.4: (a) Spectroscopy of the JBA resonators at different drive powers, recorded with a vector network analyzer. The bifurcation phenomenon corresponds to abrupt changes, mainly visible on the phase. (b) Fit of the linear resonance of JBA 1 by expression Eq. 5.10, yielding its bare frequency and internal and external quality factors. (c) Stability diagram of the JBA as a function of the reduced detuning Ω. The solid blue line correspond to the switching from L to H whereas the vertical red line indicates the reduced drive frequency $\Omega = 6.5$. (d) Switching probability as a function of driving power, for the chosen frequency $\Omega = 6.5$.

By fitting in the complex plane $\{Re[S_{21}], Im[S_{21}]\}$ each of the four linear resonances measured at low power (see example of JBA 1 in Fig. 5.4.b) with expression

$$S_{21}^{-1}(f) = 1 + \frac{Q_i}{Q_e}\frac{1}{1 + 2jQ_i(f/f_R - 1)}, \tag{5.10}$$

the resonator internal and external quality factors Q_i^i and Q_e^i are extracted. We find $Q_e^i = \{2500, 2550, 2650, 2200\}$ and $Q_i^i > 40000$ for the four readouts. Then, the JBAs are placed in their bifurcation regime and their switching probability is measured using rectangular pulses with increasing powers (see Fig 5.4.d). In order to benefit from a large readout sensitivity without suffering from the retrapping instability, we choose drive frequencies 10 MHz below the resonator frequencies in the linear regime, which corresponds to a reduced detuning $\Omega = 6.5 \gg \Omega_c = \sqrt{3}$ (see Eq. 2.32).

5.3.2 Qubit spectroscopy

The next step consists in measuring spectroscopically the qubits using the methods described in Chapter 2, as a function of the global magnetic field that can be applied to the sample with a single coil. The result is shown on Fig. 5.5, where the switching probabilities $p_{S,i}$ of the four JBAs are all superposed (see caption). These measurements are performed at sufficiently large power to show both the $|g\rangle \rightarrow |e\rangle$ spectroscopic line and the two-photon $|g\rangle \rightarrow |f\rangle$ transition, which gives access to the transmon anharmonicity $\alpha = f_{ge} - f_{ef} = -434 \pm 2\,\text{MHz}$ for the four qubits. Note that qubit 3 (red) is not tunable because of a discontinuity in the SQUID loop, already detected at room temperature. The three tunable qubits have different offset in magnetic field due to imperfect shielding of the magnetic field created by the circulators. The magnetic field periods of these qubits are different, which we attribute to a difference of the shielding currents induced in the superconducting ground electrodes by the Meissner effect canceling the magnetic field.

5.3.3 Qubit-readout resonator coupling constant

The coupling constant between each qubit and its readout resonator cannot be measured directly by observing an anticrossing between both objects, because the JBA frequencies have been placed well above the maximum qubit frequencies in this sample. Consequently, it is deduced from the qubit frequency modulation and from the resonator pull χ_i^{ge} (in the linear regime) induced by the qubit i left in its ground state: the resonator frequency f_R is measured as a function of the global magnetic field that controls the qubit frequency (see Fig. 5.6), and is fitted with the model of Eq. 2.27. Indeed, we have

$$f_i^R = f_i^{R0} + \chi_i^{ge}/2\pi \tag{5.11}$$

with f_i^{R0} the resonator frequency in the absence of qubit and χ_i^{ge} the cavity shift (Eq. 2.27). This yields $g/2\pi = 85 \pm 3\,\text{MHz}$. The coupling constant obtained for cells 2 and 4 has the same value.

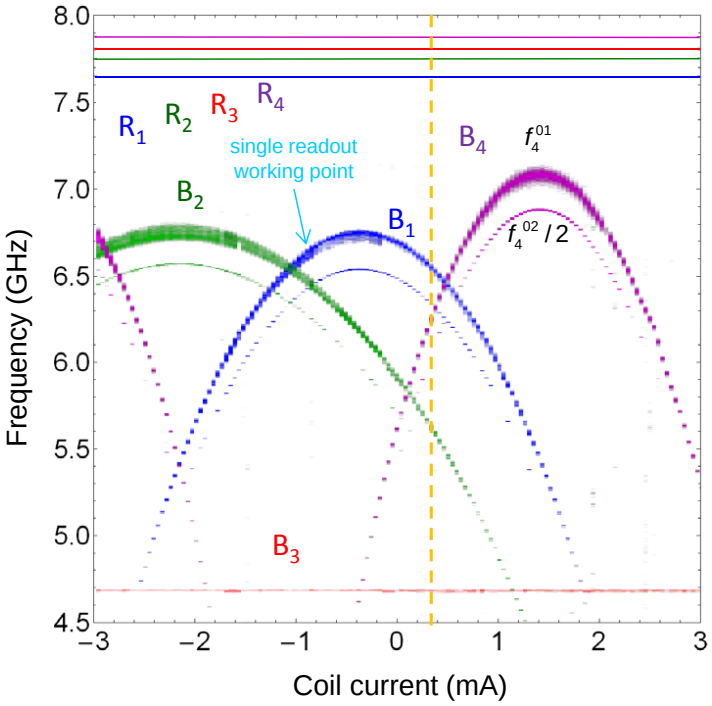

Figure 5.5: Simultaneous spectroscopy of the four qubits as a function of the global magnetic field applied to the sample: the four switching probabilities p_i are encoded from transparent for $p_i = 0$ to blue, green, red, and purple for $p_{1,2,3,4} = 1$, and are all superposed. The blue arrow corresponds to the optimal working qubit used to characterize cell 1 (Sec. 5.4), whereas the yellow dashed line corresponds to a compromised working point used for testing the multiplexed readout of all qubits (Sec. 5.5).

In the next section, we characterize the readout performance of qubit-JBA cell 1 at its optimal point for readout (cyan arrow on Fig. 5.5), where it shows good readout fidelity and sufficiently long estimated Purcell relaxation time ($T_P > 8\,\mu s$). In section 5.5, we will operate the full circuit at the magnetic field shown by the yellow line of Fig. 5.5. Due to the lack of individual control of each qubit frequency in this sample, this magnetic field is not optimal for any of the qubits: it is actually a reasonable compromise between all the qubit readout contrasts, given the complex frequency pattern of the sample.

5.4 Single qubit readout

In this section, we characterize the readout of qubit-JBA cell 1 at its optimal point, i.e. where the qubit-readout frequency difference is not too large to

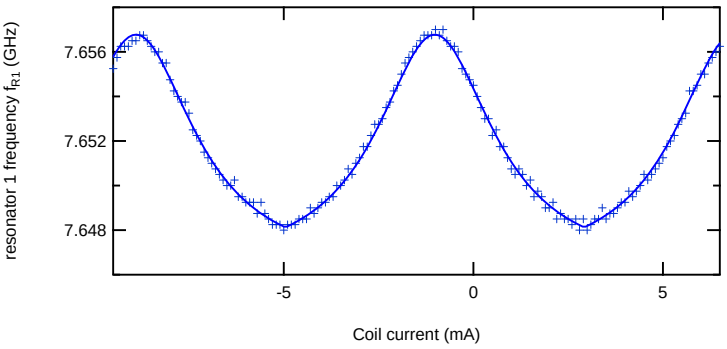

Figure 5.6: Resonator 1 linear resonance frequency as a function of the coil current that modulates all qubit frequencies. The full line is a fit yielding the coupling constant $g/2\pi = 85 \pm 3\,\mathrm{MHz}$ between the transmon and its readout resonator.

insure a sufficient resonator pull and a full separation of the switching curves corresponding to the qubit ground and excited states, but also sufficiently large for limiting the Purcell relaxation rate of Eq. 2.38.

At this operating point, the frequency difference between qubit 1 and its readout resonator is $\Delta_1 = f_{B1}^{ge} - f_{R1} = -1.08\,\mathrm{GHz}$. The qubit and readout pulse amplitudes used are shown in Fig. 5.7; the signals are produced using single sideband mixing as described in section 5.2.1.

Single qubit control pulses are carefully designed to avoid spurious population of transmon level f (see Section 3.2.2). We label θ^{ij} a resonant drive between the states $|i\rangle$ and $|j\rangle$ inducing a rotation by an angle θ. For small Rabi angles θ, the control pulses are Gaussian shaped with a time truncation at $\pm 3\sigma$ and $\sigma = 4\,\mathrm{ns}$ (24 ns foot to foot). Their amplitude is increased proportionally to the targeted θ until the maximum amplitude allowed by the setup is reached (see dashed gray line in the left panel of Fig. 5.7). Above this limit, a plateau is added to the pulse between the Gaussian rise and the Gaussian fall. For simplicity, an equivalent pulse "length" is defined as the duration of an equivalent rectangular pulse having the same area with the maximum allowed amplitude. Numerical simulations of the dynamics of a transmon with its three lowest energy levels show that such relatively long pulses with Gaussian rise and fall induce preparation errors smaller than 0.1%, which allowed us not to use the DRAG technique [37] required for shorter and stronger pulses.

As already mentioned, the JBA is driven at a frequency $\sim 10\,\mathrm{MHz}$ below its linear resonance frequency. The readout pulse consists of a 2.025 µs long almost rectangular pulse, with a first 25 ns long step at higher amplitude to accelerate the energy loading at the beginning. As discussed below and in Appendix A, the time needed by the JBA for projecting the qubit and 'deciding' to switch or not is of the order of 100 ns. After this the JBA is in a latched state and maintains its signal whatever the qubit "does". The 2.025 µs long pulse

is transmitted through the whole setup and is then digitized for subsequent digital demodulation between time 0.325 µs and time 1.325 µs (2000 sampling points).

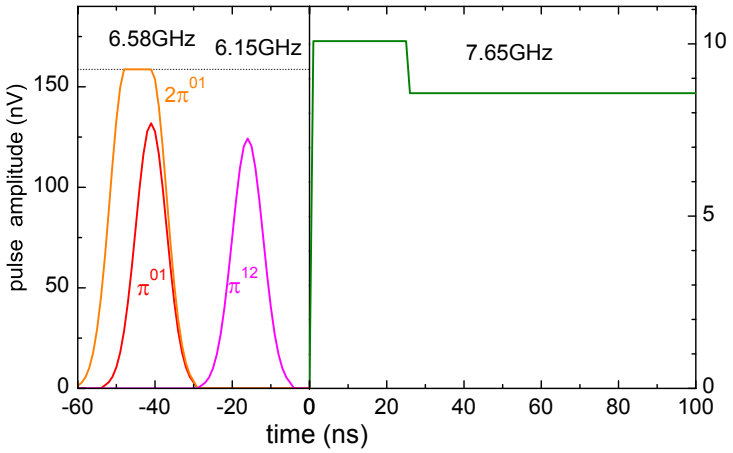

Figure 5.7: (left) Microwave control pulse envelopes for π_{ge}, π_{ef}, and $(2\pi)_{ge}$ rotations. The dotted line shows the maximum amplitude used. (right) Beginning of the microwave readout pulse envelope

The outcome of each readout sequence yields a pair of (I_1, Q_1) quadrature amplitudes, i.e. a point in the complex amplitude plane. We show in Figure 5.4 a density plot of these amplitudes on a set of 10^5 measurements taken just after applying a $\left(\frac{\pi}{2}\right)^{ge}$ pulse in order to have equal populations of the ground and excited states. On the left panel, one observes two clouds corresponding to the two dynamical states of the readout resonator. The blue dashed line represents the best separatrix between the two regions. The right panel represents the projection of the (I_1, Q_1) orthogonally to the separatrix line; the two corresponding histograms overlap by less than 10^{-4} of their area. A single-shot experiment result is labeled as low (L) if the outcome is on the left side of the red dashed line and high (H) if it is on the right.

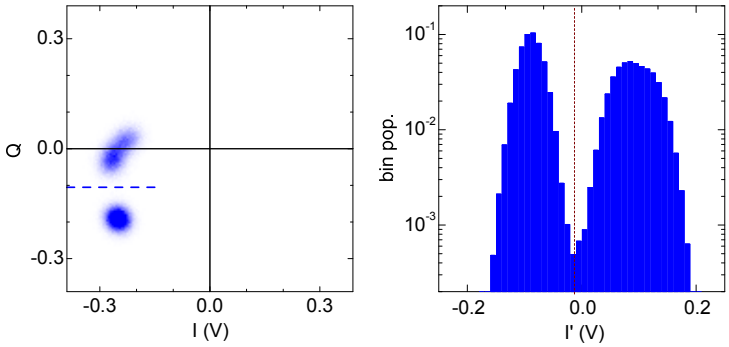

Figure 5.8: JBA 1 outgoing signal, (left) in the (I_1, Q_1) plane and (right) histogram of the projection orthogonally to the dashed blue line.

Description of the switching curves

We now define the bifurcation switching probability p_1 as the probability for the JBA to be found in its high (H) state. Figure 5.9 shows the variations of this probability as a function of the peak drive power for the qubit prepared in the $|g\rangle$, $|e\rangle$ and $|f\rangle$ states, respectively. In order to best display the difference between p_1 and 0 or 1, we plot the switching curves using a double logarithmic scale below and above 0.5.

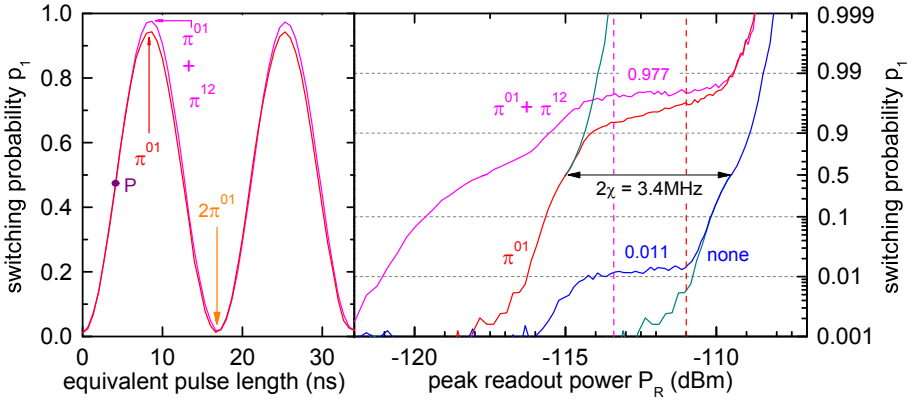

Figure 5.9: (left) Rabi oscillation of p_1 as a function of the equivalent control pulse length (duration of a rectangular pulse with maximum amplitude), without (red) and with (magenta) shelving. (right) Probability p_1 with no qubit control pulse (blue) and after a π_{ge} pulse alone (red) or with shelving (magenta). These curves are shown using a double-logarithmic scale below and above 0.5 (right axis). Thin green lines represent "ideal" S curves built by shifting the blue line to the red one above 50% switching and the red line to the blue line below 50%. The vertical dashed lines indicate the pulse power yielding the highest readout contrasts with (left) and without (right) shelving.

- No qubit pulse applied:

When no control pulse is applied to the qubit (blue curve), i.e. with the qubit supposedly in its ground state $|g\rangle$, one notices that the switching probability continuously increases with power, but presents a shoulder at a level of 1.1% that we interpret as a spurious population of the excited state $|e\rangle$ in excess compared to the expected thermal equilibrium value of $2\,10^{-5}$. The 1.1% value observed corresponds to an effective qubit temperature of 70 mK, above the 30 mK fridge temperature. Note that such a large qubit temperature is usually not observed in 2D architectures and that it was not observed on previous samples with more attenuation at low temperature. It probably results from a bad infrared shielding in this particular experiment.

- After a π^{ge} pulse:

When measuring the switching curve after a π^{ge} pulse, one obtains the switching curve displayed in red, which differs from the green one obtained by shifting the blue curve by a power corresponding to the 2χ frequency change of the readout resonator (Eq. 2.37). One observes a sloping shoulder between -114 and -111 dBm. The red line indicates the largest difference between the two switching curves without and with a π^{ge} pulse applied. The value $p_1 \simeq 0.96$ at this point is smaller than 1 for different reasons we only partly explain. First, the excess initial population in the excited state is transferred back to

the ground state by the π^{ge} pulse, hence a 1.1% missing population in the excited state. Second, relaxation during the drive pulse itself, before readout starts, results in a small error. Having independently measured $T_1 = 2\,\mu s$, we estimate this specific relaxation error at about 0.6%. Then we tentatively attribute the missing 2.3 % difference at the measurement point to relaxation during the readout itself because the effective projection time is longer than the duration of the first plateau of the readout pulse, as discussed further below.

- After a π^{ge} and a π^{ef} pulses

For further improving the readout fidelity, we have used the already described trick that consists in transferring the excited qubit population from $|e\rangle$ to $|f\rangle$. When measuring the switching probability curve after a π^{ge} and π^{ef} pulse (pink curve), ideally preparing the qubit in the $|f\rangle$ state, we see the curve shifted again, but with a plateau at about 0.977 between -114 and $-111\,dBm$ instead of a sloping shoulder. On this plateau, a relaxation from $|f\rangle$ to $|e\rangle$ has a negligible impact on readout outcome. Indeed, in absence of direct relaxation from $|f\rangle$ to $|g\rangle$, the ground state population grows quadratically as $\sim \left(t/T^{fg}\right)^2$ with $T^{fg} = \sqrt{T_1^{fe} T_1^{eg}} \approx \sqrt{2} T_1^{eg}$, where T_1^{ij} stands for the relaxation time from $|i\rangle$ to $|j\rangle$ state. This yields a really small error of $0.1 - 0.2\,\%$ during measurement, even assuming measurement times longer than 100 ns. In this composite measurement with a a π^{ef} applied before the readout pulse, the plateau close to one on the switching curve is thus quantitatively explained by excess population of the excited state combined with relaxation during the drive sequence. This observation strongly supports that the slope observed after a π^{ge} pulse is also due to relaxation.

The pink dashed line points out the maximum difference between the qubit left in its ground state and the composite pulse measurement after a π^{ge} pulse. This 96.5% contrast obtained, mainly limited by thermal population (2.2% of loss) and relaxation during drives (1.1% of loss), indicates that the intrinsic fidelity of our JBA readout could reach a 99.8% fidelity provided one makes transmon qubits with a longer relaxation time T_1 and without excess population of the excited state.

Observation of single qubit Rabi oscillations

The left part of Fig. 5.9 shows the best results obtained after a Rabi sequence, measured with simple and composite readout pulse.

One has to note that a composite measurement pulse takes the qubit out of the computational basis $\{|g\rangle, |e\rangle\}$, which prevents from continuing a computation with it. Nevertheless, this limitation is of the same nature as that of a non QND detector and can be circumvented by using ancillary qubits.

The three tunable transmons (and the one with an open loop SQUID) show similar performances at similar $\sim 1\,GHz$ qubit-JBA detuning. Moreover, at all measured transmon frequencies, they all show relaxation times in the range $T_1 : 1.7 - 3.2\,\mu s$ significantly below the estimated Purcell lower limit

$T_P > 8\,\mu s$, and shorter than in other comparable 2D transmon circuits. We tentatively attribute these short relaxation times to dielectric losses [75].

JBA internal state evolution

In order to shed light on the evolution of the internal state of the JBA resonator during readout, we have performed semi-classical numerical simulations of the JBA dynamics with parameters that correspond to those independently measured experimentally. The way these simulations are done is detailed in Appendix A. Resulting trajectories of the internal JBA complex field amplitude are shown in the left panel of Fig. 5.10. The detailed evolution of the amplitude module is shown in the right panel.

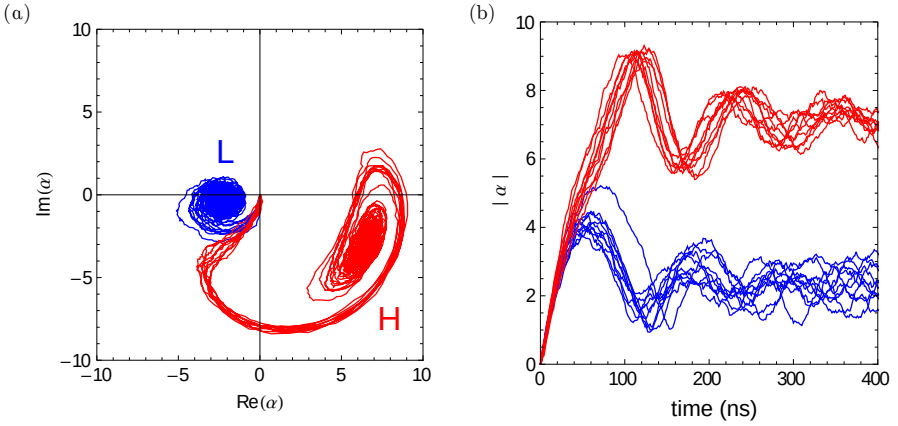

Figure 5.10: (a) Simulated internal state trajectories, colored in blue for trajectories ending in the L state (qubit in $|g\rangle$) and in red for the H state (qubit in $|e\rangle$). (b) Time evolution of the internal amplitude for switching and non-switching trajectories.

This simulation shows that the JBA bifurcates from about 4 to about 50 photons after a transient at about 16 photons. One observes that the time taken by the JBA to "decide" to switch (or not) to the H state is most of the times shorter than 100 ns, meaning that qubit relaxation after this time has no impact on the final outcome; older observations with an oscilloscope of averaged trajectories at 0% and 100% of switching confirm that L and H trajectories diverge before 100 ns, which can be taken as an upper bound for the time needed for the qubit projection. According to Eq. 2.39 and for our quality factor and dispersive shift, this projection should occur within $T^{\phi}(\alpha) \sim 86\,\mathrm{ns}/|\alpha|^2$, i.e. in about 5 ns during the transient around 16 photons. This shows that although the measurement output develops over one hundred of nanoseconds, the actual projection time is much shorter.

By simulating a large number of similar trajectories (see Appendix) of a JBA alone with qubit state dependent parameters, we obtain the switching curves shown in Fig. 5.11 , which are compared to the experimental ones. The reasonably good agreement obtained for the separation the S curves as well as for their slope, without introducing any adjustable parameters apart from the attenuation of the driving line that is known with a precision of only 2 dB, shows that Dykman's effective temperature approach works well and that simulations do capture the physics of bifurcation. The sloppy shoulder of the S curve for the qubit excited state is not predicted at all. This is not a surprise since our simulation do not really include the qubit, and especially not its relaxation during measurement. This is why our collaborators A. Blais and B. Royer have performed full quantum simulation including a three state transmon, a JBA, and the possibility for the transmon to relax during measurement.. Their simulation are also shown on Fig. 5.11. They do not fit as well the data but capture a relaxation induced small rounding at the top of the S curve for $|e\rangle$. Nevertheless the effect is much less pronounced that what is observed experimentally. Coming back to the upper bound of 100 ns for the projective time, we point out that applying the independently measured relaxation rate to this time would reduce the $|e\rangle$ population by $\sim 0.5\,\%$, which is here also insufficient to explain the experimental $p_1(|e\rangle)$ at -114dB for instance. The conclusion is that the sloppy shoulder cannot be explained by normal relaxation during the measuring time, and that an important ingredient of the dynamics of the JBA coupled to an excited qubit is missing in the theory. This issue could be related to a similar unexplained problem observed with the linear dispersive readout of transmons [76]: indeed, non-QNDness of the readout, i.e. excitation and relaxation during readout, has often (but not always) been observed with an average photon number in the cavity well below the critical photon number n_{crit} mentioned in Section 2.2.3.1. Yet our JBAs switch from about 5 to 50 photons and could suffer from this non-QNDness. Although fortunately, this effect can be eliminated by using shelving, it is still to be understood.

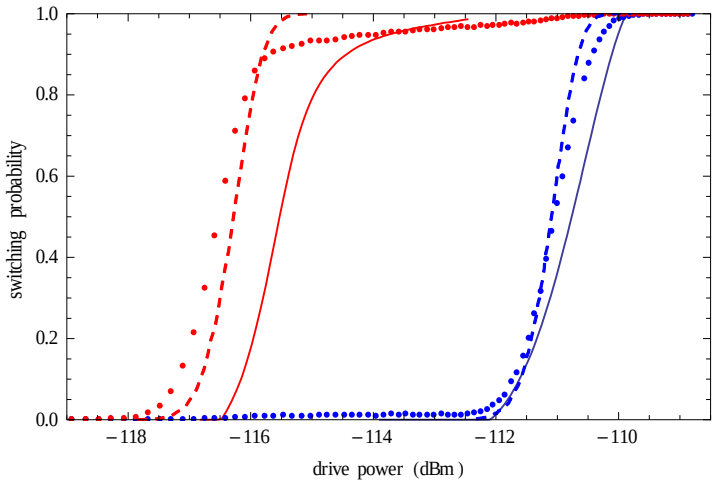

Figure 5.11: Experimentally measured (dots), semi-classical (dashed) and full quantum simulated switching curves for the qubit in the ground (blue) and excited state (red)

5.5 Multiplexed qubits readout

After having performed individual qubit readout, we investigate now the simultaneous readout of the four transmon qubits.

5.5.1 Readout frequencies, signal generation and analysis

Given the lack of individual transmon tunability, a magnetic field leading to not too large detunings $\Delta_i = \{-1.2, -1.76, -3.12, -2.06\}$ GHz was applied, placing the system at a compromise point as indicated by the yellow line on Fig. 5.5. In particular, we have to operate JBA 3 far detuned from its transmon with a broken SQUID, and for increasing the visibility, this JBA is driven ~ 5 MHz below its frequency, i.e. at $\Omega = 3.2$.

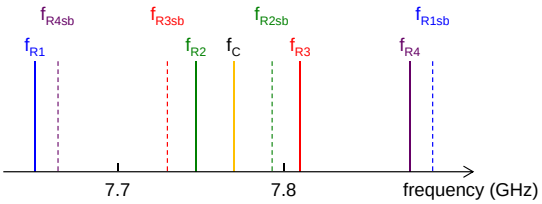

Figure 5.12: Readout frequency overview. The carrier frequency is $f_c = 7.77$ GHz, f_{Ri} stand for readout frequency and f_{Risb} represent the ideally canceled sideband.

Register state discrimination

Given these larger detunings than in the optimized case, we now use readout pulses with a 50 ns first plateau followed by a 2 µs latching plateau. The carrier frequency f_c used to generate the sideband tones $f_{Ri} = f_c + \delta_{Ri}$ is chosen so that the undesired sidebands $f_{Risb} = f_c - \delta_{Ri}$, possibly not perfectly canceled, nevertheless stand away from other relevant frequencies, as shown in Fig. 5.12. All the tones falling in a ±120 MHz bandwidth around the carrier frequency, we generate their additive combination with an arbitrary waveform generator (AWG) sampling at 1 GSample/s. After sending the four tones at their specific amplitude as in the previous experiment, the signal returned is analog-demodulated with the carrier, and one gets a signal containing the four readout signals at the different detuning frequencies. This signal is digitized and numerically demodulated at the four sideband frequencies δ_{Ri}, yielding 4 (I_i, Q_i) quadratures pairs at frequencies f_{Ri}. The density plot of the quadratures in the four complex planes is shown on the left panel of Fig. 1.7 after applying $\left(\frac{\pi}{2}\right)_i^{ge}$ pulses on all qubits. Again, one can observe that the two clouds of each pair i can be well discriminated by choosing four suitable separatrices, and the probability p_i of outcome H for JBA i is measured by repeating a measurement sequence and counting the number of H shots: the simultaneous operation of the four JBAs does not prevent us from demodulating the signals as properly as achieved in the single JBA measurements.

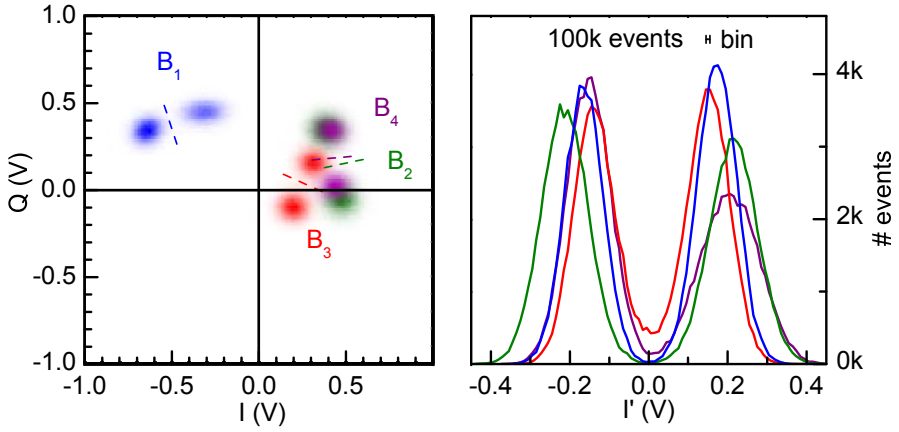

Figure 5.13: Density plot of 10^5 single-shot outcomes, each including the four (I_i, Q_i) quadratures. The colors (blue, green, red, purple) stand for $i = (1 - 4)$. (left) (I_i, Q_i) coordinates at the frequency f_{Ri}. (right) Histogram of the projection perpendicularly to the best separatrix lines.

5.5.2 Switching performance

As done in previous individual qubit readout experiments, we measure the set of switching curves for the four JBAs. These curves are represented on Fig. 5.14 for the qubits prepared in $|g\rangle$, $|e\rangle$, and $|f\rangle$ state[2]. As expected, the larger qubit-JBA detunings Δ_i lead to smaller resonator pulls χ_i, to a reduced separations between the S curves, and to lower readout sensitivities.

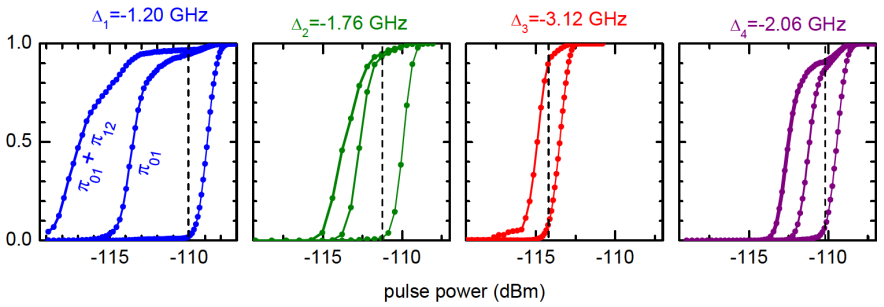

Figure 5.14: Measured S curves as a function of the drive power for the four qubit, in the ideally prepared $|g\rangle$, $|e\rangle$, and $|f\rangle$ state.

Nevertheless, the maximum contrast between the qubit left in its ground place or in the $|e\rangle$ states measured with and without composite readout is shown on Table. 5.1.

Qubit	π_i^{ge} contrast	$\pi_i^{ge} + \pi_i^{ef}$ contrast
1	92.5%	95%
2	92.3%	94%
3	79%	N/A
4	81.2%	88%

Table 5.1: Contrast obtained obtained with standard and composite pulse on the 4 qubits.

[2]Except for qubit 3 whose $|e\rangle \leftrightarrow |f\rangle$ transition frequency is out of the reachable frequency window.

5.5.3 Simultaneous qubit drive and readout

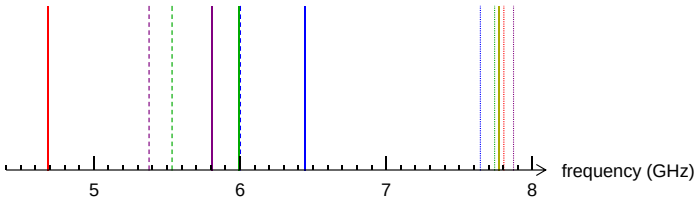

Figure 5.15: Readout frequencies (dotted lines), and transmon transition frequencies f_{ge} (solid lines) and f_{ef} (dashed lines)

For the chosen compromise working point, the frequency distribution of the transmons and their readout resonators is shown on Fig. 5.15. Several frequencies are close to each other, raising a problem often referred to as "frequency crowding" [77], which is easily solved when individual frequency control of the qubits is available. Because of the ac Stark shifts induced on qubit frequency i by drives applied to qubits $m \neq i$ (as detailed in Section 3.2.2), driving the qubits 1, 2 and 4 simultaneously would be complicated, and we prefer slightly separate their drive and use the driving sequence shown in Fig. 5.16. Nevertheless, the readout of the different transmons can overlap without any problem. For best readout performance, we apply readout pulses right after driving, and use composite readout pulses (with shelving to $|f\rangle$ state) for the qubits 2 and 3, but neither for qubit 1 because $f_1^{ef} \approx f_2^{ge}$ nor for qubit 3 because the low f_3^{ef} happens to be filtered by the readout resonator.

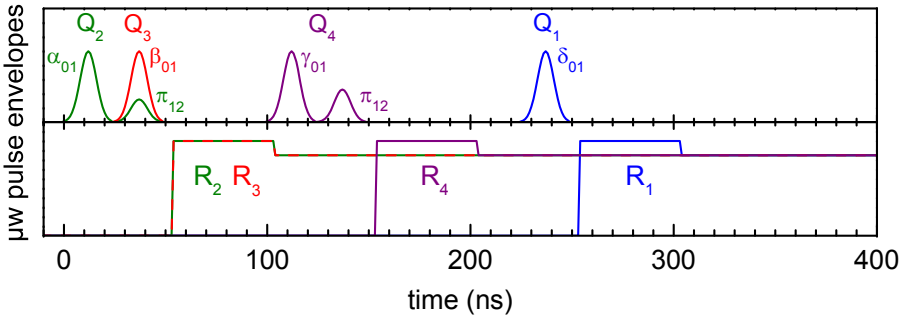

Figure 5.16: Drive sequence for simultaneous readout: (top) Qubit pulse envelopes; (bottom) readout pulse envelopes.

To demonstrate that the readout of the full register is operational, we have performed the simultaneous measurement of Rabi oscillations of all qubits by applying to all of them θ_i^{ge} pulses of increasing areas (with the same shape for all qubits except for an arbitrary amplitude factor), and then reading out the

full register. We obtain the Rabi oscillations shown in Fig. 5.17, expressed as a function of the equivalent duration defined above.

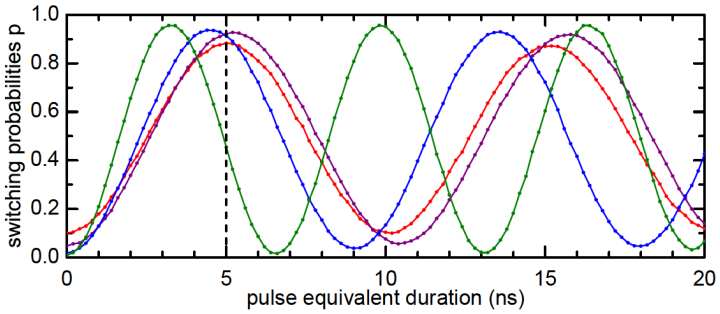

Figure 5.17: Simultaneous measurement of Rabi oscillations on 4 transmons.

The Rabi frequencies are different because of the different drive amplitudes, and their values can be controlled over similar ranges. The visibility of these Rabi oscillations is large, but significantly smaller for qubit 3 due to its very large detuning from its readout resonator $\Delta_3 = -3.12$ GHz. Figure 5.18 summarizes the readout contrast and errors obtained on the four cells, with this non optimal magnetic bias. This basic experiment demonstrates that multiplexed JBA readout is compatible with qubit driving.

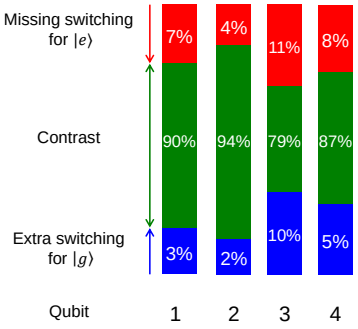

Figure 5.18: Contrast and errors obtained by quasi simultaneous qubit drives and readouts on four qubit cells.

5.5.4 Readout crosstalk between JBAs

A natural question that arises is the maximum number of transmons that our multiplexed JBA scheme could handle. Given JBAs are non-linear resonators which can a priori interfere, this raises a frequency-crowding problem different from the one faced by linear dispersive readout. It is thus important to investigate any possible crosstalk between different channels. Note that increasing

the total bandwidth needed to avoid crosstalk can increase the technical difficulty for producing all readout drive signals and to demodulate the outgoing readout signal.

The issue is how close the JBA frequencies can be without the bifurcation dynamics of a given JBA getting affected by the dynamics of the other ones, whether they switch or not. To answer this question, we had to average probabilities p_i obtained in different conditions, over large periods of time. So we first checked the stability of our measurement chain.

To measure this stability, we monitor the variance of p_i measured over N consecutive shots upon increasing N. More precisely, we compare the standard deviation σ_i for the four outcomes to the predicted value $\sigma_i = (p_i\,(1-p_i)\,/N)^{1/2}$ assuming independent statistical events. As shown in Fig. 5.19, the standard deviation follows perfectly the predictions for independent variables up to a maximum size $N < 5 \times 10^4$, limited by slow drifts in signal preparation and measurement.

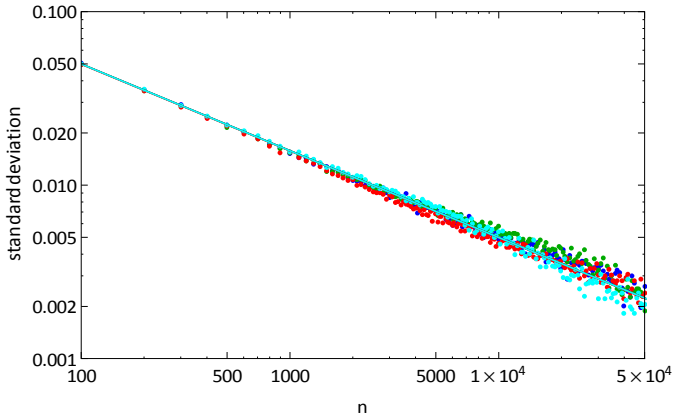

Figure 5.19: Standard deviation as a function of the number of measurement n for the 4 readout. Experimental data (dotted) and theory (solid line)

In the present setup with 70 MHz frequency difference between two neighboring JBAs, the crosstalk is quantified by preparing qubit 2 in a superposition $(|g\rangle + |e\rangle)/\sqrt{2}$ and qubit 1 either in $|g\rangle$ or in $|e\rangle$, and by averaging p_2 as much as allowed by the drifts. We find that the difference in p_2 for the two states of qubit 1 yields a crosstalk of only $0.2 \pm 0.05\%$, as shown in Fig. 5.20. This low value shows that the JBA frequency separation of 70 MHz that we have used is rather conservative, and therefore that JBA readout of a larger register is possible using the same microwave hardware. However, this empirical upper bound of 70 MHz for the JBA separation does not fully answer the question, and the crosstalk issue deserves more in-depth theoretical prediction.

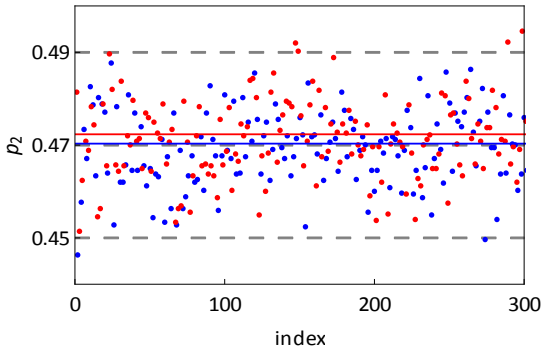

Figure 5.20: Crosstalk measurement between JBA 1 and JBA 2, on $N = 300 \times 1000$ measurements. Red point stand for the qubit 1 prepared in $|e\rangle$ and blue when left in $|g\rangle$. Blue and red line show the mean values and the difference represent the crosstalk.

5.6 Overall performance and conclusion

In conclusion, the experimental results obtained in this chapter on multiplexed JBA readout of four transmons show that JBA readout has an excellent intrinsic readout fidelity when shelving is used and that it is compatible with driving and reading transmons in a small qubit register. However, the overall readout contrast obtained with our multiplexed JBA scheme is significantly lower than that demonstrated at UCSB [78] on also four transmon qubits, using individual linear dispersive readout and a wideband quantum limited parametric amplifier. Nevertheless the larger errors in our experiment are not due to the readout method itself but (i) to the lack of individual qubit frequency control in this first simple design, (ii) to slightly too high temperature of the qubits, and (iii) to faster qubit relaxation. The UCSB team has been limited to four qubit read simultaneously because of the still limited $-107\,\mathrm{dBm}$ saturation power of their parametric amplifier. But recent developments of the Traveling Wave Parametric Amplifier [67] will probably help solving the scalability issue for linear dispersive readout. On our side, although we have measured a negligible crosstalk between the JBAs and have not found any blocking issue, the scalability of multiplexed JBAs will at some point be limited by the interactions between JBAs with close frequencies. Although the quantitative limit is still unknown, present results suggest that reading out a ten-qubit register with multiplexed JBA is possible.

Chapter 6

Characterizing a 4 qubit processor prototype: preliminary results

This chapter reports our fabrication and test of a 4-qubit processor implementing the design described in chapter 3 and fitted with the multiplexed qubit readout demonstrated in the last chapter 5. We first describe the sample and the setup used (Sec. 6.1), then the readout and qubit performances (Sections 6.2-6.2.3) that we compare with the results obtained in chapter 5. We finally characterize the qubit-qubit interaction mediated by the bus resonator (Sections 6.3and 6.4). Because of problems encountered in the fabrication process, this first prototype does not meet the performances of an operational processor, with sufficient coherence time, gate fidelity and readout fidelity for running any algorithm. We could nevertheless test different features of our architecture.

6.1 Sample and experiment setup

6.1.1 Sample

The sample used for this experiment is shown in Fig. 6.1. As in the previous experiment, it consists in four almost identical cells $1-4$. Each cell is made of a JBA resonator capacitively coupled to a single transmission line on one side, and to a transmon qubit on another side. The main difference with the sample investigated in Chapter 5 is that the transmons are independently tunable by passing current in individual local flux lines, and are coupled to a single high quality bus resonator that mediates an exchange interaction between them. As explained before, the flux lines have dedicated ground return conductors for avoiding the return current to spread in superconducting electrodes in an uncontrolled way. Because of the need of line crossings, the sample is fabricated using the *process flow 1* described in Chapter 4, and fitted with

airbridges. The flux and transmission lines, the JBA geometrical inductances and capacitances, and the coupling bus are first patterned in a niobium film on a 2" sapphire wafer. The JBA Josephson junctions are fabricated on the whole wafer using standard double-angle aluminum evaporation through a resist shadow-mask made by e-beam lithography. The transmon capacitance and Josephson junctions are then fabricated in the same way. The bridges are finally fabricated on the full wafer, prior to cutting it in individual sample chips. The sample is placed in the groove of a TMM10 printed circuit board (PCB) and the 6 lines on the PCB are wire-bonded to the sample with aluminum wires.

6.1.2 Low temperature setup

As shown on Fig. 6.2, the microwave setup is similar to the one used in the experiment of Chapter 5, except that the readout frequencies are now in the $8-12\,\mathrm{GHz}$ bandwidth. The incoming microwave line down to the sample is thermally anchored and attenuated at different temperatures. The outgoing line is composed as before, of a $8-12\,\mathrm{GHz}$ double circulator followed by a $8-12\,\mathrm{GHz}$ cryogenic bandpass filter, prior to the cryogenic amplifier at $4.2\,\mathrm{K}$.

The electrical setup now also includes four lines for driving the flux through the SQUID loops of the transmons with a large $1\,\mathrm{GHz}$ bandwidth. Since these lines carry quite a large current (few mA) at the sample level, the only $20\,\mathrm{dB}$ ($50\,\Omega$ matched) attenuator used for reducing the noise is placed on the $4.2\,\mathrm{K}$ stage, where the available cooling power is large enough to dissipate $\sim 5-30\,\mathrm{mW}$. For the same reason, the flux drive lines are routed using CuNi cables, with temperature independent attenuation between 300 and $4.2\,\mathrm{K}$, NbTi superconducting cables between $4.2\,\mathrm{K}$ and $30\,\mathrm{mK}$ to avoid heat transfer, and semi-flexible silver plated copper cables at $30\,\mathrm{mK}$. To block high frequency radiation, these lines are low-pass filtered at $1\,\mathrm{GHz}$ with a commercial filter actually acting as a stop-band filter between 1 and $\sim 20\,\mathrm{GHz}$. This filter is then followed by a soft absorptive real low-pass filter up to UV frequencies. This homemade filter is simply a coaxial waveguide with its dielectric made of Eccosorb[1], which provides a good absorptive material even at low temperature.

[1] Emerson & Cuming Microwave Products.

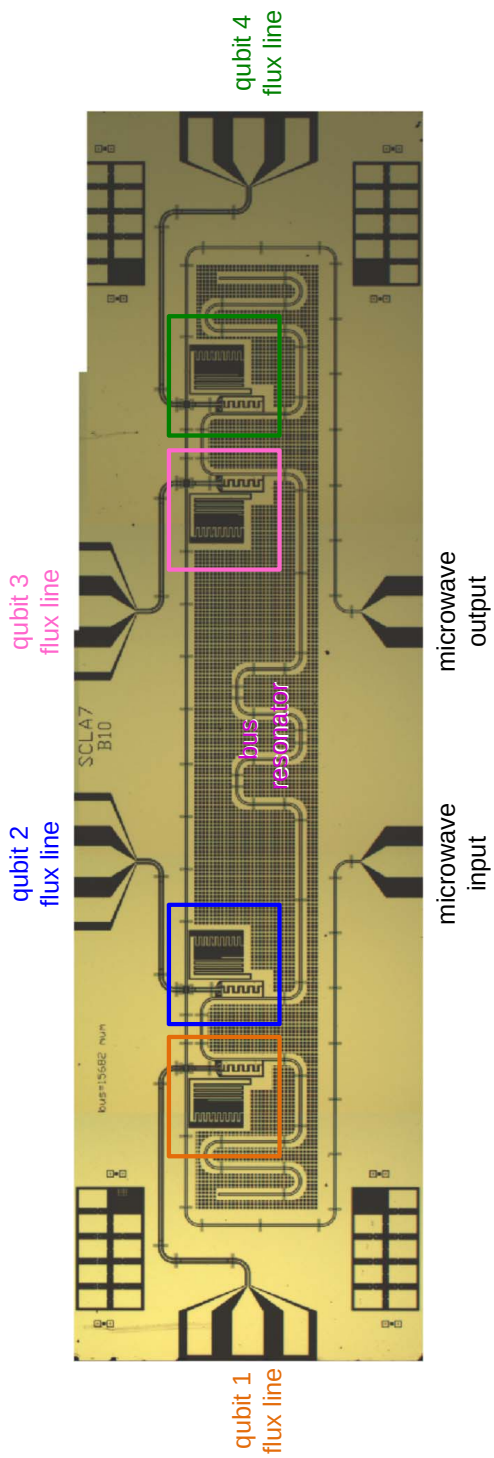

Figure 6.1: Optical micrographs of the 4-qubit processor prototype used in the experiment (four images merged). Each qubit-readout cell is shown with a color frame, and the bus resonator and the different microwave ports are labeled.

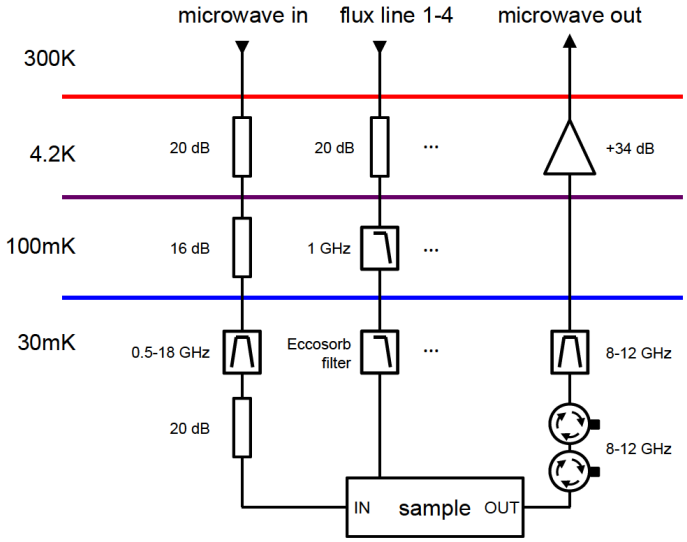

Figure 6.2: Fridge wiring. Only one on the 4 flux lines is drawn

6.1.3 Microwave setup

The microwave setup used at room temperature is again really similar to the one used in Chapter 5, except that the readout mixers are now replaced by *Hittite HMC-C042* mixers, the local oscillator frequency of which is in the $8.5 - 13.5\,\mathrm{GHz}$ range, while the readout frequencies are now at $\sim 11\,\mathrm{GHz}$. The flux lines are directly connected to the outputs of a 4 channels *Tektronix AWG5014* waveform generator, sampling at $1\,\mathrm{GSample/s}$.

6.2 Individual cell characterization

We detail here the characterization of the different functionalities of the elementary cells. We first characterize the JBA readouts (Sec. 6.2.1), then the transmon coherence and relaxation times. Finally the crosstalk in the frequency control of the transmons is investigated.

6.2.1 JBA resonator characterization

6.2.1.1 S_{21} coefficient varying with power

The frequency dependence of the S_{21} transmission coefficient measured with a VNA is shown in Fig. 6.3 for various drive powers. It clearly points out to a defective behavior of the JBA resonators. First, only 3 out of the 4 expected resonances are visible on the transmission, indicating that the Josephson junction of JBA 1 is probably open. Second, one notices on the low power curve

(top blue trace) that the resonance dip is only of $\sim 6\,\mathrm{dB}$, which clearly indicates that the quality factor of the resonators are low. Third, the power (albeit roughly calibrated) needed for observing the switching to the bifurcated state (see green, olive and red traces) is sizeably larger that for the sample of chapter 5. All these features can be well explained by an abnormally low internal quality factor of the JBA resonators, as characterized more precisely below.

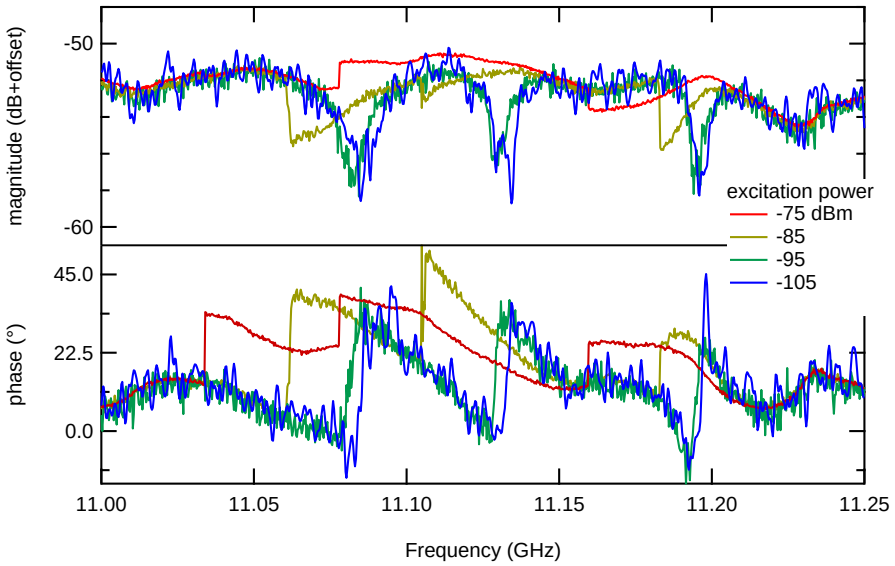

Figure 6.3: VNA measured S21 coefficient as a function of the frequency for different incident power

6.2.1.2 Quality factor in the low power linear regime

Figure 6.4 shows the complex S_{21} transmission coefficient of the three visible resonances (JBA $2-4$) in the linear regime. The fit in the complex plane yields external quality factors $Q_e \approx 3000$ in agreement with the design value, but internal quality factors $1800 < Q_i < 2900$ significantly lower than in the previous experiment. This is a clear indication that one of the last steps of the fabrication process has induced losses not present before, as discussed more precisely below.

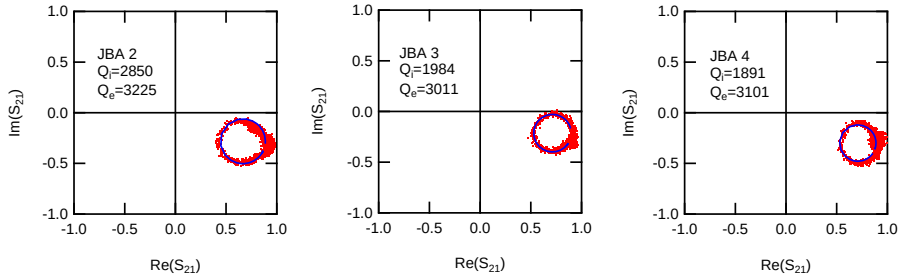

Figure 6.4: S_{21} coefficient in the linear regime around the 3 resonances, fitted to extract the external Q_e and internal Q_i quality factor

6.2.1.3 Readout contrast

Even though the internal quality factor of the JBAs resonators is low, we investigate their ability to perform qubit readout. From here to the end of the chapter, we focus only on cells (qubit + readout) 2 and 4. The switching curves of JBA 2 and 4 are shown on Fig. 6.5 for the qubits prepared in the ground or excited state. The detunings $\Delta_i = f_i^R - f_i^{ge}$ used for this characterization are $\Delta_2 = -1.01\,\mathrm{GHz}$ and $\Delta_4 = -0.85\,\mathrm{GHz}$, similar to the value used for characterizing a single JBA in Sec. 5.4. One observes that the switching curves widely differ from the almost ideal situation reached in the previous experiment, and that the achieved readout contrast $\{0.2\,, 0.4\}$ is very small compared to the value > 0.9 achieved in the previous experiment.

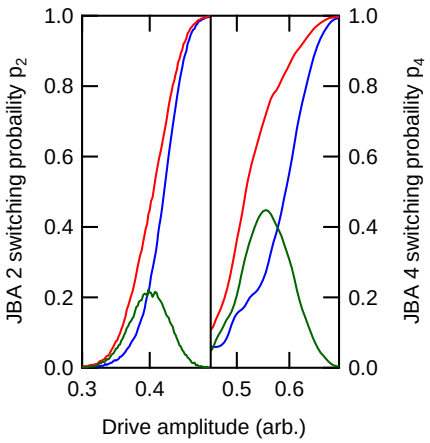

Figure 6.5: Measured switching curves for JBA 2 (left) and JBA 4 (right), for the qubit in its ground (blue) and excited state (red), as a function of the drive amplitude. The green curves are the corresponding differences, or contrast of a π pulse.

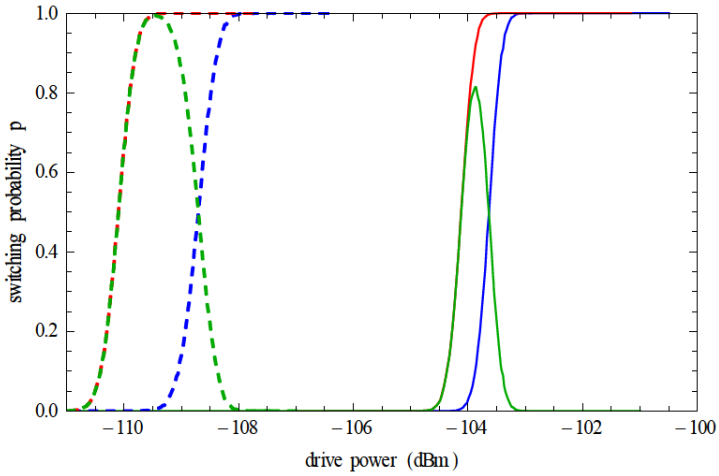

Figure 6.6: Simulated switching curves of JBA 2 for the two detunings $\Delta f_2 = -10, -13$ MHz that correspond to the qubit in its ground (blue) and excited (red) states, with the measured internal quality factor $Q_2^{ext} = 2850$ (solid lines) and for the ideal case $Q_2^{ext} \gg Q_2^{int}$ (dashed lines). Green curves indicate the contrast.

In order to check if the poor internal quality factors $1800 < Q_i < 2900$ of the JBA resonators can indeed be responsible for the poor observed readout performances, numerical simulations of the switching curves were performed using the method explained in Appendix A. An extra shunt resistor at the same quantum temperature as the external load was added across the JBAs to model Q_i. The separation between the simulated switching curves for the two qubit states (see Fig. 6.6) is indeed strongly reduced in comparison with the case of no internal loss, hence the reduced readout contrast. The agreement with the experiment is only qualitative due to the rounding of the S curve in state $|e\rangle$, as already discussed in section 5.4. Nevertheless, these simulations prove the detrimental effect of the lowered Q_i's on the JBAs readout contrasts. The exact cause of these lowered Q_i's are unknown and determining them will require further investigations on test structures all along the fabrication process flow. For the present sample we can only speculate, about the possible explanations:

- First the bridge fabrication process could introduce microwave losses by leaving resist residues below the bridges or all over the sample. This hypothesis seems however ruled out by the observation of a high quality factor ~50000 for the bus-resonator, whose resonance mode involves ground currents in airbridges.

- Second, the JBA resonators are baked at $\sim 190\,°C$ during the subsequent qubit fabrication, which could lead to oxidation of the aluminum layer.

- Third, the recontact areas of the JBAs aluminum Josephson junctions to the niobium meander inductances (see Fig. 4.1) could have been oxidized, either before aluminum deposition or at a subsequent hot temperature step. Indeed, an effective series resistance $R_s \approx 10^{-2}\,\Omega$ would be sufficient to reduce the resonator quality factor down to $Q_i \sim 2000 - 3000$.

Whatever the correct explanation, the low readout contrast found in this sample as well as the missing resonator have prevented high fidelity multiplexed readout, and thus operation as a quantum processor. Nevertheless, the different functions of the chip can be tested by rescaling the raw measured switching probability by measured readout fidelities of Fig. 6.5 for obtaining the qubit populations $p(|e_i\rangle)$ as mentioned in section 2.2.3.3.

6.2.2 Qubit characterization

6.2.2.1 Spectroscopy

The measured transition frequencies of qubit 2 and 4, together with the low power resonances of their readout resonators are plotted in Fig. 6.7 as a function of the current applied to their flux line. More precisely, a 5 µs long saturating qubit pulse followed by a readout pulse are applied every 20 µs. The qubit frequencies are perfectly fitted by Eq. 2.11 using $f_{2(4)}^{ge\,max} = 10.038$ (10.623) GHz and a SQUID asymmetry $d = 0.05\,(0.02)$. These values of d are actually only upper bounds because filters in the setup prevent from measuring resonances below 3.8 GHz, and thus from reaching the minimum transition frequencies. The small modulation of the resonator frequency with the qubit frequency gives access to the qubit-JBA resonator coupling constant. Using Eq. 2.27, one obtains $g_{2(4)}/(2\pi) = 95$ (101) MHz, slightly larger than the design value estimated in Chapter 3.

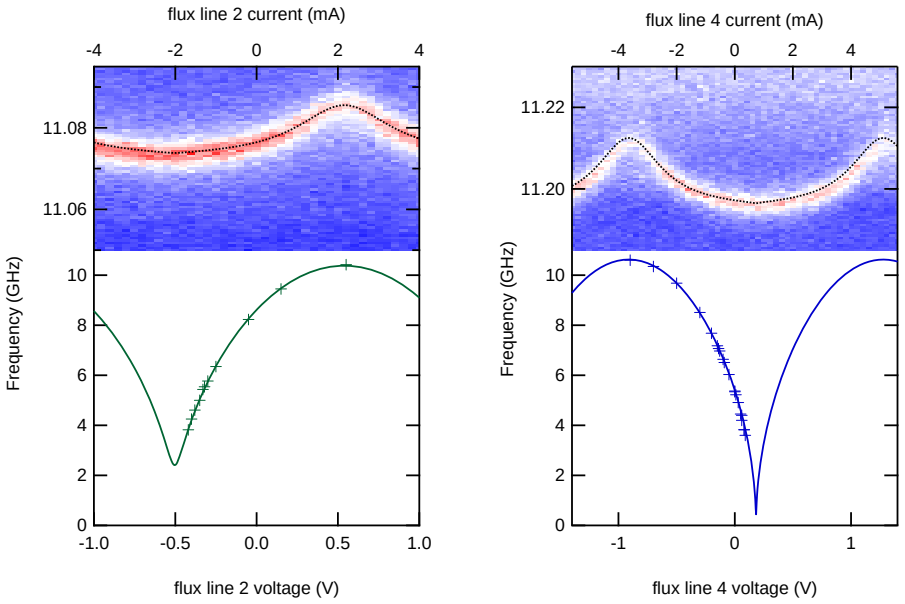

Figure 6.7: Cell 2 (left) and cell 4 (right) characterization: VNA measured readout resonator frequency in the linear regime (top) and qubit transition frequency f_2^{ge} (bottom) as a function of the flux line voltage.

6.2.2.2 Single qubit gates: Rabi oscillations

We have controlled coherently the quantum state of the qubits, as shown on Fig. 6.8 for qubit 2 and 4. Their resonant frequencies are here the maximum one indicated above, and the data show the 20 % and 40 % contrasts previously determined.

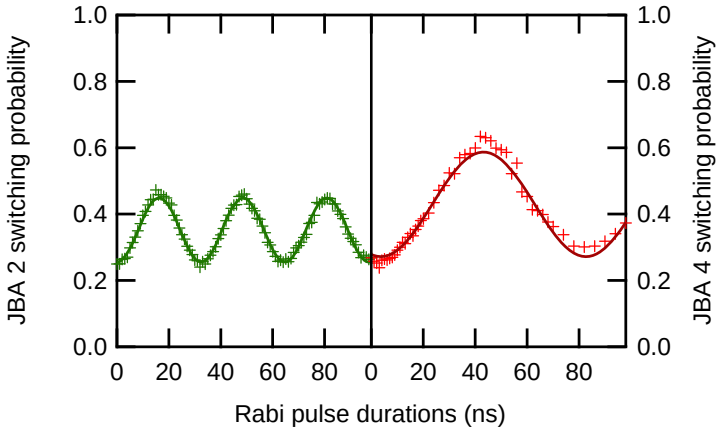

Figure 6.8: Rabi oscillation of qubit 2 and qubit 4. Raw switching probability.

6.2.2.3 Qubit relaxation and dephasing times

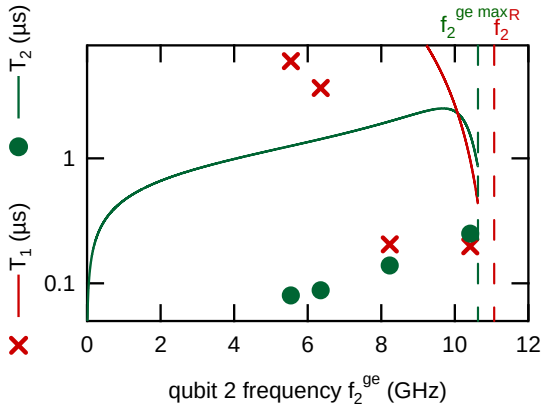

Figure 6.9: Qubit 2 decoherence (T_2) and relaxation times (T_1) at a few frequencies. The maximum qubit frequency and the readout frequency are shown by green and red dashed lines, respectively. The solid red and green lines are the expected Purcell relaxation time (Eq. 2.38) and the decoherence time $T_2^{-1} = T_{purcell}^{-1}/2 + T_\phi^{-1}$ with T_ϕ the pure dephasing time corresponding to a qubit frequency noise with a A/f spectral density with amplitude $A = 10^{-5}$ at 1 Hz.

The coherence times T_1 and T_2 measured for qubit 2 at different frequencies are shown in Fig. 6.7. These times are significantly shorter than those estimated from the parameters shown in Fig. 3.12.

First, the relaxation time at high frequency $f^{ge} > 8\,\mathrm{GHz}$ is shorter than predicted by the Purcell expression, even taking into account the reduced quality factor of the readout resonators. This points to an imperfect control of the microwave environment around the qubit at these frequencies. On the low frequency side ($f^{ge} < 7\,\mathrm{GHz}$), the measurements indicate $T_1 > 3.5\,\mu\mathrm{s}$, once again well below the Purcell limit. Because there is no reason that the relaxation in the flux line should be 20 times faster at 8-10 GHz than at 5-6 GHz, we tend to think that the strong relaxation is not due to the bad design of the flux line.

Second, the T_2 coherence time measured with a 2-pulse Ramsey sequence, is also between a factor 2 and a factor 100 shorter than the measured $2T_1$. Since the echo-coherence time is not longer, the noise responsible for the dephasing occurs mainly above 10 MHz. We cannot exclude that this noise is coming from the flux line, but the fact that its value is comparable with the one measured in the multiplexed readout experiment of Chapter 5 that had no flux lines suggest an alternative source of noise.

The qubit 4 shows similar dephasing and relaxation times, indicating once again that this sample can only be used for probing some function designs. Further investigations are clearly needed to characterize both relaxation and dephasing sources in this first prototype.

6.2.3 Frequency control, flux lines crosstalk

The spectroscopic data of Fig. 6.7 demonstrates our ability to control the qubit frequencies from ~ 3 to 10.5 GHz at low frequency (50 kHz). But our processor is based on the ability to change a qubit frequency precisely in a few nanoseconds only. To test this ability, we measure the response of the flux lines in-situ by applying to flux line 2 a voltage step with a 1 ns rise-time and measuring the qubit frequency after a variable delay. More precisely, we make the qubit swap with the bus as explained in the next section and deduce its frequency from the swap period. The result is shown on Fig. 6.10 with a time resolution of 10 ns. As for the experiment of chapter 2, the response function of the line does not correspond to a simple first order filter: it is very fast at the beginning but shows a slower increase in the last few per cent. This effect can be easily corrected by applying a pulse with a properly calculated overshoot, as done in section 2.3.

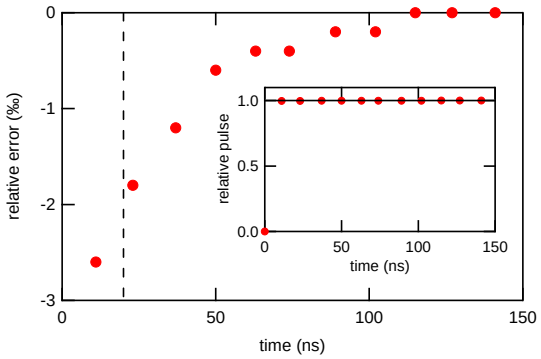

Figure 6.10: In-situ measured response function of a flux line. Relative error on the qubit frequency as a function of time, after having applied to the flux line a 0.096 V step to shift the qubit frequency from 5.4 GHz to 3.825 GHz (1 ns rise-time on the AWG). The dashed line indicates the targetted duration for two-qubit $iSWAP$ gates. (inset) relative amplitude of the frequency change.

Another important property is the crosstalk between two flux lines at low and high frequency. On the high frequency side, this crosstalk was not measured but is expected to be negligible with our design. Indeed, dedicated return current lines separated from other ground electrodes, force the current pulses to adopt the CPW quadrupolar geometry, which localize the induced fields. The situation is not as simple at low frequency, although one could think that because the qubit j is more than 200 times farther from a flux line $i \neq j$ than qubit i and because the field decays as the inverse of the distance to square, the direct crosstalk is negligible. Indeed, the field induced by flux line i is expelled from the neighboring superconducting electrodes by Meissner effect; which induces screening currents that can flow all over the sample and can generate local fields on qubit j. The low frequency crosstalk has thus to been measured at DC. This measurement is performed by placing qubit 4 at 7 GHz, where the frequency sensitivity to its flux line voltage is $\partial f_4^{ge}/\partial V_4 \approx 11\,\mathrm{GHz/V}$, and in varying the voltage of flux line 2. One finds a slope $\partial f_4^{ge}/\partial V_2 \approx 90\,\mathrm{MHz/V}$ that indicate a crosstalk of 0.8% between cells 2 and 4 at DC frequency. This crosstalk is smaller than previously achieved in similar designs without dedicated return lines ($\sim 30\,\%$ [79] for instance). It has nevertheless to be corrected when operating a processor, by applying the correction matrix mentioned in Sec. 3.2.1.

6.3 Bus characterization and coupling to the qubits

As the bus is not directly coupled to the readout resonators, it is a priori invisible without using one of the qubits as a spectrometer. However, it was detected at $f_{bus} = 3.825\,\mathrm{GHz}$ in a high-power 2-tone spectroscopy with a first spectroscopic pulse at a variable frequency and a power ~ 40 times higher

than for driving a qubit, and a second pulse to read out a JBA (see Fig. 6.11). Because this high power effect is not understood, a more controlled way to characterize the bus is to use a qubit and measure directly its coupling to the bus.

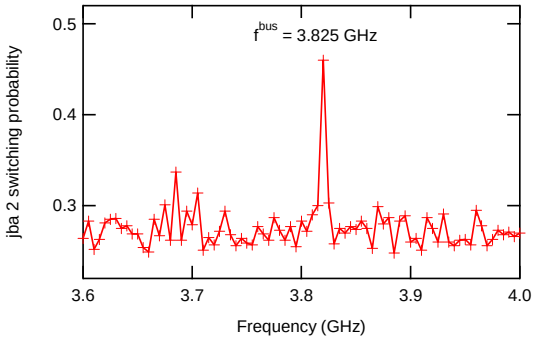

Figure 6.11: Spectroscopic line of the bus resonator observed at high excitation power on the switching probability of JBA 2.

The coupling Hamiltonian detailed in Sec. 3.3 reads

$$H_c^1 = \begin{pmatrix} \Delta_i & g_i \\ g_i & \Delta_i \end{pmatrix}_{\{|e_i 0\rangle, |g_i 1\rangle\}} \tag{6.1}$$

with $\Delta_i = \omega_R - \omega_i^{ge}$ the qubit-bus detuning, when restricted to a single qubit and a single excitation in the system. Equation 6.1 leads to vacuum Rabi oscillations observed as a chevron pattern when measured as a function of Δ_i.

Experimentally, the qubit is prepared in its excited state, is then frequency tuned across the bus frequency for a variable duration t_s, and is finally tuned to its readout frequency for measurement, as shown in the top panel of Fig. 6.12. The readout outcome is corrected for finite readout fidelity and shown in the bottom panel. The chevron pattern observed shows a small asymmetry and a drift at short time. This effect is due to the uncorrected finite rise time of the flux pulse described in Sec. 6.10 above. The data at times larger than 75 ns are fitted to determine the qubit-bus coupling constant $g_2/2\pi = 90\,\mathrm{MHz}$. The predicted chevron minima, solution of $\left(\Delta_i^2 + g_i^2\right) t_s^2 = (2N\pi)^2$, are displayed on top of the data, without taking into account the frequency drift.

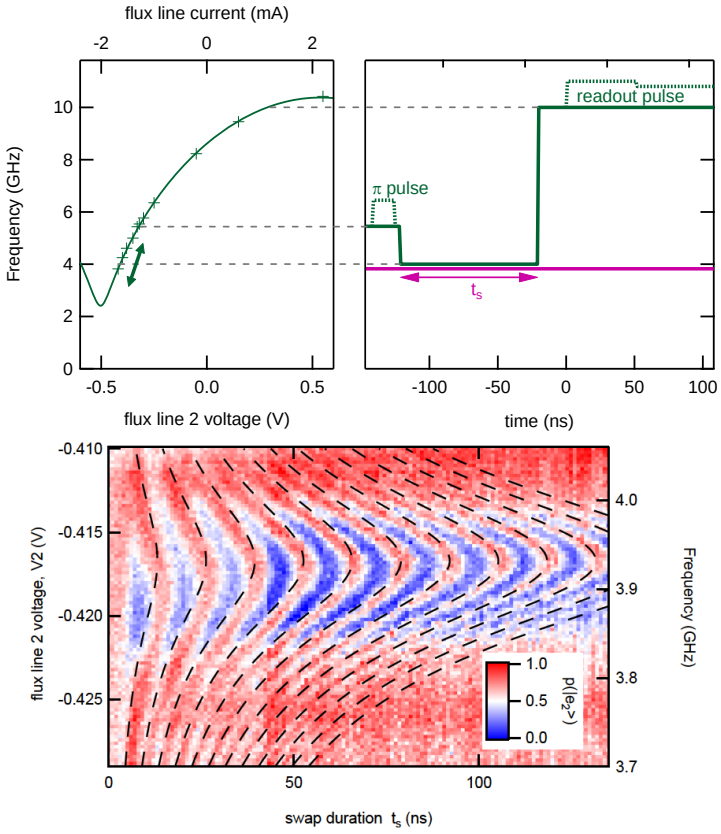

Figure 6.12: Swap between qubit 2 and bus. (top-left) qubit spectroscopic line versus current applied to the flux line. (top-right) Pulse sequence used as a function of time. The flux pulses have been converted in frequency units to share the same vertical scale as the left panel. Microwave pulses envelopes are represented on the same graph by dashed lines placed at the proper time, but with a height representing their microwave amplitude (unrelated to the frequency axis). (bottom) Qubit 2 excitation probability as a function of the flux line 2 voltage and of the swap duration. The dashed black line represent the location of the expected probability minima for the ideal frequency step on the qubit (see text).

The same experiment performed on qubit 4 (see Fig. 6.13) gives a similar chevron pattern and a coupling constant $g_4/2\pi = 101 \pm 3\,\mathrm{MHz}$.

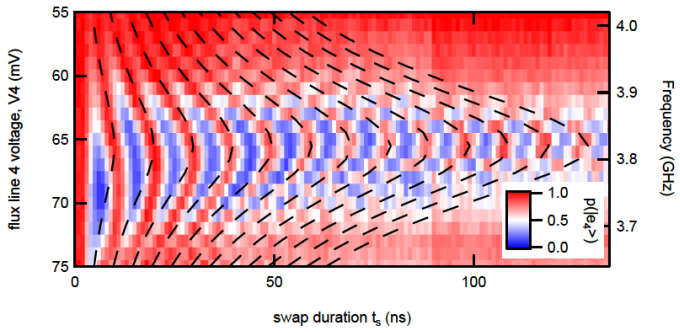

Figure 6.13: Qubit-bus swap experiment performed with qubit 4 and flux line 4.

These measured coupling are about twice as high as the designed values which is not understood but can only facilitate the test of the two-qubit gates.

Bus resonator quality factor

For determining the bus resonator quality factor, we measure the decay time of a single photon in the resonator. The protocol is sketched on Fig. 6.14.a: qubit 2 is prepared in its excited state, prior to a swap with the bus at frequency f^{bus}. The swapping time was chosen such that the qubit excitation is transferred to the bus with a high probability $> 95\%$. After this excitation swap, a waiting time Δt is applied prior to a second swap that transfers the remaining excitation back to the qubit. The excitation probability of qubit 2 shown on Fig. 6.14.b as a function of the waiting time Δt decays exponentially with a time constant $\tau = 2.2\,\mu s$, which corresponds to a quality factor $Q^{tot} = 2\pi\tau f^{bus} \approx 50,000$ for the bus. The excitation lifetime of the bus resonator is thus comparable to those of the qubits.

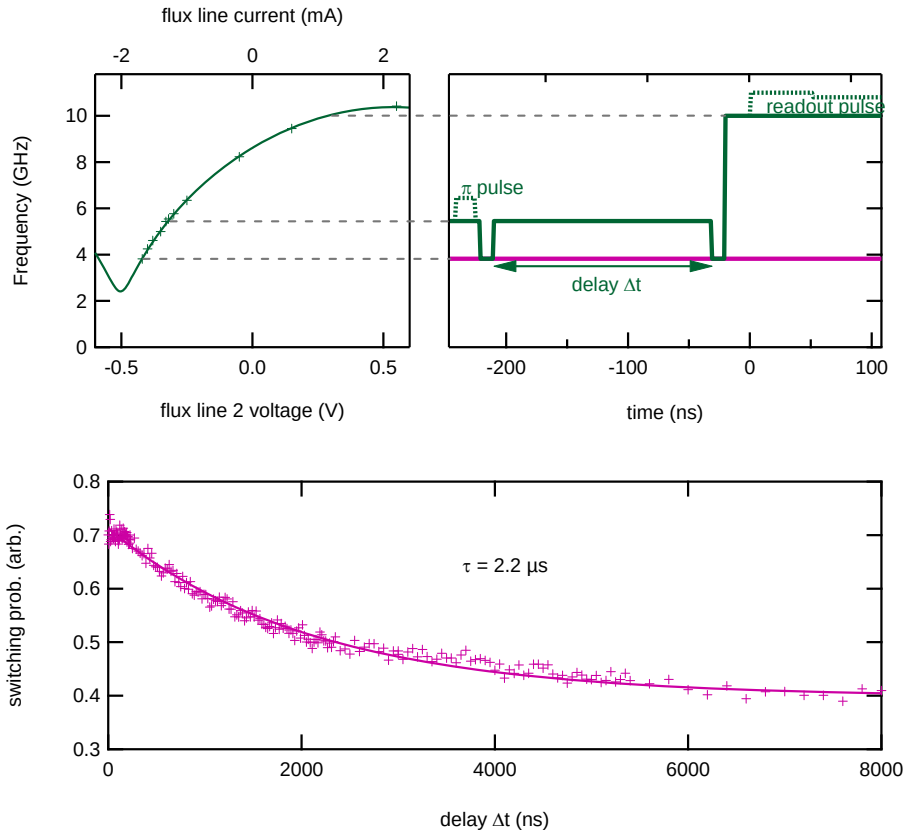

Figure 6.14: Measured decay time of the bus resonator, using qubit 2. (top) Qubit spectroscopy and pulse sequence used (see text). (b) Final switching probability of the JBA 2 reflecting the final remaining bus population.

Impact of higher harmonics of the bus resonator

A point ignored in the design, that could complicate the processor operation, is the impact of higher harmonic modes of the bus resonator. The frequency of the second harmonic around 8 GHz is indeed not far from the parking frequencies of the qubits ($6 - 7.5$ GHz, see Fig. 3.9).

Now, the coupling between the qubit and a bus resonator mode is proportional to the amplitude of the electric field for this modes at the position of the qubit. Given that the qubits are placed close to the electric nodes of the second harmonic (see Fig. 6.15), the estimated coupling to this harmonic is only $g/2\pi < 30$ MHz. Nevertheless it is not negligible and it would be useful and easy to reduce it even more by moving them slightly in the design.

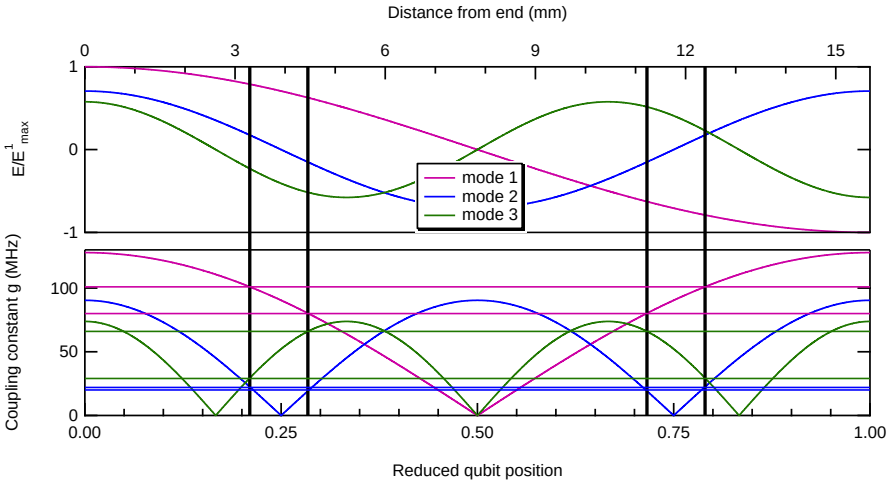

Figure 6.15: (top) Reduced electric field versus position, for the first three modes of the bus resonator. (bottom) Coupling constant between the qubit and these mode as a function of the qubit position.

6.4 Qubit-qubit bus mediated interaction

The exchange interaction $g/2\pi \approx 90{-}100$ MHz found between the bus-resonator and the qubits is expected to mediate a sizable qubit-qubit interaction. We remind here the Hamiltonian of the 2 qubits coupled to the bus (Eq. (3.3)):

$$H_{24}/\hbar = \omega^{bus} a^\dagger a + \omega_2^{ge}\sigma_Z^2 + \omega_4^{ge}\sigma_Z^4 + g_2(\sigma_2^+ a + \sigma_2^- a^\dagger) + g_4(\sigma_4^+ a + \sigma_4^- a^\dagger). \quad (6.2)$$

Tracing out the bus degrees of freedom in the dispersive regime $\left|\omega_{2(4)}^{ge} - \omega^{bus}\right| \gg g_{2(4)}$ yields the effective two-qubit Hamiltonian (Eq. (3.4))

$$H/\hbar = \omega_2^{ge}\sigma_Z^2 + \omega_4^{ge}\sigma_Z^4 + J_{24}\sigma_2^X\sigma_4^X \quad (6.3)$$

with $J_{24} = g_2 g_4 \left(\frac{1}{\Delta_2} + \frac{1}{\Delta_4}\right)$ the effective qubit-qubit coupling constant.

Since simultaneous readout of two qubits is impossible with this sample due to its too low readout efficiency, we characterize the swapping by measuring only qubit 4 at the end of a variable coupling time of qubits 2 and 4. As already mentioned, a proper calibration of readout errors makes possible to get the absolute population of the excited state of qubit 4.

6.4.1 Resonance condition for qubit-qubit swapping

One first needs to determine the flux line currents that places the 2 qubits on resonance, i.e. $f_2^{ge} = f_4^{ge}$. To do so, after having prepared qubit 2 in its

excited state, we vary the two flux line currents simultaneously for a given arbitrary amount of time, and then displace qubit 4 for readout (see top panel of Fig. 6.16). The excited state population $p(|e_4\rangle)$ of qubit 4 increases as shown in the bottom panel when the 2 qubits are on resonance and can share the same excitation. The resonance condition line is marked with a dashed black line. One also notices that the probability $p(|e_4\rangle)$ increases when the qubit 4 is resonant with the bus and gets a spurious excitation from it.

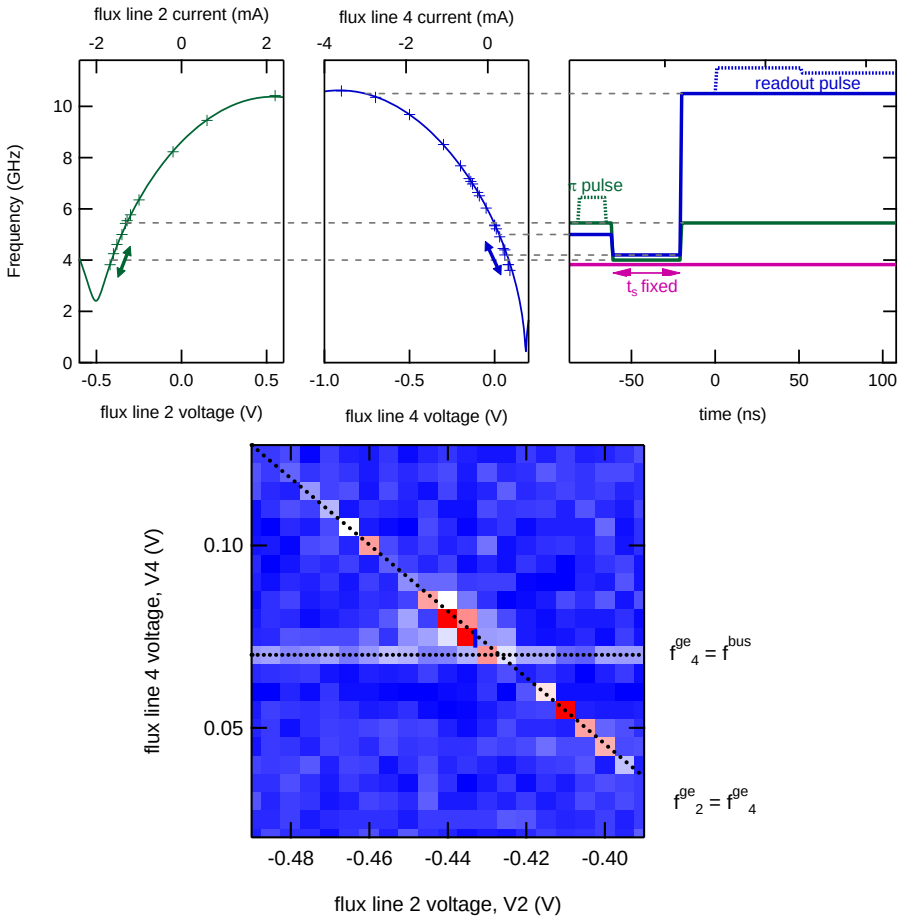

Figure 6.16: Swap between qubit 2 and qubit 4. (top-left) spectroscopic lines of qubit 2 and 4 versus current applied to their own flux lines. (top-right) Pulse sequence used as a function of time (see text). Microwave pulses envelopes are represented on the same graph by dashed lines placed at the proper time, but with a height representing their microwave amplitude (unrelated to the frequency axis). (bottom) Qubit 4 excitation probability as a function of the voltage on flux line 2 and 4, for a short swap duration $t_s = 40\,\text{ns}$. The oblique dashed black line indicates where the two qubits are on resonance, whereas the horizontal one indicates where qubit 4 is resonant with the bus.

6.4.2 Swapping coupling strength

As mentioned above, the qubit-qubit effective coupling $J_{24} = \frac{2g_2 g_4}{\Delta}$ is inversely proportional to the common detuning Δ between the resonant qubits and the bus. Given the short coherence times T_2 of the qubits, it is advantageous to use a large coupling (small detuning) to reduce the gate time and increase

its fidelity. On another hand, as discussed in Section 3.3.3, the smaller the detuning, the larger the residual population of the bus and the higher the precision needed for the gate time.

In order to find the largest coupling that does not leave a too large excitation in the bus, we measure and simulate the swap experiment for the two qubits on resonance ($f_2^{ge} = f_4^{ge}$) at different detunings Δ with the bus. To do so, we vary the swap duration t_s (along the oblique line of Fig. 6.16), as shown in the top panel of Fig. 6.17. The resulting excitation probability of qubit 4 is shown in the bottom panel Fig. 6.17, together with the results of a simulation by integration of the master equation of the system, described below in Section 6.4.4. Experimental data and simulation agree qualitatively, despite the much lower resolution used in the experiment. Note also that the theoretical time axis has been slightly shifted upward to compensate for a 14 ns delay between the current pulses in the two flux lines. The simulation shows a Moiré pattern around the symmetry axis at 3.825 GHz, between two sets of chevrons. Those pointing upwards correspond actually to the fast oscillation of the bus population discussed in section 3.3.3. To limit this unwanted population, we choose a detuning $\Delta = -0.462\,\mathrm{GHz}$ (see magenta line on Fig. 6.17), where the Moiré becomes barely visible. This correspond to $J_{24}/2\pi \approx 30\,\mathrm{MHz}$, much larger than the $J_{ij}/2\pi \approx 12.5\,\mathrm{MHz}$ value targeted in Section 3.3.

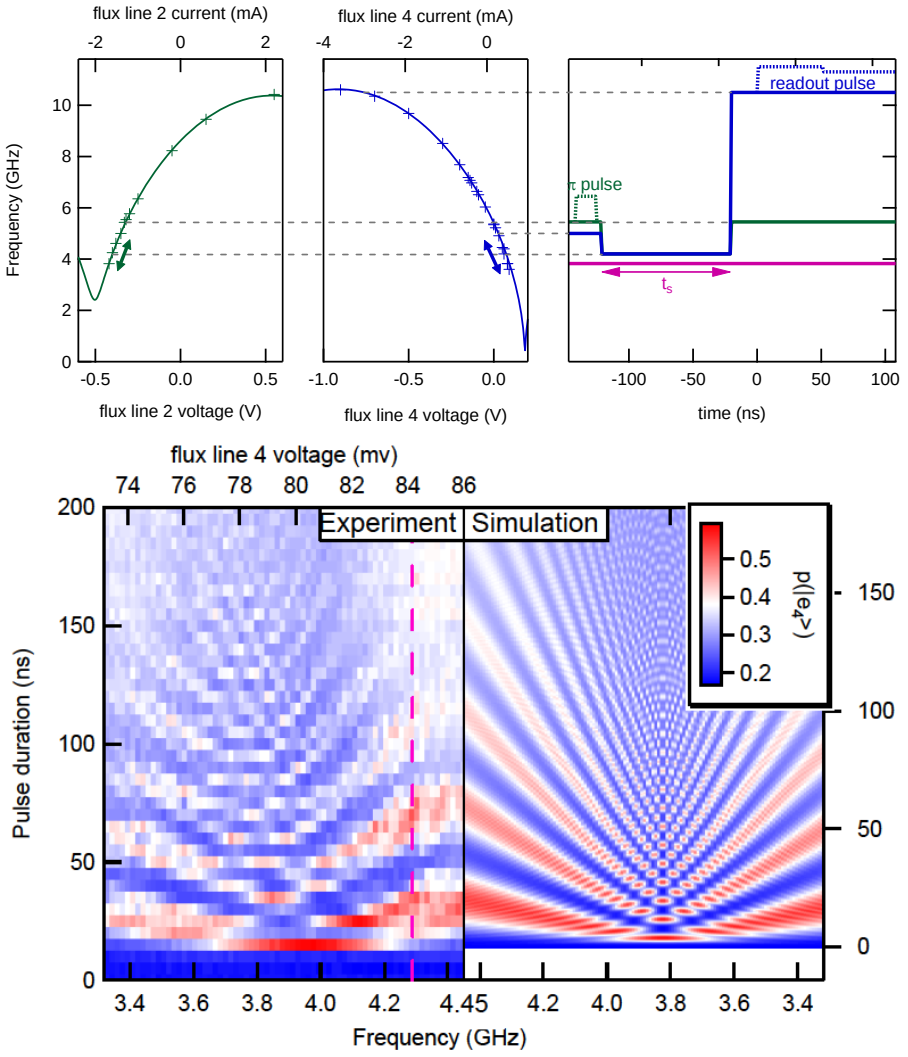

Figure 6.17: Qubit-qubit swap at different common qubits-bus detunings Δ. (top-left) spectroscopic lines of qubit 2 and 4 versus current applied to their own flux line. (top-right) Pulse sequence used as a function of time (see text). (bottom-left) Measured qubit 4 excitation probability as a function of the SWAP duration and of flux lines 2 voltage (the voltage of flux line 4 is calculated to maintain the resonance condition) (bottom-right) Simulation by integration of the master equation of the system with $T_1 = 2.7\,\mu s$, the same effective $T_2 = 170\,ns$ for the two qubits, and $\tau = 2.2\,\mu s$ (see Section. 6.4.4).

6.4.3 Bus mediated swap

The swap protocol used is sketched in the top panel of Fig. 6.18: the qubit 2 is first prepared in its excited state and placed during a variable time t_s at the frequency $f_2^{ge} = 4.29\,\mathrm{GHz}$ chosen above. During that time, qubit 4 is placed at a variable frequency around f_2^{ge}. Qubit 4 is finally moved at its readout frequency and measured. Its resulting excitation probability is shown in the central panel of Fig. 6.18 as a function of t_s and f_4^{ge}. A simulation of the very same protocol is shown on the right. It is performed using the values of the measured T_1 and τ times, and with an effective $T_2 = 170\,\mathrm{ns}$ time common to the two qubit and adjusted to fit the data (see section. 6.4.4).

The time dependence of $p(|e_2\rangle)$ and $p(|e_4\rangle)$ at the chosen frequency f_4^{ge} (see magenta line of the central panel of Fig. 6.18) is shown in the bottom panel of the figure. The agreement between data and simulation is correct. One observes fast oscillations of the bus population at the bus-qubit detuning frequency, with a maximum amplitude of 10%. This residual amplitude would be too high to implement a high fidelity gate and is the result of the small detunings chosen because of the too short decoherence times.

The maximum excited state population $p(|e_4\rangle)$ is about $\sim$ 90%, which gives the modulus of the matrix element $\langle e_2 g_4 | U_{iSWAP} | g_2 e_4 \rangle$ responsible for the SWAP. This indicates that the corresponding gate fidelity could reach this value when complemented by a σ_Z phase gate for correcting the phase accumulated during the swap. This limited fidelity is due to (i) dephasing for $\sim$9 %, (ii) relaxation for 1 % and (iii) residual population in the bus for < 1 %. With the present coupling and relaxation and effective dephasing times of 20 µs and 5 µs respectively, the gate fidelity could reach 98 % with a detuning $\Delta = -1.4\,\mathrm{GHz}$ and a gate swap time of 40 ns.

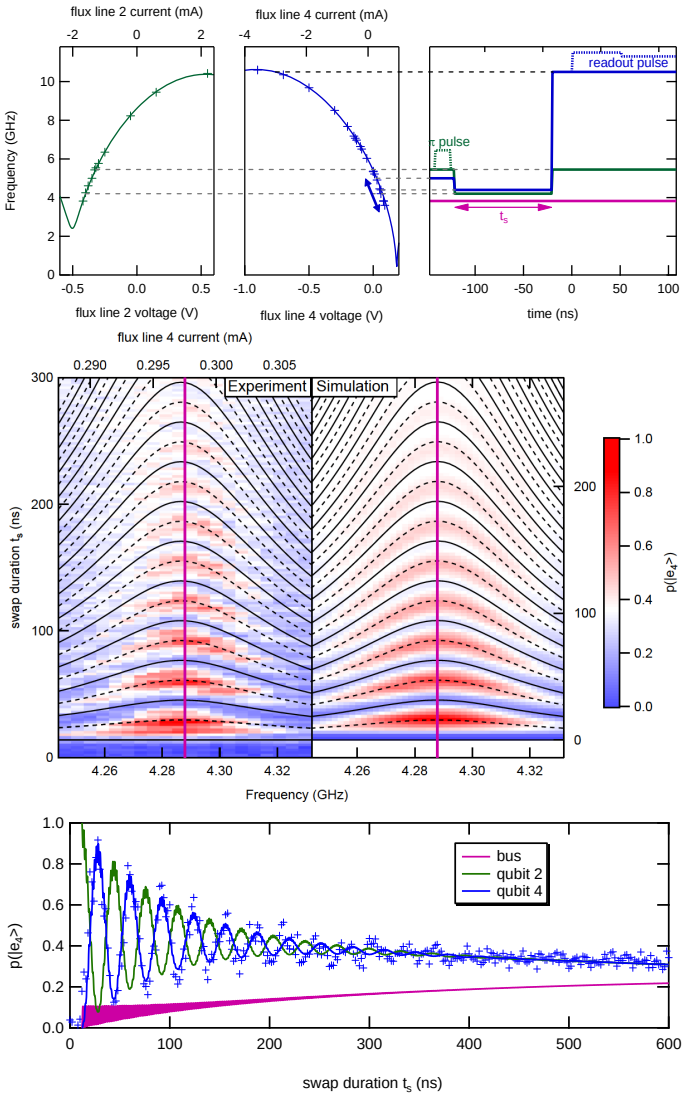

Figure 6.18: Swap between qubit 2 and 4 at fixed qubit 2 frequency ($\Delta_2 = -0.462\,\mathrm{GHz}$). (top-left) Spectroscopic lines of qubit 2 and 4 versus current applied to their own flux lines. (top-right) Pulse sequence used as a function of time (see text). (middle-left panel) Measured qubit 4 excitation probability as a function of the SWAP duration and flux lines 4 voltage (middle-right panel). Simulation by integration of the master equation of the system with the same parameters as in Fig. 6.16. Solid and dashed lines indicates the minima and maxima of $p\left(|e_4\rangle\right)$, respectively. (bottom) Measured (dots) qubit 4 population along the magenta line of middle panel. Solid lines are simulated population of qubit 2, qubit 4, and of the bus.

6.4.4 Simulation of the swap experiments

The simulated data shown in this chapter are obtained by integrating the master equation

$$\frac{\partial \rho}{\partial t} = -\frac{i}{\hbar}[H,\rho] + \sum_i D_i(\rho) \tag{6.4}$$

$$H/\hbar = \omega^{bus} a^\dagger a + \omega_2^{ge}\sigma_Z^2 + \omega_4^{ge}\sigma_Z^4 + g_2(\sigma_2^+ a + \sigma_2^- a^\dagger) + g_4(\sigma_4^+ a + \sigma_4^- a^\dagger) \tag{6.5}$$

$$D_i(\rho) = L_i \rho L_i^\dagger - \frac{1}{2} L_i^\dagger L_i \rho - \frac{1}{2}\rho L_i^\dagger L_i \tag{6.6}$$

with ρ the density matrix of system expressed in the tensorial basis $\{|g_2\rangle, |e_2\rangle\} \otimes \{|g_4\rangle, |e_4\rangle\} \otimes \{|0\rangle, |1\rangle, ..., |5\rangle\}$ truncated at 5 photons, H the Hamiltonian of the system, and $D_i(\rho)$ the decoherence super-operators. In equation 6.4, the sum is taken over all the pure dephasing and relaxation phenomena of the two qubits and the bus:

$$\text{qubit } j\text{dephasing:} \quad L_j^\phi = \sqrt{\Gamma_j^\phi/2}\sigma_j^Z \tag{6.7}$$

$$\text{qubit } j\text{relaxation:} \quad L_j^r = \sqrt{\Gamma_j^r}\sigma_j^- \tag{6.8}$$

$$\text{bus relaxation:} \quad L_{bus}^r = \sqrt{\Gamma_{bus}^r}a \tag{6.9}$$

This integration was performed with the open-source Python Quantum Toolbox named QuTiP [80] well suited for simulating the dynamics of open quantum systems. The simulator outputs the population $\mathrm{Tr}(\sigma_4^z \rho)$ of qubit 4 to be compared with the experimentally measured data points, as well as the excitation population $\mathrm{Tr}(\sigma_2^z \rho)$ of qubit 2 and of the bus $\mathrm{Tr}\left(a^\dagger a \rho\right)$ that were not measured.

The bus frequency $f^{bus} = 3.825\,\mathrm{GHz}$ and the coupling constants $g_{2(4)}/2\pi =$ 90 (100) MHz entering in the simulation are the one independently measured. The data are fitted with relaxation times $T_1 = 2.7\,\mu\mathrm{s}$ for the two qubit and a decay time $\tau = 2.2\,\mu\mathrm{s}$ previously measured for the bus resonator. Because the individually measured dephasing times of each qubits are not relevant any longer when the two qubit are resonantly coupled, and because the exact theoretical description of pure dephasing is missing in this case, we phenomenologically model dephasing by a common dephasing time acting independently on both qubits and left as a free fitting parameter. The fit yield $T_2 = 170\,\mathrm{ns}$.

6.5 Conclusion

In conclusion, several problems have been encountered on this first measured prototype that prevented to use it as a real processor. In particular, a missing JBA and other JBAs being lossy, most likely due to fabrication problem, prevented us from reproducing the good multiplexed readout results of the previous chapter. However, it was possible to demonstrated SWAP operations

between two qubits, with a fidelity clearly limited by much too short coherence times. For progressing, one has to work on the fabrication process, in particular for improving the contact between the aluminum electrodes of the Josephson junctions on the niobium layer, and for optimizing the parameters of the airbridge fabrication process in order to avoid any highly cross-linked resist layer underneath the bridges.

These preliminary tests make us think that our architecture based on multiplexed JBA readout and on the non-resonant coupling of transmons to a high Q bus resonator for gate operation is a viable concept, if and only if qubits with reproducible coherence times larger than 20 µs can be obtained.

Chapter 7

Conclusion and perspectives

7.1 Operating the 4-qubit processor

In this thesis work, we have designed, implemented and tested a prototype version of a simple electrical 4-qubit processor. Although its imperfections have prevented us from using it as a real processor, we were able to validate its functional blocks and the overall design. We describe here the solutions that we envision for solving the technical issues we have encountered, and in a broader perspective, the scalability potential of superconducting quantum processors.

Solving technical issues

In our rather complex circuits, we have obtained qubits with coherence times systematically shorter than calculated from the relaxation and dephasing one could attribute to the electromagnetic circuit in which they are embedded. These problems were even more acute in the full processor where the qubits and the JBA resonators showed quite bad performances.

Since some transmons fabricated on sapphire using the same deposition machines and measured in 3D cavities have yielded much longer coherence times, we cannot attribute the source of our problems to the superconducting thin films deposited, but rather to defects induced during the whole fabrication process. Further tests are clearly necessary for clarifying this issue. The Josephson junctions of the JBA readouts and the qubits are fabricated in two rounds, the second potentially detrimental to the first set of junctions because of the resist baking required. If this is indeed a problem, fabricating all the junctions in a single round would solve it.

Nevertheless, fabricating the airbridges requires a baking at high temperature (140°C). Because of the fragility of these bridges, they have to be made at the very end, possibly degrading the junctions. An alternative solution would be to fabricate bridges prior to the junctions with a dielectric material beneath the bridge, thus replacing the "air". We have obtained the optical masks needed for modifying our fabrication process, but had not the time for developing it. Different dielectric materials could be used, such as silicon nitride (Si_3N_4),

aluminum oxide (Al_2O_3), or low loss plastic used in microwave electronics as BCB (benzo-cyclo butene). We have performed some preliminary tests using the Cyclotene BCB photoresist that allows us to obtain thick layers of $\sim 5\,\mu m$ more easily than when using Si_3N_4 or Al_2O_3 that can be deposited at a rate of $\sim 0.1\,nm/s$. Once cured, this material is expected to have relatively small dielectric losses ($\tan\delta \sim 0.0008$). Such non-suspended strong bridges would allow us to fabricate the Josephson junctions afterwards, preventing them from re-baking.

Our circuits in which aluminum films are contacted on niobium films are also prone to interface problems even when 500 eV ion cleaning of niobium is done prior to aluminum deposition. Replacing niobium by another superconductor less prone to surface oxidation such as NbTiN has been recently successfully demonstrated [81].

In addition to that, our experiments probably suffer from imperfect filtering of the flux and microwaves lines [82].

Operating our 4-qubit processor

Assuming solving all technical issues leads to better transmon qubits and to the high fidelity JBA readout obtained on simpler samples, could one really use this 4-qubit circuit as a universal quantum processor? We have demonstrated that the coupling bus induces an effective swapping evolution between two qubits on resonance slightly above the bus frequency, but we have not determined the fidelity of the two-qubit gate one can obtain this way. Would this fidelity be as good as estimated in Chapter 3, this processor could run some simple quantum algorithms such as the Grover search algorithm on 16 items, and protocols such as the teleportation protocol.

7.2 Scalability issues faced by superconducting processors

7.2.1 The readout scalability issue

One important aim of this thesis work was to propose a more scalable solution than previously achieved for making a superconducting processor. In this respect, we have clearly demonstrated multiplexed readout on four transmons, which is the state of the art. Indeed, although a nine transmon circuit was recently operated in [64], simultaneous multiplexed single-shot readout reaching a high fidelity has not been achieved on more than four transmons using linear dispersive readout. This method is limited by the small saturation power ($\sim -105\,dBm$) of presently available Josephson parametric amplifiers [78]. The scalability of linear dispersive readout is presently estimated at about ten qubits but the recent operation of the so-called Travelling Wave parametric Amplifier (TWPA) [67, 83] may lead to a large increase.

On the side of our architecture based on multiplexed JBA readout and on a coupling bus, the scalability would be limited by the interaction between

non-linear resonators too close in frequency, and by the technical difficulty to produce and to analyze readout signals spanning a too large bandwidth. Keeping the same frequency staging of 60 MHz for preventing crosstalk would allow us to scale up to 10-15 qubits without changing our microwave setup. However, coupling more than 5-6 of our transmons to the same bus resonator seems a bit unreasonable because of residual couplings of the qubits at their parking frequencies. A way to get around this issue could be to use tunable couplers [84, 85] between each qubit and the coupling bus which mitigates the frequency crowding problem.

7.2.2 All scalability issues

Our previous analysis of scalability in terms of readout is insufficient because one needs to make a large number of coherent qubits, which implies to implement at the same time quantum error correction, definitively a formidable challenge.

First the error correcting codes already developed are extremely demanding in terms of coherence and gate performance for the physical qubits, with a threshold at about $\sim 10^{-5}$ error per gate operation, plus with a huge overhead in term of physical qubit number [8]. Given this strategy seems presently irrealistic, other approaches have been recently considered.

A new strategy less demanding in terms of gate error fidelity but far more in term of physical qubit resources is the surface code approach [86, 87]. It consists in making a 2D array of transmons and resonators coupled as shown in Fig. 7.1 (different designs are possible). The transmons, coupled to two resonators are used as data qubits and for error detection. In this scheme, one keeps track of the errors that occur without correcting them on the fly. A preliminary 1D version of a 9-qubit circuit recently achieved the 1 % error threshold needed in this approach [64]. The complexity of the surface code 2D design requires a 3D packing of the elements, and poses formidable technical challenges in term of frequency crowding and residual couplings. The estimated overhead in term of physical qubit number could be as large as 10^3.

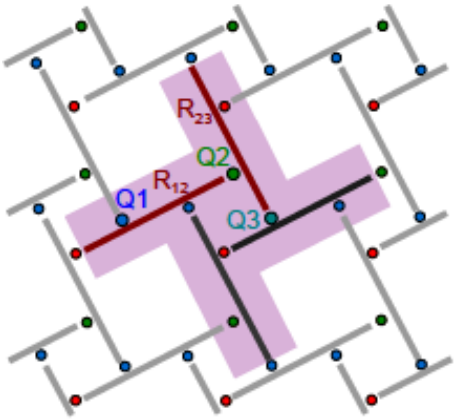

Figure 7.1: Surface code architecture with bus resonators. Each qubit Q is coupled to 2 resonators, and each resonator R to 4 qubits, including 1 logical qubit for computation and 3 ancillary qubits used for detecting errors. (taken from [86])

A very different strategy consisting in making intrinsically more robust qubits based on high quality factor resonators was recently proposed [88]. The qubits would be Schrödinger cat states encoded in the internal field of resonators, with Josephson coupling elements and extra low quality factor driven resonators for preparing them and controlling their evolution. This strategy is based on controlling dissipation in order to stabilize the qubit Hilbert subspace. Errors consisting only in the emission of single photons are detected using parity measurements, and one would simply record them. Experiments have been recently performed along these lines [89].

7.3 Other promising strategies for quantum information processing

7.3.1 The hybrid route

A completely different approach than making the processor with a large number of qubit is to combine a few-qubit processor with a RAM-style quantum memory. This memory would store the whole qubit register, and transfer on demand, qubits to the processor for performing gate operations, before transferring them back to the memory.

Hybrid systems that combine the convenient addressability of electrical circuits and the intrinsically good coherence properties of some microscopic systems have been proposed, and some results have been obtained in this direction. In the case of nitrogen-vacancy (NV) spins in diamond, a proof of concept for a memory based on a spin ensemble was demonstrated in [90]. A full protocol

for a multimode memory was proposed in [91] and preliminary results obtained [92].

A nuclear spin based quantum processor?

Nuclear spins with coherence times up to hours are probably among the best qubits. Since nuclear spins can be coupled to electronic spins by hyperfine interactions, they can be entangled, which is equivalent to operating an entangling gate on them [93]. Here, superconducting circuits would be used to transfer quantum information between the electronic spins, and thus between the nuclear spins.

7.3.2 Semiconductor qubits are back

Quantum bits based on electronic spins or quantum dots in semiconducting materials have been developed very early, but they have never achieved good enough quantum coherence for making circuits. Andrea Morello and his team at UNSW recently made a breakthrough by demonstrating qubits in a spinless semiconducting material ^{28}Si that achieve extremely long coherence times [94, 95, 96], far longer than those of superconducting qubits.

7.4 Personal viewpoint

Superconducting quantum information processors are certainly not yet around the corner, but research in this field is worth being pursued in-depth.

First, these circuits and the design flexibility they offer have recently provided excellent systems for carrying out foundational experiments in quantum mechanics that were only thought experiments. The direct observation of the quantum trajectory followed by the quantum state of an artificial atom weakly continuously measured [97, 98] was made possible thanks to the progress on superconducting qubit control.

Second, research in this field has already led to the development of interesting devices such as the Josephson parametric amplifier used in the abovementioned experiment. These amplifiers that reach the ultimate sensitivity limit imposed by quantum mechanics have already been used for improving the sensitivity of electron spin resonance spectroscopy [99]. This demonstrates the interest of superconducting quantum circuits beyond qubit research.

Appendix A

Numerical simulation of the switching dynamics of a JBA

This appendix describes numerical simulations performed to check that the switching dynamics of the Josephson Bifurcation Amplifiers (JBA) used for reading out the qubits is understood. Our goal is to produce the JBA switching curves in the different experiments. Although no complete analytical theory of the JBA exists, M. Dykman has established a quantum Langevin equation for the JBA valid for a drive frequency not too close to the critical frequency $\Omega_c = \sqrt{3}$ and a drive amplitude close to the switching one. An interesting result of his work is that the quantum dynamics is equivalent to the classical one but with an effective temperature $T = \hbar\omega_0/2k_B$ [100, 48], with ω_0 the angular frequency of the JBA resonator. We have performed such classical simulations of the JBA alone to produce the switching curves. In this approach, the influence of the qubit in taken into account in a very simple way, through a change of the JBA parameters (due to the 2χ frequency pull between ground and excited qubit states). More advanced theoretical investigations have been performed by A. Blais and his coworkers [101, 102] by treating fully quantum mechanically the coupled sytem JBA + Transmon, including the drive and the qubit decoherence. This approach was in particular used to try to reproduce the shoulder observed in the switching curve for state $|e\rangle$ (see Section 5.4), which reduces the readout fidelity. We establish below in sections A.1 and A.2 the classical Langevin equation of the JBA. This equation of motion was simulated with a program written in C and optimized for speed. Section A.3 presents simulated trajectories and the resulting switching curves obtained from these simulations.

A.1 Equivalent model of the JBA resonator

The schematic circuit of the JBA resonator connected to its source and load through the input and output lines is shown on Fig. A.1.a.

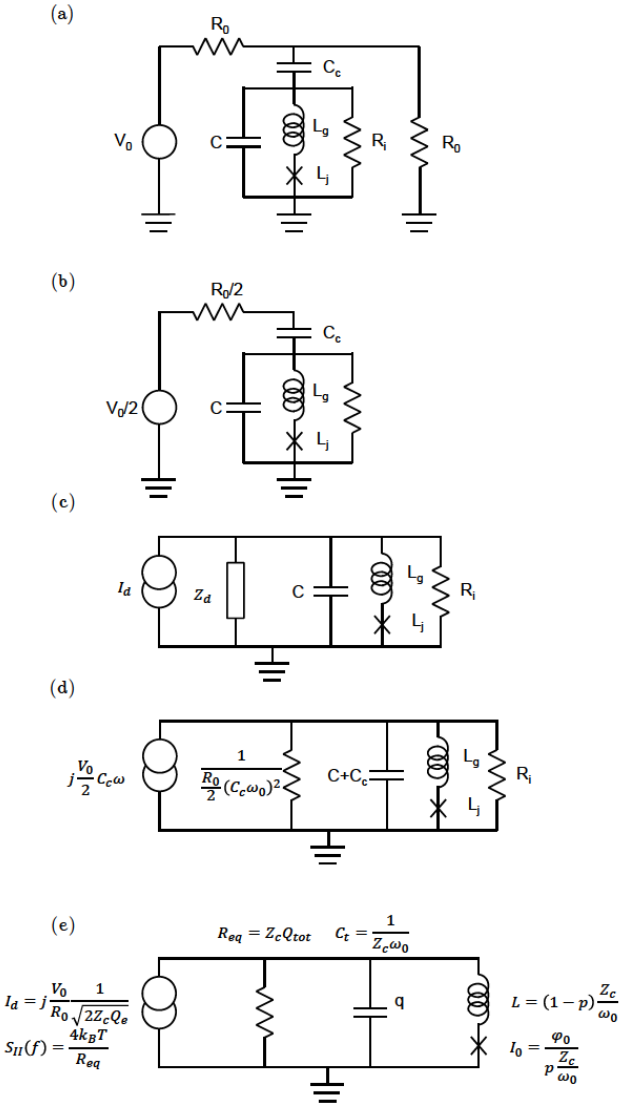

Figure A.1: Equivalent circuits of the JBA resonator connected to input and output lines. See text.

The resonator consists of its geometrical inductance L_g in series with a Josephson inductance $L_j = I_0/\varphi_0$, in parallel with an internal capacitance C and a resistance R_i modeling the losses. This resonator is capacitively coupled by a capacitance C_c to a transmission line connected to a microwave source with internal voltage V_0 and impedance $R_0 \simeq 50\,\Omega$ and to a load R_0.

Using the Norton-Thevenin theorem, one simplifies the system to a single

port circuit (see Fig. A.1.b) with the resonator driven by a voltage source $V_0/2$ through an impedance

$$Z_d = \frac{R_0}{2} + \frac{1}{jC_c\omega}. \tag{A.1}$$

Applying once more the Norton-Thevenin theorem, one obtains the circuit of Fig. A.1.c with a parallel current source.

Assuming a drive frequency ω close to resonance ω_0 as well as a large quality factor leading to $C_c\omega_0 R_0 \ll 1$, Z_d can be approximated by the capacitance C_c in parallel with a resistance $R_{eq} = 2/(R_0 C_c^2 \omega_0^2)$, and the current source by $I_d = j\frac{V_0}{2} C_c \omega_0$ (see Fig. A.1.d).

The angular frequency and characteristic impedance of the resonator are thus $\omega_0 = 1/\sqrt{L_{tot}C_{tot}}$ and $Z_c = \sqrt{L_{tot}/C_{tot}}$ with $C_{tot} = C + C_c$ and $L_{tot} = L_g + L_j$; we denote $p = L_j/L_{tot}$ the participation ratio of the Josephson junction to the total inductance.

The quality factor Q_{tot} of this parallel RLC circuit is simply the ratio of its resistance to the resonator charactic impedance

$$\begin{aligned} \frac{1}{Q_{tot}} &= \frac{Z_c}{R_i} + \frac{Z_c}{\frac{R_0}{2}\left(C_c\omega_0\right)^2} && \text{(A.2)} \\ &= \frac{Z_c}{R_i} + \frac{R_0/2}{Z_c}\left(\frac{C_c}{C_{tot}}\right)^2 && \text{(A.3)} \\ &= \frac{1}{Q_i} + \frac{1}{Q_e} && \text{(A.4)} \end{aligned}$$

where $Q_i = R_i/Z_c$ and $Q_e = \frac{Z_c}{R_0/2}\left(\frac{C_{tot}}{Cc}\right)^2$ are the internal and external quality factors, respectively.

Finally, the model can be expressed using only reduced parameters (Q, Z_c, ...) as shown on Fig. A.1.e, with a thermal current noise source included in the current source and characterized by its spectral density $S_I(\omega)$.

A.2 Equation of motion of the JBA

The charge q on the capacitor C_{tot} under a drive $I(t) = \frac{V_0}{R_0}\sqrt{\frac{2}{QZ_c}}\sin(\omega_d t)$ obeys the equation

$$\ddot{q} + \frac{\omega_0}{Q_{tot}}\dot{q} + \omega_0^2 q + \frac{p\dot{q}^2\ddot{q}}{2I_0^2} = \frac{V_0}{R_0}\sqrt{\frac{2}{Q_e Z_c}}\omega_d \cos(\omega_d t) + \dot{i_n}, \tag{A.5}$$

where i_n is a white noise source with spectral density $S_{i_n}(\omega) = 4k_B T/R_{eq}$ and temperature $T = \hbar\omega_d/2k_B$. Writing the charge on the capacitance as $q(t) = Q(t)\cos(\omega_d t + \varphi)$ with $Q(t)$ a slowly varying envelope, and using the reduced variable and parameters already mentionned in Section 2.2.3.3 and in

[103], i.e.

$$\begin{cases} u(t) & = \sqrt{\frac{pQ_{tot}}{2\Omega}}\frac{\omega_d}{I_0}Q(t) \\ \beta & = \left(\frac{V_0}{\varphi\omega_d}\right)^2\left(\frac{pQ_e}{2\Omega}\right)^3 \\ \Omega & = 2Q_{tot}\frac{\omega_d-\omega_0}{\omega_0} \\ \tau & = t(\omega_0-\omega_d) \end{cases}, \tag{A.6}$$

the equation of motion of the slow charge envelope reads

$$\frac{du}{d\tau} = -\frac{u}{\Omega} - ju\left(|u|^2-1\right) - j\sqrt{\beta} + \eta_x + j\eta_y, \tag{A.7}$$

where the noise source i_n is replaced by an in-phase and in-quadrature independant gaussian noise sources η_x and η_y with variance 1 and quadratic average $\frac{Z_c e^2 p^3}{16\hbar(1-\omega_d/\omega_0)^2}\frac{1}{Q_{tot}}\frac{2k_BT}{\hbar\omega_r}$. The reduce charge u is related to the internal number of photons in the resonator by $n = \frac{\hbar|\Omega|}{p^3e^2Z_cQ_{tot}}|u|^2$. Equation A.7 is then stepwised integrated with a compiled C program using finite differences of the real and imaginary parts of u.

A.3 Simulations

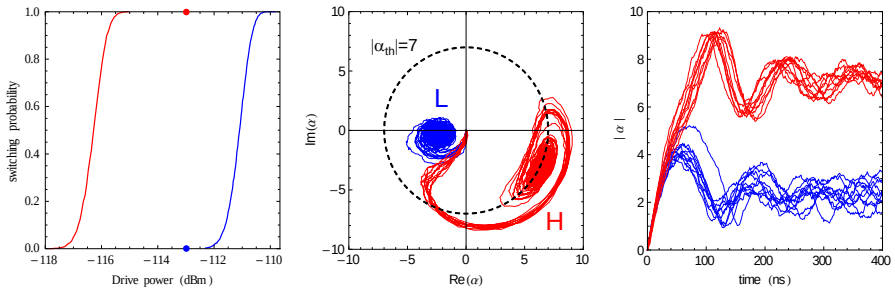

Figure A.2: Simulated trajectories of the resonator field α for non-switching (qubit in $|g\rangle$, blue) and switching (qubit in $|e\rangle$, red), in the complex plane (center) and as a function of time (right). The reduced parameters are $\{Z_c = 36\,\Omega,\ Q_{tot} = Q_e = 2500,\ f_0 = 7.75\,\text{GHz}\}$ and the driving parameters are $\Omega_g = -8.08$, $\beta_g = 0.076$ for the qubit in $|g\rangle$ and $\Omega_e = -5.8$, $\beta_e = 0.205$ for the qubit in $|e\rangle$, corresponding to the optimal readout used in Section 5.4 (left)

Figure A.2 presents the trajectories corresponding to the optimal readout point from Section 5.4, for the same absolute driving amplitude of $P_{inc} \approx -113\,\text{dBm}$, and the two detunings corresponding to the qubit in its ground and excited state $\beta = \{0.076,\ 0.205\}_{\{|g\rangle,|e\rangle\}}$. We see two sets of trajectories ending in (non-switching) L and (switching) H states; that are fully correlated to the qubit state because of the large switching curves separation.

The typical time taken by the sytem to "decide" to switch or not is below 100 ns in this case (note however that for some very rare trajectories (not shown) this 'decision' can take up to 300 ns). Given the experimentally observed good mapping of the qubit state to the switching/non-switching of the JBA, the 100 ns time before switching gives an upper bound for the qubit readout time by a JBA. As far as the qubit projection is concerned, this readout is thus as fast as a readout based on a linear resonator followed by a quantum limited amplifier.

A threshold $|\alpha_{th}|$ shown by the dashed circle of Fig. A.2 is then chosen to discriminate the switching and non-switching events. The threshold choice is made to stop the simulation as soon as the switching trajectory crosses it, which limits the simulation time (10,000 full trajectories takes approximately 10 seconds on a work station).

To produce a switching curve, we then simulate 10,000 trajectories that we stop if the threshold is crossed, for many different values of the drive amplitude in the relevant switching range. To simulate the effect of the dispersive shift due to the qubit, the drive frequency is simply changed from $\omega_d - \chi$ to $\omega_d + \chi$. We obtain the switching curves on Fig. A.3 (left) and convert them to absolute units of drive amplitude using

$$P_{inc} = \frac{\beta \left(1 - (\omega_d/\omega_0)^2\right)^3 Q_e \hbar^2 \omega_0^2}{2p^3 e^2 Z_c} \tag{A.8}$$

.

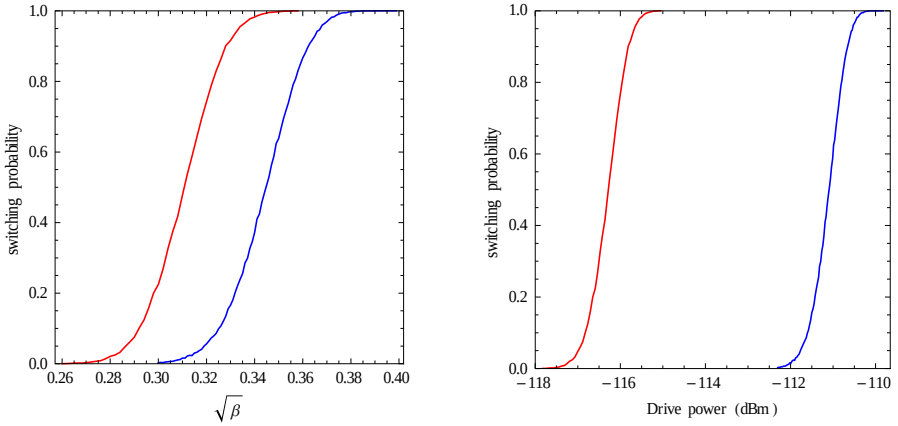

Figure A.3: Simulated switching probabilities for parameters corresponding to the experiment of Section 5.4 (mentionned in Fig. A.2). The blue (red) curve correspond to qubit state $|g\rangle$ ($|e\rangle$). Results are shown in reduced (left) and absolute (right) drive amplitude units.

The switching curves in reduced unit happens to strongly overlap whereas

those in absolute units are very well separated. This indicates that the discrimination of the two qubit states is mainly due to the change of $\Omega \sim 1-(\omega_d/\omega_0)^2$.

Comparison of experimental data with simulations

We show on Fig. A.4 the comparison between the experimentally measured switching curves with the simulated curves.

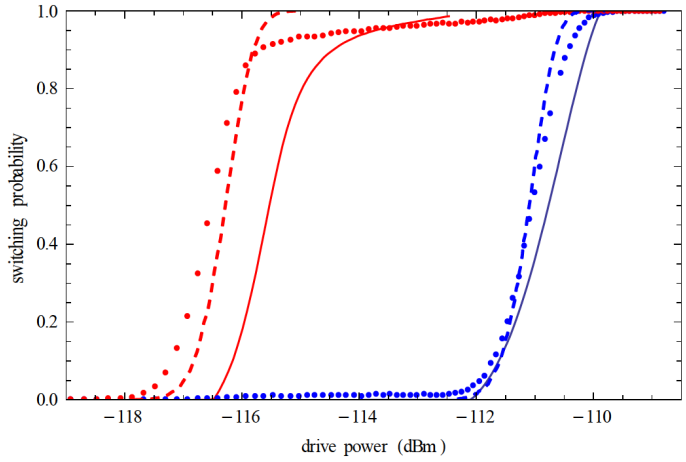

Figure A.4: Switching curves for the qubit in its ground (blue) and excited (red) state; experimental data points (dots), semi-classical simulation (dashed) and full quantum simulation (solid) including T_1 and T_2 decoherence times.

First, the curves from the semi-classical simulations agree well with the experimental data in term of slope and separation. Obviously, it does not reproduce the slow increase between 0.9 and 1 coming from relaxation, widely discussed in Chapter 5. The curves coming from the full quantum simulations from A. Blais et al. approximately agree with the data in term of slope and separations, but shows a similar but not quantitative shoulder on the switching curve from the qubit in its excited state.

These agreements indicates that the semi-classical theory with an effective temperature $T = \hbar\omega/2k_B$ is correct, and that the complex full quantum simulation needs to be futher investigated to perfectly describe the switching curves.

Bibliography

[1] Alain Aspect, Philippe Grangier, and Gerard Roger. Experimental Realization of Einstein-Podolsky-Rosen-Bohm Gedankenexperiment: A New Violation of Bell's Inequalities. *Physical Review Letters*, 49(2):91, 1982.

[2] J.S. Bell. On the Einstein-Podolsky-Rosen paradox. *Physics*, 1(3):195–200, 1964.

[3] Charles H. Bennett, Gilles Brassard, Seth Breidbart, and Stephen Wiesner. Quantum Cryptography, or Unforgeable Subway Tokens. In David Chaum, Ronald L. Rivest, and Alan T. Sherman, editors, *Advances in Cryptology*, pages 267–275. Springer US, Boston, MA, 1983.

[4] Charles H. Bennett, Gilles Brassard, and N. David Mermin. Quantum cryptography without Bell s theorem. *Physical Review Letters*, 68(5):557–559, February 1992.

[5] Richard P. Feynman. Simulating physics with computers. *International Journal of Theoretical Physics*, 21(6-7):467–488, June 1982.

[6] D. Deutsch. Quantum Theory, the Church-Turing Principle and the Universal Quantum Computer. *Proceedings of the Royal Society of London. A. Mathematical and Physical Sciences*, 400(1818):97–117, 1985.

[7] Peter W. Shor. Polynomial-Time Algorithms for Prime Factorization and Discrete Logarithms on a Quantum Computer. *SIAM Journal on Computing*, 26(5):1484–1509, October 1997.

[8] Michael A Nielsen, Author, Isaac Chuang, Author, Lov K Grover, and Reviewer. Quantum Computation and Quantum Information. *American Journal of Physics*, 70(5):558–559, 2002.

[9] David P Divincenzo. The Physical Implementation of Quantum Computation. *Fortschritte der Physik*, 48:771–783, 2000.

[10] Robert Raussendorf and Hans J. Briegel. A One-Way Quantum Computer. *Physical Review Letters*, 86(22):5188–5191, May 2001.

[11] E. Farhi, J. Goldstone, S. Gutmann, J. Lapan, A. Lundgren, and D. Preda. A Quantum Adiabatic Evolution Algorithm Applied to Random Instances of an NP-Complete Problem. *Science*, 292(5516):472–475, April 2001.

[12] Sergio Boixo, Troels F. RÃžnnow, Sergei V. Isakov, Zhihui Wang, David Wecker, Daniel A. Lidar, John M. Martinis, and Matthias Troyer. Evidence for quantum annealing with more than one hundred qubits. *Nature Physics*, 10(3):218–224, February 2014.

[13] V. M. Acosta, E. Bauch, M. P. Ledbetter, C. Santori, K.-M. C. Fu, P. E. Barclay, R. G. Beausoleil, H. Linget, J. F. Roch, F. Treussart, S. Chemerisov, W. Gawlik, and D. Budker. Diamonds with a high density of nitrogen-vacancy centers for magnetometry applications. *Physical Review B*, 80(11):115202, 2009.

[14] J. Stajic. The Future of Quantum Information Processing. *Science*, 339(6124):1163–1163, March 2013.

[15] B. P. Lanyon, C. Hempel, D. Nigg, M. Muller, R. Gerritsma, F. Zahringer, P. Schindler, J. T. Barreiro, M. Rambach, G. Kirchmair, M. Hennrich, P. Zoller, R. Blatt, and C. F. Roos. Universal Digital Quantum Simulation with Trapped Ions. *Science*, 334(6052):57–61, October 2011.

[16] Y. Nakamura, Yu. A Pashkin, and J. S Tsai. Coherent control of macroscopic quantum states in a single-Cooper-pair box. *Nature*, 398(6730):786–788, 1999.

[17] M. H. Devoret and R. J. Schoelkopf. Superconducting Circuits for Quantum Information: An Outlook. *Science*, 339(6124):1169–1174, March 2013.

[18] Alexandre Blais, Ren-Shou Huang, Andreas Wallraff, S. M Girvin, and R. J Schoelkopf. Cavity quantum electrodynamics for superconducting electrical circuits: An architecture for quantum computation. *Physical Review A*, 69:62320, 2004.

[19] A. Wallraff, D. I Schuster, A. Blais, L. Frunzio, R. S Huang, J. Majer, S. Kumar, S. M Girvin, and R. J Schoelkopf. Strong coupling of a single photon to a superconducting qubit using circuit quantum electrodynamics. *Nature*, 431(7005):162–167, 2004.

[20] S. Haroche and J. M Raimond. *Exploring the quantum*. Oxford University Press, August 2006.

[21] Jens Koch, Terri M Yu, Jay Gambetta, A. A Houck, D. I Schuster, J. Majer, Alexandre Blais, M. H Devoret, S. M Girvin, and R. J Schoelkopf. Charge-insensitive qubit design derived from the Cooper pair box. *Physical Review A*, 76:42319, October 2007.

[22] Francois Mallet, Florian R Ong, Agustin Palacios-Laloy, Francois Nguyen, Patrice Bertet, Denis Vion, and Daniel Esteve. Single-shot qubit readout in circuit quantum electrodynamics. *Nature Physics*, 5(11):791–795, November 2009.

[23] I. Siddiqi, R. Vijay, M. Metcalfe, E. Boaknin, L. Frunzio, R. J Schoelkopf, and M. H Devoret. Dispersive measurements of superconducting qubit coherence with a fast latching readout. *Physical Review B*, 73(5):054510, 2006.

[24] L. DiCarlo, J. M. Chow, J. M. Gambetta, Lev S. Bishop, B. R. Johnson, D. I. Schuster, J. Majer, A. Blais, L. Frunzio, S. M. Girvin, and R. J. Schoelkopf. Demonstration of two-qubit algorithms with a superconducting quantum processor. *Nature*, 460(7252):240–244, July 2009.

[25] T. Yamamoto, M. Neeley, E. Lucero, R. C. Bialczak, J. Kelly, M. Lenander, Matteo Mariantoni, A. D. O Connell, D. Sank, H. Wang, M. Weides, J. Wenner, Y. Yin, A. N. Cleland, and John M. Martinis. Quantum process tomography of two-qubit controlled-Z and controlled-NOT gates using superconducting phase qubits. *Physical Review B*, 82(18), November 2010.

[26] Andreas Dewes, Romain Lauro, Florian R. Ong, Vivient Schmitt, Perola Milman, Patrice Bertet, Denis Vion, and Daniel Esteve. Quantum speeding-up of computation demonstrated in a superconducting two-qubit processor. *Physical Review B*, 85(14), April 2012.

[27] A. Dewes. *Demonstrating Quantum Speed-Up with a Two-Transmon Quantum Processor, Ph.D. Thesis*. PhD thesis, UniversitÃ© Pierre et Marie Curie, Paris, France, Quantronics Group, CEA Saclay, 2012.

[28] A. Dewes, F. R. Ong, V. Schmitt, R. Lauro, N. Boulant, P. Bertet, D. Vion, and D. Esteve. Characterization of a Two-Transmon Processor with Individual Single-Shot Qubit Readout. *Physical Review Letters*, 108(5):057002, 2012.

[29] B. D Josephson. Possible new effects in superconductive tunnelling. *Phys. Lett.*, 1:251, 1962.

[30] V. Bouchiat, D. Vion, P. Joyez, D. Esteve, and M. H. Devoret. Quantum Coherence with a Single Cooper Pair. *Physica Scripta*, T76(1):165, 1998.

[31] Audrey Cottet. *Implementation of a quantum bit in a superconducting circuit*. PhD thesis, Universite Paris 6, 2002.

[32] D. Vion. Manipulating the Quantum State of an Electrical Circuit. *Science*, 296(5569):886–889, May 2002.

[33] J. M Raimond, M. Brune, and S. Haroche. Manipulating quantum entanglement with atoms and photons in a cavity. *Reviews of Modern Physics*, 73(3):565, 2001.

[34] Hanhee Paik, D. I. Schuster, Lev S. Bishop, G. Kirchmair, G. Catelani, A. P. Sears, B. R. Johnson, M. J. Reagor, L. Frunzio, L. I. Glazman, S. M. Girvin, M. H. Devoret, and R. J. Schoelkopf. Observation of High Coherence in Josephson Junction Qubits Measured in a Three-Dimensional Circuit QED Architecture. *Phys. Rev. Lett.*, 107(24):240501, December 2011.

[35] Christopher Bauer, Ray Freeman, Tom Frenkiel, James Keeler, and A.J. Shaka. Gaussian pulses. *Journal of Magnetic Resonance (1969)*, 58(3):442–457, July 1984.

[36] R. Barends, J. Kelly, A. Megrant, A. Veitia, D. Sank, E. Jeffrey, T. C. White, J. Mutus, A. G. Fowler, B. Campbell, Y. Chen, Z. Chen, B. Chiaro, A. Dunsworth, C. Neill, P. O Malley, P. Roushan, A. Vainsencher, J. Wenner, A. N. Korotkov, A. N. Cleland, and John M. Martinis. Superconducting quantum circuits at the surface code threshold for fault tolerance. *Nature*, 508(7497):500–503, April 2014.

[37] F. Motzoi, J. Gambetta, P. Rebentrost, and F. Wilhelm. Simple Pulses for Elimination of Leakage in Weakly Nonlinear Qubits. *Physical Review Letters*, 103(11), September 2009.

[38] J. M. Martinis and A. Megrant. UCSB final report for the CSQ program: Review of decoherence and materials physics for superconducting qubits. *arXiv:1410.5793 [quant-ph].*

[39] Jurgen Lisenfeld, Grigorij J. Grabovskij, Clemens Muller, Jared H. Cole, Georg Weiss, and Alexey V. Ustinov. Observation of directly interacting coherent two-level systems in an amorphous material. *Nature Communications*, 6:6182, February 2015.

[40] Jiansong Gao, Miguel Daal, Anastasios Vayonakis, Shwetank Kumar, Jonas Zmuidzinas, Bernard Sadoulet, Benjamin A. Mazin, Peter K. Day, and Henry G. Leduc. Experimental evidence for a surface distribution of two-level systems in superconducting lithographed microwave resonators. *Applied Physics Letters*, 92(15):152505, 2008.

[41] R. Barends, J. Kelly, A. Megrant, D. Sank, E. Jeffrey, Y. Chen, Y. Yin, B. Chiaro, J. Mutus, C. Neill, P. O Malley, P. Roushan, J. Wenner, T. C. White, A. N. Cleland, and John M. Martinis. Coherent Josephson Qubit Suitable for Scalable Quantum Integrated Circuits. *Physical Review Letters*, 111(8), August 2013.

[42] John M. Martinis, K. B. Cooper, R. McDermott, Matthias Steffen, Markus Ansmann, K. D. Osborn, K. Cicak, Seongshik Oh, D. P. Pappas,

R. W. Simmonds, and Clare C. Yu. Decoherence in Josephson Qubits from Dielectric Loss. *Physical Review Letters*, 95(21):210503, November 2005.

[43] J. Wenner, Yi Yin, Erik Lucero, R. Barends, Yu Chen, B. Chiaro, J. Kelly, M. Lenander, Matteo Mariantoni, A. Megrant, C. Neill, P. J. J. O Malley, D. Sank, A. Vainsencher, H. Wang, T. C. White, A. N. Cleland, and John M. Martinis. Excitation of Superconducting Qubits from Hot Nonequilibrium Quasiparticles. *Physical Review Letters*, 110(15), April 2013.

[44] A. Palacios-Laloy. *Superconducting qubit in a resonator: test of the Leggett-Garg inequality and single-shot readout, Ph.D. Thesis*. PhD thesis, 2010.

[45] M. Metcalfe, E. Boaknin, V. Manucharyan, R. Vijay, I. Siddiqi, C. Rigetti, L. Frunzio, R. J. Schoelkopf, and M. H. Devoret. Measuring the decoherence of a quantronium qubit with the cavity bifurcation amplifier. *Physical Review B*, 76(17):174516, November 2007.

[46] R. Vijay, M. H. Devoret, and I. Siddiqi. Invited Review Article: The Josephson bifurcation amplifier. *Review of Scientific Instruments*, 80(11):111101–111101–17, November 2009.

[47] I. Siddiqi, R. Vijay, F. Pierre, C. M Wilson, L. Frunzio, M. Metcalfe, C. Rigetti, R. J Schoelkopf, M. H Devoret, D. Vion, and D. Esteve. Direct Observation of Dynamical Bifurcation between Two Driven Oscillation States of a Josephson Junction. *Physical Review Letters*, 94(2):027005, January 2005.

[48] M. I. Dykman and M. A. Krivoglaz. Theory of fluctuational transitions between stable states of a nonlinear oscillator. *Soviet Journal of Experimental and Theoretical Physics*, 50:30, 1979.

[49] E. M Purcell, H. C Torrey, and R. V Pound. Resonance Absorption by Nuclear Magnetic Moments in a Solid. *Physical Review*, 69(1-2):37, January 1946.

[50] P. Bertet, I. Chiorescu, G. Burkard, K. Semba, C. J. P. M. Harmans, D. P. DiVincenzo, and J. E. Mooij. Dephasing of a Superconducting Qubit Induced by Photon Noise. *Physical Review Letters*, 95(25):257002, 2005.

[51] Chad Rigetti, Jay M. Gambetta, Stefano Poletto, B. L. T. Plourde, Jerry M. Chow, A. D. Corcoles, John A. Smolin, Seth T. Merkel, J. R. Rozen, George A. Keefe, Mary B. Rothwell, Mark B. Ketchen, and M. Steffen. Superconducting qubit in a waveguide cavity with a coherence time approaching 0.1 ms. *Physical Review B*, 86(10), September 2012.

[52] D. I. Schuster, A. Wallraff, A. Blais, L. Frunzio, R.-S. Huang, J. Majer, S. M. Girvin, and R. J. Schoelkopf. ac Stark Shift and Dephasing of a Superconducting Qubit Strongly Coupled to a Cavity Field. *Physical Review Letters*, 94(12):123602, March 2005.

[53] Matthias Steffen, M. Ansmann, Radoslaw C Bialczak, N. Katz, Erik Lucero, R. McDermott, Matthew Neeley, E. M Weig, A. N Cleland, and John M Martinis. Measurement of the Entanglement of Two Superconducting Qubits via State Tomography. *Science*, 313(5792):1423–1425, September 2006.

[54] J. F. Poyatos, J. I. Cirac, and P. Zoller. Complete Characterization of a Quantum Process: The Two-Bit Quantum Gate. *Physical Review Letters*, 78(2):390–393, January 1997.

[55] A. D. Corcoles, Jay M. Gambetta, Jerry M. Chow, John A. Smolin, Matthew Ware, Joel Strand, B. L. T. Plourde, and M. Steffen. Process verification of two-qubit quantum gates by randomized benchmarking. *Physical Review A*, 87(3), March 2013.

[56] G. J. Grabovskij, T. Peichl, J. Lisenfeld, G. Weiss, and A. V. Ustinov. Strain Tuning of Individual Atomic Tunneling Systems Detected by a Superconducting Qubit. *Science*, 338(6104):232–234, October 2012.

[57] Easwar Magesan, J. M. Gambetta, and Joseph Emerson. Scalable and Robust Randomized Benchmarking of Quantum Processes. *Physical Review Letters*, 106(18), May 2011.

[58] Lov K. Grover. A fast quantum mechanical algorithm for database search. pages 212–219, 1996.

[59] Erik Lucero, R. Barends, Y. Chen, J. Kelly, M. Mariantoni, A. Megrant, P. O Malley, D. Sank, A. Vainsencher, J. Wenner, T. White, Y. Yin, A. N. Cleland, and John M. Martinis. Computing prime factors with a Josephson phase qubit quantum processor. *Nature Physics*, 8(10):719–723, August 2012.

[60] J. Majer, J. M Chow, J. M Gambetta, Jens Koch, B. R Johnson, J. A Schreier, L. Frunzio, D. I Schuster, A. A Houck, A. Wallraff, A. Blais, M. H Devoret, S. M Girvin, and R. J Schoelkopf. Coupling superconducting qubits via a cavity bus. *Nature*, 449(7161):443–447, 2007.

[61] M. Jerger, S. Poletto, P. Macha, U. Hubner, A. Lukashenko, E. Il'ichev, and A. V. Ustinov. Readout of a qubit array via a single transmission line. *EPL (Europhysics Letters)*, 96(4):40012, November 2011.

[62] J. M. Gambetta, F. Motzoi, S. T. Merkel, and F. K. Wilhelm. Analytic control methods for high-fidelity unitary operations in a weakly nonlinear oscillator. *Physical Review A*, 83(1), January 2011.

[63] J. M. Chow, L. DiCarlo, J. M. Gambetta, F. Motzoi, L. Frunzio, S. M. Girvin, and R. J. Schoelkopf. Optimized driving of superconducting artificial atoms for improved single-qubit gates. *Physical Review A*, 82(4), October 2010.

[64] J. Kelly, R. Barends, A. G. Fowler, A. Megrant, E. Jeffrey, T. C. White, D. Sank, J. Y. Mutus, B. Campbell, Yu Chen, Z. Chen, B. Chiaro, A. Dunsworth, I.-C. Hoi, C. Neill, P. J. J. O Malley, C. Quintana, P. Roushan, A. Vainsencher, J. Wenner, A. N. Cleland, and John M. Martinis. State preservation by repetitive error detection in a superconducting quantum circuit. *Nature*, 519(7541):66–69, March 2015.

[65] L. DiCarlo, M. D. Reed, L. Sun, B. R. Johnson, J. M. Chow, J. M. Gambetta, L. Frunzio, S. M. Girvin, M. H. Devoret, and R. J. Schoelkopf. Preparation and measurement of three-qubit entanglement in a superconducting circuit. *Nature*, 467(7315):574–578, 2010.

[66] Yu Chen, D. Sank, P. O Malley, T. White, R. Barends, B. Chiaro, J. Kelly, E. Lucero, M. Mariantoni, A. Megrant, C. Neill, A. Vainsencher, J. Wenner, Y. Yin, A. N. Cleland, and John M. Martinis. Multiplexed dispersive readout of superconducting phase qubits. *Applied Physics Letters*, 101(18):182601, 2012.

[67] T. C. White, J. Y. Mutus, I.-C. Hoi, R. Barends, B. Campbell, Yu Chen, Z. Chen, B. Chiaro, A. Dunsworth, E. Jeffrey, J. Kelly, A. Megrant, C. Neill, P. J. J. O Malley, P. Roushan, D. Sank, A. Vainsencher, J. Wenner, S. Chaudhuri, J. Gao, and John M. Martinis. Traveling wave parametric amplifier with Josephson junctions using minimal resonator phase matching. *Applied Physics Letters*, 106(24):242601, June 2015.

[68] J. Y. Mutus, T. C. White, R. Barends, Yu Chen, Z. Chen, B. Chiaro, A. Dunsworth, E. Jeffrey, J. Kelly, A. Megrant, C. Neill, P. J. J. O Malley, P. Roushan, D. Sank, A. Vainsencher, J. Wenner, K. M. Sundqvist, A. N. Cleland, and John M. Martinis. Strong environmental coupling in a Josephson parametric amplifier. *Applied Physics Letters*, 104(26):263513, June 2014.

[69] Maxime Boissonneault, J. M. Gambetta, and A. Blais. Improved qubit bifurcation readout in the straddling regime of circuit QED. *Physical Review A*, 86(2), August 2012.

[70] Zijun Chen, A. Megrant, J. Kelly, R. Barends, J. Bochmann, Yu Chen, B. Chiaro, A. Dunsworth, E. Jeffrey, J. Y. Mutus, P. J. J. O'Malley, C. Neill, P. Roushan, D. Sank, A. Vainsencher, J. Wenner, T. C. White, A. N. Cleland, and John M. Martinis. Fabrication and characterization of aluminum airbridges for superconducting microwave circuits. *Applied Physics Letters*, 104(5):052602, February 2014.

[71] Simon E. Nigg, Hanhee Paik, Brian Vlastakis, Gerhard Kirchmair, S. Shankar, Luigi Frunzio, M. H. Devoret, R. J. Schoelkopf, and S. M. Girvin. Black-Box Superconducting Circuit Quantization. *Physical Review Letters*, 108(24), June 2012.

[72] L. Frunzio, A. Wallraff, D. Schuster, J. Majer, and R. Schoelkopf. Fabrication and characterization of superconducting circuit QED devices for quantum computation. *Applied Superconductivity, IEEE Transactions on*, 15(2):860–863, 2005.

[73] T. A. Fulton and G. J. Dolan. Observation of single-electron charging effects in small tunnel junctions. *Physical Review Letters*, 59(1):109–112, July 1987.

[74] A. Bruno. Private communication, TU Delft.

[75] C. M. Quintana, A. Megrant, Z. Chen, A. Dunsworth, B. Chiaro, R. Barends, B. Campbell, Yu Chen, I.-C. Hoi, E. Jeffrey, J. Kelly, J. Y. Mutus, P. J. J. O'Malley, C. Neill, P. Roushan, D. Sank, A. Vainsencher, J. Wenner, T. C. White, A. N. Cleland, and John M. Martinis. Characterization and reduction of microfabrication-induced decoherence in superconducting quantum circuits. *Applied Physics Letters*, 105(6):062601, August 2014.

[76] Maxime Boissonneault, J. M. Gambetta, and Alexandre Blais. Nonlinear dispersive regime of cavity QED: The dressed dephasing model. *Physical Review A*, 77(6):060305, 2008.

[77] R. Schutjens, F. Abu Dagga, D. J. Egger, and F. K. Wilhelm. Single-qubit gates in frequency-crowded transmon systems. *Physical Review A*, 88(5), November 2013.

[78] E. Jeffrey, D. Sank, J.Y. Mutus, T.C. White, J. Kelly, R. Barends, Y. Chen, Z. Chen, B. Chiaro, A. Dunsworth, A. Megrant, P.J.J. O Malley, C. Neill, P. Roushan, A. Vainsencher, J. Wenner, A.N. Cleland, and John M. Martinis. Fast Accurate State Measurement with Superconducting Qubits. *Physical Review Letters*, 112(19), May 2014.

[79] J.M. Chow. *Quantum Information Processing with Superconducting Qubits*. PhD thesis, Yale University, 2010.

[80] J.R. Johansson, P.D. Nation, and Franco Nori. QuTiP 2: A Python framework for the dynamics of open quantum systems. *Computer Physics Communications*, 184(4):1234–1240, April 2013.

[81] D. Riste, S. Poletto, M.-Z. Huang, A. Bruno, V. Vesterinen, O.-P. Saira, and L. DiCarlo. Detecting bit-flip errors in a logical qubit using stabilizer measurements. *Nature Communications*, 6:6983, April 2015.

[82] R. Barends, J. Wenner, M. Lenander, Y. Chen, R. C. Bialczak, J. Kelly, E. Lucero, P. O Malley, M. Mariantoni, D. Sank, H. Wang, T. C. White, Y. Yin, J. Zhao, A. N. Cleland, John M. Martinis, and J. J. A. Baselmans. Minimizing quasiparticle generation from stray infrared light in superconducting quantum circuits. *Applied Physics Letters*, 99(11):113507, 2011.

[83] Kevin O Brien, Chris Macklin, Irfan Siddiqi, and Xiang Zhang. Resonant Phase Matching of Josephson Junction Traveling Wave Parametric Amplifiers. *Physical Review Letters*, 113(15), October 2014.

[84] A. O. Niskanen, K. Harrabi, F. Yoshihara, Y. Nakamura, S. Lloyd, and J. S. Tsai. Quantum Coherent Tunable Coupling of Superconducting Qubits. *Science*, 316(5825):723–726, May 2007.

[85] R. C. Bialczak, M. Ansmann, M. Hofheinz, M. Lenander, E. Lucero, M. Neeley, A. D. O Connell, D. Sank, H. Wang, M. Weides, J. Wenner, T. Yamamoto, A. N. Cleland, and J. M. Martinis. Fast Tunable Coupler for Superconducting Qubits. *Physical Review Letters*, 106(6), February 2011.

[86] Jerry M. Chow, Jay M. Gambetta, Easwar Magesan, David W. Abraham, Andrew W. Cross, B R Johnson, Nicholas A. Masluk, Colm A. Ryan, John A. Smolin, Srikanth J. Srinivasan, and M Steffen. Implementing a strand of a scalable fault-tolerant quantum computing fabric. *Nature Communications*, 5, June 2014.

[87] Austin G. Fowler, Matteo Mariantoni, John M. Martinis, and Andrew N. Cleland. Surface codes: Towards practical large-scale quantum computation. *Physical Review A*, 86(3), September 2012.

[88] Mazyar Mirrahimi, Zaki Leghtas, Victor V Albert, Steven Touzard, Robert J Schoelkopf, Liang Jiang, and Michel H Devoret. Dynamically protected cat-qubits: a new paradigm for universal quantum computation. *New Journal of Physics*, 16(4):045014, April 2014.

[89] Z. Leghtas, S. Touzard, I. M. Pop, A. Kou, B. Vlastakis, A. Petrenko, K. M. Sliwa, A. Narla, S. Shankar, M. J. Hatridge, M. Reagor, L. Frunzio, R. J. Schoelkopf, M. Mirrahimi, and M. H. Devoret. Confining the state of light to a quantum manifold by engineered two-photon loss. *Science*, 347(6224):853–857, February 2015.

[90] Y. Kubo, C. Grezes, A. Dewes, T. Umeda, J. Isoya, H. Sumiya, N. Morishita, H. Abe, S. Onoda, T. Ohshima, V. Jacques, A. Dreau, J.-F. Roch, I. Diniz, A. Auffeves, D. Vion, D. Esteve, and P. Bertet. Hybrid Quantum Circuit with a Superconducting Qubit Coupled to a Spin Ensemble. *Physical Review Letters*, 107(22):220501, November 2011.

[91] Brian Julsgaard, Cecile Grezes, Patrice Bertet, and Klaus Molmer. Quantum Memory for Microwave Photons in an Inhomogeneously Broadened Spin Ensemble. *Physical Review Letters*, 110(25), June 2013.

[92] C. Grezes, B. Julsgaard, Y. Kubo, M. Stern, T. Umeda, J. Isoya, H. Sumiya, H. Abe, S. Onoda, T. Ohshima, V. Jacques, J. Esteve, D. Vion, D. Esteve, K. Molmer, and P. Bertet. Multimode Storage and Retrieval of Microwave Fields in a Spin Ensemble. *Physical Review X*, 4(2), June 2014.

[93] W. Pfaff, B. J. Hensen, H. Bernien, S. B. van Dam, M. S. Blok, T. H. Taminiau, M. J. Tiggelman, R. N. Schouten, M. Markham, D. J. Twitchen, and R. Hanson. Unconditional quantum teleportation between distant solid-state quantum bits. *Science*, 345(6196):532–535, August 2014.

[94] Guilherme Tosi, Fahd A. Mohiyaddin, Hans Huebl, and Andrea Morello. Circuit-quantum electrodynamics with direct magnetic coupling to single-atom spin qubits in isotopically enriched 28si. *AIP Advances*, 4(8):087122, August 2014.

[95] Juha T. Muhonen, Juan P. Dehollain, Arne Laucht, Fay E. Hudson, Rachpon Kalra, Takeharu Sekiguchi, Kohei M. Itoh, David N. Jamieson, Jeffrey C. McCallum, Andrew S. Dzurak, and Andrea Morello. Storing quantum information for 30 seconds in a nanoelectronic device. *Nature Nanotechnology*, 9(12):986–991, October 2014.

[96] Jarryd J. Pla, Fahd A. Mohiyaddin, Kuan Y. Tan, Juan P. Dehollain, Rajib Rahman, Gerhard Klimeck, David N. Jamieson, Andrew S. Dzurak, and Andrea Morello. Coherent Control of a Single Si 29 Nuclear Spin Qubit. *Physical Review Letters*, 113(24), December 2014.

[97] K. W. Murch, S. J. Weber, C. Macklin, and I. Siddiqi. Observing single quantum trajectories of a superconducting quantum bit. *Nature*, 502(7470):211–214, October 2013.

[98] P. Campagne-Ibarcq. *Measurement backaction and feedback on a superconducting qubit.* PhD thesis, 2015.

[99] P. Bertet. Private communication, Quantronics.

[100] M. Marthaler and M. I Dykman. Switching via quantum activation: A parametrically modulated oscillator. *Physical Review A*, 73(4):042108, 2006.

[101] I. Serban, M. I. Dykman, and F. K. Wilhelm. Relaxation of a qubit measured by a driven Duffing oscillator. *Physical Review A*, 81(2):022305, 2010.

[102] Maxime Boissonneault, A. C. Doherty, F. R. Ong, P. Bertet, D. Vion, D. Esteve, and A. Blais. Back-action of a driven nonlinear resonator on a superconducting qubit. *Physical Review A*, 85(2):022305, 2012.

[103] Michael Metcalfe. *A new microwave readout for superconducting qubits.* PhD thesis, Yale University, 2008.

Publications

- *Characterization of a Two-Transmon Processor with Individual Single-Shot Qubit Readout*
  A. Dewes, F. R. Ong, V. Schmitt, R. Lauro, N. Boulant, P. Bertet, D. Vion, and D. Esteve
  Phys. Rev. Lett. 108, 057002 – Published 2 February 2012

- *Quantum speeding-up of computation demonstrated in a superconducting two-qubit processor*
  A. Dewes, R. Lauro, F. R. Ong, V. Schmitt, P. Milman, P. Bertet, D. Vion, and D. Esteve
  Phys. Rev. B 85, 140503(R) – Published 5 April 2012

- *High-gain weakly nonlinear flux-modulated Josephson parametric amplifier using a SQUID array*
  X. Zhou, V. Schmitt, P. Bertet, D. Vion, W. Wustmann, V. Shumeiko, and D. Esteve
  Phys. Rev. B 89, 214517 – Published 30 June 2014

- *Multiplexed readout of transmon qubits with Josephson bifurcation amplifiers*
  V. Schmitt, X. Zhou, K. Juliusson, B. Royer, A. Blais, P. Bertet, D. Vion, and D. Esteve
  Phys. Rev. A 90, 062333 – Published 22 December 2014

Characterization of a Two-Transmon Processor with Individual Single-Shot Qubit Readout

A. Dewes,[1] F. R. Ong,[1] V. Schmitt,[1] R. Lauro,[1] N. Boulant,[2] P. Bertet,[1] D. Vion,[1] and D. Esteve[1]
[1]Quantronics group, Service de Physique de l'État Condensé (CNRS URA 2464), IRAMIS, DSM, CEA-Saclay, 91191 Gif-sur-Yvette, France
[2]LRMN, Neurospin, I2BM, DSV, 91191CEA-Saclay, 91191 Gif-sur-Yvette, France
(Received 26 September 2011; published 2 February 2012)

We report the characterization of a two-qubit processor implemented with two capacitively coupled tunable superconducting qubits of the transmon type, each qubit having its own nondestructive single-shot readout. The fixed capacitive coupling yields the $\sqrt{i\mathrm{SWAP}}$ two-qubit gate for a suitable interaction time. We reconstruct by state tomography the coherent dynamics of the two-bit register as a function of the interaction time, observe a violation of the Bell inequality by 22 standard deviations after correcting readout errors, and measure by quantum process tomography a gate fidelity of 90%.

DOI: 10.1103/PhysRevLett.108.057002 PACS numbers: 85.25.Cp, 03.67.Lx, 74.78.Na

Quantum-information processing is one of the most appealing ideas for exploiting the resources of quantum physics and performing tasks beyond the reach of classical machines [1]. Ideally, a quantum processor consists of an ensemble of highly coherent two-level systems, the qubits, that can be efficiently reset, that can follow any unitary evolution needed by an algorithm using a universal set of single- and two-qubit gates, and that can be readout projectively. In the domain of electrical quantum circuits [2], important progress [3–7] has been achieved recently with the operation of elementary quantum processors based on different superconducting qubits. Those based on transmon qubits [3,4,8,9] are well protected against decoherence but embed all the qubits in a single resonator used both for coupling them and for joint readout. Consequently, individual readout of the qubits is not possible and the results of a calculation, as the Grover search algorithm demonstrated on two qubits [3], cannot be obtained by running the algorithm only once. Furthermore, the overhead for getting a result from such a processor without single-shot readout but with a larger number of qubits overcomes the speed-up gain expected for any useful algorithm. The situation is different for processors based on phase qubits [5,6,10], where the qubits are more sensitive to decoherence but can be read individually with high fidelity, although destructively. This significant departure from the wished scheme can be circumvented, when needed, since a destructive readout can be transformed into a nondestructive one at the cost of adding one ancilla qubit and one extra two-qubit gate for each qubit to be read projectively. Moreover, energy release during a destructive readout can result in a sizable cross talk between the readout outcomes, which can also be solved at the expense of a more complex architecture [10,11].

In this work, we operate a new architecture that comes closer to the ideal quantum processor design than the above-mentioned ones. Our circuit is based on frequency tunable transmons that are capacitively coupled. Although the coupling is fixed, the interaction is effective only when the qubits are on resonance, which yields the $\sqrt{i\mathrm{SWAP}}$ universal gate for an adequate coupling duration. Each qubit is equipped with its own nondestructive single-shot readout [12,13] and the two qubits can be read with low cross talk. In order to characterize the circuit operation, we reconstruct the time evolution of the two-qubit register density matrix during the resonant and coherent exchange of a single quantum of excitation between the qubits by quantum state tomography. Then, we prepare a Bell state with concurrence 0.85, measure the Clauser-Horne-Shimony-Holt (CHSH) entanglement witness, and find a violation of the corresponding Bell inequality by 22 standard deviations. We then characterize the $\sqrt{i\mathrm{SWAP}}$ universal gate operation by determining its process map with quantum process tomography [1]. We find a gate fidelity of 90% due to qubit decoherence and systematic unitary errors.

The circuit implemented is schematized in Fig. 1(a): the coupled qubits with their respective control and readout subcircuits are fabricated on a Si chip [see Supplemental Material (SM), Sec. I [14]]. The chip is cooled down to 20 mK in a dilution refrigerator and connected to room-temperature sources and measurement devices by attenuated and filtered control lines and by two measurement lines equipped with cryogenic amplifiers. Each transmon $j = \mathrm{I}, \mathrm{II}$ is a capacitively shunted SQUID characterized by its Coulomb energy E_C^j for a Cooper pair, the asymmetry d_j between its two Josephson junctions, and its total effective Josephson energy $E_J^j(\phi_j) = E_J^j|\cos(x_j)|\sqrt{1 + d_j^2\tan^2(x_j)}$, with $x_j = \pi\phi_j/\phi_0$, ϕ_0 the flux quantum, and ϕ_j the magnetic flux through the SQUIDs induced by two local current lines with a 0.5 GHz bandwidth. The transition frequencies $\nu_j \simeq \sqrt{2E_C^jE_J^j}/h$ between the two lowest energy states $|0\rangle_j$ and $|1\rangle_j$ can thus be tuned by ϕ_j. The qubits are coupled by a capacitor with nominal value $C_c \simeq 0.13$ fF and form a register with the Hamiltonian (see Sec. II of the SM [14])

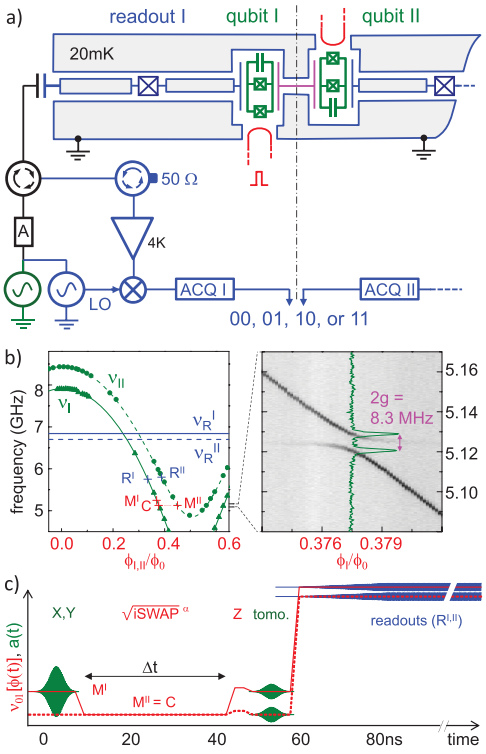

FIG. 1 (color). (a) Circuit schematics of the experiment showing the qubits I and II in green, their readout devices in grayed blue, and the homodyne detection circuits with their digitizer (ACQ) in blue. (b) Left-hand panel: Spectroscopy of the sample showing the resonator frequencies $\nu_R^{\mathrm{I}} = 6.84$ GHz and $\nu_R^{\mathrm{II}} = 6.70$ GHz (horizontal lines), and the measured (disks, triangles) and fitted (lines) qubit frequencies $\nu_{\mathrm{I,II}}$ as a function of their flux bias $\phi_{\mathrm{I,II}}$ when the other qubit is far detuned. Right-hand panel: Spectroscopic anticrossing of the two qubits revealed by the 2D plot of $p_{01} + p_{10}$ as a function of the probe frequency and of ϕ_{I}, at $\nu_{\mathrm{II}} = 5.124$ GHz. (c) Typical pulse sequence including X or Y rotations, a $\sqrt{i\mathrm{SWAP}}^{\alpha}$ gate, Z rotations, and tomographic and readout pulses. Microwave pulses $a(t)$ for qubit (green) and for readout (blue) are drawn on top of the $\nu_{\mathrm{I,II}}(\phi)$ dc pulses (red lines).

$H = h(-\nu_{\mathrm{I}}\sigma_z^{\mathrm{I}} - \nu_{\mathrm{II}}\sigma_z^{\mathrm{II}} + 2g\sigma_y^{\mathrm{I}}\sigma_y^{\mathrm{II}})/2$. Here h is the Planck constant, $\sigma_{x,y,z}$ are the Pauli operators, $2g = \sqrt{E_C^{\mathrm{I}}E_C^{\mathrm{II}}\nu_{\mathrm{I}}\nu_{\mathrm{II}}}/E_{Cc} \ll \nu_{\mathrm{I,II}}$ is the coupling frequency, and E_{Cc} the Coulomb energy of a Cooper pair on the coupling capacitor. The two-qubit gate is defined in the uncoupled basis $\{|uv\rangle\} \equiv \{|0\rangle_{\mathrm{I}}, |1\rangle_{\mathrm{I}}\} \otimes \{|0\rangle_{\mathrm{II}}, |1\rangle_{\mathrm{II}}\}$, at a working point $M_{\mathrm{I,II}}$ where the qubits are sufficiently detuned ($\nu_{\mathrm{II}} - \nu_{\mathrm{I}} \gg 2g$) to be negligibly coupled. Bringing them on resonance at a frequency ν in a time much shorter than $1/2g$ but much longer than $1/\nu$, and keeping them on resonance during a time Δt, one implements an operation $\Theta_{\mathrm{I}}\Theta_{\mathrm{II}}\sqrt{i\mathrm{SWAP}}^{(8g\Delta t)}$, which is the product of the

$$\sqrt{i\mathrm{SWAP}} = \begin{pmatrix} 1 & 0 & 0 & 0 \\ 0 & 1/\sqrt{2} & -i/\sqrt{2} & 0 \\ 0 & -i/\sqrt{2} & 1/\sqrt{2} & 0 \\ 0 & 0 & 0 & 1 \end{pmatrix}$$

gate to an adjustable power and of two single qubit phase gates $\Theta_j = \exp(i\theta_j\sigma_z^j/2)$ accounting for the dynamical phases $\theta_j = \int 2\pi(\nu - \nu_J)dt$ accumulated during the coupling. The exact $\sqrt{i\mathrm{SWAP}}$ gate can thus be obtained by choosing $\Delta t = 1/8g$ and by applying a compensation rotation Θ_j^{-1} to each qubit afterward.

For readout, each qubit is capacitively coupled to its own $\lambda/2$ coplanar waveguide resonator with frequency ν_R^j and quality factor $Q_j \simeq 700$. The frequency ν_R^j is shifted by $\pm\chi$ depending on the measured qubit state, with $\chi \simeq g_0^2/(\nu_R^j - \nu_j)$ and g_0 the qubit-resonator coupling frequency. Each resonator is made nonlinear with a Josephson junction and is operated as a Josephson bifurcation amplifier, as explained in detail in [13]: ideally, it switches from a low to a high amplitude oscillating state when qubit state $|1\rangle$ is measured. Consequently, the homodyne measurement [see Fig. 1(a)] of two microwave pulses simultaneously applied to and reflected from the two resonators yields a two-bit outcome uv that maps with a high fidelity the state $|uv\rangle$ on which the register is projected; the probabilities p_{uv} of the four possible outcomes are determined by repeating the same experimental sequence a few 10^4 times. Single qubit rotations $u(\theta)$ by an angle θ around an axis $\vec{u}$ of the XY plane of the Bloch sphere are obtained by applying Gaussian microwave pulses directly through the readout resonators, with frequencies ν_j, phases $\varphi_j = (\vec{X}, \vec{u})$, and calibrated areas $A_j \propto \theta$; a sufficiently high power is used to compensate for the filtering effect of each resonator, which depends on the detuning $\nu_j - \nu_R^j$. Rotations around Z are obtained by changing temporarily $\nu_{\mathrm{I,II}}$ with dc pulses on the current lines.

The sample is first characterized by spectroscopy [see Fig. 1(b)], and a fit of the transmon model to the data yields the sample parameters (see Sec. III of the SM [14]). The working points where the qubits are manipulated ($M^{\mathrm{I,II}}$), resonantly coupled (C), and readout ($R^{\mathrm{I,II}}$) are chosen to yield sufficiently long relaxation times ~ 0.5 μs [15] during gates, negligible residual coupling during single qubit rotations and readout, and best possible fidelities at readout. Figure 1(b) shows these points as well as the spectroscopic anticrossing of the two qubits at point C, where $2g = 8.3$ MHz in agreement with the design value of C_c. Then, readout errors are characterized at $R^{\mathrm{I,II}}$ (see Sec. IV of the SM [14]): In a first approximation, the errors are independent for the two readouts and are of about 10% and 20% when reading $|0\rangle$ and $|1\rangle$, respectively. This limited

fidelity results for a large part from energy relaxation of the qubits at readout. In addition, we observe a small readout cross talk, i.e., a variation of up to 2% in the probability of an outcome of readout j depending on the state of the other qubit. All these effects are calibrated by measuring the four p_{uv} probabilities for each of the four $|uv\rangle$ states, which allows us to calculate a 4×4 readout matrix $\mathcal{R}$ linking the p_{uv}'s to the $|uv\rangle$ populations.

Repeating the pulse sequence shown in Fig. 1(c) at $M^{\mathrm{I}} = 5.247$ GHz, $M^{\mathrm{II}} = C = 5.125$ GHz, $R^{\mathrm{I}} = 5.80$ GHz, $R^{\mathrm{II}} = 5.75$ GHz, and applying the readout corrections $\mathcal{R}$, we observe the coherent exchange of a single excitation initially stored in qubit I. We show in Fig. 2 the time evolution of the measured $|uv\rangle$ populations, in fair agreement with a prediction obtained by integration of a simple time independent Liouville master equation of the system, involving the independently measured relaxation times $T_1^{\mathrm{I}} = 0.44$ μs and $T_1^{\mathrm{II}} = 0.52$ μs, and two independent effective pure dephasing times $T_\varphi^{\mathrm{I}} = T_\varphi^{\mathrm{II}} = 2.0$ μs as fitting parameters. Tomographic reconstruction of the register density matrix ρ is obtained by measuring the expectation values of the 15 two-qubit Pauli operators $\{P_k\} = \{I, X, Y, Z\}_{\mathrm{I}} \otimes \{I, X, Y, Z\}_{\mathrm{II}} - \{II\}$, the X_j and Y_j measurements being obtained using tomographic pulses $\vec{Y}_j\,(-90°)$ or $\vec{X}_j\,(90°)$ just before readout. The ρ matrix is calculated from the Pauli set by global minimization of the Hilbert-Schmidt distance between the possibly nonphysical ρ and all physical (i.e., positive-semidefinite) ρ's. This can be done at regular intervals of the coupling time to produce a movie of $\rho(\Delta t)$ (see the Supplemental Material [14]) showing the swapping of the $|10\rangle$ and $|01\rangle$ populations at frequency $2g$, the corresponding oscillation of the coherences, as well as the relaxation towards $|00\rangle$. Figure 2 shows $\{\langle P_k\rangle\}$ and ρ only at $\Delta t = 0$ ns and after a $\sqrt{i\mathrm{SWAP}}$ obtained at $\Delta t = 31$ ns with Θ_j^{-1} rotations of $\theta_{\mathrm{I}} \simeq -65°$ and $\theta_{\mathrm{II}} \simeq +60°$. The fidelity $F = \langle\psi_{\mathrm{id}}|\rho|\psi_{\mathrm{id}}\rangle$ of ρ with the ideal density matrices $|\psi_{\mathrm{id}}\rangle\langle\psi_{\mathrm{id}}|$ is 95% and 91%, respectively, and is limited by errors on the preparation pulse, statistical noise, and relaxation.

To quantify in a different way our ability to entangle the two qubits, we prepare a Bell state $|10\rangle + e^{i\psi}|01\rangle$ (with $\psi = \theta_{\mathrm{II}} - \theta_{\mathrm{I}}$) using the pulse sequence of Fig. 1(c) with $\Delta t = 31$ ns and no Θ_j^{-1} rotations, and measure the CHSH

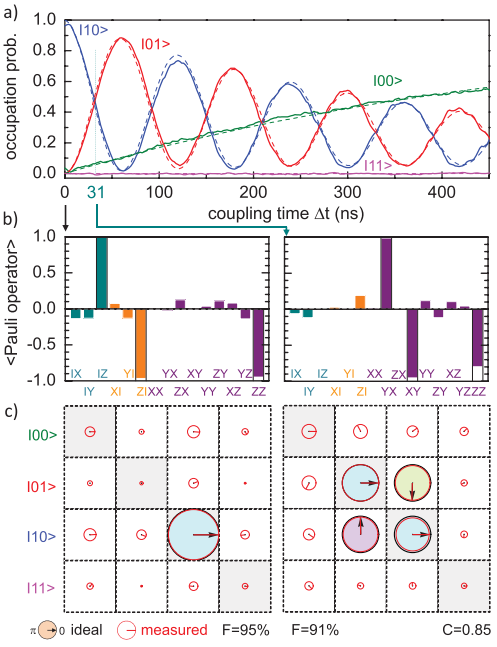

FIG. 2 (color). Coherent swapping of a single excitation between the qubits. (a) Experimental (solid lines) and fitted (dashed lines) occupation probabilities of the four computational states $|00\rangle \ldots |11\rangle$ as a function of the coupling duration. No Z or tomographic pulses are applied here. (b),(c) State tomography of the initial state (left) and of the state produced by the $\sqrt{i\mathrm{SWAP}}$ gate (right). (b) Ideal (empty bars) and experimental (color filling) expected values of the 15 Pauli operators $IX, \ldots, ZZ$. (c) Corresponding ideal (color-filled black circles with black arrow) and experimental (red circle and arrow) density matrices, as well as fidelity F and concurrence C. Each complex matrix element is represented by a circle with an area proportional to its modulus (diameter equals cell size for unit modulus) and by an arrow giving its argument. See Sec. VI of the SM [14] for a real and imaginary part representation of the matrices.

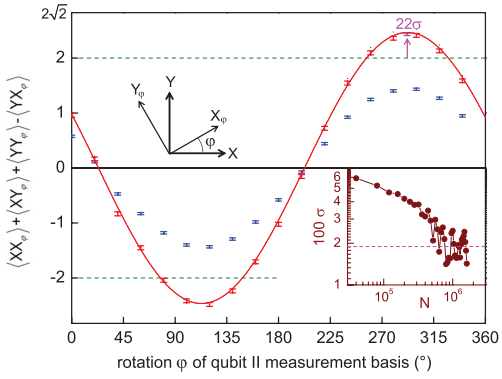

FIG. 3 (color). Test of the CHSH-Bell inequality on a $|10\rangle + e^{i\psi}|01\rangle$ state by measuring the qubits along X^{I} or Y^{I} and X_φ^{II} or Y_φ^{II} (see top-left inset), respectively. Blue (red) error bars are the experimental CHSH entanglement witness determined from the raw (readout-error corrected) measurements as a function of the angle φ between the measuring basis, whereas solid line is a fit using ψ as the only fitting parameter. Height of error bars is ± 1 standard deviation $\sigma(N)$ (see bottom-right inset), with N the number of sequences per point. Note that averaging beyond $N = 10^6$ does not improve the violation because of a slow drift of φ.

entanglement witness $\langle XX_\varphi\rangle + \langle XY_\varphi\rangle + \langle YY_\varphi\rangle - \langle YX_\varphi\rangle$ as a function of the angle φ between the orthogonal measurement bases of qubits I and II. Figure 3 compares the results obtained with and without correcting the readout errors with what is theoretically expected from the decoherence parameters indicated previously: unlike in [11] and because of a readout contrast limited to 70%–75%, the witness does not exceed the classical bound of 2 without correcting the readout errors. After correction, it reaches 2.43, in good agreement with the theoretical prediction (see also [16]), and exceeds the classical bound by up to 22 standard deviations when averaged over 10^6 sequences.

In a last experiment, we characterize the imperfections of our $\sqrt{i\mathrm{SWAP}}$ gate by quantum process tomography [1]. We build a completely positive map $\rho_{\mathrm{out}} = \mathcal{E}(\rho_{\mathrm{in}}) = \sum_{m,n}\chi_{mn}P'_m\rho_{\mathrm{in}}P'^{\dagger}_n$ characterized by a 16×16 matrix χ expressed here in the modified Pauli operator basis $\{P'_k\} = \{I, X, Y' = iY, Z\}^{\otimes 2}$, for which all matrices are real. For that purpose, we apply the gate (using pulse sequences similar to that of Fig. 1(c), with $\Delta t = 31$ ns and Θ_j^{-1} rotations) to the 16 input states $\{|0\rangle, |1\rangle, |0\rangle + |1\rangle, |0\rangle + i|1\rangle\}^{\otimes 2}$ and characterize both the input and output states by quantum state tomography. By operating as described previously, we would obtain apparent input and output density matrices including errors made in the state tomography itself, which we do not want to include in the gate map. Instead, we fit the 16 experimental input Pauli sets by a model (see Sec. V of the SM [14]) including amplitude and phase errors for the X and Y preparation and tomographic pulses, in order to determine which operator set $\{P_k^e\}$ is actually measured. The input and output matrices $\rho_{\mathrm{in,out}}$ corrected from the tomographic errors only are calculated by inverting the linear relation $\{\langle P_k^e\rangle = \mathrm{Tr}(\rho P_k^e)\}$ and by applying it to the experimental Pauli sets. We then calculate from the $\{\rho_{\mathrm{in,out}}\}$ set an Hermitian χ matrix that is not necessarily physical due to statistical errors, and which we render physical by taking the nearest Hermitian positive matrix. This final χ matrix is shown and compared to the ideal matrix χ_{id} in Fig. 4, which yields a gate fidelity $F_g = \mathrm{Tr}(\chi\chi_{\mathrm{id}}) = 0.9$ [17] for a single run of the gate. To better understand the imperfections, we also show the map $\tilde{\chi}$ of the actual process preceded by the inverse ideal process [18]. The first diagonal element of $\tilde{\chi}$ is equal to F_g by construction. Then, main visible errors arise from unitary operations and reduce fidelity by 1%–2% (a fit yields a too long coupling time inducing a 95° swap instead of 90° and $\theta_{\mathrm{I,II}}$ rotations too small by 3.5° and 7°, respectively). On the other hand the known relaxation and dephasing times reduce fidelity by 8% but is barely visible in $\tilde{\chi}$ due to a spread over many matrix elements with modulus of the order of or below the 1%–2% noise level.

In conclusion, we have demonstrated a high fidelity $\sqrt{i\mathrm{SWAP}}$ gate in a two Josephson qubit circuit with individual nondestructive single-shot readouts, observed a violation of the CHSH-Bell inequality, and followed the register's dynamics by tomography. Although quantum coherence and readout fidelity are still limited in this circuit, they are sufficient to test in the near future simple quantum algorithms and get their result in a single run, which would demonstrate the concept of quantum speed-up.

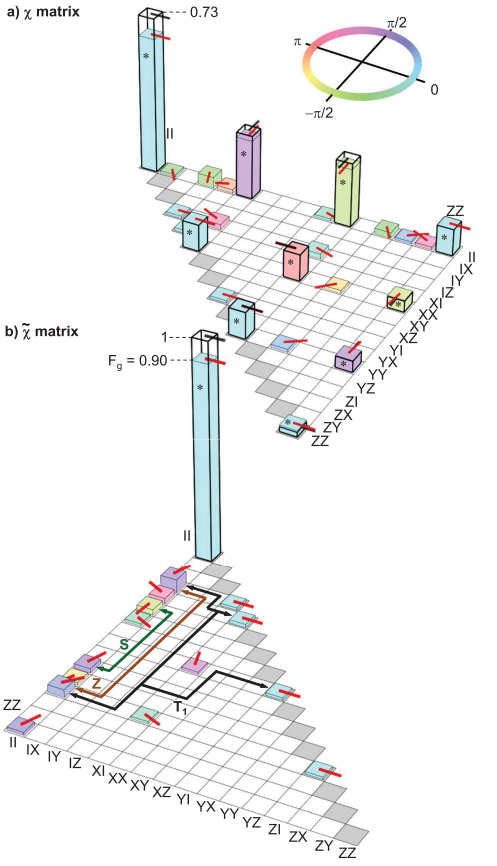

FIG. 4 (color). Map of the implemented $\sqrt{i\mathrm{SWAP}}$ gate yielding a fidelity $F_g = 90\%$. Superposition of the ideal (empty thick bars) and experimental (color-filled bars) upper part of the Hermitian process matrix χ (a) and lower part of the Hermitian error matrix $\tilde{\chi}$ (b), in the two-qubit Pauli operators basis $\{II, \ldots, ZZ\}$. Expected elements are marked with a star, and elements below 1% are not shown. Each complex matrix element is represented by a bar with height proportional to its modulus and by an arrow at the top of the bar (as well as a filling color for the experiment—see top inset) giving its argument. See also Sec. VI of the SM [14] for a real and imaginary part representation of these matrices and for additional information. Labeled arrows indicate the main visible contributions to errors, i.e., a too long swapping time (S), too small rotations $\theta_{\mathrm{I,II}}$ (Z), and relaxation (T_1)—see text.

We gratefully acknowledge discussions with J. Martinis and his co-workers, with M. Devoret, D. DiVicenzo, A. Korotkov, P. Milman, and within the Quantronics group, technical support from P. Orfila, P. Senat, and J. C. Tack, as well as financial support from the European research contracts MIDAS and SOLID, from ANR Masquelspec and C'Nano, and from the German Ministry of Education and Research.

[1] M. A. Nielsen and I. L. Chuang, *Quantum Computation and Quantum Information* (Cambridge University Press, Cambridge, England, 2000).
[2] J. Clarke and F. Wilhelm, Nature (London) **453**, 1031 (2008).
[3] L. DiCarlo *et al.*, Nature (London) **460**, 240 (2009).
[4] L. DiCarlo *et al.*, Nature (London) **467**, 574 (2010).
[5] T. Yamamoto *et al.*, Phys. Rev. B **82**, 184515 (2010).
[6] R. C. Bialczak *et al.*, Nature Phys. **6**, 409 (2010).
[7] J. M. Chow *et al.*, Phys. Rev. Lett. **107**, 080502 (2011).
[8] J. Koch *et al.*, Phys. Rev. A **76**, 042319 (2007).
[9] J. A. Schreier *et al.*, Phys. Rev. B **77**, 180502(R) (2008).
[10] M. Mariantoni *et al.*, Science **334**, 61 (2011).
[11] M. Ansmann *et al.*, Nature (London) **461**, 504 (2009).
[12] I. Siddiqi *et al.*, Phys. Rev. Lett. **93**, 207002 (2004).
[13] F. Mallet *et al.*, Nature Phys. **5**, 791 (2009).
[14] See Supplemental Material at http://link.aps.org/supplemental/10.1103/PhysRevLett.108.057002 for additional information about the sample preparation and experimental setup, the two-qubit Hamiltonian, the sample parameters, the readout characterization, the removal of errors on tomographic pulses, as well as for different representations of the matrices shown in Figs. 2 and 4.
[15] The relaxation times $T_1 \sim 0.5$ μs are twice as low as in Ref. [13], which is likely due to a lack of control of the electromagnetic impedance as seen from the qubit in the present and more complicated circuit and/or to the large asymmetry d of the transmons that opens a new relaxation channel.
[16] J. M. Chow *et al.*, Phys. Rev. A **81**, 062325 (2010).
[17] Note that $F_{\bar{g}}$ is also equal to Shumacher's fidelity $\mathrm{Tr}[S_{\mathrm{id}}^{\dagger}S]/\mathrm{Tr}[S_{\mathrm{id}}^{\dagger}S_{\mathrm{id}}]$ with S (S_{id}) the super operator of the actual (ideal unitary) process and that fidelities F for the 16 output states range between 80% and 99.5%.
[18] A. G. Kofman and A. N. Korotkov, Phys. Rev. A **80**, 042103 (2009); private communication.

Supplementary Information for Characterization of a two-transmon processor with individual single-shot qubit readout

A. Dewes[1], F. R. Ong[1], V. Schmitt[1], R. Lauro[1], N. Boulant[2], P. Bertet[1], D. Vion[1], and D. Esteve[1]
[1] *Quantronics group, Service de Physique de l'État Condensé (CNRS URA 2464), IRAMIS, DSM, CEA-Saclay, 91191 Gif-sur-Yvette, France and*
[2] *I2BM, Neurospin, LRMN, 91191CEA-Saclay, 91191 Gif-sur-Yvette, France*
(Dated: December 8, 2011)

I. SAMPLE PREPARATION AND EXPERIMENTAL SETUP

- Sample fabrication: the sample is fabricated on a silicon chip oxidized over 50 nm. A 150 nm thick niobium layer is first deposited by magnetron sputtering and then dry-etched in a SF_6 plasma to pattern the readout resonators, the current lines for frequency tuning, and their ports. Finally, the transmon qubit, the coupling capacitance and the Josephson junctions of the resonators are fabricated by double-angle evaporation of aluminum through a shadow mask patterned by e-beam lithography. The first layer of aluminum is oxidized in a $Ar - O_2$ mixture to form the oxide barrier of the junctions. The chip is glued with wax on a printed circuit board (PCB) and wire bonded to it. The PCB is then screwed in a copper box anchored to the cold plate of a dilution refrigerator.
- Qubit microwave pulses: The qubit drive pulses are generated by two phase-locked microwave generators whose continuous wave outputs are fed to a pair of I/Q-mixers. The two IF inputs of each of these mixers are provided by a 4-Channel 1 GS/s arbitrary waveform generator (AWG Tektronix AWG5014). Single-sideband mixing in the frequency range of $50 - 300$ MHz is used to generate multi-tone drive pulses and to obtain a high ON/OFF ratio (> 50 dB) of the signal at the output of the mixers. Phase and amplitude errors of the mixers are corrected by measuring the signals at the output and applying sideband and carrier frequency dependent corrections in amplitude and offset to the IF input channels.
- Flux Pulses: The flux control pulses are generated by a second AWG and sent to the chip through a transmission line, equipped with 40 dB of attenuation distributed over different temperature stages and a pair of 1 GHz absorptive low-pass filters at 4 K. The input signal of each flux line is fed back to room temperature through an identical transmission line and is then measured to compensate the non-ideal frequency response of the line.
- Readout Pulses: The pulses for the Josephson bifurcation amplifier (JBA) readouts are generated by mixing the continuous signals of a pair of microwave generators with IF pulses provided by a 1 GS/s arbitrary function generator. Each readout pulse consists of a measurement part with a rise time of 30 ns and a hold time of 100 ns, followed by a $2\,\mu s$ long latching part at 90 % of the pulse height.
- Drive and Measurement Lines: The drive and readout microwave signals of each qubit are combined and sent to the sample through a pair of transmission lines that are attenuated by 70 dB over different temperature stages and filtered at 4 K and 300 mK. A microwave circulator at 20 mK separates the input signals going to the chip from the reflected signals coming from the chip. The latter are amplified by 36 dB at 4 K by two cryogenic HEMT amplifiers (CIT Cryo 1) with noise temperature 5 K. The reflected readout pulses get further amplified at room temperature and are then demodulated with the continuous signals of the readout microwave sources. The IQ quadratures of the demodulated signals are sampled at 1 GS/s by a 4-channel Data Acquisition system (Acqiris DC282).

II. TWO-QUBIT HAMILTONIAN

The Hamiltonian of a Cooper pair box j [s2, s1] with total Coulomb energy $E_{\rm C}^{\rm j}$ (for a Cooper pair), with total Josephson energy $E_{\rm J}^{\rm j}(\phi_{\rm j})$, with island charge $N_{\rm j}$ (in Cooper pair units) and conjugated phase variable $\delta_{\rm j}$, biased by a gate charge $N_{\rm g,j}$, is $H_{\rm j} = E_{\rm C}^{\rm j}\left(\widehat{N_{\rm j}} - N_{\rm g,j}\right)^2 - E_{\rm J}^{\rm j}(\phi_{\rm j})\cos\left[\widehat{\delta_{\rm j}} - \delta_{\rm j,0}(\phi_{\rm j})\right]$ with $\tan\left(\delta_{\rm j,0}\right) = d_{\rm j}\tan\left(\pi\phi_{\rm j}/\phi_0\right)$. In the limit $E_{\rm J}^{\rm j} \gg E_{\rm C}^{\rm j}$ [8] that corresponds to the transmon qubit and when restricting the Hilbert space to the two lowest eigenstates $\{|0\rangle_{\rm j}, |1\rangle_{\rm j}\}$, the $N_{\rm g,j}$ parameters become irrelevant, and one has $\langle 0|\,\widehat{N_{\rm j}}\,|0\rangle \simeq \langle 1|\,\widehat{N_{\rm j}}\,|1\rangle \simeq 0$, $\langle 1|\,\widehat{N_{\rm j}}\,|0\rangle = 2^{-3/4}i\left(E_{\rm J}^{\rm j}/E_{\rm C}^{\rm j}\right)^{1/4}$, and $H_{\rm j} = -h\nu_{\rm j}\sigma_z^{\rm j}/2$ with $\nu_{\rm j} \simeq \sqrt{2E_{\rm C}^{\rm j}E_{\rm J}^{\rm j}(\phi_{\rm j})}/h$. When coupling two such transmon qubits by

a capacitance C_c much smaller than each total island capacitance, the total Hamiltonian is $H = H_1 + H_2 + H_{\rm int}$ with $H_{\rm int} = 2E_{\rm C}^{\rm I}E_{\rm C}^{\rm II}/E_{\rm Cc}\widehat{N_1}\widehat{N_2}$ and $E_{\rm Cc}$ the Coulomb energy of a Cooper pair on the coupling capacitor. Using the matrix elements above leads to $H_{\rm int} = hg\sigma_{\rm y}^{\rm I}\sigma_{\rm y}^{\rm II}$ with $g = \sqrt{E_{\rm C}^{\rm I}E_{\rm C}^{\rm II}\nu_{\rm I}\nu_{\rm II}}/(2E_{\rm Cc})$. This symmetric and purely transverse coupling term $\sigma_{\rm y}^{\rm I}\sigma_{\rm y}^{\rm II}$ (exchange term) is not surprising since each charge on a transmon island varying at the frequency of the other qubit plays the role of a resonant gate drive for this second qubit, and makes it rotate around an equatorial axis of its Bloch sphere. The precise YY nature (rather than XX for instance) is on the other hand meaningless and is a matter of initial convention for the global phases of the $|0\rangle$ and $|1\rangle$ states.

III. SAMPLE PARAMETERS

The sample is first characterized by spectroscopy (see Fig. 1.b of main text). The incident power used is high enough to observe the resonator frequency $\nu_{\rm R}$, the qubit line ν_{01}, and the two-photon transition at frequency $\nu_{02}/2$ between the ground and second excited states of each transmon (data not shown). A fit of the transmon model to the data yields the sample parameters $E_{\rm J}^{\rm I}/h = 36.2\,{\rm GHz}$, $E_{\rm C}^{\rm I}/h = 0.98\,{\rm GHz}$, $d_I = 0.2$, $E_{\rm J}^{\rm II}/h = 43.1\,{\rm GHz}$, $E_{\rm C}^{\rm II}/h = 0.87\,{\rm GHz}$, $d_{\rm II} = 0.35$, $\nu_{\rm R}^{\rm I} = 6.84\,{\rm GHz}$, and $\nu_{\rm R}^{\rm II} = 6.70\,{\rm GHz}$. The qubit-readout anti crossing at $\nu = \nu_{\rm R}$ yields the qubit-readout couplings $g_0^{\rm I} \simeq g_0^{\rm II} \simeq 50\,{\rm MHz}$. Independent measurements of the resonator dynamics (data not shown) yield quality factors $Q_{\rm I} = Q_{\rm II} = 730$ and Kerr non linearities [s3],[13] $K_{\rm I}/\nu_{\rm R}^{\rm I} \simeq K_{\rm II}/\nu_{\rm R}^{II} \simeq -2.3 \pm 0.5 \times 10^{-5}$.

IV. READOUT CHARACTERIZATION

Errors in our readout scheme are discussed in detail in [13] for a single qubit. First, incorrect mapping $|0\rangle \to 1$ or $|1\rangle \to 0$ of the projected state of the qubit to the dynamical state of the resonator can occur, due to the stochastic nature of the switching between the two dynamical states. As shown in Fig. IV.1, the probability p to obtain the outcome 1 varies continuously from 0 to 1 over a certain range of drive power $P_{\rm d}$ applied to the readout. When the shift in power between the two $p_{|0\rangle,|1\rangle}(P_{\rm d})$ curves is not much larger than this range, the two curves overlap and errors are significant even at the optimal drive power where the difference in p is maximum. Second, even in the case of non overlapping $p_{|0\rangle,|1\rangle}(P_{\rm d})$ curves, the qubit initially projected in state$|1\rangle$ can relax down to $|0\rangle$ before the end of the measurement, yielding an outcome 0 instead of 1. The probability of these two types of errors vary in opposite directions as a function of the frequency detuning $\Delta = \nu_{\rm R} - \nu > 0$ between the resonator and the qubit, so that a compromise has to be found for Δ. Besides, the contrast $c = Max\left(p_{|1\rangle} - p_{|0\rangle}\right)$ can be increased [13] by shelving state $|1\rangle$ into state $|2\rangle$ with a microwave π pulse at frequency ν_{12} just before the readout resonator pulse. The smallest errors $e_0^{\rm I,II}$ and $e_1^{\rm I,II}$ when reading $|0\rangle$ and $|1\rangle$ are found for $\Delta_{\rm I} = 440\,{\rm MHz}$ and $\Delta_{\rm II} = 575\,{\rm MHz}$ and are shown by arrows in the top panels of Fig. IV.1: $e_0^{\rm I} = 5\%$ and $e_1^{\rm I} = 13\%$ (contrast $c_{\rm I} = 1 - e_0^{\rm I} - e_1^{\rm I} = 82\%$), and $e_0^{\rm II} = 5.5\%$ and $e_1^{\rm II} = 12\%$ ($c_{\rm II} = 82\%$). When using the $|1\rangle \to |2\rangle$ shelving before readout, $e_0^{\rm I} = 2.5\%$ and $e_2^{\rm I} = 9.5\%$ (contrast $c_{\rm I} = 1 - e_0^{\rm I} - e_2^{\rm I} = 88\%$), and $e_0^{\rm II} = 3\%$ and $e_2^{\rm II} = 8\%$ ($c_{\rm II} = 89\%$). These best results are very close to those obtained in [12], but are unfortunately not relevant to this work.

Indeed, when the two qubits are measured simultaneously, one has also to take into account a possible readout crosstalk, i.e. an influence of the projected state of each qubit on the outcome of the readout of the other qubit. We do observe such an effect and have to minimize it by increasing $\Delta_{\rm I,II}$ up to $\sim 1\,{\rm GHz}$ (where the dispersive shift $\chi \simeq 2.5\,{\rm MHz}$ is still large enough), and by not using the shelving technique. An immediate consequence shown in Fig. IV.1(b) is a reduction of the $c_{\rm I,II}$ contrasts. The errors when reading $|0\rangle$ and $|1\rangle$ are now $e_0^{\rm I} = 19\,\%$ and $e_1^{\rm I} = 7\,\%$ (contrast $c_{\rm I} = 74\%$) and $e_0^{\rm II} = 19\,\%$ and $e_1^{\rm II} = 12\,\%$ (contrast $c_{\rm II} = 69\%$). Then to characterize the errors due to crosstalk, we measure the 4×4 readout matrix $\mathcal{R}$ linking the probabilities $p_{\rm uv}$ of the four possible uv outcomes to the population of the four $|uv\rangle$ states. As shown in Fig. IV.1(c-d), we then rewrite $\mathcal{R} = \mathcal{C}_{\rm CT}.(\mathcal{C}_{\rm I} \otimes \mathcal{C}_{\rm II})$ as the product of a 4×4 pure crosstalk matrix $\mathcal{C}_{\rm CT}$ with the tensorial product of the two 2×2 single qubit readout matrices

$$\mathcal{C}_{I,II} = \begin{pmatrix} 1 - e_0^{\rm I,II} & e_1^{\rm I,II} \\ e_0^{\rm I,II} & 1 - e_1^{\rm I,II} \end{pmatrix}.$$

In the worst case, the readout crosstalk is 2.1%. We also illustrate on the figure the impact of the readout errors on our swapping experiment by comparing the bare readout outcomes uv, the outcomes corrected from the independent readout errors only, and the$|uv\rangle$ population calculated with the full correction including crosstalk.

We now explain briefly the cause of the readout crosstalk in our processor. Unlike what was observed for other qubit readout schemes using switching detectors [5], the crosstalk we observe is not directly due to an electromagnetic perturbation induced by the switching of one detector that would help or prevent the switching of the other one.

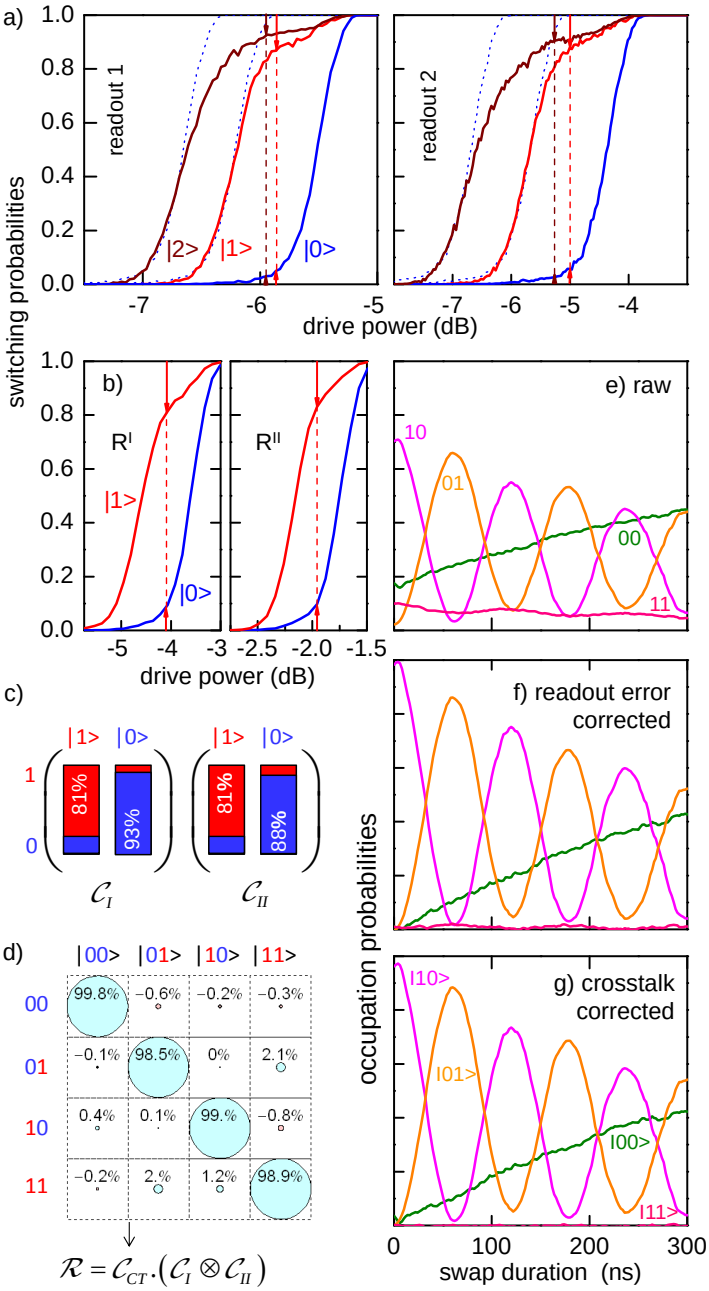

Figure IV.1: Readout imperfections and their correction. (a) Switching probabilities of the readouts as a function of their driving power, with the qubit prepared in state$|0\rangle$ (blue), $|1\rangle$ (red), or $|2\rangle$ (brown), at the optimal readout points. The arrows and dashed segments indicate the readout errors and contrast, at the power where the later is maximum. (b) Same as (a) but at readout points $R^{\mathrm{I,II}}$ used in this work. (c-d) Single readout matrices $\mathcal{C}_{\mathrm{I,II}}$ and pure readout crosstalk matrix $\mathcal{C}_{\mathrm{CT}}$ characterizing the simultaneous readout of the two qubits. (e-g) bare readout outcomes uv, outcomes corrected from the independent readout errors only, and$|uv\rangle$ population calculated with the full correction including crosstalk for the swapping experiment of Fig. 2.

Indeed, when both qubits frequencies $\nu_{\rm I,II}$ are moved far below $\nu_{\rm R}^{\rm I,II}$, the readout crosstalk disappears: the switching of a detector has no measurable effect on the switching of the other one. The crosstalk is actually due to the rather strong ac-Stark shift $\sim 2\,(n_{\rm H}-n_{\rm L})\,g_0^2/(R-\nu_{\rm R}) \sim 500\,$MHz of the qubit frequency when a readout resonator switches from its low to high amplitude dynamical state with $n_{\rm L}\sim 10$ and $n_{\rm H}\sim 10^2$ photons, respectively. The small residual effective coupling between the qubits at readout can then slightly shift the frequency of the other resonator, yielding a change of its switching probability by a few percent. Note that coupling the two qubits by a resonator rather than by a fixed capacitor would solve this problem.

V. REMOVING ERRORS ON TOMOGRAPHIC PULSES BEFORE CALCULATING THE GATE PROCESS MAP

Tomographic errors are removed from the process map of our $\sqrt{iSWAP}$ gate using the following method. The measured Pauli sets corresponding to the sixteen input states are first fitted by a model including errors both in the preparation of the state (index *prep*) and in the tomographic pulses (index *tomo*). The errors included are angular errors $\varepsilon_{\rm I,II}^{\rm prep}$ on the nominal π rotations around $X_{\rm I,II}$, $\eta_{\rm I,II}^{\rm prep,tomo}$and $\delta_{\rm I,II}^{\rm prep,tomo}$ on the nominal $\pi/2$ rotations around $X_{\rm I,II}$ and $Y_{\rm I,II}$, a possible departure $\xi_{\rm I,II}$ from orthogonality of $\left(\overrightarrow{X_{\rm I}},\overrightarrow{Y_{\rm I}}\right)$ and $\left(\overrightarrow{X_{\rm II}},\overrightarrow{Y_{\rm II}}\right)$, and a possible rotation $\mu_{\rm I,II}$ of the tomographic XY frame with respect to the preparation one. The rotation operators used for preparing the states and for doing their tomography are thus given by

$$
\begin{aligned}
X_{\rm I,II}^{\rm prep}(\pi) &= e^{-{\rm i}\left(\pi+\varepsilon_{\rm I,II}^{\rm prep}\right)\sigma_{\rm x}^{\rm I,II}/2},\\
X_{\rm I,II}^{\rm prep}(-\pi/2) &= e^{+{\rm i}\left(\pi/2+\eta_{\rm I,II}^{\rm prep}\right)\sigma_{\rm x}^{\rm I,II}/2},\\
Y_{\rm I,II}^{\rm prep}(\pi/2) &= e^{-{\rm i}\left(\pi/2+\delta_{\rm I,II}^{\rm prep}\right)\left[\cos(\xi_{\rm I,II})\sigma_{\rm y}^{\rm I,II}-\sin(\xi_{\rm I,II})\sigma_{\rm x}^{\rm I,II}\right]/2},\\
X_{\rm I,II}^{\rm tomo}(\pi/2) &= e^{-{\rm i}\left(\pi/2+\eta_{\rm I,II}^{\rm tomo}\right)\left[\sin(\mu_{\rm I,II})\sigma_{\rm x}^{\rm I,II}+\cos(\mu_{\rm I,II})\sigma_{\rm y}^{\rm I,II}\right]/2},\\
Y_{\rm I,II}^{\rm tomo}(-\pi/2) &= e^{+{\rm i}\left(\pi/2+\delta_{\rm I,II}^{\rm tomo}\right)\left[\cos(\mu_{\rm I,II}+\xi_{\rm I,II})\sigma_{\rm y}^{\rm I,II}-\sin(\mu_{\rm I,II}+\xi_{\rm I,II})\sigma_{x}^{\rm I,II}\right]/2}.
\end{aligned}
$$

The sixteen input states are then $\left\{\rho_{\rm in}^{\rm e}=U\left|0\right\rangle\left\langle 0\right|U^{\dagger}\right\}$ with $\{U\} = \{I_{\rm I},X_{\rm I}^{\rm prep}(\pi),Y_{\rm I}^{\rm prep}(\pi/2),X_{\rm I}^{\rm prep}(-\pi/2)\}\otimes\{I_{\rm II},X_{\rm II}^{\rm prep}(\pi),Y_{\rm II}^{\rm prep}(\pi/2),X_{\rm II}^{\rm prep}(-\pi/2)\}$, and each input state yields a Pauli set $\{\langle P_{\rm k}^{\rm e}\rangle = Tr\left(\rho_{\rm in}^{\rm e}P_{\rm k}^{\rm e}\right)\}$ with $\{P_{\rm k}^{\rm e}\} = \{I_{\rm I},X_{\rm I}^{\rm e},Y_{\rm I}^{\rm e},Z_{\rm I}\}\otimes\{I_{\rm II},X_{\rm II}^{\rm e},Y_{\rm II}^{\rm e},Z_{\rm II}\}$, $X^{\rm e}=Y^{\rm tomo}(-\pi/2)^{\dagger}\sigma_z Y^{\rm tomo}(-\pi/2)$, and $Y^{\rm e}=X^{\rm tomo}(\pi/2)^{\dagger}\sigma_z X^{\rm tomo}(\pi/2)$. Figure V.1 shows the best fit of the modeled $\{\langle P_k^e\rangle\}$ set to the measured input Pauli sets, yielding $\varepsilon_{\rm I}^{\rm prep}=-1^{\circ}$, $\varepsilon_{\rm II}^{\rm prep}=-3^{\circ}$, $\eta_{\rm I}^{\rm prep}=3^{\circ}$, $\eta_{\rm II}^{\rm prep}=4^{\circ}$, $\delta_{\rm I}^{\rm prep}=-6^{\circ}$, $\delta_{\rm II}^{\rm prep}=-3^{\circ}$, $\eta_{\rm I}^{\rm tomo}=-6^{\circ}$, $\eta_{\rm II}^{\rm tomo}=-4^{\circ}$, $\lambda_{\rm I}^{\rm tomo}=12^{\circ}$, $\lambda_{\rm II}^{\rm tomo}=5^{\circ}$, $\xi_{\rm I}=1^{\circ}$, $\xi_{\rm II}=-2^{\circ}$, and $\mu_{\rm I}=\mu_{\rm II}=-11^{\circ}$.

Knowing the tomographic errors and thus $\{\langle P_{\rm k}^{\rm e}\rangle\}$, we then invert the linear relation $\{\langle P_{\rm k}^{\rm e}\rangle = Tr\left(\rho P_{\rm k}^{\rm e}\right)\}$ to find the 16×16 matrix B that links the vector $\overrightarrow{\langle P_{\rm k}^{\rm e}\rangle}$ to the columnized density matrix $\overrightarrow{\rho}$, i.e. $\overrightarrow{\rho}=B.\overrightarrow{\langle P_{\rm k}^{\rm e}\rangle}$. The matrix B is finally applied to the measured sixteen input and sixteen output Pauli sets to find the sixteen $(\rho_{\rm in,},\rho_{\rm out})_{\rm k}$ couples to be used for calculating the gate map.

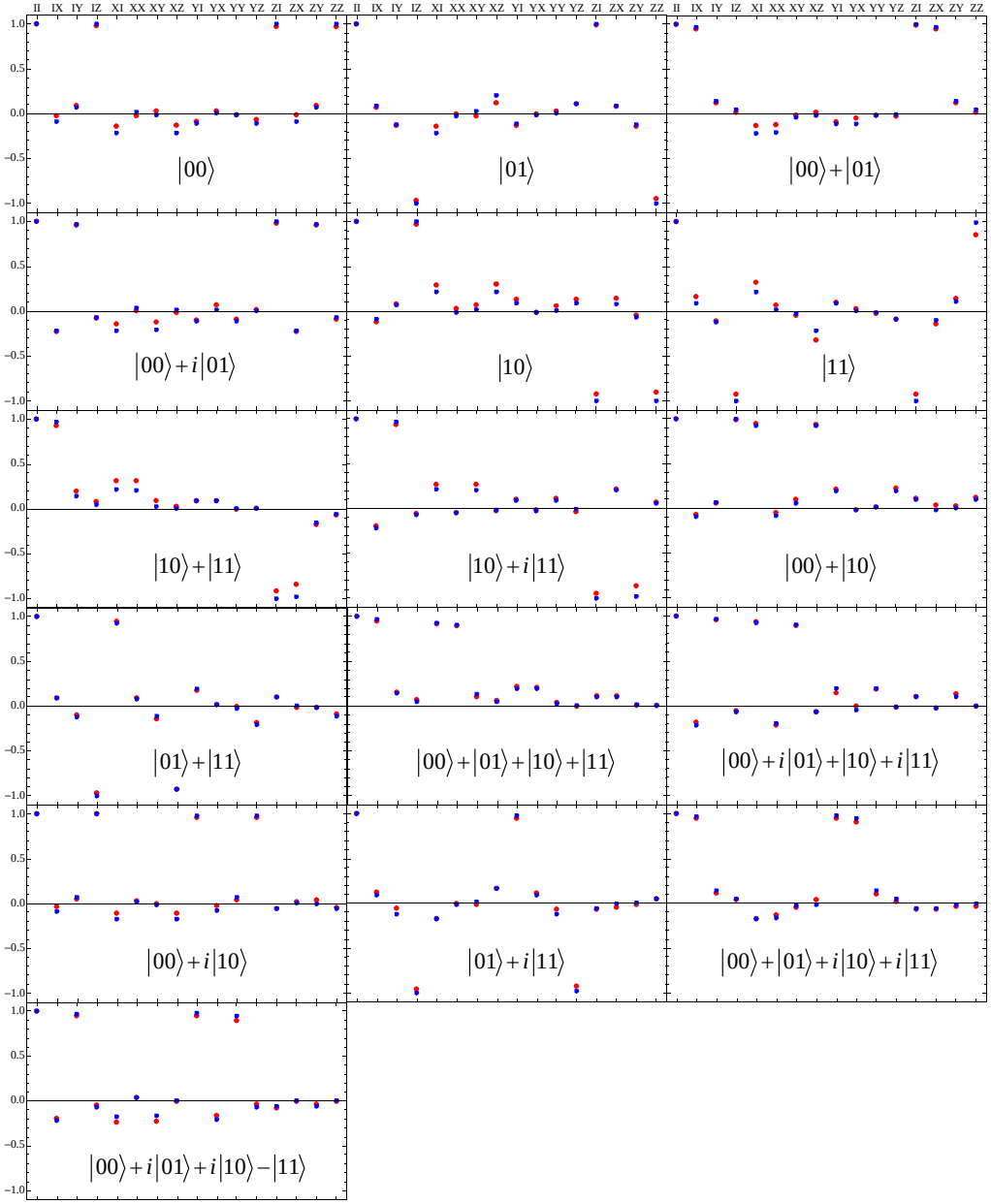

Figure V.1: Fitting of the pulse errors at state preparation and tomography. Measured (red) and fitted (blue - see text) Pauli sets $\langle P_k^e \rangle$ for the sixteen targeted input states $\{|0\rangle, |1\rangle, |0\rangle + |1\rangle, |0\rangle + i|1\rangle\}^{\otimes 2}$. The $\{II, IX, IY, IZ, XI, ...\}$ operators indicated in abscissa are the targeted operators and not those actually measured (due to tomographic errors).

VI. REAL AND IMAGINARY PART REPRESENTATION OF THE MATRICES OF MAIN FIGURES 2 AND 4.

The ρ , χ and $\widetilde{\chi}$ matrices of figures 2 and 4 of the main text are represented in an unconventional way that allows to encode both the modulus and the argument of each matrix element in the same matrix cell. Figures VI.1 to VI.3 show the same matrices using the more conventional real and imaginary part representation.

In addition, we show in Fig. VI.4 the contributions of relaxation, of inaccurate swapping time and of inaccurate rotations $\theta_{\mathrm{I,II}}$ to the error matrix $\widetilde{\chi}$. Contribution of relaxation is directly calculated from the independently measured values of the relaxation time T_1, whereas the two other contributions result from a fit to the whole experimental $\widetilde{\chi}$ matrix.

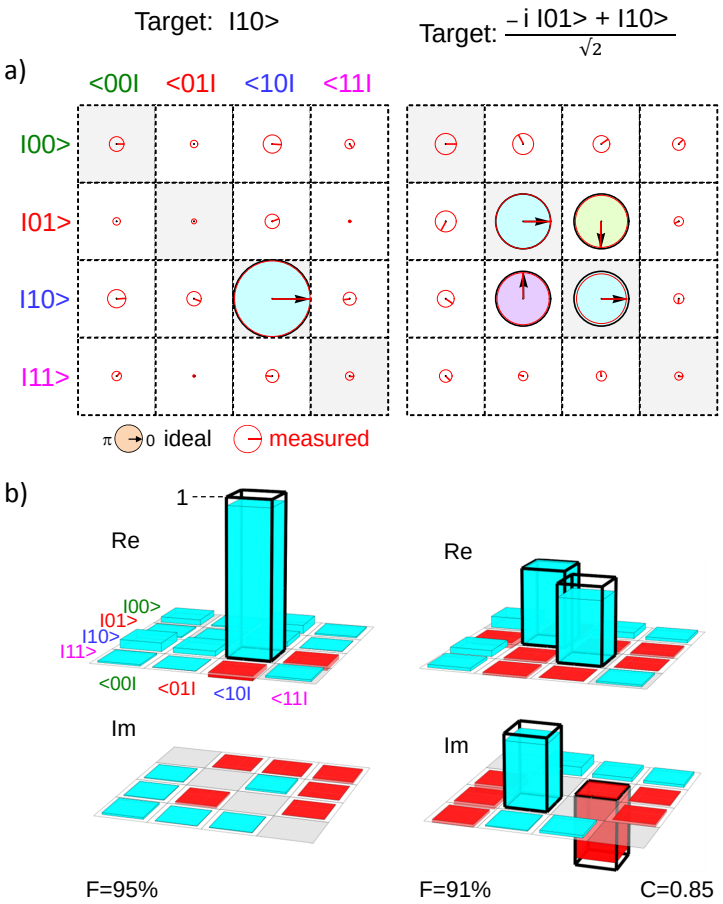

Figure VI.1: Same ideal and experimental density matrices as in Fig. 2, before and after one operation of the $\sqrt{iSWAP}$ gate. (a) Color-filled black circles with black arrow is the ideal matrix whereas red circles and arrows is the experimental one. Each complex matrix element is represented by a circle with an area proportional to its modulus (diameter = cell size for unit modulus) and by an arrow giving its argument (usual trigonometric convention). (b) Real (top) and imaginary (bottom) parts of the same matrices, with positive and negative numbers being encoded along the vertical direction. The ideal matrix is represented by thick black empty bars, whereas experimental data are shown as blue-filled (positive) or red-filled (negative) thin bars.

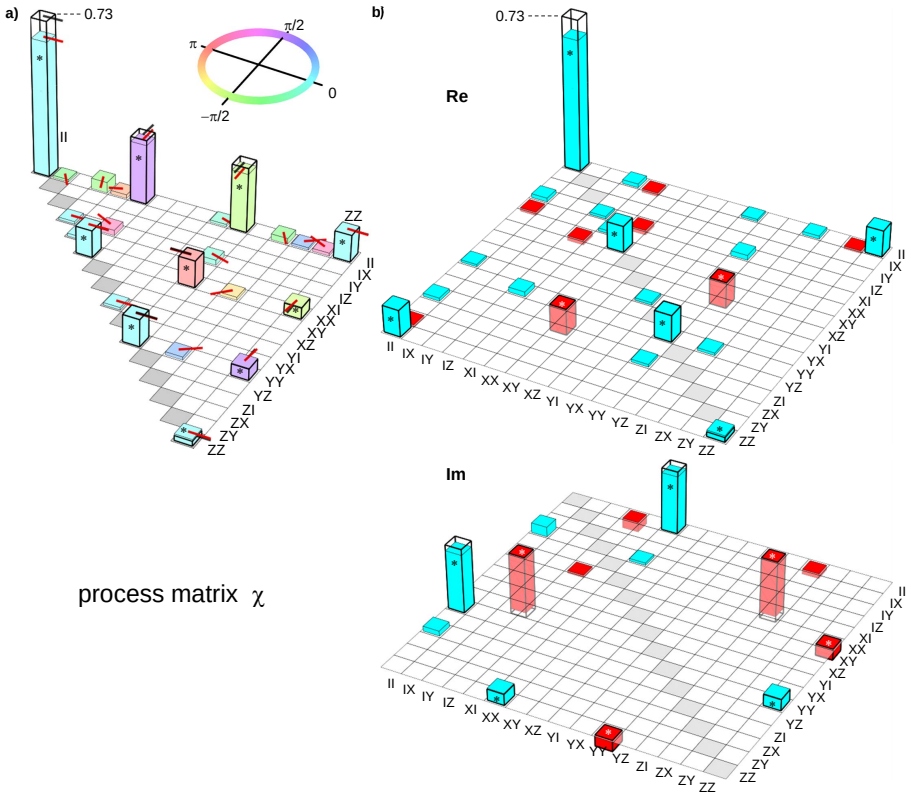

Figure VI.2: Same ideal and experimental process matrix χ as in Fig. 4(a). Expected elements are marked with a star and elements below 1% are not shown. (a) Each complex matrix element is represented by a bar with height proportional to its modulus and by an arrow at the top of the bar (as well as a filling color for the experiment - see top inset) giving its argument. (b) Real (top) and imaginary (bottom) parts of the same matrix, with positive and negative numbers being encoded along the vertical direction. The ideal matrix is represented by thick black empty bars, whereas experimental data are shown as blue-filled (positive) or red-filled (negative) thin bars.

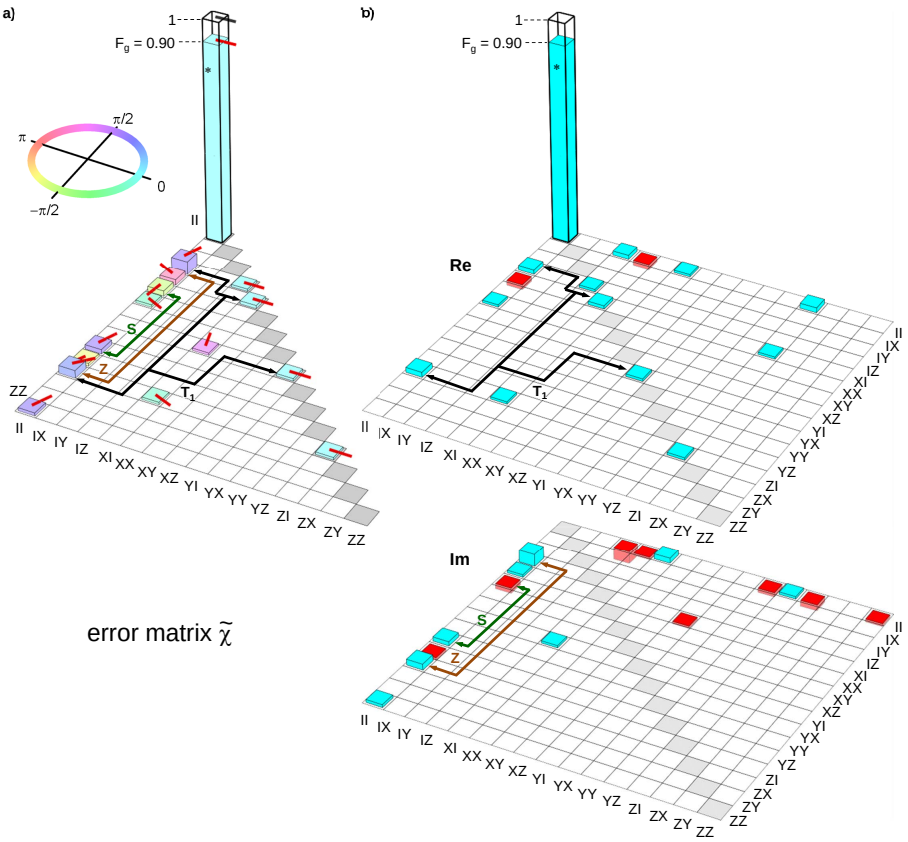

Figure VI.3: Same ideal and experimental error matrix $\tilde{\chi}$ as in Fig. 4(b). The $IIII$ matrix element is the only expected one; elements with modulus below 1% are not shown. (a) Each complex matrix element is represented by a bar with height proportional to its modulus and by an arrow at the top of the bar (as well as a filling color for the experiment - see left inset) giving its argument. (b) Real (top) and imaginary (bottom) parts of the same matrix, with positive and negative numbers being encoded along the vertical direction. The ideal matrix is represented by thick black empty bars, whereas experimental data are shown as blue-filled (positive) or red-filled (negative) thin bars. Labeled arrows indicate the main visible contributions to errors, i.e. a too long swapping time (S), too small rotations $\theta_{\mathrm{I,II}}$ (Z), and relaxation (T_1).

[s1] D. Vion *et al.*, Science 296, 886 (2002).
[s2] A. Cottet, Ph.D. thesis, Universite Paris VI, 2002.
[s3] F. R. Ong *et al.*, Phys. Rev. Lett. 106, 167002 (2011).

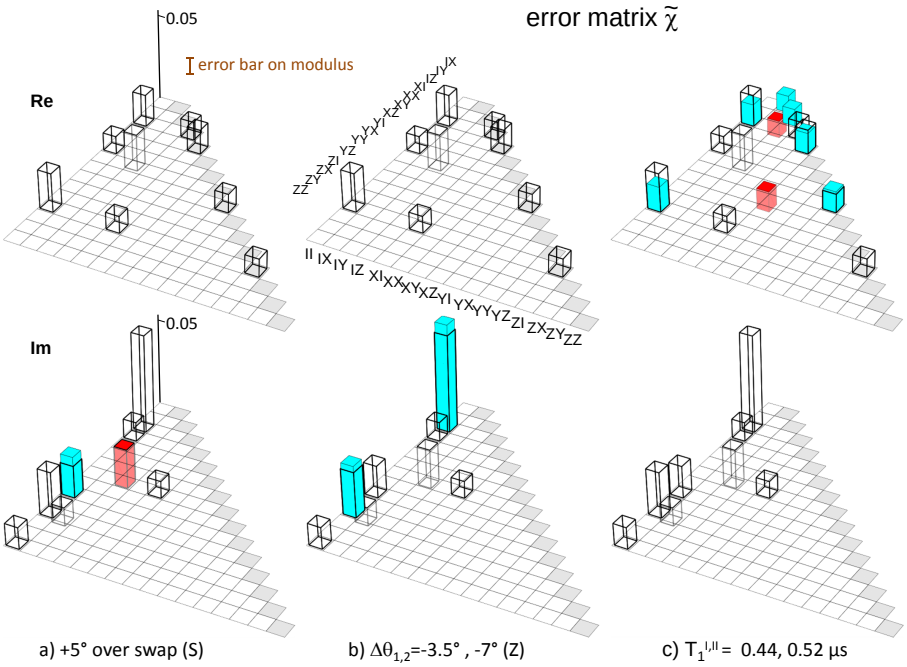

Figure VI.4: Experimental (empty bars) and calculated (color-filled thin bars) $\widetilde{\chi}$ matrix for the three error contributions S, Z, and T_1 mentionned in the text and indicated in Figs. 4(b) and VI.3. Note that the vertical scale is expanded by a factor 10 with respect to other figures, and that matrix element $IIII$ as well as elements with modulus below the statistical error of 1% (see error bar) are not shown. Contribution T_1 is directly calculated from the independently measured values of the relaxation time T_1, whereas contributions S and Z result from a fit to the whole experimental $\widetilde{\chi}$ matrix (including the many small elements below 1%).

PHYSICAL REVIEW B **85**, 140503(R) (2012)

Quantum speeding-up of computation demonstrated in a superconducting two-qubit processor

Andreas Dewes,[1] Romain Lauro,[1] Florian R. Ong,[1] Vivient Schmitt,[1] Perola Milman,[2,3] Patrice Bertet,[1] Denis Vion,[1] and Daniel Esteve[1]

[1]*Service de Physique de l'Etat Condensé/IRAMIS/DSM (CNRS URA 2464), CEA Saclay, 91191 Gif-sur-Yvette, France*

[2]*Laboratoire Matériaux et Phénomènes Quantiques, Université Paris Diderot, 10 rue Alice Domon et Léonie Duquet, 75205 Paris, France*

[3]*Université Paris-Sud 11, Institut de Sciences Moléculaires d'Orsay (CNRS), 91405 Orsay, France*

(Received 20 October 2011; revised manuscript received 31 January 2012; published 5 April 2012)

We operate a superconducting quantum processor consisting of two tunable transmon qubits coupled by a swapping interaction, and equipped with nondestructive single-shot readout of the two qubits. With this processor, we run the Grover search algorithm among four objects and find that the correct answer is retrieved after a single run with a success probability between 0.52 and 0.67, which is significantly larger than the 0.25 achieved with a classical algorithm. This constitutes a proof of concept for the quantum speed-up of electrical quantum processors.

DOI: 10.1103/PhysRevB.85.140503 PACS number(s): 85.25.Cp, 03.67.Lx, 74.78.Na

The proposition of quantum algorithms[1–3] that perform useful computational tasks more efficiently than classical algorithms has motivated the realization of physical systems[4] able to implement them and to demonstrate quantum speed-up. The versatility and the potential scalability of electrical circuits make them very appealing for implementing a quantum processor built as sketched in Fig. 1. Ideally, a quantum processor consists of a scalable set of quantum bits that can be efficiently reset, that can follow any unitary evolution needed by an algorithm using a universal set of single- and two-qubit gates, and that can be read projectively.[5] The nonunitary projective readout operations can be performed at various stages of an algorithm, and in any case at the end in order to get the final outcome. Quantum processors based on superconducting qubits have already been operated, but they fail to meet the above criteria in different aspects. With the transmon qubit[6,7] derived from the Cooper pair box,[8] simple quantum algorithms, namely, the Deutsch-Jozsa algorithm,[9] the Grover search algorithm,[1] and a three-qubit quantum error correction code, were demonstrated in two- and three-qubit processors with the coupling between the qubits mediated by a cavity also used for readout.[10,11] In this circuit, the qubits are not read independently, but the value of a single collective variable is determined from the cavity transmission measured over a large number of repeated sequences. By applying suitable qubit rotations prior to this measurement, the density matrix of the two-qubit register was inferred at different steps of the algorithm, and it was found to be in good agreement with the predicted one. Demonstrating quantum speed-up is, however, more demanding than measuring a collective qubit variable since it requests to obtain an outcome after a single run, i.e., to perform the single-shot readout of the qubit register. Up to now, single-shot readout in superconducting processors has been achieved only for phase qubits.[12,13] In a multiphase-qubit processor equipped with single-shot but destructive readout of each qubit, the Deutsch-Jozsa algorithm[9] was demonstrated in Ref. 12 with a success probability of order 0.7 in a single run, to be compared to 0.5 for a classical algorithm. Very recently a similar processor ran a compiled version of Shor's algorithm,[2] yielding prime factors of 15 with a 48% success rate.[14]

Since the Deutsch-Jozsa classification algorithm is not directly related to any practical situation, demonstrating quantum speed-up for more useful algorithms in an electrical processor designed along the blueprint of Fig. 1 is an important goal.[14] In this Rapid Communication, we report the operation of a two-transmon-qubit processor[15] that comes closer to the ideal scheme than those previously mentioned, and the single-shot run of the Grover search algorithm among four objects. Since, in this case, the algorithm ideally yields the answer after one algorithm step, its success probability after a single run provides a simple benchmark. We find that our processor yields the correct answer at each run, with a success probability that ranges between 0.52 and 0.67, whereas a single-step classical algorithm using a random query would yield the correct answer with probability 0.25.

The sample and the setup used for this experiment are the very same as those described and characterized in detail in Ref. 15. The sample fabrication and parameters are summarized in Secs. I and II of the Supplemental Material,[16] whereas the scheme of our processor and its mode of operation are recalled in Fig. 2: Two tunable transmon qubits coupled by a fixed capacitor are embedded in two identical control and readout subcircuits. The Hamiltonian of the two qubits {I,II} is $H/h = (-\nu_{\rm I}\sigma_z^{\rm I} - \nu_{\rm II}\sigma_z^{\rm II} + 2g\sigma_y^{\rm I}\sigma_y^{\rm II})/2$, where $\sigma_{x,y,z}$ are the Pauli operators, $\nu_{\rm I,II}$ are the qubit frequencies controlled by the flux applied to each transmon superconducting quantum interference device (SQUID) loop with fast (0.5-GHz bandwidth) local current lines, and $g = 4.6$ MHz $\ll \nu_{\rm I,II}$ is the coupling frequency controlled by the coupling capacitance (see Sec. II of the Supplemental Material and Ref. 17). The achieved frequency control allows us to place the two transmons on resonance during times precise enough for performing the universal two-qubit gate $\sqrt{\rm iSWAP}$ (Ref. 15) and the exchange gate iSWAP used in this work. The qubit frequencies are tuned to different values for single-qubit manipulation, two-qubit gate operation, and readout (see Sec. III of the Supplemental Material[16]). The readout is independently and simultaneously performed for each qubit using the single-shot method of Ref. 18. It is based on the dynamical transition of a nonlinear resonator[19,20] that maps the quantum state of each transmon to the bifurcated or nonbifurcated state of its resonator, which

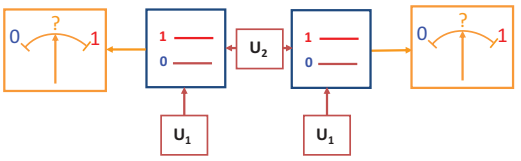

FIG. 1. (Color online) Schematic blueprint of a quantum processor based on quantum gates, represented here in the two-qubit case relevant for our experiment. A quantum processor consists of a qubit register that can perform any unitary evolution needed by an algorithm under the effect of a universal set of quantum gates (single-qubit gate U_1, two-qubit gate U_2). Ideally, all the qubits may be read projectively, and may be reset.

yields a binary outcome for each qubit. This readout method is potentially nondestructive, but its nondestructive character is presently limited by relaxation during the readout pulse. In order to further improve the readout fidelity, we resort to a shelving method that exploits the second excited state of the transmon. For this purpose, a microwave pulse that induces a transition from state $|1\rangle$ toward the second excited state $|2\rangle$ of the transmon is applied just before the readout pulse, as demonstrated in Ref. 18 (this variant does not alter the nondestructive aspect of the readout method since an extra pulse bringing state $|2\rangle$ back to state $|1\rangle$ could be applied after readout). Although the readout contrast achieved with this shelving method and with optimized microwave pulses reaches 0.88 and 0.89 for the two qubits, respectively, the values achieved at working points suitable for processor operation are lower and equal to 0.84 and 0.83. The sources of readout errors are discussed in Sec. IV of the Supplemental Material[16] and include a small readout crosstalk contribution. The overall readout fidelity is thus characterized by a 4×4 matrix $\mathcal{R}$, giving the readout outcome probabilities for each of the input states of the two-qubit register.

In order to characterize the evolution of this register during the algorithm, we determine its density matrix by state tomography. For this purpose, we measure the expectation values of the extended Pauli set of operators $\{\sigma_x I, \ldots, \sigma_z \sigma_z\}$ by applying the suitable rotations just before readout and by averaging typically 10^4 times. Note that the readout errors are corrected by inverting the readout matrix $\mathcal{R}$ when determining the expectation value of the Pauli set, and thus do not contribute to tomography errors, as explained in Ref. 15. The density matrix ρ is then taken as the acceptable positive-semidefinite matrix that, according to the Hilbert-Schmidt distance, is the closest to the possibly nonphysical one derived from the measurement set. In order to characterize the fidelity of the algorithm at all steps, we use the state fidelity $F = \langle\psi|\rho|\psi\rangle$, with $|\psi\rangle$ the ideal quantum state at the step considered; F is in this case the probability for the qubit register to be in state $|\psi\rangle$.

The Grover search algorithm[1] consists of retrieving a particular basis state in a Hilbert space of size N using a function able to discriminate it from the other ones. This function is used to build an oracle operator that tags the searched state. Starting from the superposition $|\phi\rangle$ of all register states, a unitary sequence that incorporates the oracle operator is repeated about $\sqrt{N}$ times, and eventually yields the

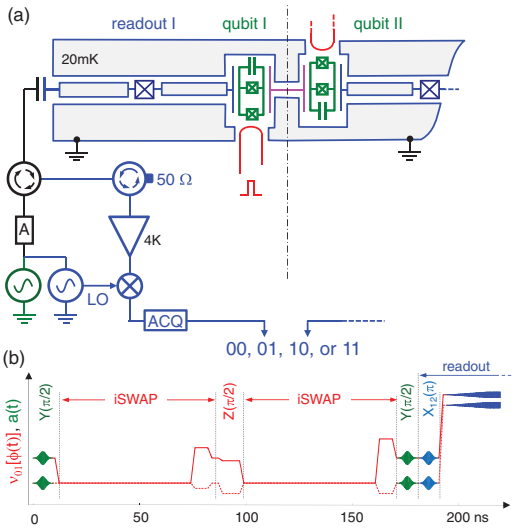

FIG. 2. (Color online) Electrical scheme of the two-qubit circuit operated and typical sequence during processor operation. (a) Two capacitively coupled transmon qubits have tunable frequencies controlled by the flux induced in their SQUID loop by a local current line. The coupling capacitance (center) yields a swapping evolution between the qubits when on resonance. Each transmon is embedded in a nonlinear resonator used for single-shot readout. Each reflected readout pulse is routed to a cryogenic amplifier through circulators, homodyned at room temperature, and acquired digitally, which yields a two-bit outcome. (b) Typical operation of the processor showing the resonant microwave pulses $a(t)$ applied to the qubits and to the readouts, on top of the dc pulses (polylines) that vary the transition frequencies of qubit I (solid) and II (dashed). With the qubits tuned at a first working point for single-qubit gates, resonant pulses are applied for performing X and Y rotations, as well as small flux pulses for Z rotations; qubits are then moved to the interaction point for two-qubit gate operations. Such sequences can be combined as needed by the algorithm. Qubits are then moved to their initial working points for applying tomography pulses as well as a $|1\rangle \rightarrow |2\rangle$ pulse $X_{12}(\pi)$ to increase the fidelity of the forthcoming readout. Finally, they are moved to better readout points and read.

searched state with a high probability. The implementation of Grover's algorithm in a two-qubit Hilbert space often proceeds in a simpler way[21–26] since the result is obtained with certainty after a single algorithm step. The algorithm then consists of an encoding sequence depending on the searched state, followed by a universal decoding sequence that retrieves it. Grover's algorithm thus provides a simple benchmark for two-qubit processors. Its implementation with our quantum processor is shown in Fig. 3(a). First, the superposed state $|\phi\rangle$ is obtained by applying $\pi/2$ rotations around the Y axis for the two qubits. The oracle operator O_{uv} tagging the two-qubit state $|uv\rangle \equiv |u\rangle_{\mathrm{I}} \otimes |v\rangle_{\mathrm{II}}$ to be searched is then applied to state $|\phi\rangle$. Each O_{uv} consists of an iSWAP gate followed by a $Z(\pm\pi/2)$ rotation on each qubit, with the four possible sign combinations $(-,-)$, $(+,-)$, $(-,+)$, and $(+,+)$ corresponding to $uv = 00$, 01, 10, and 11, respectively. In the algorithm we

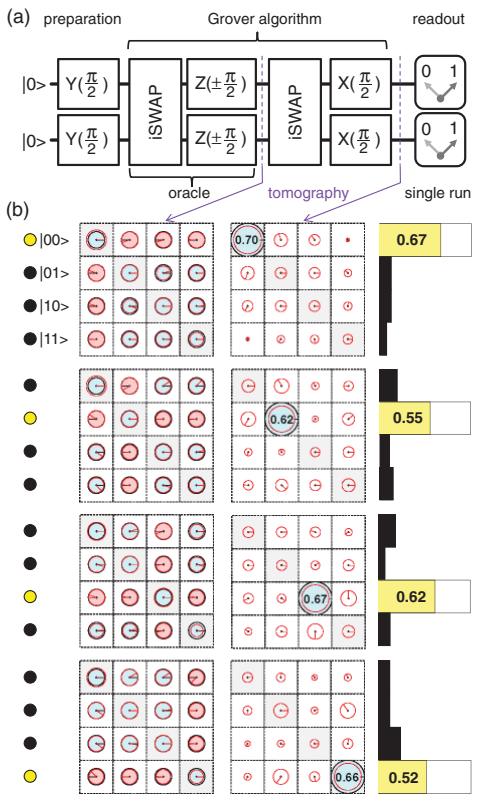

FIG. 3. (Color online) (a) Experimental sequence used for implementing the Grover search algorithm on four objects. First, $Y(\pi/2)$ rotations are applied to produce the superposition $|\phi\rangle = (1/2)\sum_{u,v}|uv\rangle$ of all basis states; then one of the four possible oracles (corresponding to the four sign combinations of the Z rotations) is applied. The tagged state is then decoded in all cases using an iSWAP operation followed by $X(\pi/2)$ rotations. (b) State tomography at two steps of the algorithm (ρ matrices) and success probability after a single run (histograms). The bright dots on the left-hand side mark the basis state tagged by each oracle operator used. The amplitude of each matrix element is represented by a disk [black for the ideal density matrix, red (gray) for the measured one] and its phase by an arrow (as well as a filling color for the ideal matrix). After applying the oracle, the information on the tagged state is encoded in the phase of six particular elements of ρ. After decoding, the tagged state should be the only matrix element present in ρ. The fidelity F_{final} actually obtained is indicated in this element. The probability distribution of the single-run readout outcomes is shown on the right-hand side (bright box for the correct answer, solid dark boxes for the wrong ones).

use, the encoding is a phase encoding as in Ref. 10. When applied to $|\phi\rangle$, each oracle operator inverts the sign of the component corresponding to the state it tags, respectively, to the other ones. The density matrix, after applying the oracle, ideally takes a simple form: The amplitude of all coefficients is 1/4, and the phase of an element ρ_{rs} is $\varphi_{rs} = \pi(\delta_{rt} + \delta_{st})$, where t corresponds to the state tagged by the oracle operator. The state tomography performed after applying the oracle, shown in Fig. 3(b), is in good agreement with this prediction. More quantitatively, we find that after having applied the oracle operator, the intermediate fidelity is $F_{\text{int}} = 0.87$, 0.80, 0.84, and 0.82, respectively. The last part of the algorithm consists in transforming the obtained state in the searched state irrespectively of it, or equivalently to transform the phase information distributed over the elements of the density matrix in a weight information with the whole weight on the searched state. This operation is readily performed by applying an iSWAP gate followed by $X(\pi/2)$ rotations for both qubits. We find that the fidelity of the density matrix at the end of the algorithm is $F_{\text{final}} = 0.70$, 0.62, 0.67, and 0.66, respectively. We explain both F_{int} and F_{final} by gate errors at a 2% level, by errors in the tomography pulses at a 2% level, as well as by decoherence during the whole experimental sequence [at the coupling point, relaxation times are $T_1^{\text{I}} \simeq 450$ ns and $T_1^{\text{II}} \simeq 500$ ns, and the effective dephasing times $T_\varphi^{\text{I}} \simeq T_\varphi^{\text{II}} \simeq 2$ μs (Ref. 15)].

We now consider the success probability obtained after a single run (with no tomography pulses), which probes the quantum speed-up actually achieved by the processor. We find (see Fig. 3) that our processor does yield the correct answer with a success probability $P_{\text{S}} = 0.67$, 0.55, 0.62, and 0.52 for the four basis states, which is smaller than the density matrix fidelity F_{final}. One notices that the difference between F_{final} and P_{S}, mostly due to readout errors, slightly depends on the searched state: The larger the energy of the searched state, the larger is the difference. This dependence is well explained by the effect of relaxation during the readout pulse, which is the main error source at readout, the second one being readout crosstalk. One also notices that the outcome errors are distributed over all the wrong answers. To summarize, the errors of our implementation of Grover's algorithm originate both from small unitary errors accumulated during the algorithm, and from decoherence during the whole sequence, in particular, during the final readout.

We finally discuss the significance of the obtained results in terms of quantum information processing. The achieved success probability is smaller than the theoretically achievable value 1, but nevertheless it is sizably larger than the value of 0.25 obtained by running once the classical algorithm that consists in making a random trial. From the point of view of a user who has to find out which unknown oracle has been given to him, the fidelity of the algorithm outcome is $f_{ab} = 0.57$, 0.63, 0.57, and 0.59 for the 00, 01, 10, and 11 outcomes, respectively, as explained in Sec. V of the Supplemental Material.[16] Despite the presence of errors, this result demonstrates the quantum speed-up for Grover's algorithm when searching in a Hilbert space with a small size $N = 4$.

In conclusion, we have demonstrated the operation of the Grover search algorithm in a superconducting two-qubit processor with a single-shot nondestructive readout. This result indicates that the quantum speed-up expected from quantum algorithms is within reach of superconducting quantum bit processors. Demonstrating the $\sqrt{N}$ speed-up for Grover's algorithm in larger Hilbert spaces requires a qubit architecture

more scalable than the present one, which presently is a major challenge in the field.

We gratefully acknowledge discussions with M. Devoret, D. DiVicenzo, L. DiCarlo, and within the Quantronics group, technical support from P. Orfila, P. Senat, and J. C. Tack, as well as financial support from the European research contract SOLID, from ANR Masquelspec and C'Nano, and from the German Ministry of Education and Research.

[1] L. K. Grover, in *Proceedings of the 28th Annual ACM Symposium on the Theory of Computing*, edited by G. L. Miller (ACM, New York, 1996), p. 212; Am. J. Phys. **69**, 769 (2001).

[2] P. W. Shor, *Proceedings of the 35th Annual Symposium on Foundations of Computer Science* (IEEE, Los Alamitos, CA, 1994); SIAM J. Comput. **26**, 1484 (1997).

[3] M. A. Nielsen and I. L. Chuang, *Quantum Computation and Quantum Information* (Cambridge University Press, Cambridge, UK, 2000).

[4] T. D. Ladd, F. Jelezko, R. Laflamme, Y. Nakamura, C. Monroe, and J. L. O'Brien, Nature (London) **464**, 45 (2010).

[5] D. P. DiVincenzo, Fortschr. Phys. **48**, 771 (2000).

[6] J. Koch, T. M. Yu, J. Gambetta, A. A. Houck, D. I. Schuster, J. Majer, A. Blais, M. H. Devoret, S. M. Girvin, and R. J. Schoelkopf, Phys. Rev. A **76**, 042319 (2007).

[7] J. A. Schreier, A. A. Houck, J. Koch, D. I. Schuster, B. R. Johnson, J. M. Chow, J. M. Gambetta, J. Majer, L. Frunzio, M. H. Devoret, S. M. Girvin, and R. J. Schoelkopf, Phys. Rev. B **77**, 180502 (2008).

[8] Y. Nakamura, Yu. A. Pashkin, and J. S. Tsai1, Nature (London) **398**, 786 (1999).

[9] D. Deutsch and R. Jozsa, Proc. R. Soc. London A**439**, 553 (1992).

[10] L. DiCarlo, J. M. Chow, J. M. Gambetta, L. S. Bishop, B. R. Johnson, D. I. Schuster, J. Majer, A. Blais, L. Frunzio, S. M. Girvin, and R. J. Schoelkopf, Nature (London) **460**, 240 (2009).

[11] M. D. Reed, L. DiCarlo, S. E. Nigg, L. Sun, L. Frunzio, S. M. Girvin, and R. J. Schoelkopf, Nature (London) **482**, 382 (2012).

[12] T. Yamamoto, M. Neeley, E. Lucero, R. C. Bialczak, J. Kelly, M. Lenander, M. Mariantoni, A. D. O'Connell, D. Sank, H. Wang, M. Weides, J. Wenner, Y. Yin, A. N. Cleland, and J. M. Martinis, Phys. Rev. B **82**, 184515 (2010).

[13] M. Mariantoni, H. Wang, T. Yamamoto, M. Neeley, R. C. Bialczak, Y. Chen, M. Lenander, E. Lucero, A. D. O'Connell, D. Sank, M. Weides, J. Wenner, Y. Yin, J. Zhao, A. N. Korotkov, A. N. Cleland, and J. M. Martinis, Science **334**, 6052 (2011).

[14] E. Lucero, R. Barends, Y. Chen, J. Kelly, M. Mariantoni, A. Megrant, P. O'Malley, D. Sank, A. Vainsencher, J. Wenner, T. White, Y. Yin, A. N. Cleland, and J. M. Martinis, e-print arXiv:1202.5707.

[15] A. Dewes, F. R. Ong, V. Schmitt, R. Lauro, N. Boulant, P. Bertet, D. Vion, and D. Esteve, Phys. Rev. Lett. **108**, 057002 (2012).

[16] See Supplemental Material at http://link.aps.org/supplemental/10.1103/PhysRevB.85.140503 for technical information about the sample preparation (I), sample parameters (II), and experimental setup (III), and for the detailed analysis of readout errors (IV) and algorithm fidelity (V).

[17] F. R. Ong, M. Boissonneault, F. Mallet, A. Palacios-Laloy, A. Dewes, A. C. Doherty, A. Blais, P. Bertet, D. Vion, and D. Esteve, Phys. Rev. Lett. **106**, 167002 (2011).

[18] F. Mallet, Florian R. Ong, A. Palacios-Laloy, F. Nguyen, P. Bertet, D. Vion, and D. Esteve, Nat. Phys. **5**, 791 (2009).

[19] I. Siddiqi, R. Vijay, F. Pierre, C. M. Wilson, M. Metcalfe, C. Rigetti, L. Frunzio, and M. H. Devoret, Phys. Rev. Lett. **93**, 207002 (2004).

[20] M. B. Metcalfe, E. Boaknin, V. Manucharyan, R. Vijay, I. Siddiqi, C. Rigetti, L. Frunzio, R. J. Schoelkopf, and M. H. Devoret, Phys. Rev. B **76**, 174516 (2007).

[21] J. A. Jones, M. Mosca, and R. H. Hansen, Nature (London) **393**, 344 (1998).

[22] I. L. Chuang, N. Gershenfeld, and M. Kubinec, Phys. Rev. Lett. **80**, 3408 (1998).

[23] K. A. Brickman, P. C. Haljan, P. J. Lee, M. Acton, L. Deslauriers, and C. Monroe, Phys. Rev. A **72**, 050306 (2005).

[24] N. Bhattacharya, H. B. van Linden van den Heuvell, and R. J. C. Spreeuw, Phys. Rev. Lett. **88**, 137901 (2002).

[25] P. Walther, K. J. Resch, T. Rudolph, E. Schenck, H. Weinfurter, V. Vedral, M. Aspelmeyer, and A. Zeilinger, Nature (London) **434**, 169 (2005).

[26] J. Ahn, T. C. Weinacht, and P. H. Bucksbaum, Science **287**, 463 (2000).

Supplemental material

Demonstrating quantum speed-up in a superconducting two-qubit processor

A. Dewes[1], R. Lauro[1], F.R. Ong[1], V. Schmitt[1],
P. Milman[2], P. Bertet[1], D. Vion[1], and D. Esteve[1]
[1]*Service de Physique de l'Etat Condensé/IRAMIS/DSM (CNRS URA 2464),*
CEA Saclay, F-91191 Gif-sur-Yvette, France and
[2]*Laboratoire Matériaux et Phénomènes Quantiques,*
Université Paris Diderot, Bâtiment Condorcet, 10,
rue Alice Domon et Léonie Duquet, F75205 Paris, France

I. SAMPLE PREPARATION

The sample is fabricated on a silicon chip oxidized over 50 nm. A 150 nm thick niobium layer is first deposited by magnetron sputtering and then dry-etched in a SF_6 plasma to pattern the readout resonators, the current lines for frequency tuning, and their ports. Finally, the transmon qubit, the coupling capacitance and the Josephson junctions of the resonators are fabricated by double-angle evaporation of aluminum through a shadow mask patterned by e-beam lithography. The first layer of aluminum is oxidized in a $Ar - O_2$ mixture to form the oxide barrier of the junctions. The chip is glued with wax on a printed circuit board (PCB) and wire bonded to it. The PCB is then screwed in a copper box anchored to the cold plate of a dilution refrigerator.

II. SAMPLE PARAMETERS

The sample is first characterized by spectroscopy [15]. The incident power used is high enough to observe the resonator frequency $\nu_{\rm R}$, the qubit line ν_{01}, and the two-photon transition at frequency $\nu_{02}/2$ between the ground and second excited states of each transmon. A fit of the transmon model to the data yields the sample parameters, i.e. total Josephson energies of the transmons in zero magnetic field $E_{\rm J}^{\rm I}/h = 36.2\,{\rm GHz}$ and $E_{\rm J}^{\rm II}/h = 43.1\,{\rm GHz}$, total charging energies $E_{\rm C}^{\rm I}/h = 0.98\,{\rm GHz}$ and $E_{\rm C}^{\rm II}/h = 0.87\,{\rm GHz}$, assymetries between the two junctions of a transmon $d_I = 0.2$ and $d_{\rm II} = 0.35$. The measured resonance frequencies of the readout resonators are $\nu_{\rm R}^{\rm I} = 6.84\,{\rm GHz}$, and $\nu_{\rm R}^{\rm II} = 6.70\,{\rm GHz}$. The qubit-readout anticrossing at $\nu = \nu_{\rm R}$ yields the qubit-readout couplings $g_0^{\rm I} \simeq g_0^{\rm II} \simeq (2\pi)\,50\,{\rm MHz}$. Independent measurements of the resonator dynamics yield quality factors $Q_{\rm I} = Q_{\rm II} = 730$ and Kerr non linearities [15,17] $K_{\rm I}/\nu_{\rm R}^{\rm I} \simeq K_{\rm II}/\nu_{\rm R}^{II} \simeq -2.3 \pm 0.5 \times 10^{-5}$.

III. EXPERIMENTAL SETUP

- Qubit resonant microwave pulses: The qubit drive pulses are generated by two phase-locked microwave generators feeding a pair of I/Q-mixers. The IF inputs are provided by a 4-Channel1 GS/s arbitrary waveform generator (AWG Tektronix AWG5014). Single-sideband mixing in the frequency range of 50-300 MHz is used to generate

multi-tone drive pulses and to obtain a high ON/OFF ratio ($> 50\,\mathrm{dB}$). Phase and amplitude errors are corrected by applying suitable sideband and carrier frequency dependent corrections to the amplitude and offset of the IF signals.

- Qubit frequency control: Flux control pulses are generated by a second AWG and sent to the chip through a transmission line equipped with 40 dB total attenuation and a pair of 1 GHz dissipative low-pass filters at 4 K. The input signal of each flux line is returned to room temperature through an identical transmission line and measured, which allows to compensate the non-ideal frequency response of the line.

- Readout pulses: The driving pulses for the Josephson bifurcation amplifier (JBA) readouts are generated by mixing the continuous signals of a pair of microwave generators with IF pulses provided by a 1 GS/s arbitrary waveform generator (AWG Tektronix AWG5014). Each readout pulse consists of a measurement part with a rise time of 30 ns and a hold time of 100 ns, followed by a $2\,\mu s$ long latching part at 90 % of the pulse height.

- Drive and measurement lines: The drive and readout microwave signals of each qubit are combined and sent to the sample through a pair of transmission lines with total attenuation 70 dB and filtered at 4 K and 300 mK. A microwave circulator at 20 mK protects the chip from the amplifier noise. The signals are amplified by 36 dB at 4 K by two cryogenic HEMT amplifiers (CIT Cryo 1) with noise temperature 5 K. The reflected readout pulses are amplified and demodulated at room temperature. The IQ quadratures of the demodulated signals are sampled at 1 GS/s by a 4-channel data acquisition system (Acqiris DC282).

IV. READOUT ERRORS

Errors in our readout scheme are discussed in detail in Ref. [15] for a single qubit. First, incorrect mapping $|0\rangle \rightarrow 1$ or$|1\rangle \rightarrow 0$ of the projected state of the qubit to the dynamical state of the resonator can occur, due to the stochastic nature of the switching between the two dynamical states. As shown in Fig. 4.1, the probability p to obtain the outcome 1 varies continuously from 0 to 1 over a certain range of drive power P_d applied to the readout. When the shift in power between the two $p_{|0\rangle,|1\rangle}(P_\mathrm{d})$ curves is not much larger than

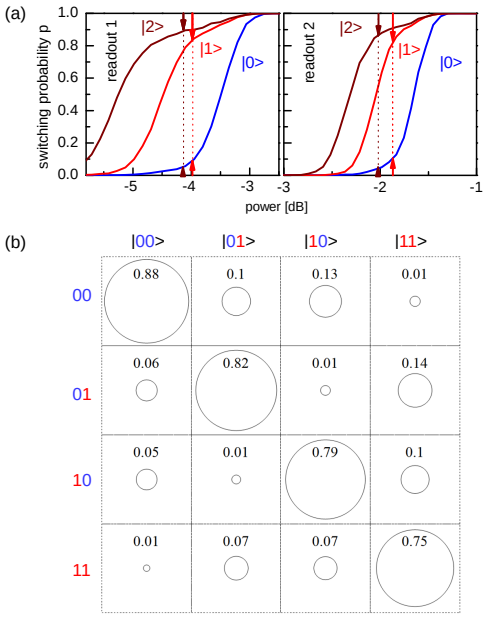

Figure IV.1:

(a) Switching probability p of each readout as a function of its peak driving power, when its qubit is prepared in state $|0\rangle$ (blue), $|1\rangle$ (red), or $|2\rangle$ (brown), with the other qubit being far detuned. The arrows indicate the readout errors where the contrast is optimal with (brown) and without (red) $|1\rangle \rightarrow |2\rangle$ shelving. (b) Readout matrix $\mathcal{R}$ giving the probabilities of the four ab outcomes, for the four computational input states $|uv\rangle$, when using $|1\rangle \rightarrow |2\rangle$ shelving. Each matrix elements is represented by a circle of area proportional to its value (a unit circle would touch the cell borders).

this range, the two curves overlap and errors are significant even at the optimal drive power where the difference in p is maximum. Second, even in the case of non overlapping $p_{|0\rangle,|1\rangle}(P_{\rm d})$ curves, the qubit initially projected in state$|1\rangle$ can relax down to $|0\rangle$ before the end of the measurement, yielding an outcome 0 instead of 1. The probability of these two types of errors vary in opposite directions as a function of the frequency detuning $\Delta = \nu_{\rm R} - \nu > 0$ between the resonator and the qubit, so that a compromise has to be found for Δ. As explained in the main text, we use a shelving method to the second excited state in order to improve the readout contrast $c = Max\left(p_{|1\rangle} - p_{|0\rangle}\right)$, with a microwave π pulse at frequency

ν_{12} bringing state $|1\rangle$ into state $|2\rangle$ just before the readout pulse. The smallest errors $e_0^{\mathrm{I,II}}$ and $e_1^{\mathrm{I,II}}$ when reading $|0\rangle$ and $|1\rangle$ are found for $\Delta_{\mathrm{I}} = 440\,\mathrm{MHz}$ and $\Delta_{\mathrm{II}} = 575\,\mathrm{MHz}$: $e_0^{\mathrm{I}} = 5\%$ and $e_1^{\mathrm{I}} = 13\%$ (contrast $c_{\mathrm{I}} = 1 - e_0^{\mathrm{I}} - e_1^{\mathrm{I}} = 82\%$), and $e_0^{\mathrm{II}} = 5.5\%$ and $e_1^{\mathrm{II}} = 12\%$ ($c_{\mathrm{II}} = 82\%$). When using the $|1\rangle \rightarrow |2\rangle$ shelving before readout, $e_0^{\mathrm{I}} = 2.5\%$ and $e_2^{\mathrm{I}} = 9.5\%$ (contrast $c_{\mathrm{I}} == 1 - e_0^{\mathrm{I}} - e_2^{\mathrm{I}} = 88\%$), and $e_0^{\mathrm{II}} = 3\%$ and $e_2^{\mathrm{II}} = 8\%$ ($c_{\mathrm{II}} = 89\%$). These best results are very close to those obtained in Ref. [15] of main text, but cannot however be exploited for simultaneous readout of the two qubits.

Indeed, when the two qubits are measured simultaneously, we find an influence of the projected state of each qubit on the outcome of the readout of the other one. In order to to minimize this spurious effect, we increase the detuning $\Delta_{\mathrm{I,II}}$ up to $\sim 1\,\mathrm{GHz}$ with respect to previous optimal values. An immediate consequence shown in Fig. S4.1(a) is a reduction of the $c_{\mathrm{I,II}}$ contrasts. The errors when reading $|0\rangle$ and $|1\rangle$ are then $e_0^{\mathrm{I}} = 10\,\%$ and $e_1^{\mathrm{I}} = 16\,\%$ (contrast $c_{\mathrm{I}} = 74\%$) and $e_0^{\mathrm{II}} = 12\,\%$ and $e_1^{\mathrm{II}} = 15\,\%$ (contrast $c_{\mathrm{II}} = 73\%$). When shelving the qubit in state $|2\rangle$, the errors are $e_0^{\mathrm{I}} = 5\,\%$, $e_2^{\mathrm{I}} = 11\,\%$ (contrast $c_{\mathrm{I}} = 84\%$), $e_0^{\mathrm{II}} = 5\,\%$, $e_2^{\mathrm{II}} = 12\,\%$ (contrast $c_{\mathrm{I}} = 83\%$). The readout errors are captured in the 4×4 readout matrix $\mathcal{R}$ shown in Fig. S4.1(c), that gives the probabilities p_{uv} of the four possible outcomes for the different input states using the $|1\rangle \rightarrow |2\rangle$ shelving technique. This matrix $\mathcal{R}$ is used to correct the readout errors only when doing state tomography, and not when the running the algorithm once. The cause of the readout crosstalk in our processor is discussed in Ref. [15].

V. ALGORITHM FIDELITY

From the point of view of a user that would search which unknown oracle has been given to him, the fidelity f_{ab} of the algorithm for each possible outcome ab is $f_{ab} = p_{ab/O_{ab}} / \left(p_{ab/O_{00}} + p_{ab/O_{01}} + p_{ab/O_{10}} + p_{ab/O_{11}}\right)$ with $p_{ab/O_{uv}}$ the probability of obtaining outcome ab knowing that O_{uv} has been used. These probabilities are shown in table V.1, yielding $f_{00,01,10,11} = 0.57$, 0.63, 0.57, and 0.59.

ab/O_{uv}	O_{00}	O_{01}	O_{10}	O_{11}	$\sum$	f_{ab}
00	0.666	0.192	0.188	0.122	1.168	57.0 %
01	0.127	0.554	0.071	0.122	0.874	63.4 %
10	0.128	0.106	0.615	0.239	1.088	56.5 %
11	0.079	0.148	0.126	0.517	0.870	59.4 %

Table V.1: Conditional probabilities $p_{ab/O_{uv}}$ and statistical fidelities f_{ab} for all possible outcomes ab, measured for our version of Grover's algorithm.

High-gain weakly nonlinear flux-modulated Josephson parametric amplifier using a SQUID array

X. Zhou,[1] V. Schmitt,[1] P. Bertet,[1] D. Vion,[1] W. Wustmann,[2] V. Shumeiko,[2] and D. Esteve[1]
[1]*Service de Physique de l'Etat Condensé/IRAMIS/DSM (CNRS URA 2464), CEA Saclay, 91191 Gif-sur-Yvette, France*
[2]*Chalmers University of Technology, S-41296 Goteborg, Sweden*
(Received 28 February 2014; revised manuscript received 2 June 2014; published 30 June 2014)

We have developed and measured a high-gain quantum-limited microwave parametric amplifier based on a superconducting lumped *LC* resonator with the inductor *L* including an array of eight superconducting quantum interference devices (SQUIDs). This amplifier is parametrically pumped by modulating the flux threading the SQUIDs at twice the resonator frequency. Around 5 GHz, a maximum gain of 31 dB, a product amplitude gain × bandwidth above 60 MHz, and a 1 dB compression point of −123 dBm at 20 dB gain are obtained in the nondegenerate mode of operation. Phase-sensitive amplification-deamplification is also measured in the degenerate mode and yields a maximum gain of 37 dB. The compression point obtained is 18 dB above what would be obtained with a single SQUID of the same inductance, due to the smaller nonlinearity of the SQUID array.

DOI: 10.1103/PhysRevB.89.214517 PACS number(s): 85.25.Dq, 84.40.Dc, 42.50.Lc, 42.65.Yj

Although superconducting parametric amplifiers based on Josephson junctions have been known and understood for decades [1,2], they have recently received increased attention [3] because of their ability to measure single quantum objects and engineer quantum fluctuations of a microwave field. They are extensively used to readout superconducting quantum bits [4–6] or mechanical resonators [7] at or near the quantum limit, i.e., with minimum backaction imposed by quantum mechanics for the given amount of information taken on the system. They have permitted, for instance, the measurement of quantum trajectories [4] and the implementation of quantum feedback schemes [8,9]. In the field of quantum microwaves, they are also used to squeeze quantum noise and produce itinerant squeezed states for encoding quantum information [10,11] or demonstrating fundamental effects such as the reduction of the radiative decay of an artificial atom [12].

Compared to the noisier high electron mobility transistor (HEMT)-based amplifiers, these Josephson parametric amplifiers (JPAs) suffer from limited bandwidth and from gain saturation at extremely low input power. A strong effort is thus made to increase the bandwidth and to mitigate saturation of JPAs by varying their design and mode of operation [13–16]. In all cases, parametric amplification of a signal at angular frequency ω_S occurs by transfer of energy from a pump at frequency ω_P to the signal and to a complementary idler frequency ω_I. For amplifiers based on resonators, one distinguishes the case of intrinsically nonlinear resonators, with bare frequency ω_R that are pumped at $\omega_P \simeq \omega_S \simeq \omega_R$ directly on their signal line, from the (possibly linear) resonators, whose frequency ω_R is parametrically modulated with a pump tone at $\omega_P \simeq 2\omega_S \simeq 2\omega_R$ on a dedicated line separated from the signal port. In the first case, the intrinsic nonlinearity of the resonator is usually obtained by implementing all or part of its inductance by Josephson junctions (or superconducting weak links). The pumping at ω_P at sufficiently high amplitude modulates this nonlinear inductance at $2\omega_P$, and is responsible for a four-wave mixing such that $2\omega_P = \omega_S + \omega_I$. In the present work, we are interested in the second case [17,18], for which the nonlinearity is due to an externally imposed parametric modulation of the frequency and is responsible for a three-wave mixing such that $\omega_P = \omega_S + \omega_I$. The interest of this three-wave mixing is that no pump mode propagates along the input and output signal lines and can blind a detector or spoil a squeezed field, at a close frequency. In practice, the true parametric modulation is usually obtained by embedding in the resonator inductance one or several superconducting quantum interference devices (SQUIDs), the Josephson inductance of which is modulated by an ac magnetic flux. The nonlinearity of the resonator inherited from the SQUID(s) is, in this case, an unwanted feature, which leads to saturation of amplification and should thus be kept low. So besides the advantage of getting rid of the pump along the signal lines, a truly parametrically pumped amplifier can also be made more robust against saturation by reducing its nonlinearity without having to pump it more strongly. In this work, we test this idea and demonstrate a weakly nonlinear JPA with high gain, made of a lumped *LC* resonator with the inductor *L* terminated by a SQUID array. This paper first summarizes the theoretical description of such a JPA, then describes the device implemented and its characterization setup, and finally presents the experimental data and a comparison between measured and calculated gain, bandwidth, and saturation.

I. THEORETICAL SUMMARY AND DESIGN CHOICES

The specificity of the JPA presented here (pure three-wave mixing with spurious nonlinearity) makes the standard classical description of parametric amplifiers [2] not directly applicable to it. This is why a comprehensive theoretical summary is given here, based on the theoretical work [19] (note that a similar theoretical treatment can be found in [20]). The equivalent circuit of the JPA is shown in the bottom-right corner of Fig. 1(b). For a dc flux bias Φ_{DC}, a parametric modulation $\delta L_A \cos(\omega_P t)$ of its array inductance L_A, and a microwave input signal $V_S \cos(\omega_S t + \chi)$, the JPA equation of motion at the lowest nonlinear order in phase $\varphi = 1/\varphi_0 \int V dt$ across the total inductance $L = L_g + L_A(\Phi_{DC})$ or the capacitance C_R is

$$\varphi'' + 2\Gamma_a \varphi' + \omega_R^2[1 + a_P(\Phi_{AC})\cos(\omega_P t)]\varphi + \alpha_1 \varphi^3 = \varphi_S \cos(\omega_S t + \chi), \quad (1)$$

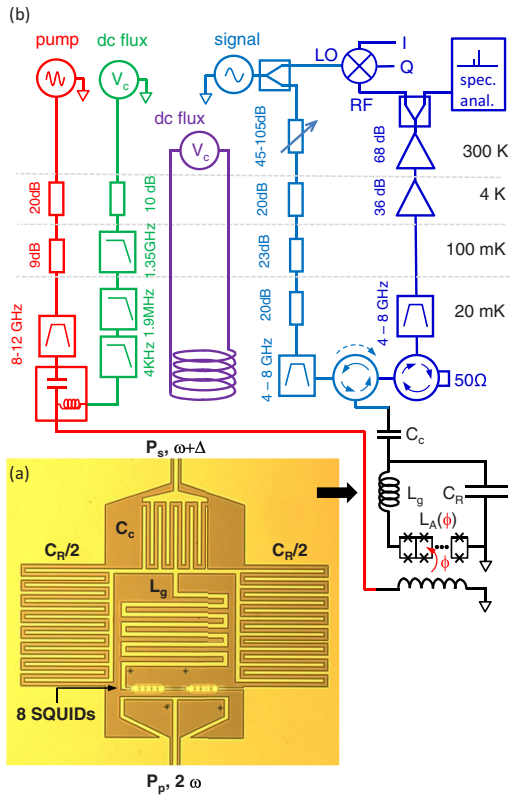

FIG. 1. (Color online) Experimental setup. (a) Optical micrograph of the tested parametric amplifier showing its 50 Ω coplanar waveguide (CPW) signal input port (top), its coupling capacitor C_c, its capacitor C_R (left and right), its inductor L_g (middle) terminated by an eight-SQUID array with total inductance $L_A(\Phi)$, and its split magnetic flux line coupled to a 50 Ω CPW (bottom). The dc current in the flux line sets the dc flux Φ_{DC} and the resonance frequency f_R of the resonator, whereas the ac current parametrically pumps the resonator at $\omega_P \simeq 2\omega_R$. The black arrow points to the equivalent circuit. (b) Electrical circuit diagram showing (from left to right) the pump line, the dc flux line added to the pump with a bias tee, an additional flux line feeding a coil for compensating any flux offsets, the signal line, and a circulator routing the reflected and amplified signal to a measurement line through an isolator protecting the sample from the noise of the first amplifier placed at 4 K. Feeding lines are attenuated and filtered. The output signal is split after amplification and analyzed both with a spectrum analyzer and by homodyne demodulation.

where $\varphi_0 = \hbar/2e = \Phi_0/2\pi$ is the reduced flux quantum, $\omega_R = 2\pi f_R = 1/\sqrt{L(C_R + C_c)}$ is the frequency of the resonator, $\omega_P = 2\pi f_P$ is the pumping frequency, $\Gamma_a = \omega_R/2Q$ is its amplitude decay rate, $a_P = \delta L_A(\Phi_{AC})/L$ is the relative pumping amplitude, $\alpha_1 = -\omega_R^2 p^3/2N^2$ is the Josephson nonlinearity coefficient with N the number of SQUIDs and $p = L_J/L$ the so-called participation ratio of the total Josephson inductance L_J to the total inductance L, and φ_S is the drive amplitude proportional to V_S. Taking into account the finite ratio β of each SQUID loop inductance to the inductance L_{J1} of a single junction, the SQUID array inductance is $L_A = NL_{J1}\beta/4 + L_J$, with $L_J = NL_{J1}/\{2[\cos(x) + \beta/2\sin^2(x)]\}$ [21] and $x = \pi\Phi/\Phi_0$.

Equation (1) contains the parametric nonlinearity $\cos(\omega_P t)\varphi$ and the intrinsic Josephson nonlinearity $\alpha_1\varphi^3$ mentioned in the introduction. We rewrite it in the frame rotating at $\omega_P/2$ using the slow complex internal amplitude $A(t)$ defined by $\varphi(t) = A(t)\sqrt{Z_R}e^{-i\omega_P t/2} + \text{c.c.}$, as well as the constant complex amplitude B_S of the input signal and the slow output amplitude $C(t)$ related to the input and output voltages $V_{\text{in,out}}$ by $V_{\text{in}}(t) = i\varphi_0\sqrt{Z_0\omega_S}B_S e^{-i\omega_S t}/2 + \text{c.c.}$ and $V_{\text{out}}(t) = i\varphi_0\sqrt{Z_0\omega_S}C(t)e^{-i\omega_S t}/2 + \text{c.c.}$ Here, Z_0 is the impedance of the line, $Z_R = \sqrt{L/(C_R + C_c)}$ is the characteristic impedance of the resonator, and c.c. stands for the complex conjugate of the previous term. Neglecting fast oscillating terms (rotating wave approximation), one obtains [19]

$$iA' + (i\Gamma_a + \delta + \alpha|A^2|)A + \epsilon A^* = \sqrt{2\Gamma_a}B_S e^{-i\Delta t},$$
$$C = -i\sqrt{2\Gamma_a}A + B_S, \quad (2)$$

where $\delta = \omega_P/2 - \omega_R$ is the pump to resonator detuning, $\Delta = \omega_S - \omega_P/2$ is the signal to pump detuning, $\alpha = -p^3 Z_R\omega_R/16N^2$ is the new nonlinear coefficient, and $\epsilon = \omega_R a_P = 2\omega_R\kappa\Phi_{AC}/\Phi_0$ is the pumping strength, with $\kappa \propto pQ$ the relative frequency change per flux quantum deduced from the slope of the modulation curve $\omega_R(\Phi_{DC})$.

Although the most general stationary solution of Eq. (2) is a sum $\sum_{k\in\mathbb{Z}} A_k e^{-ik\Delta t}$ of all harmonics at frequencies $\omega_P/2 + k\Delta$, only the signal $A_S = A_1$ and the idler $A_I = A_{-1}$ contributions happen to be non-negligible at not too high pumping strength. In this case, they obey

$$\{[\delta_r + \alpha_r(|A_S|^2 + 2|A_I|^2)] + \Delta_r + i\}A_S + \epsilon_r A_I^* = \sqrt{2/\Gamma_a}B_S,$$
$$\{[\delta_r + \alpha_r(2|A_S|^2 + |A_I|^2)] - \Delta_r + i\}A_I + \epsilon_r A_S^* = 0,$$
$$C_S = -i\sqrt{2\Gamma_a}A_S + B_S, \quad C_I = -i\sqrt{2\Gamma_a}A_I, \quad (3)$$

with $\delta_r = \delta/\Gamma_a$, $\Delta_r = \Delta/\Gamma_a$, $\alpha_r = \alpha/\Gamma_a = -p^3 Z_R Q/8N^2$, and $\epsilon_r = \epsilon/\Gamma_a$ the dimensionless detunings, nonlinear coefficient, and pumping strength, respectively.

Our goal is to make the nonlinearity α_r as small as possible and benefit from the linear signal and idler complex gains given by system (3) when $\alpha_r = 0$, i.e.,

$$G_S = \frac{C_S}{B_S} = \frac{\delta_r^2 - \Delta_r^2 - 1 - \epsilon_r^2 - 2i\delta_r}{\delta_r^2 - \Delta_r^2 + 1 - \epsilon_r^2 - 2i\Delta_r},$$
$$G_I = \frac{C_I}{B_S} = \frac{2i\epsilon_r}{\delta_r^2 - \Delta_r^2 + 1 - \epsilon_r^2 + 2i\Delta_r}e^{i2\chi}, \quad (4)$$

yielding the power gains

$$|G_S|^2 = 1 + |G_I|^2 = 1 + \frac{4\epsilon_r^2}{\left[1 - \epsilon_r^2 + \delta_r^2 - \Delta_r^2\right]^2 + 4\Delta_r^2}. \quad (5)$$

In the degenerate case corresponding to $\Delta = 0$, the signal power gain becomes phase χ dependent and is given by

$$|G_{S,\mathrm{deg}}|^2(\chi) = 1 + 4\epsilon_r \frac{2[\epsilon_r - \delta_r \cos(2\chi)] + \left(1 + \epsilon_r^2 - \delta_r^2\right)\sin(2\chi)}{\left(1 - \epsilon_r^2 + \delta_r^2\right)^2}. \tag{6}$$

Equations (4)–(6) are valid only below the onset of parametric oscillations, that is, of pump-induced auto-oscillations at zero signal B_S for $\epsilon_r > 1 + \delta_r^2$. For sufficiently large pumping strength $\epsilon_r > 0.42$, the power gain $|G_S|^2$ is larger than 2 at small Δ_r and δ_r, and a gain bandwidth $\Delta\omega = 2\pi\Delta f$ at -3 dB can be defined. For the optimal pumping frequency $\delta_r = 0$, we find

$$\frac{\Delta\omega}{2\Gamma_a} = \sqrt{\left(1 + \epsilon_r^2\right)\left(\frac{2\epsilon_r}{\sqrt{\epsilon_r^4 - 6\epsilon_r^2 - 1}} - 1\right)}, \tag{7}$$

which yields a gain bandwidth product

$$|G_S|\Delta\omega/2\Gamma_a \simeq 1 \tag{8}$$

that is constant within 10% above the 7 dB gain. Then, saturation can be evaluated approximately in an easy way by noticing that as the internal amplitudes of oscillation A_S and A_I increase with the pumping strength and gain, they tend to the same value when $|G_S|^2 \simeq |G_I|^2 \gg 1$ [see Eq. (5)]. Consequently, the terms in α_r in the first two equations of system (3) also converge to close values and play the very same role as the pump to resonator detuning δ_r, which is itself responsible for a gain drop given by Eq. (6). Equating $\alpha_r|A_S^2 + 2A_I^2|$ at $\delta_r = 0$ to the value $\delta_{r,\mathrm{sat}} = 0.35\sqrt{1 - \epsilon_r^2}$ that produces a -1 dB drop of $|G_S|^2 - 1$ leads to the following equivalent values for A_S and B_S (so-called 1 dB compression point):

$$A_{S,\mathrm{sat}}^2 \simeq \frac{0.35}{|\alpha_R|}\frac{\sqrt{1 - \epsilon_r^2}}{1 + 2\epsilon_r^2}, \qquad \frac{B_{S,\mathrm{sat}}^2}{\Gamma_a} \simeq \frac{0.17}{|\alpha_R|}\frac{\left(1 - \epsilon_r^2\right)^{5/2}}{1 + 2\epsilon_r^2}. \tag{9}$$

In addition, saturation at large gain $|G_S|$ has to occur when the peak current i in the junctions is still well below their critical current i_c. Since at $\delta_r \sim 0$, $i/i_c = (1 + \epsilon_r)|A_S|p\sqrt{Z_r}/N$, keeping $i/i_c < 0.5$ yields the design rule

$$pQ > 21/\sqrt{|G_{S,\max}| + 1}, \tag{10}$$

which imposes a minimum p for low-Q and wide-bandwidth JPAs.

In this work, we choose to implement a tunable amplifier in the 5–6 GHz range with a quality factor Q of order 100, which should have a product gain × bandwidth of ∼50 MHz according to Eq. (8). To reduce the maximum microwave pumping power corresponding to $\epsilon_r = Qa_P/2 = 1$, i.e., to a modulation $a_P \sim 1\%$ of the total inductance, a high participation ratio $p \simeq 0.5$ is chosen. On the other hand, in order to keep the nonlinearity α_r weak and to increase the 1 dB compression point $B_{S,\mathrm{sat}}$, the tunable inductance is implemented with $N = 8$ SQUIDs. In this case, the saturation power is increased by N^2 or 18 dB, compared to the case of a single SQUID with the same total Josephson inductance. Finally, as Z_r plays only a minor role in the nonlinearity α_r (in comparison with $p^3$and N^{-2}), its value will be simply chosen at the best convenience for implementing the lumped element resonator.

II. SAMPLE AND MEASUREMENT SETUP

An optical micrograph of the JPA and its equivalent circuit are shown in Fig. 1(a). This JPA is made of an interdigitated coplanar capacitor to ground (split in two parts) with capacitance $C_R = 0.40$ pF, in parallel with an inductance to ground L combining in series a meander of inductance $L_g = 0.80$ nH with an array of eight SQUIDs of total Josephson inductance $L_J = 0.88$ nH at zero magnetic flux Φ. Being designed to be operated in reflection, this LC circuit is coupled to a single input-output signal line [50 Ω coplanar waveguide (CPW)] through a $C_c = 55$ fF capacitance yielding a characteristic impedance $Z_r \backsimeq 65$ Ω and a quality factor $Q \simeq 70$ at $\Phi = 0$. On the other side of the device, a 50 Ω CPW line shorted to ground by two loops coupled inductively to four SQUIDS each serves both for their dc flux biasing and for parametric pumping. Note that after compensation of any global dc flux offset, the magnetic fluxes Φ are exactly opposite in the left and right four SQUID subarrays, which yields the same inductance modulation.

The device was fabricated on a thermally oxidized Si chip by sputtering 170 nm of niobium and patterning the whole structure (except the SQUID array) by optical lithography and CF_4-Ar reactive ion etching. The SQUID array was then fabricated by electron-beam lithography and double-angle evaporation of aluminum with oxidation of the first Al layer. Each SQUID has a loop area of 8×15 μm and two junctions with nominal area 2.2×0.7 μm and tunnel resistance 141 Ω, yielding $\beta \simeq 0.1$. The active antenna wires of the pump line are positioned 16 μm away from the SQUID centers.

The measurement setup is schematized in Fig. 1(b). A small superconducting coil is used to compensate the global dc flux offset. The dc flux biasing and ac pumping of the SQUIDs are obtained by two attenuated and filtered lines combined with a bias tee. The input line includes attenuators at various temperatures and a 4–8 GHz bandpass filter. The -71.5 and -51 dB transmissions of the input and pumping lines are calibrated with a ± 1 dB uncertainty. The reflected and amplified signal is routed to the output line by a cryogenic circulator with -18 dB isolation. This output line includes an isolator for protecting the sample from higher-temperature noise, a 4–8 GHz filter, a cryogenic high electron mobility transistor (HEMT) amplifier at 4 K with 38 dB gain and a calibrated noise temperature of 3.8 K, as well as additional room-temperature amplifiers. The output signal is finally analyzed using a spectrum analyzer or a homodyne demodulator followed by a digitizer. Microwave generators for the input signal and pump are precisely phase locked.

III. EXPERIMENTAL RESULTS

Measurements were performed in a dilution refrigerator at the temperature of 30–40 mK. As a preliminary

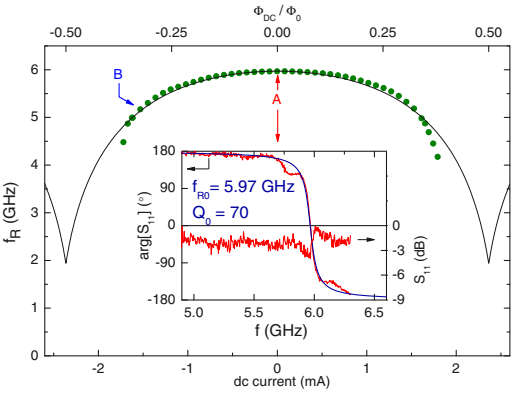

FIG. 2. (Color online) DC flux modulation. Experimental (dots) and calculated (line) resonator frequency f_R as a function of the dc current in the on-chip flux line [see Fig. 1(a)] measured by fitting the phase of a weak signal reflected on the resonator in the absence of parametric pumping, as shown in the inset for zero flux bias (point A). We attribute the two shoulders on the sides of the measured resonance to multiple wave interferences due to an imperfect impedance matching somewhere in the setup. Parameters used for calculation of the modulation curve are f_{R0}, $p = 0.45$, and $\beta = 0.1$. Full characterization in the next figures are done at working point B.

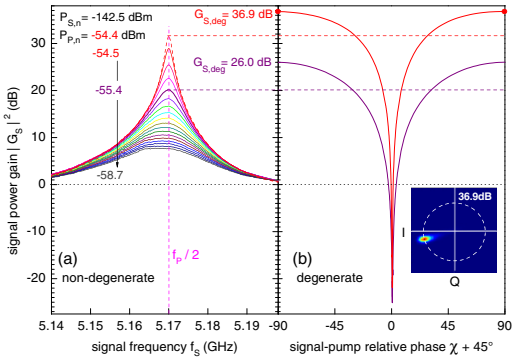

FIG. 3. (Color online) Signal power gain $|G_S|^2$ at working point B of Fig. 2 for a nominal input power $P_{S,n} = -142.5$ dBm. Left: Nondegenerate gain as a function of the signal frequency f_S at different nominal pumping powers $P_{P,n}$ between -58.7 and -54.4 dBm (top dashed curve just before the onset of parametric oscillation in the absence of incident signal). (b) Phase-sensitive degenerate gain for $P_{P,n} = -54.4$ and -55.4 dBm. Inset: Demodulated signal in the IQ plane at maximum gain ($P_{P,n} = -54.4$ dBm) filtered at 1 MHz. I and Q voltages are digitized at 1 MSample/s during 2 s, and the color encodes the density of samples from 0 (dark blue) to maximum (red).

characterization, the resonance was measured with a vectorial network analyzer by recording the phase of the reflected signal at zero pumping and at a nominal input power, $P_{S,n} = -126$ dBm, that is small enough to avoid any nonlinear effects (all nominal powers mentioned here and below refer to powers at the sample ports given the calibration of the lines). The inset of Fig. 2 shows this resonance at zero flux with a fit of the curve yielding a maximum frequency $f_{R0} = 5.97$ GHz. The comparison with the $f_{R1} = 8.06$ GHz resonance frequency of a similar resonator with shorted junctions yields $p = 1 - (f_{R0}/f_{R1})^2 = 0.45$, close to the 0.42 design value. Fitting the expression $-2\arctan[2Q(f_S/f_R - 1)]$ to the measured resonance curve also gives the quality factor $Q_0 \simeq 70$, with, however, limited accuracy due to a setup imperfection yielding spurious multiple wave interferences (see shoulders in inset of Fig. 2). The main graph of Fig. 2 shows the variation of f_R as a function of the applied flux Φ and its comparison with the theoretical prediction from Sec. I. The agreement is only qualitative, especially above 0.35 Φ_0, where f_R decreases faster than predicted by our simple model that does not include either the flux inhomogeneity in the different SQUIDs or the possible penetration of the flux through the junctions.

For characterizing amplification, the input and output lines are then connected as shown in Fig. 1. The signal and idler gains are measured with the spectrum analyzer by comparing the output powers of the signal and idler without and with parametric pumping at $f_P = 2f_R$. The gains increase with $|\Phi_{DC}|$ and the slope of the modulation curve at fixed absolute pumping power. In the following measurement, signal amplification is fully characterized at the working point ($\Phi_1/\Phi_0 = -0.32$, $f_{R1} = 5.17$ GHz), i.e., point B on Fig. 2, where the slope $\kappa_1 = 1.62$ is at the same time large and in agreement with the predicted value. At this point, the SQUID array model predicts a participation ratio $p_1 = 0.59$ and a quality factor $Q_1 = 81$.

The nondegenerate ($\Delta \neq 0$) signal power gain $|G_S|^2$ is measured with the pump frequency $f_P = 2f_R$ ($\delta = 0$) as a function of the signal frequency f_S for increasing nominal pump power $P_{P,n}$, at an input power $P_{S,n} = -142.5$ dBm that is sufficiently low to avoid the saturation at the highest gain. Close to the resonance, a minimum detuning $\delta/2\pi = 5$ kHz is used to avoid operation in the degenerate mode. Figure 3(a) shows the gain increase up to 31.8 dB (dashed top curve, for which parametric oscillations are about to start) and the corresponding bandwidth decrease. The maximum power gain $|G_S|^2$ and the corresponding -3 dB bandwidth Δf deduced from Fig. 3 are plotted in Fig. 4(b) together with the amplitude gain $\times$ bandwidth product $|G_S|\Delta f$. This product happens to be almost constant around 61 MHz over the whole 7–30 dB gain range. Besides, the idler gain (data not shown) approaches the signal gain at large values.

In order to check that the amplifier operates close to the quantum limit, i.e., with a noise temperature of order $T_N = hf_R/2k_B \simeq 125$ mK [22], the variation of the signal and noise powers are compared when switching on and off the pump: From the 2.9 dB increase of the noise when switching on a 18.4 dB gain, from the calibrated 3.8 ± 0.3 K noise temperature of the HEMT amplifier alone in a separate run, and from the 1.7 ± 0.2 dB attenuation of elements placed below 250 mK between the sample and the HEMT amplifier, we deduce an apparent noise temperature of

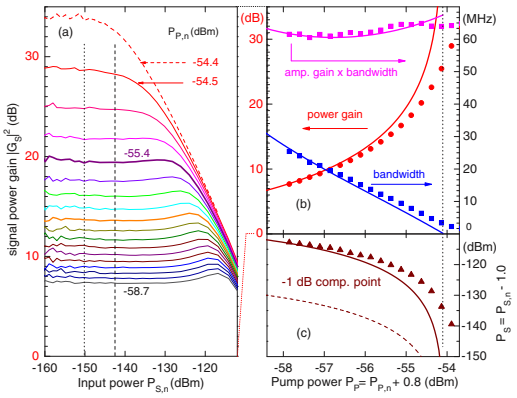

FIG. 4. (Color online) Amplifier characterization at the working point B of Fig. 2 for nondegenerate pumping. (a) Signal power gain as a function of the nominal input power $P_{S,n}$ showing the saturation at the same nominal pumping powers $P_{P,n}$ as in Fig. 3(a) (top dashed line corresponds again to the onset of parametric oscillation). Vertical dashed and dotted lines correspond to the input powers where gain was measured in Fig. 3 and where reference gain for saturation was defined, respectively. (b) Power gain $|G_S|^2$, bandwidth BW, and product $|G_S| \times BW$ deduced from measurements (dots) of Fig. 3(a) at $P_{S,n} = -142.0$ dBm, and calculated (solid lines) from the model with the parameters indicated in the text. (c) 1 dB compression point deduced from (a) (dots), calculated from the model (solid line), and calculated with the same parameters but only one SQUID (dashed line). Note that given the ± 1 dB precision on the calibration of the pumping and signal lines, $+0.8$ and -1.0 dB were added to the nominal $P_{P,n}$ and $P_{S,n}$ values to match the data to the theoretical curves at low pumping strength. The vertical dotted line indicates the frontier between parametric amplification and parametric oscillation (infinite gain) for the linear model.

only 80 ± 10 mK. This value is smaller than the expected quantum limit of 125 mK, a discrepancy that shows that modeling the line by a simple attenuator is not sufficient, as supported by our observation of the setup imperfection already mentioned. This result, nevertheless, indicates that our JPA is not far from the quantum limit. A more precise determination of T_N would require a much more precise control and calibration of the low-temperature part of the measurement line, as well as a switch to connect the detection chain either to the JPA or to a low-temperature reference noise source [10].

The phase-dependent gain in the degenerate case ($\delta = 0$) was then measured with $f_S = 5.17$ GHz by varying the phase χ of the signal with respect to the pump; it is shown in Fig. 3(b) for the two values of the pump power that correspond to a 20 dB gain and to the maximum gain in the nondegenerate mode. As expected, the maximum degenerate gain is 6 dB larger than the nondegenerate gain at almost the same frequency. At the highest degenerate gain of 36.9 dB, it was checked using the IQ demodulator [see inset of Fig. 3(b)] that the phase of the amplified signal is stable over minutes and that the output signal drops down to zero (no parametric oscillation) when the input signal is switched off. As the phase χ is varied, the measured degenerate gain varies as expected, i.e., the lowest value of -25 dB resulting from the uncontrolled interference between the deamplified signal and the ~ -18 dB leak of input signal through the circulator (see Fig. 1). This strong deamplification and the low noise temperature indicate that our JPA could also be used as a vacuum squeezer. In the inset of Fig. 3, the elongation of the Gaussian spot along the amplified quadrature shows that after parametric amplification, the noise coming from the sample at $f_S = 5.17$ GHz overcomes the noise of the cryogenic amplifier placed at 4 K, the size of which is given by the spot size in the perpendicular direction. In this latter direction, we observe that the spot size is reduced by 1.1% when switching on the parametric pumping. This reduction is twice as small as the 2.2% expected from deamplification of vacuum noise, which is again related to the difficulty to determine the noise temperature of the whole setup.

Finally, the saturation of the JPA is measured by recording the nondegenerate signal power gain as a function of the signal input power $P_{S,n}$ for the same series of pump powers $P_{P,n}$ as before [see Fig. 4(a)]. The signal gain is almost constant at low input power and then decreases above a $P_{P,n}$ dependent threshold in $P_{S,n}$ (however, with a small bump of up to 1 dB just before saturation, possibly due to higher orders in nonlinearity). In practice, the 1 dB compression point is defined as the input power $P_{S,\mathrm{sat}}$ at which the gain is 1 dB lower than at $P_{S,n} = -150$ dBm; it is plotted in Fig. 4(c). The set of measurements of Figs. 4(b) and 4(c) is then compared to the linear model of Sec. I: the power gain, bandwidth, product amplitude gain $\times$ bandwidth, as well as the 1 dB compression point of Eqs. (6)–(9) are calculated by using the values of f_{R1}, p_1, κ_1, and Q_1 indicated above and are plotted in Fig. 4. Given the ± 1 dB uncertainty on the calibration of the signal and pump lines, the nominal input and pump powers were shifted by $+0.8$ and -1.0 dB to match the theory at the lowest pumping power. The agreement between the overall measured data and the model is surprisingly good given the crudeness of the linear model. This fair agreement validates the idea of increasing the number N of SQUIDs to increase the saturation power that scales with N^2. With a single SQUID having the same total inductance as the array implemented here (about 1.7 nH), the saturation would have been $N^2 = 18$ dB lower, as indicated by the dashed line of Fig. 4(c). The discrepancy between experimental data and the model increases with P_p as the nonlinearity plays a more important role, and the actual parametric amplification region extends a bit over the theoretical parametric oscillation region of the linear model (dotted line of Fig. 4).

The performances of the present device are comparable to those of other truly parametric amplifiers recently made. Due to our choice of a rather large $Q \sim 70$, the gain bandwidth product is smaller than what was obtained, for instance, in [23] with $Q \sim 10$. In [15], the direct coupling of the resonator to a cleverly engineered, frequency-dependent external impedance yielded an even lower Q and a bandwidth above 500 MHz. Despite the use of $N = 8$ SQUIDs, the 1 dB compression point obtained here is not very high due to its scaling as $N^2 Q^{-2} p^{-3}$ and to the large participation ratio and quality factors chosen to minimize the pump power. It is, however, about 12 dB above

a similar amplifier made of a single SQUID with about the same critical current [18], and only a few dB below another one [23] with smaller participation ratio p (three times larger critical current i_c) and Q.

In terms of perspectives, Eqs. (8)–(10) predict that with a similar geometry, $N \sim 10$, a smaller $Q \sim 10$, and higher critical currents yielding $p \sim 0.25$, a bandwidth of ∼50 MHz, and a compression point ∼−100 dBm should be obtained at 20dB gain. This would require a larger pump power, i.e., a larger flux modulation $\Phi_{AC} \propto 1/pQ$ at constant gain, which would reach $0.1\Phi_0$. Such a large modulation could be technically difficult to achieve. Increasing the number of SQUIDs is also an obvious optimization axis: If theoretically the array length has just to be kept much smaller than the pump wavelength so that all SQUIDS are pumped in phase, the practical difficulty is to dc flux bias and modulate all of the SQUIDs homogeneously.

In summary, a lumped element, truly parametric Josephson amplifier has been designed and characterized. Its inductance is implemented by a SQUID array to limit its nonlinearity and increase the maximum allowed input power. With a quality factor of 70–80, this simple device provides a gain of up to 30 dB, a product amplitude gain × bandwidth of 61MHz, and a 1 dB compression point of −123 dBm at 20 dB gain. Although its behavior is in agreement with theory and demonstrates the advantage of using a SQUID array, it can still be optimized by reducing both its quality factor and its Josephson participation ratio to the inductance and/or by increasing the number of SQUIDs in the array. Operated close to the quantum limit, this truly parametric amplifier could also be used as a quiet and strong squeezer in degenerate mode or as the first stage of amplification in a superconducting quantum bit readout.

ACKNOWLEDGMENTS

We gratefully acknowledge discussions within the Quantronics group, technical support from P. Orfila, P. Senat, J. C. Tack, and Dominique Duet, as well as financial support from the European Research Contract SCALEQIT.

[1] A. Barone and G. Paterno, *Physics and Applications of the Josephson Effect* (Wiley, New York, 1982), Chap. 11.

[2] B. Yurke, L. R. Corruccini, P. G. Kaminsky, L. W. Rupp, A. D. Smith, A. H. Silver, R. W. Simon, and E. A. Whittaker, Phys. Rev. A **39**, 2519 (1989).

[3] M. A. Castellanos-Beltran and K. W. Lehnert, Appl. Phys. Lett. **91**, 083509 (2007).

[4] K. W. Murch, S. J. Weber, C. Macklin, and I. Siddiqi, Nature (London) **502**, 211 (2013).

[5] B. Abdo, F. Schackert, M. Hatridge, C. Rigetti, and M. Devoret, Appl. Phys. Lett. **99**, 162506 (2011).

[6] Z. R. Lin, K. Inomata1, W. D. Oliver, K. Koshino, Y. Nakamura, J. S. Tsai, and T. Yamamoto, Appl. Phys. Lett. **103**, 132602 (2013).

[7] J. D. Teufel, T. Donner, Dale Li, J. W. Harlow, M. S. Allman, K. Cicak, A. J. Sirois, J. D. Whittaker, K. W. Lehnert, and R. W. Simmonds, Nature (London) **475**, 359 (2011).

[8] R. Vijay, C. Macklin, D. H. Slichter, S. J. Weber, K. W. Murch, R. Naik, A. N. Korotkov, and I. Siddiqi, Nature (London) **490**, 77 (2012).

[9] G. de Lange, D. Ristè, M. J. Tiggelman, C. Eichler, L. Tornberg, G. Johansson, A. Wallraff, R. N. Schouten, and L. DiCarlo, Phys. Rev. Lett. **112**, 080501 (2014).

[10] F. Mallet, M. A. Castellanos-Beltran, H. S. Ku, S. Glancy, E. Knill, K. D. Irwin, G. C. Hilton, L.R. Vale, and K. W. Lehnert, Phys. Rev. Lett. **106**, 220502 (2011).

[11] E. P. Menzel, R. Di Candia, F. Deppe, P. Eder, L. Zhong, M. Ihmig, M. Haeberlein, A. Baust, E. Hoffmann, D. Ballester, K. Inomata, T. Yamamoto, Y. Nakamura, E. Solano, A. Marx, and R. Gross, Phys. Rev. Lett. **109**, 250502 (2012).

[12] K. W. Murch, S. J. Weber, K. M. Beck, E. Ginossar, and I. Siddiqi, Nature (London) **499**, 62 (2013).

[13] O. Yaakobi, L. Friedland, C. Macklin, and I. Siddiqi, Phys. Rev. B **87**, 144301 (2013).

[14] B. H. Eom, P. K. Day, H. G. LeDuc, and J. Zmuidzinas, Nat. Phys. **8**, 623 (2012).

[15] Josh Mutus, Ted White, Rami Barends, Yu Chen, Zijun Chen, Ben Chiaro, Andrew Dunsworth, Evan Jeffrey, Julian Kelly, Anthony Megrant, Charles Neill, Peter O'Malley, Pedram Roushan, Daniel Sank, Amit Vainsencher, James Wenner, Kyle Sundqvist, Andrew Cleland, and John Martinis, arXiv:1401.3799.

[16] A. Narla, K. M. Sliwa, M. Hatridge, S. Shankar, L. Frunzio, R. J. Schoelkopf, and M. H. Devoret, App. Phys. Lett. **104**, 232605 (2014).

[17] C. M. Wilson, T. Duty, M. Sandberg, F. Persson, V. Shumeiko, and P. Delsing, Phys. Rev. Lett. **105**, 233907 (2010).

[18] T. Yamamoto, K. Inomata, M. Watanabe, K. Matsuba, T. Miyazaki, W. D. Oliver, Y. Nakamura, and J. S. Tsai, Appl. Phys. Lett. **93**, 042510 (2008).

[19] W. Wustmann and V. Shumeiko, Phys. Rev. B **87**, 184501 (2013).

[20] C. Eichler and A. Wallraff, EPJ Quantum Technol. **1**, 2 (2014).

[21] A. Palacios-Laloy, Ph.D. thesis, Université Pierre et marie Curie, Paris, France, 2010.

[22] A. A. Clerk, M. H. Devoret, S. M. Girvin, Florian Marquardt, and R. J. Schoelkopf, Rev. Mod. Phys. **82**, 1155 (2010).

[23] M. Hatridge, R. Vijay, D. H. Slichter, John Clarke, and I. Siddiqi, Phys. Rev. B **83**, 134501 (2011).

Multiplexed readout of transmon qubits with Josephson bifurcation amplifiers

V. Schmitt,[1] X. Zhou,[1] K. Juliusson,[1] B. Royer,[2] A. Blais,[2,3] P. Bertet,[1] D. Vion,[1] and D. Esteve[1]
[1]*Quantronics group, Service de Physique de l'Etat Condensé, CNRS UMR 3680, CEA Saclay, 91191 Gif-sur-Yvette, France*
[2]*Département de Physique, Université de Sherbrooke, Sherbrooke, Québec, Canada*
[3]*Canadian Institute for Advanced Research, Toronto, Ontario, Canada*
(Received 1 September 2014; revised manuscript received 23 October 2014; published 22 December 2014)

Achieving individual qubit readout is a major challenge in the development of scalable superconducting quantum processors. We have implemented the multiplexed readout of a four transmon qubit circuit using nonlinear resonators operated as Josephson bifurcation amplifiers. We demonstrate the simultaneous measurement of Rabi oscillations of the four transmons. We find that multiplexed Josephson bifurcation is a high-fidelity readout method, the scalability of which is not limited by the need of a large-bandwidth, nearly quantum-limited amplifier as is the case with linear readout resonators.

DOI: 10.1103/PhysRevA.90.062333 PACS number(s): 03.67.Lx, 74.78.Na, 85.25.Cp

I. INTRODUCTION

Since the demonstration of quantum coherence in single Cooper pair boxes [1,2], the coherence time of superconducting quantum bits (qubits) has increased by orders of magnitude [3–5], and high-fidelity operation has been achieved [6,7]. Quantum speedup of the Deutsch-Josza [8], Grover search [9], and Shor's factorization [10] algorithms, as well as deterministic teleportation [11] and measurement-based entanglement [12,13] protocols, were recently demonstrated in circuits with a few (2–5) qubits. Nevertheless, no superconducting quantum processor able to run algorithms demonstrating the power of quantum computation [14] has been operated yet. Making operational processors with a large number of qubits faces the challenge of maintaining quantum coherence in complex circuits, of implementing multiple individual qubit readout, and of performing high-fidelity gates in parallel with quantum error correction. Much effort is presently devoted to solving these different scalability issues [15].

We address here the problem of simultaneous readout of transmon qubits [3] in a single shot. Readout of Josephson qubits is commonly performed by coupling each of them to a linear microwave resonator whose resonance frequency is shifted by a qubit-state-dependent value $\pm\chi$ [16]. Measuring the reflection or the transmission of a microwave pulse by the resonator then reveals the qubit state [17]. High-fidelity readout has been reached in several experiments [13,18] by using quantum-limited Josephson parametric amplifiers [19]. Besides, simultaneous readout of several qubits was achieved by using resonators with staggered frequencies, all coupled to a single line on which microwave readout pulses were frequency multiplexed [20]. However, reaching single-shot fidelity in this case requires parametric amplifiers with both large bandwidth to accommodate all of these frequencies and large saturation power to linearly amplify all simultaneous pulses. The recent implementation of this method in a four-transmon circuit [21] achieved fast readout with a fidelity compatible with surface-code error correction.

An alternative method for transmon readout that does not require a Josephson parametric amplifier consists in turning each readout resonator into a nonlinear one, operated as a Josephson bifurcation amplifier (JBA) [22–24]. Indeed, driving a JBA with a suitable microwave pulse yields a fast and hysteretic transition between dynamical states with widely different field amplitude and phase, which can discriminate with high fidelity the transmon ground state $|0\rangle$ from its excited states $|i\rangle = |1\rangle, |2\rangle$. The determination of the dynamical state then requires a subsequent longer measuring time at a lower power level [25]. In this work, we demonstrate multiplexed high-fidelity single-shot readout of four transmons using the circuit described in Fig. 1.

II. EXPERIMENTAL SETUP

The chip consists of four cells, labeled $i = 1$–4, coupled to a single transmission line that carries the multiple qubit control and JBA signals. The sample is fabricated on a sapphire substrate in a two-step lithography process. The transmission line and the readout resonators are first patterned in a niobium film using optical lithography and reactive ion etching. The transmons and JBA junctions are then fabricated by electron lithography and double-angle evaporation of aluminum through a suspended shadow mask, with intermediate oxidation. It is measured in a dilution refrigerator with base temperature 30 mK. Each transmon B_i includes a superconducting quantum interference device (SQUID) [see Fig. 1(d)] that makes its $|0\rangle \leftrightarrow |1\rangle$ transition frequency f_{Bi}^{01} tunable with magnetic field [26]. In this experiment dedicated to readout, only a global magnetic field produced by a single coil can be applied to all transmons simultaneously. Each qubit is coupled to its JBA with a coupling constant $g_i/2\pi \simeq 85$ MHz. The JBAs have staggered frequencies f_{Ri} around 7.75 GHz separated by 61, 69, and 96 MHz, and quality factors of 2500, 2550, 2650, and 2200. All have the same Kerr nonlinearity [27] $K/2\pi \backsimeq -225$ kHz (that corresponds to a frequency reduction of 112.5 kHz per photon).

The qubits are controlled resonantly and we note θ_i^{kl} a rotation of qubit i by an angle θ between its states $|k\rangle$ and $|l\rangle$. The microwave control pulses at frequencies f_{Bi}^{kl} are obtained by translating the frequency f_{B0} of a single carrier using the technique of single-sideband mixing: using an IQ mixer, the carrier is multiplied by two signals I and Q delivered by an arbitrary waveform generator (AWG). I and Q are a sum of signals at frequencies $\delta_{Bi}^{kl} = f_{Bi}^{kl} - f_{B0}$, with suitable envelopes and phases. Another mixer is used to produce the JBA drive signals in the same way, that is by

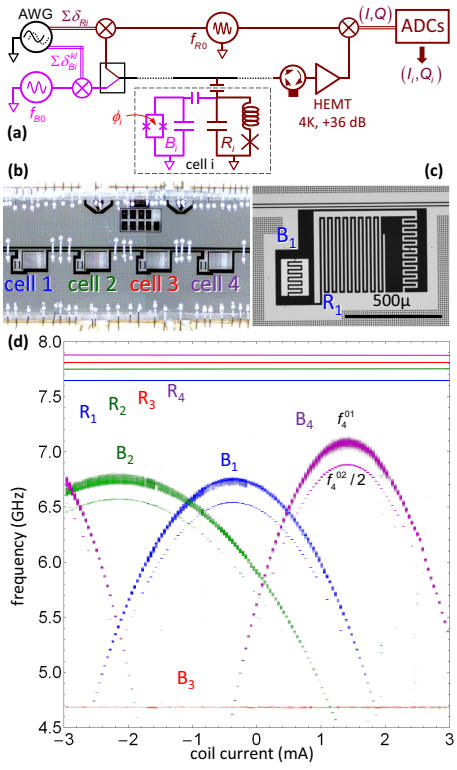

FIG. 1. (Color online) Readout of transmon qubits based on multiplexed JBAs. (a) Schematic electrical circuit. Four qubit-readout cells i (only one shown) are capacitively coupled to a microwave transmission line (black central line). Each cell is made of a tunable transmon qubit B_i [26] of transition frequencies f_{Bi}^{kl}, capacitively coupled to a JBA resonator R_i of frequency f_{Ri}. Control and readout pulses are produced and analyzed as described in the text. (b), (c) Optical micrographs showing (b) the measured chip with four cells, and (c) cell 1 with transmon B_1 and lumped element JBA R_1. (d) Spectroscopy of the four qubits B_i and readouts R_i as a function of the coil current inducing a global magnetic field. Frequencies f_{Ri} are indicated by lines, whereas qubit spectra are obtained by exciting the qubits with a 4 μs long single-frequency control pulse, reading out simultaneously the four JBAs, and color-plotting their switching probabilities.

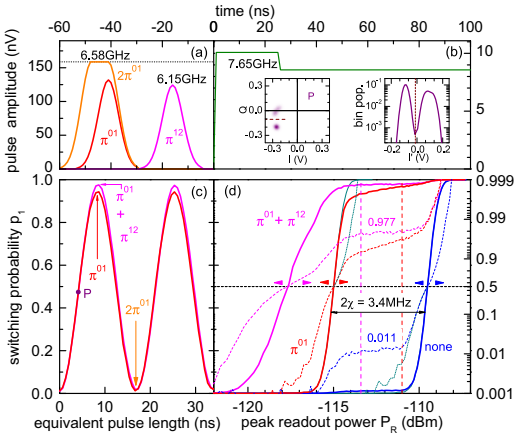

FIG. 2. (Color online) Characterization of cell 1 at detuning $\Delta_1/2\pi = 1.08$ GHz. (a) Microwave control pulse envelopes for π_1^{01}, π_1^{12}, and $(2\pi)_1^{01}$ rotations (see text). The dotted line shows the maximum amplitude used. (b) Beginning of the microwave readout pulse envelope (solid green line). Left inset: Density plot of (I_1, Q_1) obtained from 10^5 repetitions of a $(\pi/2)_1^{01}$ pulse [purple dot P in (c)] followed by a readout pulse. Right inset: Corresponding histogram (population in 10 mV wide bins) along the direction I' joining the two cloud centers. (c) Rabi oscillation of p_1 as a function of the equivalent control pulse length (duration of a rectangular pulse with maximum amplitude), without (red) and with (magenta) shelving (see text). (d) Probability p_1 with no qubit control pulse (blue) and after a π_1^{01} pulse alone (red) or with shelving (magenta). Solid lines represent p_1 on a linear scale (left axis) whereas dashed and dotted lines show it using a double-logarithmic scale below and above 0.5 (right axis). Thin solid and dotted lines represent "ideal" S curves (see text). The vertical dashed lines indicate the pulse power yielding the highest readout contrasts with (left) and without (right) shelving.

IQ-mixing a carrier f_{R0} with a sum of signals at frequencies $\delta_{Ri} = f_{Ri} - f_{R0}$. Figure 1(a) illustrates the setup used. Driven at frequencies f_{Ri} chosen 9 MHz below their bare frequencies (with the transmon in its ground state), the JBAs switch at bifurcation from a state with average photon number 11 ± 1 to a state between 40 and 100 photons [27,28].

The transmon-JBA detuning $\Delta_i/2\pi = f_{Bi}^{01} - f_{Ri}$ determines both the readout sensitivity (through χ_i) and the Purcell energy relaxation rate $T_{P,i}^{-1} \simeq 2\pi f_{Ri}/Q_i(g_i/\Delta_i)^2$ of the qubit through the resonator input line [3]. The readout pulses have a first short 25 ns long step [see Fig. 2(b)] and a longer 2 μs latching step at 85% of the peak power. In practice, bifurcation develops (or not) between 50 ns and 500 ns, whereas I and Q are averaged between 325 ns and 1325 ns. Readout pulses can overlap in time [see for instance Fig. 4(a)] so that the output signal contains contributions of different JBAs. In order to extract these contributions, the output signal is demodulated in two steps: An analog demodulation at the readout carrier frequency f_{R0} is first performed; the resulting signal is then digitized at 2 Gsample/s with a 1 GHz analog bandwidth that widely covers the 250 MHz frequency range spanned by the four JBAs; it is then demodulated numerically by a dedicated PC, which directly multiplies it with cosine functions at frequencies δ_{Ri} and averages the result. The outcome of a readout sequence is four points (I_i, Q_i) in the in-phase and quadrature plane (one for each JBA frequency f_{Ri}), as shown in Fig. 3(b). The outcome of a readout sequence is thus four points (I_i, Q_i) in the in-phase and quadrature plane.

Spectroscopic data of the qubits and readout resonators as a function of the coil current are displayed in Fig. 1(d). These data were recorded at high excitation power to show spectroscopic lines at both f_{Bi}^{01} and $f_{Bi}^{02}/2$. Frequencies f_{Bi}^{01} of tunable qubits $B_{1,2,4}$ peak at about 0.7–1 GHz below the

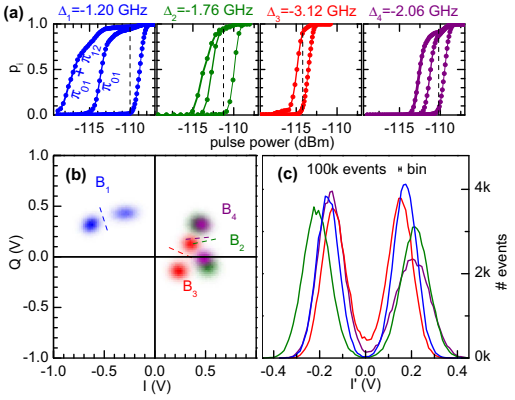

FIG. 3. (Color online) Simultaneous readout of the four qubits at a magnetic field such that $\Delta_{1-4}/2\pi = (-1.2, -1.76, -3.12, -2.06)$ GHz. (a) Switching probabilities p_i of the four readouts as a function of readout power P_R, after no control pulse (right curves in each panel), and after a π_i^{01} pulse without (middle) and with shelving (left curves for $B_{1,2,3}$). Dashed vertical lines indicate the optimal readout powers used in (b) and (c) and in Fig. 4 (shelving used only for B_2 and B_4). (b) Density plots of the four (I_i, Q_i) obtained from 10^5 measurements. Segments indicate the separatrices between switching and nonswitching events. (c) Corresponding histograms along the lines perpendicular to separatrices.

frequency of their respective JBA, and the anharmonicity $\alpha = f_{Bi}^{12} - f_{Bi}^{01} \simeq -434 \pm 2$ MHz. The measured relaxation times of all transmons are found to be in the range $T_1 = 1.7$–3.2 μs for $|\Delta_i/2\pi| \gtrsim 1$ GHz. This is significantly below the Purcell limit $T_P > 8$ μs and shorter than in comparable 2D transmon circuits [21], probably due to dielectric losses [29].

III. READOUT PERFORMANCE

All qubit-readout cells yielded similar performances at equal detuning Δ_i. Performance of cell 1, operated at a qubit-JBA detuning $\Delta_1/2\pi = -1.08$ GHz, is summarized in Fig. 2. All qubit control pulses have 3σ long Gaussian rises and falls with $\sigma = 4$ ns, as shown in Fig. 2(a). Numerical simulations of the transmon dynamics including its three lowest levels show that such control pulses do not introduce preparation errors larger than 0.1% [30]. Readout is performed either immediately after applying a θ_1^{01} Rabi pulse, or after a subsequent π_1^{12} pulse that shelves the excited qubit in state $|2\rangle$, as in [23]. This shelving decreases the error made in measuring the excited qubit by blocking its relaxation down to state $|0\rangle$ before the measurement is completed [31].

The density plot of (I_1, Q_1) obtained from 10^5 repetitions of the readout after a $(\pi/2)_1^{01}$ pulse is shown in the left inset of Fig. 2(b). The two clouds with a small relative overlap of order 10^{-5} (estimated from the corresponding histogram in the right inset) reveal an excellent discrimination of the JBA states. The fidelity of the qubit to JBA mapping is investigated by measuring the variations of the switching probability p_1 as a function of the peak readout power P_R. These so-called S curves are shown in Fig. 2(d) in three different cases: when the qubit is left in its ground state $|0\rangle$ with no applied control pulse (blue), after a π_1^{01} pulse aiming at preparing state $|1\rangle$ (red), and after a π_1^{01} pulse followed by a π_1^{12} shelving pulse (magenta). One observes that the S curves for the two states $|0\rangle$ and $|1\rangle$ are separated in P_R by about 5.5 dB (or equivalently by $2\chi = 3.4$ MHz in resonator or drive frequency), which is much larger than the 2.4 dB (1.5 MHz) width of the ground-state S curve, defined here by $1\% < p < 99\%$. This result implies that, in the absence of preparation errors and relaxation before and during measurement, readout errors would be negligible.

In practice, at the optimal powers P_R [see Fig. 2(d)], the measured total errors are 1.1% for $|0\rangle$, and 3.1% and 2.2% for $|1\rangle$ without and with shelving, respectively. These errors result from two effects. First, the 1.1% error in the ground state is due to a residual thermal excitation of the qubit (corresponding to a qubit temperature of 70 mK), as evidenced by the flat shoulder on the ground-state S curve at low power. This spurious excitation is also responsible for the same absolute 1.1% error in preparing state $|1\rangle$. The remaining errors in $|1\rangle$ are thus 2.0% and 1.1% without and with shelving. Second, numerical simulations including relaxation during the control pulses, using the independently measured relaxation time $(\Gamma_1^{10})^{-1} = 2.0$ μs, account for absolute errors of 0.6% and 1.1% without and with shelving. The shelving case is thus fully understood: errors in $|1\rangle$ are only due to thermal population and relaxation at preparation, and relaxation to $|0\rangle$ during readout is efficiently blocked as proven by the horizontal plateau at $p_1(P_R) \simeq 0.98$. The intrinsic readout fidelity with shelving is thus excellent.

Without shelving, the remaining readout error is 1.4% at the optimal P_R, but with a slow increase of $p_1(P_R)$ as it approaches 1. This behavior is not understood and quantum simulation of the JBA + excited qubit dynamics is needed to address this question. Nevertheless, to infer what would be the intrinsic readout fidelity in the absence of preparation errors and extra relaxation at readout, we reconstruct ideal S curves: for the ground state, the lower part $p_1 \leqslant 0.5$ is replaced by the S curve measured for the qubit excited state and shifted in power to remove the effect of residual thermal excitation; for the excited state, its upper part $p_1 > 0.5$ is replaced by the one measured in the ground state and shifted in power to remove the effect of relaxation at readout. These ideal S curves, illustrated by thin solid and dotted lines in Fig. 2(d), give intrinsic readout errors lower than 2×10^{-3} both for the ground and excited states.

We now discuss the simultaneous readout of the four qubits. Given the lack of individual transmon tunability, a magnetic field leading to not too large detunings $\Delta_i/2\pi = (-1.2, -1.76, -3.12, -2.06)$ GHz was applied. In addition, longer readout pulses with 50 ns measurement step and 2 μs latching step are used, as shown in Fig. 4(a). The measurement outcomes for the four qubits prepared with control pulses close to $(\pi/2)_{01}$ and with π_{12} shelving only for B_2 and B_4 [32] are shown in Fig. 3. The density plots in the (I_i, Q_i) planes are shown with their best separatrix between switching and nonswitching events. As illustrated in Fig. 3(c), the switching histograms measured along an axis perpendicular to the separatrix show a good separation, albeit smaller than obtained at the optimal working point of each

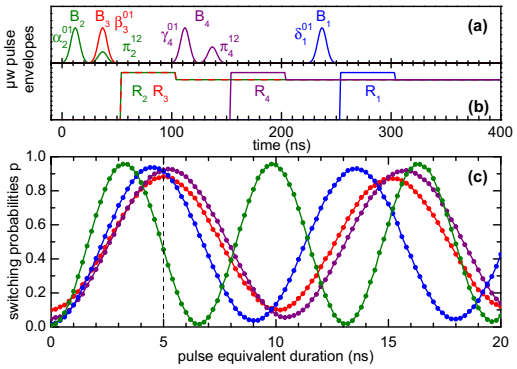

FIG. 4. (Color online) Simultaneous measurement of Rabi oscillations of the four qubits at readout powers indicated in Fig. 3. Microwave control (a) and readout (b) pulse envelopes used at 5 ns equivalent Rabi pulse duration. Only B_2 and B_4 are shelved on their second excited levels before readout. (c) Simultaneous Rabi oscillations of p_{1-4} as a function of the equivalent control pulse duration.

cell. The standard deviation of the switching probability for all cells was checked to decrease as expected for independent events.

Having characterized simultaneous readout of the four qubits, we now include qubit drive (see Fig. 4). For simplicity, the control pulses are not applied simultaneously in order to avoid having to take into account the qubit ac Stark shift resulting from other qubit drives. The control and readout pulses are shown in Fig. 4(a). The switching curves of the four JBAs are shown in Fig. 4(b) after no qubit pulse, and after a π_i^{01} pulse without or with shelving. Rabi oscillations of the four qubits, measured at the optimal powers indicated in Fig. 4(b), are shown in Fig. 4(c). These data show that JBA readout is compatible with qubit driving and simultaneous multiplexed operation. The overall performance of our multiplexed JBA is thus comparable with that achieved using linear dispersive readout and parametric amplifiers [21], albeit with larger errors *not* due to the readout method itself.

IV. CONCLUSION

A natural question that arises is the maximum number of transmons that multiplexed JBA could handle. Indeed, due the nonlinear character of JBAs, bifurcation of a given JBA can be affected by the dynamics of other JBAs that are close in frequency. How close their frequencies can be without inducing readout crosstalk is not known. In the present setup, this phenomenon was quantified by preparing B_1 in $|0\rangle$ or $|1\rangle$ and B_2 in a superposition $(|0\rangle + |1\rangle)/\sqrt{2}$. The difference between the values of p_2 for the two B_1 states gives a crosstalk of only $0.2\% \pm 0.05\%$. This low value shows that a JBA frequency separation of 60 MHz is conservative, and therefore that more qubits could be read out in parallel.

In conclusion, multiplexed JBA readout of transmons has an excellent intrinsic readout fidelity when shelving is used, and is compatible with driving and reading transmons in a small qubit register. Its scalability, limited by the interactions between JBAs with close frequencies, is still under investigation, but the present results suggest that reading out a ten-qubit register is possible.

ACKNOWLEDGMENTS

We gratefully acknowledge discussions within the Quantronics group, and technical support from P. Orfila, P. Senat, J. C. Tack, and D. Duet. This work was supported by the European FP7 QIPC project ScaleQIT, by the CCQED network, and by the NSERC (Canada).

[1] Y. Nakamura, Yu. A. Pashkin, and J. S. Tsai, Nature (London) **398**, 786 (1999).

[2] D. Vion, A. Aassime, A. Cottet, P. Joyez, H. Pothier, C. Urbina, D. Esteve, and M. H. Devoret, Science **296**, 886 (2002).

[3] J. Koch, Terri M. Yu, Jay Gambetta, A. A. Houck, D. I. Schuster, J. Majer, Alexandre Blais, M. H. Devoret, S. M. Girvin, and R. J. Schoelkopf, Phys. Rev. A **76**, 042319 (2007).

[4] J. A. Schreier, A. A. Houck, Jens Koch, D. I. Schuster, B. R. Johnson, J. M. Chow, J. M. Gambetta, J. Majer, L. Frunzio, M. H. Devoret, S. M. Girvin, and R. J. Schoelkopf, Phys. Rev. B **77**, 180502 (2008).

[5] Hanhee Paik, D. I. Schuster, Lev S. Bishop, G. Kirchmair, G. Catelani, A. P. Sears, B. R. Johnson, M. J. Reagor, L. Frunzio, L. I. Glazman, S. M. Girvin, M. H. Devoret, and R. J. Schoelkopf, Phys. Rev. Lett. **107**, 240501 (2011).

[6] A. Dewes, F. R. Ong, V. Schmitt, R. Lauro, N. Boulant, P. Bertet, D. Vion, and D. Esteve, Phys. Rev. Lett. **108**, 057002 (2012).

[7] R. Barends, J. Kelly, A. Megrant, A. Veitia, D. Sank, E. Jeffrey, T. C. White, J. Mutus, A. G. Fowler, B. Campbell, Y. Chen, Z. Chen, B. Chiaro, A. Dunsworth, C. Neill, P. O'Malley, P. Roushan, A. Vainsencher, J. Wenner, A. N. Korotkov, A. N. Cleland, and John M. Martinis, Nature (London) **508**, 500 (2014).

[8] T. Yamamoto, M. Neeley, E. Lucero, R. C. Bialczak, J. Kelly, M. Lenander, M. Mariantoni, A. D. O'Connell, D. Sank, H. Wang, M. Weides, J. Wenner, Y. Yin, A. N. Cleland, and J. M. Martinis, Phys. Rev. B **82**, 184515 (2010).

[9] A. Dewes, R. Lauro, F. R. Ong, V. Schmitt, P. Milman, P. Bertet, D. Vion, and D. Esteve, Phys. Rev. B **85**, 140503 (2012).

[10] Erik Lucero, R. Barends, Y. Chen, J. Kelly, M. Mariantoni, A. Megrant, P. O'Malley, D. Sank, A. Vainsencher, J. Wenner, T. White, Y. Yin, A. N. Cleland, and John M. Martinis, Nat. Phys. **8**, 719 (2012).

[11] L. Steffen, Y. Salathe, M. Oppliger, P. Kurpiers, M. Baur, C. Lang, C. Eichler, G. Puebla-Hellmann, A. Fedorov, and A. Wallraff, Nature (London) **500**, 319 (2013).

[12] D. Ristè, M. Dukalski, C. A. Watson, G. de Lange, M. J. Tiggelman, Ya. M. Blanter, K. W. Lehnert, R. N. Schouten, and L. DiCarlo, Nature (London) **502**, 350 (2013).

[13] N. Roch, M. E. Schwartz, F. Motzoi, C. Macklin, R. Vijay, A. W. Eddins, A. N. Korotkov, K. B. Whaley, M. Sarovar, and I. Siddiqi, Phys. Rev. Lett. **112**, 170501 (2014).

[14] M. A. Nielsen and I. L. Chuang, *Quantum Computation and Quantum Information* (Cambridge University Press, Cambridge, 2000).

[15] M. H. Devoret and R. J. Schoelkopf, Science **339**, 1169 (2013).

[16] A. Blais, J. Gambetta, A. Wallraff, D. I. Schuster, S. M. Girvin, M. H. Devoret, and R. J. Schoelkopf, Phys. Rev. A **75**, 032329 (2007).

[17] A. Wallraff, D. I. Schuster, A. Blais, L. Frunzio, J. Majer, M. H. Devoret, S. M. Girvin, and R. J. Schoelkopf, Phys. Rev. Lett. **95**, 060501 (2005).

[18] L. Sun, A. Petrenko, Z. Leghtas, B. Vlastakis, G. Kirchmair, K. M. Sliwa, A. Narla, M. Hatridge, S. Shankar, J. Blumoff, L. Frunzio, M. Mirrahimi, M. H. Devoret, and R. J. Schoelkopf, Nature (London) **511**, 444 (2014).

[19] M. A. Castellanos-Beltran, K. D. Irwin, G. C. Hilton, L. R. Vale, and K. W. Lehnert, Nat. Phys. **4**, 929 (2008).

[20] M. Jerger, S. Poletto, P. Macha, U. Hübner, E. Il'ichev, and A. V. Ustinov, Appl. Phys. Lett. **101**, 042604 (2012).

[21] Evan Jeffrey, Daniel Sank, J. Y. Mutus, T. C. White, J. Kelly, R. Barends, Y. Chen, Z. Chen, B. Chiaro, A. Dunsworth, A. Megrant, P. J. J. O'Malley, C. Neill, P. Roushan, A. Vainsencher, J. Wenner, A. N. Cleland, and John M. Martinis, Phys. Rev. Lett. **112**, 190504 (2014).

[22] V. E. Manucharyan, E. Boaknin, M. Metcalfe, R. Vijay, I. Siddiqi, and M. H. Devoret, Phys. Rev. B **76**, 014524 (2007).

[23] F. Mallet, Florian R. Ong, A. Palacios-Laloy, F. Nguyen, P. Bertet, D. Vion, and D. Esteve, Nat. Phys. **5**, 791 (2009).

[24] P. C. de Groot, A. F. van Loo, J. Lisenfeld, R. N. Schouten, A. Lupascu, C. J. P. M. Harmans, and J. E. Mooij, Appl. Phys. Lett. **96**, 123508 (2010).

[25] Because a new readout can only start after the resonator field has decayed, this method is better suited for single-shot readout than for continuous measurements of a qubit [20].

[26] B_3 has one of its two Josephson junctions open and is consequently not tunable.

[27] F. R. Ong, M. Boissonneault, F. Mallet, A. Palacios-Laloy, A. Dewes, A. C. Doherty, A. Blais, P. Bertet, D. Vion, and D. Esteve, Phys. Rev. Lett. **106**, 167002 (2011).

[28] M. Boissonneault, A. C. Doherty, F. R. Ong, P. Bertet, D. Vion, D. Esteve, and A. Blais, Phys. Rev. A **85**, 022305 (2012).

[29] C. M. Quintana, A. Megrant, Z. Chen, A. Dunsworth, B. Chiaro, R. Barends, B. Campbell, Yu Chen, I.-C. Hoi, E. Jeffrey, J. Kelly, J. Y. Mutus, P. J. J. O'Malley, C. Neill, P. Roushan, D. Sank, A. Vainsencher, J. Wenner, T. C. White, A. N. Cleland, and John M. Martinis, Appl. Phys. Lett. **105**, 062601 (2014).

[30] Consequently, we do not use the DRAG correction technique used in J. M. Chow, L. DiCarlo, J. M. Gambetta, F. Motzoi, L. Frunzio, S. M. Girvin, and R. J. Schoelkopf, Phys. Rev. A **82**, 040305 (2010).

[31] This blockade occurs because the direct relaxation from state $|2\rangle$ to $|0\rangle$ involves a very small matrix element; consequently, the decay to $|0\rangle$ results from the two relaxation processes $|2\rangle \rightarrow |1\rangle$ and $|1\rangle \rightarrow |0\rangle$ in series, and varies quadratically at short time, as $1-(\Gamma^{\mathrm{eff}}t)^2$ with $\Gamma^{\mathrm{eff}} = \sqrt{\Gamma_1^{21}\Gamma_1^{10}} \sim \sqrt{2}\Gamma_1^{10}$. Note however that shelving takes the qubit out of the computational Hilbert space and thus makes the readout destructive.

[32] Shelving was neither used for qubit B_1 because f_1^{12} being too close from f_4^{01}, it would have driven qubit B_4, nor for qubit B_3 whose frequency f_3^{12} was outside the bandpass of the driving line.